

Available to the Public

(NASA-CR-114638) THE APPLICABILITY OF
FRAME IMAGING FROM A SPINNING SPACECRAFT.
VOLUME 2: TECHNICAL REPORT (CBS Labs.)
333 p HC \$19.75 CSCL 14E

N74-17164

G3/14 Unclas
30554

THE APPLICABILITY OF FRAME IMAGING
FROM A SPINNING SPACECRAFT

VOLUME 2

TECHNICAL REPORT

by Robert A. Botticelli, Richard O. Johnson,
and Gerald N. Wallmark

June 30, 1973

Prepared Under Contract NAS 2-7107 by
CBS Laboratories, A Division of
Columbia Broadcasting System, Incorporated
Stamford, Connecticut 06905

for

AMES RESEARCH CENTER
NATIONAL AERONAUTICS AND SPACE ADMINISTRATION

TABLE OF CONTENTS

SECTION OR PARAGRAPH	TITLE	PAGE
I	INTRODUCTION	1
1.1	BACKGROUND AND STUDY GOALS	1
1.2	ORGANIZATION OF THE VOLUME	2
1.3	CONCLUSIONS OF THE STUDY	6
II	SELECTION OF CANDIDATE SYSTEMS	11
2.1	INTRODUCTION	11
2.2	BASIS FOR CANDIDATE SELECTION	12
2.3	CANDIDATE SYSTEMS SELECTED	13
2.3.1	SLOW-SCAN VIDICON	15
2.3.2	SILICON VIDICON	16
2.3.3	SIT VIDICON	17
2.3.4	SEC VIDICON	18
2.3.5	RETURN BEAM VIDICON	19
2.3.6	SILICON DIOXIDE VIDICON	20
2.3.7	ELECTROSTATIC CAMERA SYSTEM	21
2.3.8	CHARGE-COUPLED IMAGER	22
2.3.9	IMAGE ORTHICON	24
2.3.10	IMAGE ISOCON	25
2.3.11	SMOOTHING DISSECTOR	26
III	CAMERA MODELING	27
3.1	INTRODUCTION	27
3.2	EXPOSURE CALCULATION FOR ANALYTICAL MODELS	27

TABLE OF CONTENTS

SECTION OR PARAGRAPH	TITLE	PAGE
3.2.1	GENERAL RELATIONSHIPS	28
3.2.1.1	Orbiting Camera Relationships	28
3.2.2	DETECTOR QUANTUM EFFICIENCY - GENERAL REQUIREMENTS	30
3.2.2.1	Orbiting Camera Relationships	30
3.3	MODULATION TRANSFER FUNCTION	31
3.3.1	COMPONENT MODULATION TRANSFER FUNCTIONS	34
3.3.1.1	Camera System MTF	34
3.3.1.2	Image Motion MTF	34
3.3.1.3	Lens MTF	37
3.3.1.4	Sensor MTF	37
3.3.1.4.1	Readout MTF	38
3.3.1.4.2	Target MTF	38
3.3.1.5	Image Section MTF	41
3.4	AERIAL IMAGE MODULATION CURVES	42
3.4.1	APPLICATION OF AIM CURVES	45
3.5	SIGNAL-TO-NOISE RATIO	47
3.5.1	SIGNAL-TO-NOISE RATIO AFTER RECONSTRUCTION	47
3.6	RESOLUTION RELATIONSHIPS	49
3.7	MAXIMUM SIGNAL-TO-NOISE RATIO	50
IV	COMPUTER PROGRAMS	51
4.1	INTRODUCTION	51
4.2	COMPUTER PROGRAMS	51

TABLE OF CONTENTS

SECTION OR PARAGRAPH	TITLE	PAGE
V	RADIATION AND RELIABILITY FACTORS	53
5.1	INTRODUCTION	53
5.2	DISCUSSION OF RADIATION	53
5.2.1	MISSION DURATION	53
5.2.2	EXPECTED RADIATION DOSAGE	54
5.2.3	RTG RADIATION	54
5.2.4	JOVIAN RADIATION BELTS	54
5.3	SENSOR RADIATION RESISTANCE DATA	55
5.3.1	SEC TUBE	57
5.3.2	SIT TUBE/SILICON VIDICON	58
5.3.3	CHARGE-COUPLED DEVICES	60
5.3.4	ELECTROSTATIC STORAGE CAMERA	61
5.3.5	SLOW-SCAN VIDICON	63
5.3.6	CONCLUSIONS	64
5.4	DISCUSSION OF RELIABILITY	65
5.4.1	RELIABILITY ASSESSMENT	65
5.4.2	CANDIDATE CAMERA SYSTEM RELIABILITY	67
5.4.3	CONCLUSIONS	69
VI	IMAGE MOTION ANALYSIS	71
6.1	INTRODUCTION	71
6.2	PERFORMANCE ANALYSIS OF IDEAL SENSORS	71
6.2.1	SNR DEGRADATION DUE TO IMAGE MOTION	72
6.2.1.1	Motion of the Spacecraft Relative to Jupiter	72

TABLE OF CONTENTS

SECTION OR PARAGRAPH	TITLE	PAGE
6.2.1.2	Spacecraft Rotation	74
6.2.1.3	Platform Motion	76
6.2.1.4	Conclusions	77
6.2.1.5	Image-Motion Transfer Functions	77
6.2.2	OPTIMIZATION OF EXPOSURE TIME	78
6.2.3	PERFORMANCE OF "IDEAL SENSORS" UNDER NO-IMAGE- MOTION-COMPENSATION CONDITIONS	79
6.3	PERFORMANCE ANALYSIS OF SELECTED CANDIDATE SENSORS UNDER NO-IMAGE-MOTION-COMPENSATION CONDITIONS	80
6.3.1	OPTIMIZATION OF EXPOSURE TIME	82
6.3.2	RESULTS OF PERFORMANCE ANALYSIS OF SELECTED SENSORS UNDER NO-IMAGE MOTION-COMPENSATION CONDITIONS	84
6.4	PERFORMANCE OF SELECTED CANDIDATE SENSORS UNDER COMPLETE-IMAGE-MOTION-COMPENSATION CONDITIONS	89
VII	WORST-CASE ANALYSIS, COMPARISON OF CAMERAS, AND SELECTION OF BEST SYSTEMS	93
7.1	INTRODUCTION	93
7.2	SELECTION CRITERIA AND REQUIREMENTS	94
7.2.1	STUDY CONSTRAINTS	94
7.2.2	PERFORMANCE REQUIREMENTS	96
7.2.2.1	Imaging Requirements	96
7.2.2.2	Image Smear Constraint	97
7.2.2.3	Data Transmission Requirements	98
7.2.3	PRACTICAL SYSTEM PARAMETERS	99
7.2.4	OTHER REQUIREMENTS	100

TABLE OF CONTENTS

SECTION OR PARAGRAPH	TITLE	PAGE
7.3	WORST-CASE PARAMETRIC ANALYSIS	100
7.3.1	AERIAL IMAGE MODULATION CURVES	101
7.3.2	CANDIDATE SENSOR AIM CURVES	104
7.3.3	SIGNAL-TO-NOISE RATIO VERSUS RESOLUTION	109
7.3.4	RESOLVING POWER VERSUS EXPOSURE	114
7.4	SELECTION OF CAMERA SYSTEMS FOR DETAILED STUDY	118
7.4.1	SEC VIDICON	118
7.4.2	ELECTROSTATIC STORAGE CAMERA	121
7.4.3	CHARGE-COUPLED IMAGERS	122
7.4.3.1	Charge-Coupled Device	122
7.4.3.2	Intensified Charge-Coupled Device	125
7.4.4	SIT VIDICON,	125
7.4.5	SILICON VIDICON	128
7.4.6	SLOW-SCAN VIDICON	129
7.4.7	SILICON DIOXIDE VIDICON	130
7.4.8	RETURN BEAM VIDICON	131
7.5	CONCLUSION	132
VIII	ANALYSIS FOR SPECIFIED JUPITER ORBITER MISSION USING SELECTED CAMERA SYSTEMS	133
8.1	INTRODUCTION	133
8.2	DISCUSSION	133
8.2.1	SPECIFIED JUPITER ORBITER MISSION	133

TABLE OF CONTENTS

SECTION OR PARAGRAPH	TITLE	PAGE
8.3	PERFORMANCE ANALYSIS	137
8.3.1	EFFECT OF IMC ON PERFORMANCE	137
8.3.2	EFFECT OF VARYING PHASE ANGLE	139
8.3.3	EFFECT OF VARYING OPTICAL PARAMETERS	141
8.3.4	PERFORMANCE AT JUPITER AND ITS SATELLITES	145
8.3.4.1	Satellite Encounters	150
8.3.5	RESOLVING POWER VERSUS EXPOSURE	151
8.3.6	CAMERA PERFORMANCE VERSUS ORBITAL TIME BEFORE PERIAPSIS	151
8.4	OTHER OUTER PLANET MISSIONS	154
8.4.1	SATURN AND URANUS	154
8.4.2	BEYOND URANUS	155
8.4.3	FLYBY MISSIONS	156
8.5	CONCLUSIONS	157
IX	DESIGN STUDY AND TECHNOLOGICAL ASSESSMENT	159
9.1	SUMMARY	159
9.2	PERIPHERAL EQUIPMENT	160
9.2.1	OPTICS	160
9.2.2	SHUTTER AND FILTER WHEEL	162
9.2.3	IMAGE MOTION COMPENSATION	165
9.2.4	THERMAL CONTROL	167
9.2.5	DATA STORAGE	169

TABLE OF CONTENTS

SECTION OR PARAGRAPH	TITLE	PAGE
9.3	BASIC SENSOR PARAMETERS	170
9.3.1	ELECTROSTATIC CAMERA SYSTEM	170
9.3.2	SEC VIDICON	175
9.3.3	INTENSIFIED CHARGE-COUPLED DEVICE CAMERA	180
9.4	CAMERA SYSTEM TECHNOLOGICAL ASSESSMENT	185
9.4.1	SENSOR DEVELOPMENT: STATE OF THE ART	185
9.4.2	MISSION PARAMETERS	186
9.4.2.1	Electrostatic Camera System	186
9.4.2.2	SEC Camera System	188
9.4.2.3	ICCD Camera System	190
9.5	CAMERA SYSTEM TRADEOFFS	192
9.6	RECOMMENDED TECHNOLOGY IMPROVEMENTS	194
X	COSTS AND DEVELOPMENT SCHEDULES	197
10.1	INTRODUCTION	197
10.2	HISTORIC COST ESTIMATES	197
10.2.1	INPUTS	198
10.2.2	CER RESULTS	199
10.2.3	MAXIMUM CER INPUTS	199
10.2.4	MAXIMUM CER RESULTS	200
10.3	ENGINEERING COST ESTIMATES	201
10.4	COST COMPARISONS	201
10.5	DEVELOPMENT SCHEDULES	205

TABLE OF CONTENTS

SECTION OR PARAGRAPH	TITLE	PAGE
APPENDIX A	CAMERA MODELING	209
A.1	INTRODUCTION	209
A.2	DEVELOPMENT OF ANALYTICAL PEAK-SIGNAL-TO-RMS-NOISE MODELS FOR SELECTED CANDIDATE SENSORS	209
A.2.1	ANALYTICAL PEAK-SIGNAL-TO-RMS-NOISE MODEL FOR SIT-SEC-SiO ₂ VIDICONS	209
A.2.1.1	Output Signal Current	210
A.2.1.2	Output Noise Current	211
A.2.1.2.1	Quantum (Image) and Target Noise Terms	212
A.2.1.2.2	Readout Beam Shot Noise	214
A.2.1.2.3	Target Dark Current Shot Noise	214
A.2.1.2.4	Thermal Noise of Load Impedance	215
A.2.1.2.5	Shot Noise in Channel Current of Preamp Field Effect Transistor (FET)	215
A.2.2	ANALYTICAL PEAK-SIGNAL-TO-RMS-NOISE MODEL FOR THE SEC VIDICON WITH AN IMAGE INTENSIFIER	215
A.2.3	ANALYTICAL PEAK-SIGNAL-TO-RMS-NOISE MODEL FOR SILICON AND SLOW-SCAN VIDICON	218
A.2.4	ANALYTICAL PEAK-SIGNAL-TO-RMS-NOISE MODEL FOR SILICON AND SLOW-SCAN VIDICONS WITH IMAGE INTENSIFIERS	219
A.2.5	ANALYTICAL PEAK-SIGNAL-TO-RMS-NOISE MODEL FOR RETURN BEAM VIDICON	220
A.2.5.1	Output Signal Current	221
A.2.5.2	Output Noise Current	
A.2.5.2.1	Quantum (Image) Noise	221
A.2.5.2.2	Read Beam Shot Noise	221
A.2.5.2.3	Noise due to Electron Multiplier	223

TABLE OF CONTENTS

SECTION OR PARAGRAPH	TITLE	PAGE
A.2.6	ANALYTICAL PEAK-SIGNAL-TO-RMS-NOISE MODEL FOR THE IMAGE ORTHICON	223
A.2.6.1	Noise due to the Secondary Electron Emission of the Target	224
A.2.7	ANALYTICAL PEAK-SIGNAL-TO-RMS-NOISE MODEL FOR THE IMAGE ISOCON	225
A.2.8	ANALYTICAL PEAK-SIGNAL-TO-RMS-NOISE MODEL FOR THE ELECTROSTATIC STORAGE CAMERA	226
A.2.8.1	Output Signal Current	227
A.2.8.2	Output Noise Current	228
A.2.8.2.1	Quantum (Image) and Target Noise Terms	229
A.2.8.2.2	Dielectric Charging Noise during Readout	230
A.2.8.2.3	Read Beam Shot Noise	231
A.2.8.2.4	Secondary Emission Noise of Dielectric Target	231
A.2.8.2.5	Energy Analyzer Partition Noise	232
A.2.8.2.6	Electron Multiplier Secondary Emission Noise	232
A.2.9	ANALYTICAL PEAK-SIGNAL-TO-RMS-NOISE MODEL FOR THE CHARGE-COUPLED IMAGER AND INTENSIFIED (PHOTOEMITTER) CHARGE-COUPLED DEVICE	232
A.2.9.1	Output Signal Charge	233
A.2.9.2	Output Noise Charge	234
A.2.9.2.1	Quantum (Image) and Target Noise	234
A.2.9.2.2	Dark Current Noise	235
A.2.9.2.3	Interface State Noise	236
A.2.9.2.4	Shot Noise in Channel Current of Preamp FET	237

TABLE OF CONTENTS

SECTION OR PARAGRAPH	TITLE	PAGE
A.2.9.2.5	Thermal Noise of Preamp Input Impedance	238
A.2.10	GAIN CALCULATION OF IMAGE INTENSIFIERS FOR USE IN ANALYTICAL MODELS	238
A.2.10.1	Determination of Gain of Image Intensifier to be used with the SEC Vidicon	238
A.2.11	DETERMINATION OF THE GAIN OF THE IMAGE INTENSIFIER TO BE USED WITH THE SILICON VIDICON AND SLOW-SCAN VIDICON	240
A.2.12	ANALYTICAL PEAK-SIGNAL-TO-RMS-NOISE MODELS FOR SELECTED CANDIDATE SENSORS	241
A.2.13	ANALYTICAL MODEL PARAMETERS	241
APPENDIX B	PREPARATION OF COMPUTER PROGRAMS	257
B.1	INTRODUCTION	257
B.2	COMPUTER PROGRAMS	257
B.3	SIT VIDICON COMPUTER PROGRAM	259
B.3.1	SIT VIDICON FLOW DIAGRAMS	260
B.3.2	SIT VIDICON PROGRAM DESCRIPTION	260
B.3.2.1	SITV Line Description	268
B.3.2.2	IRWATT Subroutine Line Description	271
B.3.2.3	MTFAVA Subroutine Line Description	274
B.3.3	SIT VIDICON INPUT/OUTPUT FORMAT	276
B.4	LISTING OF COMPUTER PROGRAMS	278
B.4.1	SECV PROGRAM LIST - ELECTROSTATIC FOCUS	279
B.4.2	SECV PROGRAM LIST - ELECTROMAGNETIC FOCUS	281
B.4.3	ESC PROGRAM LIST - ELECTROSTATIC FOCUS	283

TABLE OF CONTENTS

SECTION OR PARAGRAPH	TITLE	PAGE
B.4.4	ESCMF PROGRAM LIST - ELECTROMAGNETIC FOCUS	286
B.4.5	CCD PROGRAM LIST	288
B.4.6	ICCDEF PROGRAM LIST - ELECTROSTATIC FOCUS	291
B.4.7	ICCD PROGRAM LIST - ELECTROMAGNETIC FOCUS	294
B.4.8	RBV PROGRAM LIST	297
B.4.9	SDV PROGRAM LIST	300
B.4.10	SILV PROGRAM LIST	302
B.4.11	SSV PROGRAM LIST - DOPED SELENIUM PHOTOCONDUCTOR	305
B.4.12	SSV PROGRAM LIST - ASOS	308
B.4.13	SUBROUTINE IRWATM PROGRAM LIST	311
B.4.14	SUBROUTINE SDTAR PROGRAM LIST	312
B.4.15	SUBROUTINE VTAR PROGRAM LIST	312
REFERENCES		313
ABBREVIATIONS		316

LIST OF ILLUSTRATIONS

FIGURE NUMBER	TITLE	PAGE
1-1	PROGRAM PLAN	3
2-1	CANDIDATE FRAM CAMERAS SELECTED FOR STUDY	14
3-1	IMAGE MOTION TRANSFER FUNCTION	36
3-2	AIM CURVE (HYPOTHETICAL EXAMPLE)	44
3-3	AIM CURVE (HYPOTHETICAL EXAMPLE)	44
3-4	SYSTEM MODULATION (HYPOTHETICAL EXAMPLE)	46
3-5	RESOLUTION RELATIONSHIPS	49
5-1	RADIATION MODELS FOR JUPITER	56
5-2	PARTICLE FLUENCE VERSUS RELATIVE INCREASE IN DARK CURRENT FOR BARE SILICON DIODE ARRAYS	59
6-1	PERFORMANCE OF IDEAL SENSORS UNDER NO-IMAGE-MOTION- COMPENSATION CONDITIONS	81
6-2	PERFORMANCE OF SELECTED SENSORS UNDER NO-IMAGE- MOTION-COMPENSATION CONDITIONS	86
6-3	PERFORMANCE OF SELECTED SENSORS UNDER NO-IMAGE- MOTION-COMPENSATION CONDITIONS	86
6-4	PERFORMANCE OF SELECTED SENSORS UNDER COMPLETE- IMAGE-MOTION-COMPENSATION CONDITIONS	90
6-5	PERFORMANCE OF SELECTED SENSORS UNDER COMPLETE- IMAGE-MOTION-COMPENSATION CONDITIONS	90
6-6	IMAGE MOTION COMPENSATION REQUIREMENTS	91
7-1	AVAILABLE AERIAL IMAGE MODULATION VERSUS RESOLUTION	102
7-2	AVAILABLE AERIAL IMAGE MODULATION VERSUS RESOLUTION	103
7-3	THRESHOLD MODULATION CURVES FOR CANDIDATE FRAME IMAGERS	105
7-4	THRESHOLD MODULATION CURVES FOR CANDIDATE FRAME IMAGERS	106
7-5	THRESHOLD MODULATION CURVES FOR CANDIDATE FRAME IMAGERS	107

LIST OF ILLUSTRATIONS

FIGURE NUMBER	TITLE	PAGE
7-6	THRESHOLD MODULATION CURVES FOR CANDIDATE FRAME IMAGERS	110
7-7	SIGNAL-TO-NOISE RATIO (DATA LINK) VERSUS RESOLUTION	111
7-8	SIGNAL-TO-NOISE RATIO (DATA LINK) VERSUS RESOLUTION	112
7-9	SIGNAL-TO-NOISE RATIO (RECONSTRUCTED IMAGE) VERSUS RESOLUTION	113
7-10	RESOLVING POWER VERSUS RESOLUTION	115
7-11	SEC VIDICON SYSTEM THRESHOLD MODULATION	116
7-12	ESC SYSTEM THRESHOLD MODULATION	117
8-1	JUPITER ORBITER GEOMETRY WITH THREE SATELLITE ENCOUNTERS	134
8-2	1976 ENCOUNTER CHARACTERISTICS	135
8-3	SEC VIDICON SYSTEM MODULATION CURVES	138
8-4	SEC VIDICON SYSTEM MODULATION CURVES AS A FUNCTION OF PHASE ANGLE	140
8-5	SEC VIDICON PERFORMANCE AS A FUNCTION OF OPTICAL APERTURE DIAMETER	142
8-6	SEC VIDICON PERFORMANCE AS A FUNCTION OF FOCAL LENGTH	143
8-7	FIELD OF VIEW VERSUS FOCAL LENGTH FOR DIFFERENT CAMERA FORMATS	144
8-8	SEC VIDICON SYSTEM MODULATION CURVES	146
8-9	ELECTROSTATIC STORAGE CAMERA SYSTEM MODULATION CURVES	148
8-10	INTENSIFIED CHARGE-COUPLED DEVICE MODULATION CURVES	149
8-11	RESOLVING POWER VERSUS EXPOSURE	152
8-12	CAMERA PERFORMANCE CHARACTERISTICS FOR 2.29 X 45.1 R _J JUPITER ORBITER	153

LIST OF ILLUSTRATIONS

FIGURE NUMBER	TITLE	PAGE
9-1	ELECTROSTATIC STORAGE CAMERA TUBE 30 FRAME STORAGE	171
9-2	ELECTROSTATIC STORAGE CAMERA PACKAGING CONFIGURATION	172
9-3	ELECTROSTATIC STORAGE CAMERA SIMPLIFIED BLOCK DIAGRAM	173
9-4	SEC VIDICON CAMERA TUBE	176
9-5	SEC VIDICON CAMERA PACKAGING CONFIGURATION	177
9-6	SEC VIDICON CAMERA SIMPLIFIED BLOCK DIAGRAM	178
9-7	INTENSIFIED CHARGE-COUPLED DEVICE	181
9-8	INTENSIFIED CHARGE-COUPLED CAMERA PACKAGING CONFIGURATION	182
9-9	INTENSIFIED CHARGE-COUPLED CAMERA SIMPLIFIED BLOCK DIAGRAM	183
B-1	COMPUTER PROGRAMS SUMMARY MATRIX	258
B-2	FLOWCHART - SITV PROGRAM	261
B-3	FLOWCHART - SUBROUTINE IRWATT FLOWCHART - SUBROUTINE MTFAVA	262
B-4	SITV PROGRAM INPUT/OUTPUT FORMAT	277

LIST OF TABLES

TABLE NUMBER	TITLE	PAGE
5-1	PARTICLE BOMBARDMENT OF ESC STORAGE TARGET	62
6-1	OPTIMUM EXPOSURE TIMES AND CORRESPONDING $\tau_{IM}(K)$ VALUES USED IN PERFORMANCE ANALYSIS	87
7-1	WEIGHT OF CATADIOPTRIC SYSTEMS	99
7-2	SUMMARY SENSOR SELECTION MATRIX	119
9-1	30-FRAME ELECTROSTATIC CAMERA PARAMETERS	174
9-2	SEC VIDICON CAMERA PARAMETERS	179
9-3	ICCD CAMERA PARAMETERS	184
9-4	ELECTROSTATIC STORAGE CAMERA SYSTEM CONFIGURATIONS	187
9-5	SEC VIDICON CAMERA SYSTEM CONFIGURATIONS	189
9-6	ICCD CAMERA SYSTEM CONFIGURATIONS	191
9-7	PERFORMANCE TRADEOFFS FOR SELECTED JUPITER ORBITER MISSION	193
9-8	PERFORMANCE TRADEOFFS FOR OTHER OUTER PLANET MISSIONS REQUIRING MULTIFRAME STORAGE	193
10-1	INPUTS USED IN COST ESTIMATING RELATIONSHIPS	198
10-2	MAXIMUM INPUTS TO THE CERs	200
10-3	ESC CAMERA COSTS	202
10-4	SEC CAMERA COSTS	203
10-5	ICCD CAMERA COSTS	204
10-6	MODEL COST COMPARISONS	205
10-7	ESC CAMERA DEVELOPMENT SCHEDULE	206
10-8	SEC VIDICON CAMERA DEVELOPMENT SCHEDULE	207
10-9	ICCD CAMERA DEVELOPMENT SCHEDULE	208

SECTION I
INTRODUCTION

1.1 BACKGROUND AND STUDY GOALS

This report presents the technical results of the "Study of the Applicability of Frame Imaging from a Spinning Spacecraft", performed by CBS Laboratories, Stamford, Connecticut, for the National Aeronautics and Space Administration, Ames Research Center, under Contract NAS2-7107. The study was performed over a 10-month period from July 1972 through May 1973. This is Volume 2 of the final report of the study. Volume 1 is a brief summary of the results.

The basic purpose of this work was to study the applicability of frame-type imaging systems for use on board a spin-stabilized spacecraft for outer planets applications, as distinguished from spin-scan imaging systems and three-axis stabilized vehicles. The major goals of the study were to objectively select the most feasible imaging system(s) for this class of missions and to prepare preliminary design information which defines the system(s) for a specified Jupiter orbiter mission. Sufficient generality was included to permit the application of these techniques to a variety of missions. In addition, the interaction of system performance specifications on cost and development schedule was to be investigated.

The scope of this study encompassed frame imagers only, on an orbiting mission of Jupiter including encounters with the Galilean satellites. All types of frame imagers capable of performing this mission were considered, regardless of the current state of the art. Detailed sensor models of these systems were developed at the component level and used in the subsequent analyses. An overall assessment was then made of the various systems based upon results of a worst-case performance analysis, foreseeable technology problems, and the relative reliability and radiation tolerance of the systems. Special attention was directed at restraints imposed by image motion and the limited data transmission and storage capability of the spacecraft. Based upon this overall assessment, the most promising systems were selected and then examined in detail for a specified Jupiter orbiter mission. The relative merits of each selected system were then analyzed, and the system design characteristics were presented using preliminary configurations, block diagrams, and tables of estimated weights, volumes and power consumption. Performance tradeoffs were then discussed. Finally, cost and development schedules were presented for the selected frame imaging systems.

1.2 ORGANIZATION OF THE VOLUME

As depicted in Figure 1-1, the study was divided into nine separate study tasks, progressing from the initial selection of candidate frame imaging systems to the final task of preparing cost and development schedules. This volume is organized in a similar manner. The technical details of each task are contained within the separate report sections.

PROGRAM PLAN

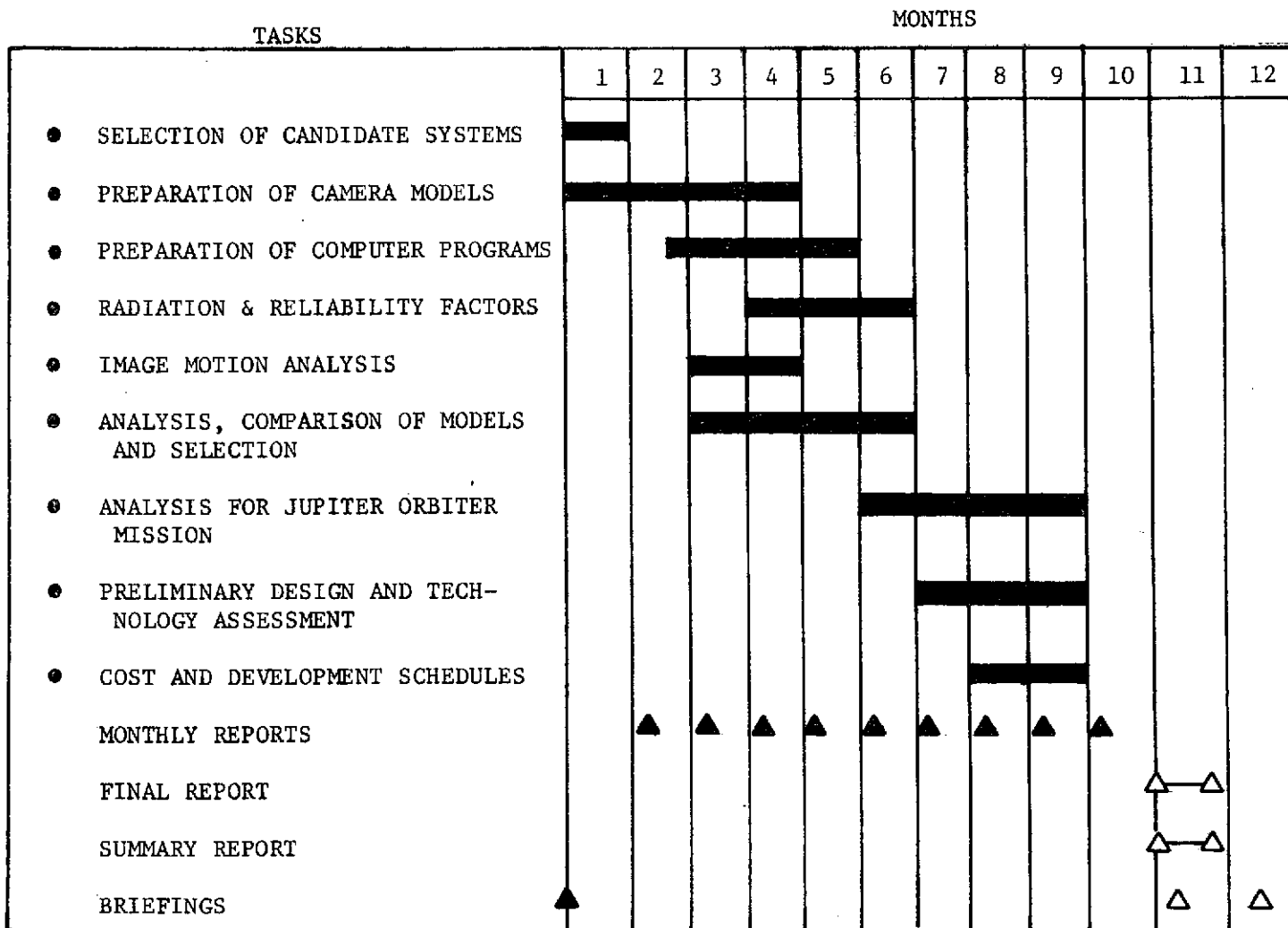


Figure 1-1

Section 2 reviews the selection of the candidate frame imaging systems. A brief description of the operation of each sensor is given. The general performance requirements and constraints used as selection criteria are also discussed, and the reasons why each camera system was rejected or selected as a candidate are given.

Section 3 describes the development of the analytical camera models. The basic relationships used in developing the camera models are introduced and methods of plotting camera performance are described. A detailed derivation of the theoretical signal-to-noise ratio models is given in Appendix A. In Section 4, computer programs for the analytical camera models are introduced. Detailed program descriptions and listings are given in Appendix B.

Section 5 presents a relative assessment of the reliability factors and the tolerance of the candidate systems to the postulated radiation environment.

Section 6 investigates the effects of various spacecraft and planetary motions which influence camera performance. The extent to which the performance of the sensors can be improved through the use of image motion compensation is established.

Section 7 presents the results of a worst-case parametric analysis using the candidate systems. In order to properly evaluate the candidates, more specific requirements and selection criteria are established. Then each candidate sensor system is examined in detail and given an overall assessment. Finally, three camera systems — the SEC vidicon, electrostatic storage camera and the intensified charge-coupled device — are selected for additional analysis for a specific Jupiter orbiter mission.

Section 8 analyzes the capability of the three best systems for the specified Jupiter orbiter mission with satellite encounters. The effects of various system and mission parameters on performance are presented. The suitability of the best camera systems for other outer planet missions is discussed and their performance at Saturn and Uranus is determined.

Section 9 gives the preliminary design configurations for the three selected camera systems. Preliminary information, including physical configurations, system block diagrams, weight, volume, and power consumption, is presented. Alternative system configurations and anticipated performance versus cost are compared. Finally, the technology problems associated with each system are assessed.

Section 10 gives the approximate costs and development schedules associated with each of the three selected systems.

1.3 CONCLUSIONS OF THE STUDY

The major conclusions of the study are summarized below:

- The use of frame imaging systems from a spinning spacecraft typified by Pioneer F and G is feasible. However, an image motion compensation system is required to limit image smear during exposure and thereby maintain the resolution capability of the camera.
- Only a short exposure time (generally less than one millisecond) can be used because of the residual smear, even when image motion compensation is provided. This precludes the use of many frame imagers having insufficient sensitivity.
- In general, a frame imager requires a modest amount of prestorage target gain to overcome the limited scene illumination encountered on this type of mission. Frame imagers such as the slow-scan vidicon, silicon vidicon, and return beam vidicon are not sensitive enough to perform adequately at the anticipated light levels.

- In selecting an appropriate frame imager for a Jupiter orbiter mission, emphasis was placed on camera systems capable of slow-scan operation. It is desirable to have a camera system that can store an image until the data handling and communications system can unload the data to Earth without using an ancillary storage system such as a tape recorder. The SEC vidicon and electrostatic storage camera (ESC) meet this and other criteria, and are accordingly considered acceptable for a Jupiter orbiter mission.
- Almost all frame imagers are capable of slow-scan operation and long-term storage if sufficiently cooled. The SIT vidicon can provide integration times of several hours by cooling to -60°C . Implementing thermal control, however, can involve the use of considerable weight and power and other practical difficulties. The SIT vidicon was rejected for this reason. It is more applicable to missions using on-board storage at higher video bandwidths.

- The charge-coupled imager requires cooling to achieve a slow-scan capability and thereby be able to operate without an auxiliary storage unit. However, charge transport is a significant new concept in imaging which has attracted much interest. The potential attributes of excellent performance at low power, low weight, and good reliability are very appealing. For these reasons, a charge-coupled imager was one of the systems selected for the Jupiter mission. An intensified charge-coupled device (ICCD) was selected, as it contains an image section which makes electronic shuttering and electronic image motion compensation feasible. Unlike the basic charge-coupled device, its performance is less sensitive to readout noise at low clock rates.
- Based on a worst-case parametric analysis and an overall assessment of all potential frame imagers, the SEC vidicon, the electrostatic storage camera, and the intensified charge-coupled device were found to be the best systems for the class of missions studied.
- The three selected camera systems all perform satisfactorily when applied to the $2.29 \times 45.1 R_J$ Jupiter orbiter mission. Ground resolution of 5 to 8 km can be achieved at Jupiter near periapsis using these systems.

- Performance appears to be limited more by other system parameters than by the sensors themselves, particularly for the high-performance electromagnetically focused camera configurations. If, for instance, the camera parameters were not dominated by factors such as image smear, versions with even higher performance could be constructed. However, such systems are not required for the Jupiter orbiter mission as defined for this study.
- When photographing the satellites of Jupiter, the three selected camera systems all perform satisfactorily. If multispectral pictures are to be taken with filters over several color bands, the ESC offers an advantage. Because of its unique bulk storage capability, the ESC can rapidly expose a sequence of pictures during satellite encounters and transmit them back to Earth afterwards. Contiguous ground coverage over several spectral bands can be achieved in this manner over a wide resolution range from close-up shots to full-disc photographs. The ICCD and SEC vidicon would require a tape recorder to obtain similar results.

- The selected cameras appear suitable for missions to Saturn and Uranus without any major design changes. However, the resolution of the sensors deteriorates due to the low available illumination when missions to Uranus are considered, more so with the SEC vidicon than the others because its MTF is lower. The ESC is considered the best sensor for both the outer planet missions and for flybys when tape recorders cannot be used.

SECTION II

SELECTION OF CANDIDATE SYSTEMS

2.1 INTRODUCTION

In performing the Study of the Applicability of Frame Imaging from Spinning Spacecraft, all types of frame imaging systems having potential for the class of missions of interest are considered, regardless of the current state of the art.

The objective of this task is to select the candidate systems to be analyzed in the initial phase of the study. Detailed sensor models of these systems are developed at the component level for use in subsequent analyses.

The principal requirements for the ideal imaging sensors for planetary missions are high resolution, high quantum efficiency, long life, and compatibility with the spacecraft and planetary environments. Almost equally important are characteristics such as radiation tolerance, reliability, quantum-noise-limited operation, large dynamic range, low weight, low power consumption, wide spectral range, low cost and adaptability to other outer planets missions. For spacecraft with limited data storage equipment, long target storage with a slow-scan capability is also essential. No currently available imaging sensor comes close to satisfying all of these requirements. At best, camera systems must be selected on the basis of compromise, accepting the shortcomings of the device as well as its merits and satisfying only the most important requirements for a particular mission.

Based upon these imaging system requirements, candidate camera systems have been selected for a worst-case analysis. Imaging systems which have been employed in previous space missions, along with other systems offering many distinct advantages but which are still in the development stage, are among the candidates which will be considered. Included in this study as candidates will be the slow-scan vidicon, silicon vidicon, SIT vidicon, SEC vidicon, return beam vidicon, silicon dioxide vidicon, electrostatic storage camera and charge-coupled imagers. The use of an intensifier stage coupled to the candidate sensors will be also considered where applicable. Although the image orthicon and image isocon will be modeled, they will not be studied in detail.

2.2 BASIS FOR CANDIDATE SELECTION

The actual requirements for an imaging system to be used for planetary exploration, typified by a Jupiter orbiter mission, differs substantially from mission to mission depending on the particular scientific objectives. However, general objectives and requirements have been established and can be used to select candidate systems for analysis. In general, the camera system must be restricted in size, weight and power consumption, and it must produce pictures at the desired resolution. It must operate at an adequate signal-to-noise ratio (SNR) over the range of illumination levels available. The camera system must be rugged enough to survive the hazards of shock, acceleration, vibration during launch, and trapped particles in the planetary radiation belts. These missions will be of long duration, imposing severe lifetime and reliability requirements on the camera system. Development costs and readiness are also

important factors to consider.

Utilization of a spin-stabilized spacecraft, rather than the more sophisticated and costly three-axis stabilized vehicle, imposes additional constraints on the camera's performance. Image motion, caused by the spin rate of the spacecraft, can blur the image and degrade the resolution capability of the sensor. Camera characteristics such as high effective quantum efficiency and photoelectron noise-limited operation are desirable. These factors shorten the required exposure time by efficiently using the reflected light available at distant planets, thus reducing the susceptibility to image motion.

The limited data transmission and storage capabilities of spin-stabilized spacecraft place additional requirements on the camera system. Either an on-board storage system must be provided, or the imaging system must be capable of long-term storage and slow-scan operation at the radio frequency transmission bit rate.

Another important factor in candidate selection is previous experience. Many camera systems have been flown on previous missions and their performance levels are well documented.

2.3 CANDIDATE SYSTEMS SELECTED

A listing of all potential candidate framing systems is shown in Figure 2-1 along with the candidate selections to be included in this study. Camera systems that have been previously flown⁽¹⁾ are indicated. Framing systems that were considered in the TRW System Group study of "Follow-on Pioneer Missions to Jupiter"⁽²⁾ are shown. Also included is a column showing

TYPE FRAMING SYSTEM	SYSTEMS FLOWN (3)	TRW STUDY (1) PIONEER FOLLOW-ON	GRAND TOUR (2) DEFINITION STUDY	SELECTED AS STUDY CANDIDATE
SLOW SCAN VIDICON (1)	MARINER PROBES OTHERS	INCLUDED IN STUDY	INCLUDED IN STUDY	YES
SILICON VIDICON (1)		INCLUDED IN STUDY	INCLUDED IN STUDY	YES
SIT VIDICON	APOLLO #15 & 16	INCLUDED IN STUDY	INCLUDED IN STUDY	YES
SEC VIDICON (1)	APOLLO #9 THROUGH #13, NRL, GAO & OSO	INCLUDED IN STUDY		YES
RETURN BEAM VIDICON	EARTH RESOURCES TECHNOLOGY SATELLITE	INCLUDED IN STUDY		YES
SiO ₂ VIDICON				YES
ELECTROSTATIC CAMERA SYSTEM			INCLUDED IN STUDY	YES
CHARGE-COUPLED IMAGER (2)				YES
IMAGE ORTHICON	ATS 4			NO
IMAGE ISOCON				NO
SMOOTHING DISSECTOR				NO

(1) WITHOUT AND WITH INTENSIFIER
(2) WITHOUT AND WITH PHOTOEMITTER

CANDIDATE FRAME CAMERAS SELECTED FOR STUDY

Figure 2-1

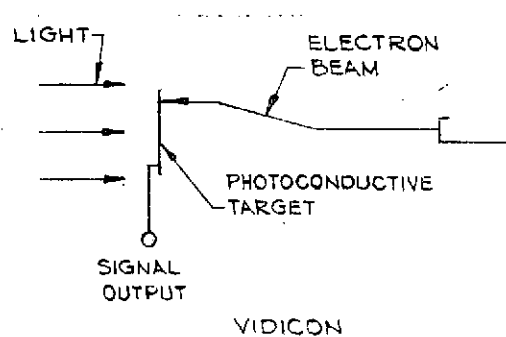
candidate systems mentioned as possible Grand Tour alternatives by the Grand Tour Imaging Science Team (3).

A short discussion on each of these camera systems follows, giving the reasons for inclusion or omission from the study.

2.3.1 SLOW-SCAN VIDICON

The slow-scan vidicon or SSV (with and without intensifier) is included as one of the candidate systems to be studied. The selenium vidicon has been used extensively in the Mariner series of space probes as well as on Surveyor. The Viking lander will use a slow-scan vidicon with a single image intensifier so that electronic shuttering and image motion compensation can be applied. The selenium vidicon offers relatively high resolution, acceptable format, simplicity, low weight, good reliability, and excellent slow-scan characteristics. However, it lacks wide spectral response and has no prestorage gain, a requirement for quantum-noise-limited operation at low light levels in sensors using charge-replacement readout. Its sensitivity is low, so intensification will be needed to allow short exposures under the low light levels found on outer-planet missions.

The selenium vidicon tube employs a selenium target and a low-energy read-erase electron beam. Writing is effected by illuminating the uniformly charged photoconductor target with light from the scene. The resulting increase in the conductivity of the target



elements causes the surface potential of these elements to shift towards the potential of the backing plate. A potential pattern corresponding to the incident scene is thus established on the photoconductive target.

During reading, the target is scanned by the low-energy electron beam. This beam replaces the charge on the surface of the target and shifts the target elements back to their original potential. This charge replacement process results in a capacitive current through the target which is proportional to the amount of charge deposited on a particular target element. This current passes through a load resistor to produce a halftone output signal voltage. Since the selenium target has a high dark resistivity, slow-scan readout is possible.

2.3.2 SILICON VIDICON

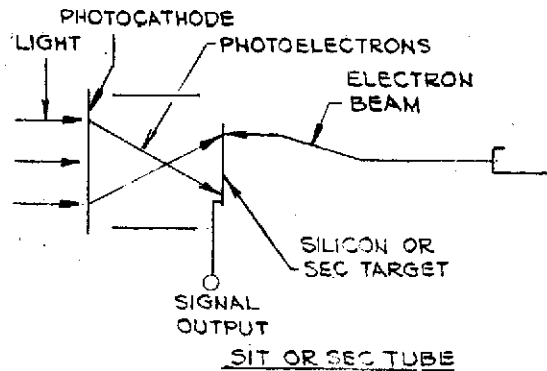
The silicon vidicon is identical to the slow-scan vidicon except that it utilizes a silicon target and is more sensitive. It has excellent red response, low weight, and the potential for long life. The quantum efficiency of silicon is high and the target capacitance is moderately high. The shortcomings are modest resolution, the absence of prestorage target gain, and the possible need for target cooling to achieve slow-scan performance.

The silicon vidicon will be included as a candidate during this study. Although the silicon target is quite sensitive, a relatively fast optical system will still be required at the further planets. An intensifier placed in front of the silicon vidicon will also be considered in the analysis.

2.3.3 SIT VIDICON

The Silicon Intensifier Target (SIT) vidicon has excellent potential for planetary exploration, having already been used on the Appollo 15 and 16 missions.

The SIT vidicon combines a photocathode and an electrostatic (or magnetic) image section with a silicon diode array target. As with the selenium vidicon, a low-energy electron gun is used for image readout and erasure.



An electric field established across the target by means of the low-energy read beam is in a direction such that the target diodes are reverse biased. During writing, electrons from the photocathode are accelerated by the image section through a potential difference of 6-10 kV. When these accelerated electrons strike the diode array, a large number of electron-hole pairs are generated within the target (~ 1 pair/3.4 eV). These electron-hole pairs, accelerated under the influence of the field across the target, result in partial discharge of the individual diodes. Readout of the stored image is accomplished in the same manner as with the selenium vidicon.

The high gain associated with the silicon diode target permits near-quantum noise operation of the camera over a wide range of exposure levels. The SIT vidicon has excellent sensitivity. Slow-scan operation involving

several minutes of target integration can be achieved but requires modest target cooling. The spectral range is presently limited in extended red response because of the S-20 intensifier photocathode. Red sensitivity improvement can be expected, however, with an S-25 or in the future with a III-V compound photocathode.

2.3.4 SEC VIDICON

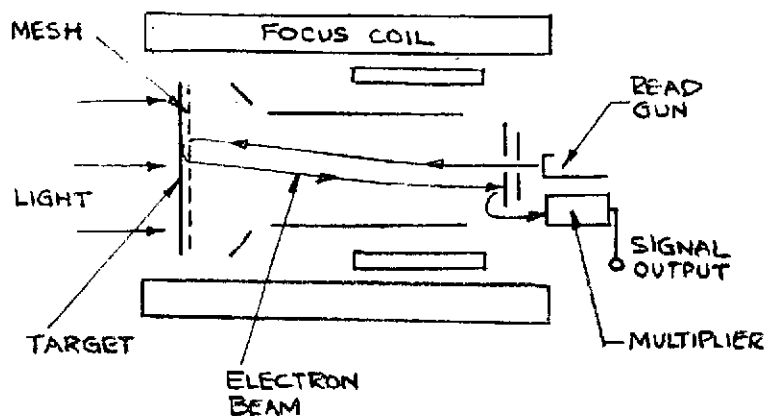
The Secondary Electron Conduction (SEC) vidicon has long-term integration capability and can store an image for many hours. An auxiliary storage unit would not be required for many missions. It also has a low target capacitance and a sufficiently high gain to make the amplifier noise negligible. The resolution is about the same as that of the SIT vidicon. A disadvantage is its relatively fragile target; this, however, is being improved. An intensified SEC will also be considered.

The operation of the SEC camera tube⁽⁴⁾ is similar to that of the SIT vidicon. The principal difference is the type of storage target and the corresponding method by which localized areas of the target are discharged. The target used in the SEC vidicon consists of a thin insulating layer on which a thin metallic film (backplate) and a porous storage layer (e.g., $\sim 20 \mu$ thick KCl) are deposited. High-energy photoelectrons pass through the insulating and metallic films and penetrate the storage layer. Due to the porous nature of the storage layer, secondary electrons generated within the film are swept through the layer. This results in localized areas of increased target conductivity, which, in turn, causes these areas to partially discharge. Replacing this surface charge by scanning the surface of the target with a low-energy

electron beam results in a modulated output current through the target and the series resistor.

2.3.5 RETURN BEAM VIDICON

The return beam vidicon (RBV) used in the Earth Resources Technology Satellite has high resolution and higher signal-to-noise ratios than can be obtained with a conventional vidicon, and it operates in a slow-scan mode. Disadvantages of the RBV are its moderate sensitivity, bulkiness, and added complexity compared to the conventional vidicon.



RETURN BEAM VIDICON

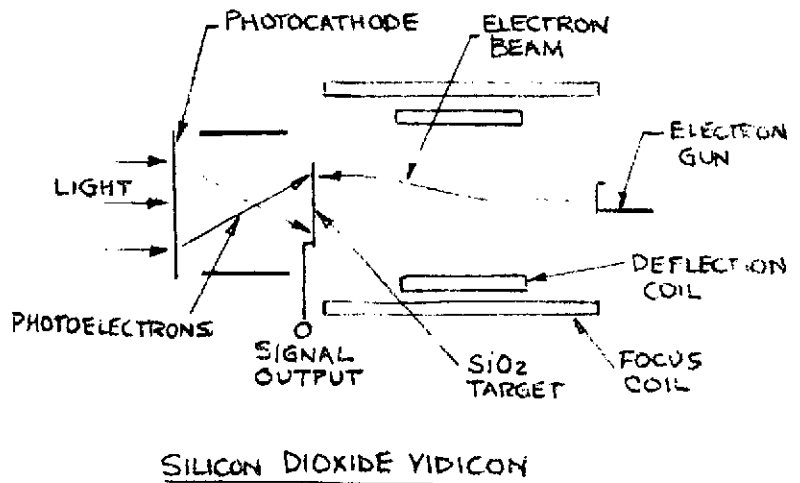
The RBV⁽⁵⁾ is composed of an electron gun, electron multiplier, and antimony trisulfide-oxisulfide (ASOS) photoconductor, along with a deflection yoke and a magnetic focus coil. During exposure the imaged optical pattern is transformed into a charge pattern on the gun side of the photoconductor. During the read cycle the electron beam scans the photoconductor with low-velocity electrons and charges each incremental element. The number of electrons reflected from the target is proportional to the initial potential established during exposure. The modulated return beam is collected and amplified by an electron multiplier. Between exposures, the photoconductor is flooded with light to prepare the surface.

2.3.6 SILICON DIOXIDE VIDICON

The silicon dioxide vidicon does not exist and must be developed. It would be similar to an Ebicon with an SiO_2 target. The camera tube would provide amplification at the SiO_2 target through the process of electron-bombardment-induced conductivity (EBIC), resulting in near-quantum-noise-limited performance at decreased light levels. The system would offer a long-term storage capability and slow-scan operation.

Operation of the silicon dioxide vidicon is as follows.

During writing, the pattern of photoelectrons generated at the photocathode is imaged onto the thin SiO_2 storage target. A charge pattern is produced at the target by electron-bombardment conductivity (instead of by secondary emission like in the SEC vidicon). Target gains of up to a hundred are associated with this writing process.

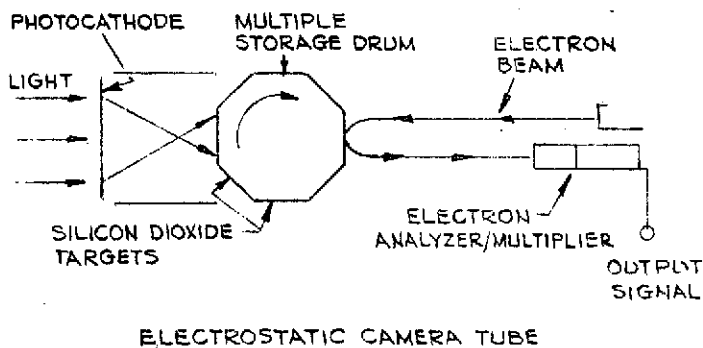


The method of reading is similar to that of the vidicon. The storage insulator is scanned by the low-velocity read beam. Since the secondary emission ratio is less than unity, each target element is shifted down to the cathode potential of the electron gun. As the potential of each

individual element becomes more negative, a capacitive current is produced through the insulating layer. This current flows through the load resistor in series with the backplate, producing signal voltages corresponding to the stored charge pattern.

2.3.7 ELECTROSTATIC CAMERA SYSTEM

The electrostatic camera system or ESC, presently under development, differs from the sensors previously described in several respects. The storage medium (thin film SiO_2 deposited on a metal substrate) can retain stored images for weeks. The number of frames can be increased, thus permitting the writing-in and storage of many frames of information before readout. In addition, the output signal is obtained by analyzing the energy of the secondary electrons generated on the surface by a high-energy reading beam. Since the energy of these secondaries is a function of the surface potential of the SiO_2 from which they were generated, the output signal corresponds to the potential variations on the storage surface. Furthermore, since the reading electrons strike the target with an energy above the secondary-emission first-crossover energy of the target, the reading process does not tend to stabilize the surface potential of the storage medium to the cathode potential of the reading gun. The read-out process is, therefore, non-destructive, and multiple read-outs of the stored information are possible. The high-energy readout also results in high intrinsic resolution and excellent geometric fidelity.



The electrostatic camera consists of a photocathode, image section, dielectric storage medium, priming/reading gun, energy analyzer, and electron multiplier. Prior to imaging, a field gradient is established across the thickness of the storage material by priming the surface to the cathode potential of the electron gun. During exposure, electrons from the photocathode are accelerated by the image section to an energy of about 6kV and strike the storage surface. These high-energy photoelectrons discharge the storage surface by the process of electron-bombardment-induced conductivity (EBIC). This results in a charge pattern which corresponds to the scene being imaged onto the photocathode. The high EBIC gain associated with this process leads to near-quantum-noise-limited camera operation over a wide range of exposure levels.

2.3.8 CHARGE-COUPLED IMAGER

Over the past few years solid-state imaging technology has matured rapidly. Camera systems are being built around matrix-array photosensors of 400 x 500 elements using charge-coupled-device (CCD) technology^(6, 7). Charge-coupled devices used as the primary sensor and used in conjunction with a photoemissive image section will be analyzed in this study.

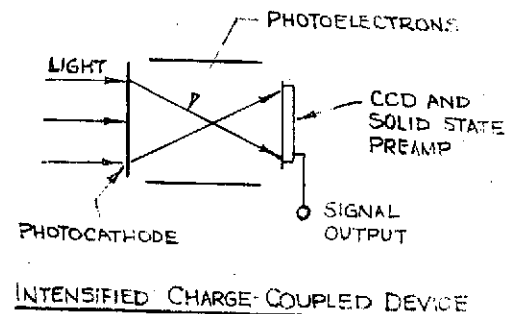
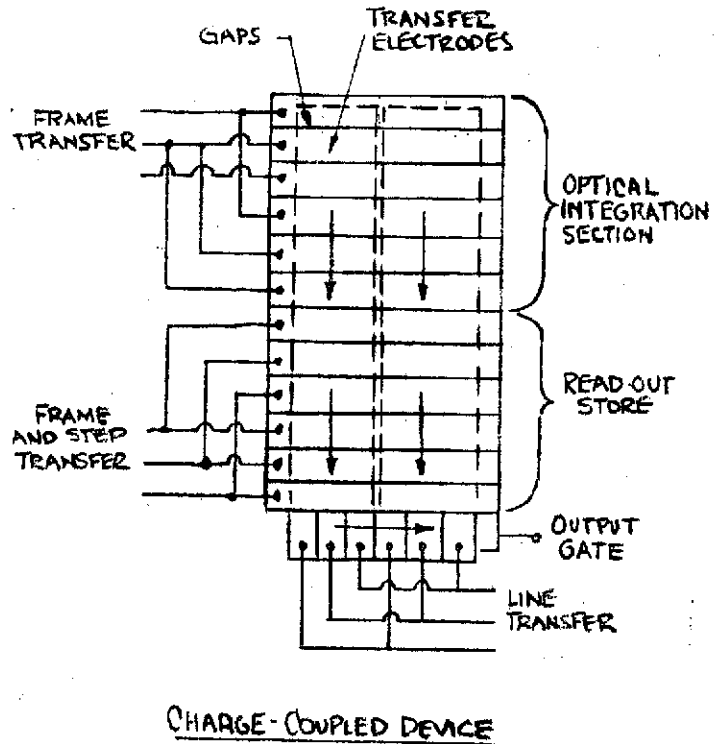
CCD technology is apparently the first successful approach to all-solid-state image sensing. The devices are simple, small, of low weight, and require little power. Once transfer efficiencies and format size are increased and blemish levels are reduced, CCD devices for planetary missions should become practical. CCD imagers are not capable of slow-scan operation without being cooled, and they will require auxiliary storage if thermal control is not

provided.

In its simplest form the CCD structure consists of an array of closely spaced metal electrodes that overlay an insulator deposited on a uniformly doped semiconductor substrate. An optical system focuses the light from the scene onto the surface of the substrate. The silicon converts the light quanta into carriers that collect in a pattern of charge under the

electrodes. During readout this charge is transferred by sequentially shifting the substrate bias voltage. When the charge, which is proportional to the light intensity in the original image, is moved to one end of the device, an output shift register removes it row by row from the sensor area.

The intensified charge-coupled device (ICCD) consists of a charge-coupled device preceded by a photocathode and an image section. The device has a high prestorage target gain, which provides a quantum-noise-limited signal-to-noise ratio at very low exposures.



Unlike the CCD, image motion compensation can be applied electronically, and its performance is less sensitive to readout noise at low clock rates. Electronic gating is also feasible.

2.3.9 IMAGE ORTHICON

The image orthicon tube will not be studied; however, a mathematical model of the sensor will be presented. The image orthicon is not generally considered for planetary missions although it was to have been flown in the ATS-4 (which did not achieve orbit). The image orthicon has been eliminated because of its complexity and low gain when compared to modern devices such as the SEC and SIT vidicons. The collector mesh associated with the device collects a large fraction of the photoelectrons, lowering the net quantum efficiency of the photocathode and degrading the modulation transfer function (MTF) in single-exposure readout. The image orthicon becomes limited at low light levels because of electron beam noise.

The image orthicon (8) utilizes a photocathode as the initial sensor. The photoelectron image pattern developed at the photocathode is focused magnetically onto a thin, insulating target surface. Secondary emission from the target then results in a positive charge pattern on the target. The electron beam from the gun scans the charge, losing some electrons to the more positively charged areas of the target, and the

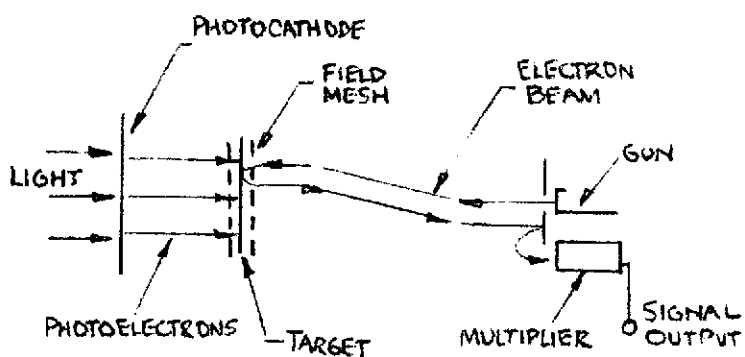
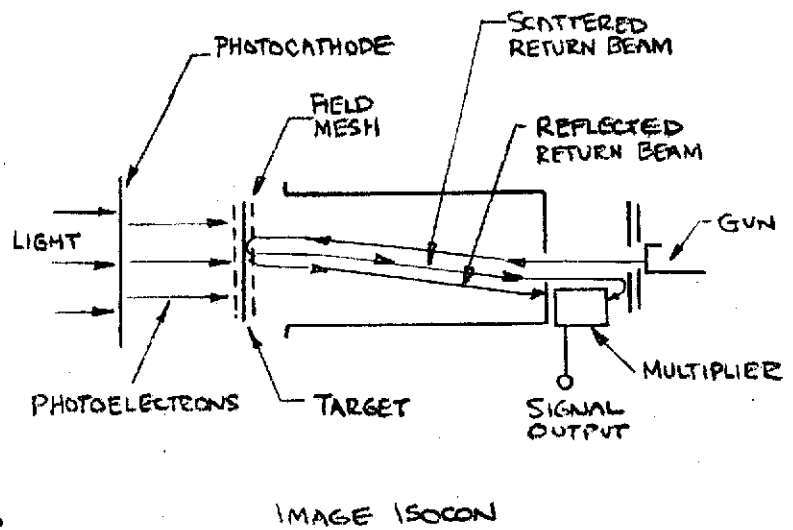


IMAGE ORTHICON

remainder of the beam returns to the electron multiplier surrounding the electron gun. The signal is the current output from the anode of the electron multiplier.

2.3.10 IMAGE ISOCON

Although image isocon will not be studied, an analytical model of the sensor will be presented. The image isocon is a modification of the image orthicon in which an improved electron-optic system has been introduced and in which the problem of inherent beam noise has been largely overcome. The electron-optical system permits separation of the scattered and reflected portions of the electron beam. Whereas the image orthicon accepts all of the return beam for amplification, the image isocon camera tube derives its video signal only from the scanning-beam electrons that are scattered by the storage target.



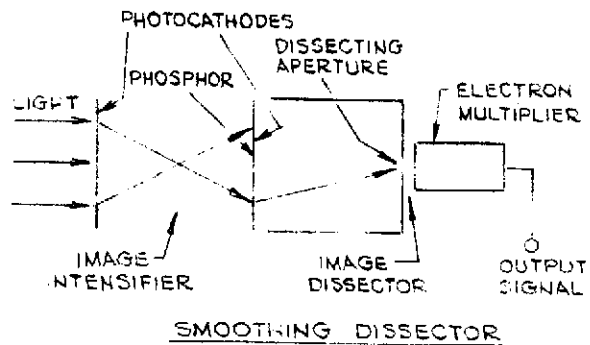
The image isocon has been eliminated as one of the initial camera candidates for the study for many of the same reasons as the image orthicon. It is much more complex and has a lower gain than both the SEC and SIT vidicons. The field mesh lowers the net quantum efficiency by attenuating the

photoelectron image, and it creates a charge image that seriously degrades the sensor MTF during single-exposure readout.

2.3.11 SMOOTHING DISSECTOR

The smoothing dissector will not be analyzed in this study, as it does not appear to have the qualities required to operate as a frame imager for the class of planetary missions of interest.

The combination of an image intensifier tube coupled to the input of an image dissector is called a "smoothing dissector". The image intensifier contains a slow-decay phosphor screen that acts as a temporary storage element. The method offers a high quantum efficiency, wide spectral range, a better signal-to-noise ratio than either a single scanned photomultiplier tube or scanning image dissector, and low light level operation. However, the smoothing dissector lacks long-term storage and slow-scan capability. It is used more efficiently in the line-scan mode.



SECTION III
CAMERA MODELING

3.1 INTRODUCTION

Analytical models have been developed at the component level for those frame-type imaging systems which have been selected as candidate systems for possible use on board a spin-stabilized spacecraft for outer planet applications. These models describe the resolution and peak-signal-to-RMS-noise characteristics of the sensors. Details of the development of the camera models are given in Appendix A, along with a list of the analytical signal-to-noise ratio models for the candidate camera systems.

The basic relationships used in developing the camera models are introduced in this section and several methods of plotting camera performance are described. The methods for calculating the irradiance in the focal plane of a camera imaged on a distant object and for converting that irradiance into the sensor's photocurrent is described first. Then the modulation transfer function (MTF) concept and the MTF treatment of the analytical models are presented. This is followed by a description of the aerial image modulation curve and other methods of plotting camera performance used in this study.

3.2 EXPOSURE CALCULATION FOR ANALYTICAL MODELS

In the process of calculating the irradiance in the focal plane of a camera imaged on a distant object and of converting that irradiance into the sensor's photocurrent, radiometric units (rather than photometric units) will be used to define the spectral response of the detector and spectral irradiance.

3.2.1 GENERAL RELATIONSHIPS

If the relative spectral distribution of the input flux is designated by W_λ , and W_p is the peak spectral density of the input flux in $(W/m^2)/nm$, then the input flux, F_L , is given by:

$$F_L = W_p \int_0^\infty W_\lambda d\lambda \quad (3-1)$$

The detector output current density, I , can be computed from

$$I = S_p W_p \int_0^\infty \sigma_\lambda W_\lambda d\lambda \quad (3-2)$$

where S_p is the peak monochromatic responsivity of the detector in A/W , and σ_λ is the relative spectral responsivity of the detector.

The responsivity R_D of the detector ⁽⁹⁾ can be defined by:

$$R_D = I/F_L = S_p \int_0^\infty \sigma_\lambda W_\lambda d\lambda / \int_0^\infty W_\lambda d\lambda \quad (3-3)$$

3.2.1.1 Orbiting Camera Relationships - For the specific case of a Jupiter orbiter, where the solar irradiance is reflected off of the planet into the focal plane of a camera, additional parameters enter the calculation. The sun-planet distance, planet albedo, phase angle, optical system, and detector characteristics must also be considered.

It can be shown ⁽¹⁰⁾ that the irradiance F_o of an object which fills the field of view at the image plane of the optical lens system is

$$F_o = \frac{W_p t_L \cos \theta}{4r^2 f^2} \int_0^\infty W_\lambda P_\lambda d\lambda \quad (3-4)$$

where the solar irradiance is defined by W_p and W_λ , r is the sun-planet distance in astronomical units, t_L is the transmission of the optical lens, f is the f-number of the lens, θ is the phase angle, and P_λ is the geometric albedo of the planet as a function of wavelength. Since the actual phase functions of the outer planets are not known, a simple Lambert phase function has been assumed.

The detector current density can now be determined from the integral of the product of the spectral response of the detector, the input flux at the image plane, and the spectral transmission of the detector faceplate, $t_{o\lambda}$.

$$I = \frac{W S t_L \cos \theta}{4r^2 f^2} \int_0^\infty W_\lambda P_\lambda t_{o\lambda} \sigma_\lambda d\lambda \quad (3-5)$$

As an alternate method, the responsivity, R_D , and the flux density at the photocathode surface, F_{pc} , could be calculated separately and then combined as follows:

$$R_D = S \int_0^\infty \sigma_\lambda W_\lambda P_\lambda t_{o\lambda} d\lambda / \int_0^\infty W_\lambda P_\lambda t_{o\lambda} d\lambda \quad (3-6)$$

$$F_{pc} = \frac{W t_L \cos \theta}{4r^2 f^2} \int_0^\infty W_\lambda P_\lambda t_{o\lambda} d\lambda \quad (3-7)$$

then

$$I = R_D F_{pc} \text{ amps/meter}^2 \quad (3-8)$$

3.2.2 DETECTOR QUANTUM EFFICIENCY - GENERAL RELATIONSHIPS

The detector current density could also be expressed in terms of the integral quantum efficiency, η , in electrons/photon by

$$I = \eta F_v e \quad (3-9)$$

where F_v is the rate of flow of photons

$$F_v = \frac{P}{hc} \int_0^\infty \lambda W_\lambda d\lambda, \quad (3-10)$$

h is Planck's constant (6.62×10^{-34} joule-sec), c is the velocity of light (3×10^8 m/sec), e is the electronic charge (1.6×10^{-19} coulombs), and λ is the wavelength in meters.

If the detector quantum efficiency, η_λ , is known as a function of wavelength, then the detector current density can be obtained from

$$I = \frac{eW}{hc} \int_0^\infty \lambda W_\lambda \eta_\lambda d\lambda \quad (3-11)$$

3.2.2.1 Orbiting Camera Relationships - For the specific case of an imaging device on an orbiting spacecraft, Equation (3-4) can be rewritten in terms of the rate of flow of photons at the sensor's faceplate as

$$F_o = \frac{W t_L \cos\theta}{4hcr^2 f^2} \int_0^\infty \lambda W_\lambda P_\lambda d\lambda \quad (3-12)$$

The detector current density then is expressed by

$$I = \frac{eW t_L \cos\theta}{4hcr^2 f^2} \int_0^\infty \lambda W_\lambda P_\lambda t_{o\lambda} \eta_\lambda d\lambda \quad (3-13)$$

3.3 MODULATION TRANSFER FUNCTIONS

The analytical models for the candidate cameras (signal-to-noise ratio equations) have been developed for predicting performance through the use of the aerial image modulation (AIM) curve concept (also called the threshold modulation method). The AIM curve, which is the locus of constant signal-to-noise ratio of the camera system, shows the relationship between input modulation and spatial frequency and makes it possible to determine the resolving power of a camera system from its modulation transfer function.

The modulation transfer function (MTF) describes the ability of the camera system, or one of its components, to reproduce an input sine-wave image.⁽¹¹⁾ The MTF is defined as the amplitude response of the system. (It represents the amplitude term of the optical transfer function which also contains a phase term. In camera system analyses, only the amplitude term is important.) The overall system modulation transfer function, designated $\tau_s(K)$, is the ratio of the modulation in the image to that in the object as a function of the frequency of the sine-wave input.

$$\tau_s(K) = \frac{M_i(K)}{M_o} \quad (3-14)$$

where

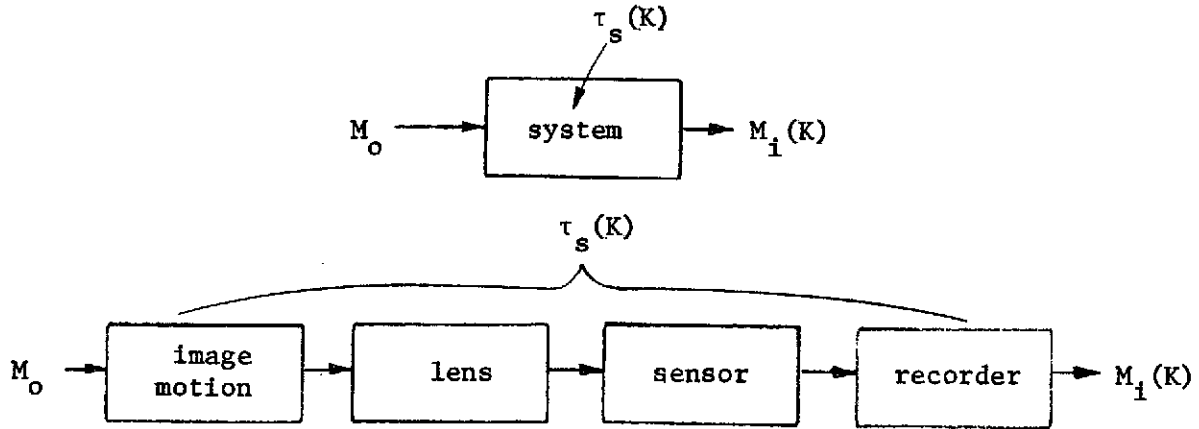
$\tau_s(K)$ = the MTF value for a sine wave of K cycles/mm

K = the spatial frequency

$M_i(K)$ = the modulation in the image

M_o = the modulation in the object

A schematic representation of the equation would look like:



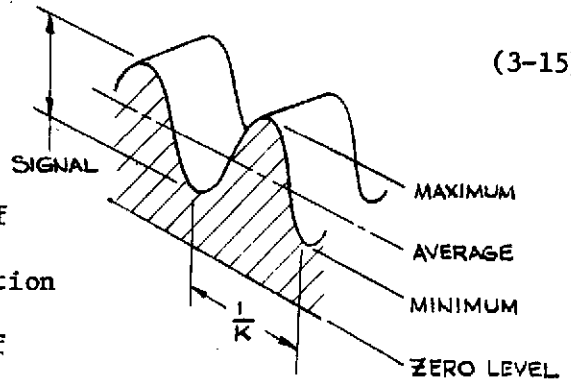
The object modulation, M_o , is defined for an object (the scene) with a sinusoidal distribution of light as follows:

$$M_o = \frac{E_{\max} - E_{\min}}{E_{\max} + E_{\min}} \quad (3-15)$$

where

E_{\max} = the maximum intensity of light from the object with sine-wave distribution

E_{\min} = the minimum intensity of light from the object



The object modulation can also be defined in terms of the contrast ratio of the scene by

$$M_o = \frac{C_R - 1}{C_R + 1} \quad (3-16)$$

where

$$C_R = \frac{E_{\max}}{E_{\min}} \quad (3-17)$$

and C_R = the contrast ratio of the scene.

In the analytical models for the camera systems, the signal is expressed in terms of the object (input) modulation. The optical signal is defined in all cases as the difference in extreme intensity levels.

$$S_o = \Delta E = E_{\max} - E_{\min} \quad (3-18)$$

In the same manner, if we assume that for all values of K, the average intensity, \bar{E} , is defined as:

$$\bar{E} = \frac{E_{\max} + E_{\min}}{2} \quad (3-19)$$

then equation (3-15) becomes

$$M_o = \frac{\Delta E}{2\bar{E}} \quad (3-20)$$

or

$$S_o = 2M_o \bar{E} \quad (3-21)$$

When the entire camera system is considered, the optical signal is transferred through many individual components, each having a unique MTF. The processes that convert the average light intensity of the scene to an average camera output current also reduce the modulation of the input signal. The output signal of the camera system, $S(K)$, is therefore given by

$$S(K) = 2M_i(K)I_i \quad (3-22)$$

or

$$S(K) = 2M_{o\tau_s}(K)I_i \quad (3-23)$$

where I_i is the output current.

Equation (3-23) has been used to develop the signal expressions in all of the camera analytical models in Appendix A.

3.3.1 COMPONENT MODULATION TRANSFER FUNCTIONS

3.3.1.1 Camera System MTF - The camera system MTF, $\tau_s(K)$, used in the analytical models, is the product of all of the component MTFs.

$$\tau_s(K) = \tau_{IM}(K)\tau_{LENS}(K)\tau_{SEN}(K)\tau_{REC}(K) \quad (3-24)$$

where

$\tau_{IM}(K)$ = the image motion MTF

$\tau_{LENS}(K)$ = the optical MTF

$\tau_{SEN}(K)$ = the sensor MTF

$\tau_{REC}(K)$ = the recorder MTF

The variable $\tau_{SEN}(K)$, can also be derived from the product of the sensor component MTFs. The MTFs for components such as the fiber optic face-plate (when electrostatic focusing is employed), the photoemitter, image section, target, field mesh, and read beam can be multiplied together to obtain the sensor MTF.

3.3.1.2 Image Motion MTF - Several types of image motion can reduce the performance of a camera system because of movement during exposure, such as linear motion, random motion, vibrations and parabolic movement. Only the linear image motion MTF, caused by the spacecraft spin rate, appears to be significant enough to be considered in the camera models because of the short exposure time required. The relative magnitude and effects of the various types of image motion are presented in Section 6.

The transfer function for linear image motion⁽¹¹⁾ is

$$\tau_{IM}(K) = \frac{\sin(\pi A_m K)}{\pi A_m K} \quad (3-25)$$

where A_m is the magnitude of image motion relative to the sensor's faceplate during the exposure time, and K is the spatial frequency.

$\tau_{IM}(K)$ is shown as a function of the product $A_m K$ in Figure 3.1. Note that when the uncompensated image motion is equivalent to the spatial frequency (i.e., $A_m K = 1.0$), exactly two pixels are smeared and the modulation becomes zero. A maximum smear of 0.5 to 1.0 pixel is generally selected as a performance criterion in order to maintain a satisfactory modulation.

For use in the camera models, the image motion MTF is more convenient if expressed in terms of the spin rate, focal length of the optical system, and exposure time instead of A_m .

$$A_m = V_s t_e = \frac{2\pi}{60} F R_s t_e \quad (3-26)$$

therefore

$$\tau_{IM}(K) = \frac{\sin[2\pi^2 R_s t_e F K / 60]}{[2\pi^2 R_s t_e F K / 60]} \quad (3-27)$$

where

V_s = velocity of the image with respect to the object

t_e = exposure time

F = focal length of the lens

R_s = spin rate (rpm)

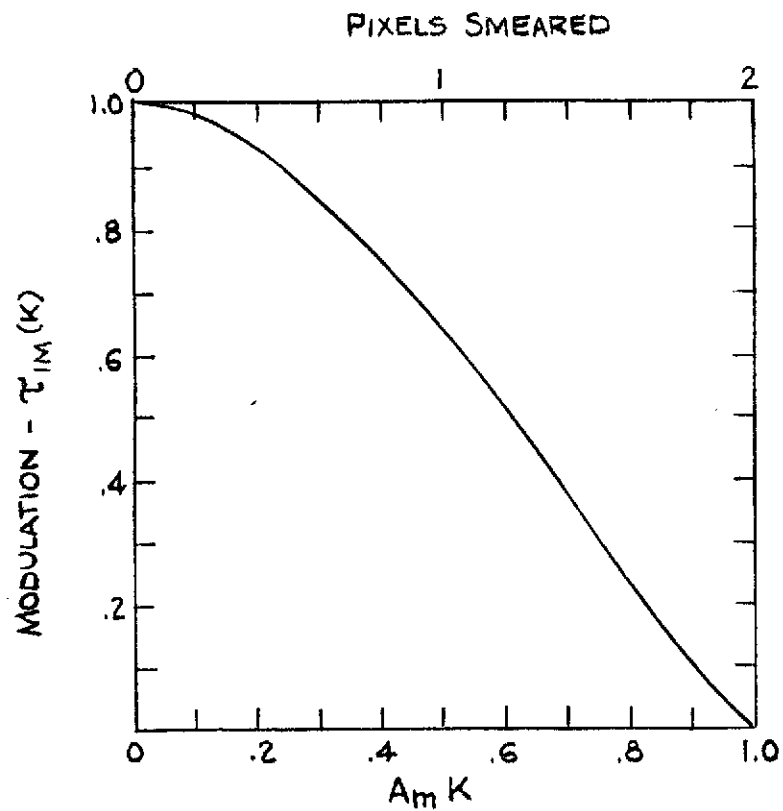


IMAGE MOTION TRANSFER FUNCTION

FIGURE 3-1

3.3.1.3 Lens MTF - In selecting the MTF of the optical system, diffraction-limited lenses will be modeled. Aberration-limited lenses and optics where both diffraction-limited and aberration-limited effects exist will not be considered.

The MTF of a perfect diffraction-limited lens is ⁽¹⁰⁾

$$\tau_{\text{LENS}}(K) = \frac{2}{\pi} \left[\cos^{-1} \left(\frac{\pi K}{b} \right) - \left(\frac{\pi K}{b} \right) \sqrt{1 - \left(\frac{\pi K}{b} \right)^2} \right] \quad (3-28)$$

where

$$b = \frac{\pi D}{F\lambda}$$

and

λ is the wavelength

D is the lens aperture diameter

3.3.1.4 Sensor MTF - The MTF of the camera tube or sensing device will be handled in several ways in the analytical models. When possible, mathematical expressions for sensor components will be used, if good correlation with actual device performance is indicated. In some cases, where the mathematical expressions are not available (such as for complex electron optical sections), actual MTF data will be used in tabular form.

The general expression for the sensor MTF consists of the product of all the sensor components, provided that all the elements are linear.

Therefore

$$\tau_{\text{SEN}}(K) = \tau_{\text{IS}}(K) \tau_{\text{T}}(K) \tau_{\text{R}}(K) \quad (3-29)$$

where

- $\tau_{IS}(K)$ = the image section MTF
- $\tau_T(K)$ = the target MTF
- $\tau_R(K)$ = the readout MTF

3.3.1.4.1 Readout MTF - The MTF of the readout beam can be readily calculated assuming the scanning electron beam spot has a Gaussian shape⁽¹⁰⁾. The readout MTF is determined by taking the Fourier transform of a Gaussian distribution.

$$\tau_R(K) = e^{-2\pi^2 K^2 \sigma^2} \tag{3-30}$$

where

σ = standard deviation

To perform this calculation σ must be defined in terms of the beam diameter. This can be accomplished in a number of ways. Sometimes the beam diameter is defined as the full width at half maximum on the Gaussian curve, which yields a spot diameter $d = 2.35 \sigma$. In this study, the beam diameter will be defined as the full width of the Gaussian curve at the 5% amplitude point. This yields a spot diameter of $d = 4\sigma$.

3.3.1.4.2 Target MTF - Analytical expressions for the target MTF can be obtained for all camera models. Expressions for the theoretical MTF of the electrostatic storage targets have been derived by Krittman.⁽¹²⁾

For a slow-scan vidicon or SEC target, the target MTF is:

$$\tau_T(K) = \frac{1 - e^{-4\pi K t_1}}{4\pi K t_1}, \quad (3-31)$$

where

t_1 = the target thickness.

For the image orthicon and image isocon, the target MTF is:

$$\tau_T = \frac{e^{-4\pi K t_1} - e^{-4\pi K (t_1 + t_2)}}{4\pi K t_2} \quad (3-32)$$

where

t_2 = target-to-mesh spacing.

In the electrostatic storage camera and SiO_2 vidicon where the dielectric constant, k_1 , of the storage medium is not unity, the target MTF becomes:

$$\tau(K)_{\text{target}} = \frac{1 - e^{-4\pi K t_1}}{4\pi K t_1} \left[\frac{2k_1}{(k_1 + 1) + (k_1 - 1)e^{-4\pi K t_1}} \right] \quad (3-33)$$

The modulation transfer function for the silicon target used in the silicon vidicon and SIT vidicon will be determined analytically. The target MTF, which dominates the overall sensor MTF, is made up of three factors: the diode spacing; the lateral diffusion; and electrostatic thickness.

Crowell⁽¹³⁾ describes the first two effects which are summarized below.

The MTF resulting from lateral hole diffusion, $\tau_H(K)$, is given

by:

$$\tau_H(K) = \eta_K / \eta_0 \quad (3-34)$$

where

$$\eta_K = \frac{\alpha L (1-R)}{\alpha^2 L^2 - 1} \left[\frac{2(\alpha L + S_v L / D_h) - (\beta_+ - \beta_-) \exp(-\alpha L_a)}{\beta_+ - \beta_-} - (\alpha L)^{-1} \exp(-\alpha L_a) \right] - (1-R) \exp(-\alpha L_b) \quad (3-35)$$

and

$$\eta_0 = \eta_K \Big|_{K=0} \quad (3-36)$$

and in which

$$\beta_{\pm} = (1 \pm S_v L / D_h) \exp \pm (L_a / L) \quad (3-37)$$

and

$$1/L^2(K) = 1/L_0^2 + K^2 \quad (3-38)$$

α = silicon absorption coefficient at the wavelength of interest

R = silicon reflectivity at the wavelength of interest

S_v = surface recombination velocity for holes at the illuminated surface

D_h = hole diffusion constant in n-type silicon

L_a = thickness of undepleted region

L_b = thickness of the n-type region plus width of depleted region

K = spatial frequency

L_0 = diffusion length.

The MTF for the finite diode spacing, $\tau_D(K)$, is given by

$$\tau_D(K) = \frac{\sin 2\pi K d_p}{2\pi K d_p} \quad (3-39)$$

where

$$2d_p = \text{center-to-center spacing of diodes.}$$

The third silicon target MTF component due to the electrostatic thickness (the first-scan effect), $\tau_E(K)$, is described by Krittman⁽¹²⁾ as

$$\tau_E(K) = \frac{1 - e^{-4\pi K t_1}}{4\pi K t_1} \quad (3-40)$$

where t_1 is the thickness.

By combining these effects, the target MTF, $\tau_T(K)$, is then determined.

$$\tau_T(K) = \tau_D(K) \tau_H(K) \tau_E(K) \quad (3-41)$$

3.3.1.5 Image Section MTF - The MTF of the image section is the product of the imaging electron optics MTF, the photoconductor or photoemitter MTF, and the fiber optics faceplate MTF when used. The image section MTF will most likely be introduced into the analytical models in tabular form from experimental data rather than as mathematical expressions, because the theoretical expressions are generally not available.

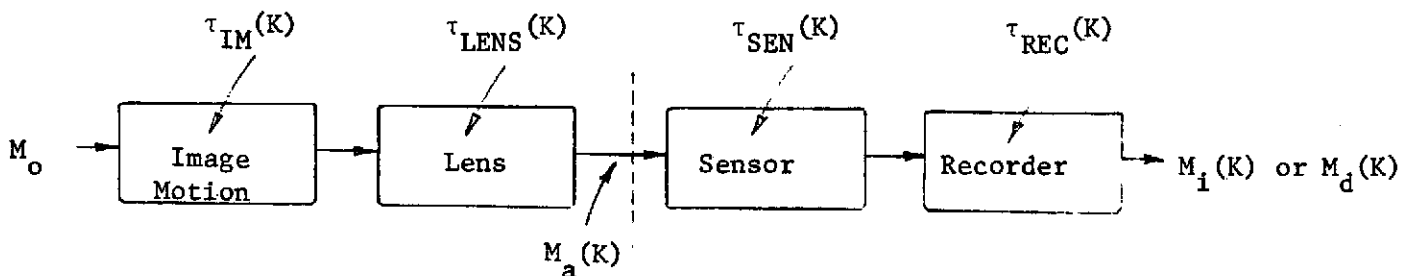
3.4 AERIAL IMAGE MODULATION CURVES

The limiting resolving power of a camera system can be calculated in numerous ways. One method that will be used to compare systems in this study is the aerial image modulation curve (AIM). Using this method, the limiting resolution of a system can be obtained from the intersection of the sensor AIM curve (also called the modulation detectability curve) $M_d(K)$, with the available aerial image modulation function, $M_a(K)$.

The available aerial image modulation⁽¹⁴⁾ can be defined at any point within the camera system. However, it is convenient to define $M_a(K)$ as the aerial image modulation at the sensor faceplate in order to obtain a better comparison of the performance of the candidate sensors. The analytical expression for $M_a(K)$ is given by

$$M_a(K) = M_o \tau_{IM}(K) \tau_{LENS}(K) \tag{3-42}$$

The modulation, $M_a(K)$, at the sensor faceplate is determined by considering all MTFs occurring prior to the sensor. A schematic representation of the camera system showing this relationship follows.



The modulation detectability curve $M_d(K)$ (also called the threshold modulation) is developed from the relationship

$$M_d(K) = \frac{SNR_L}{SNR(K)} \quad (3-43)$$

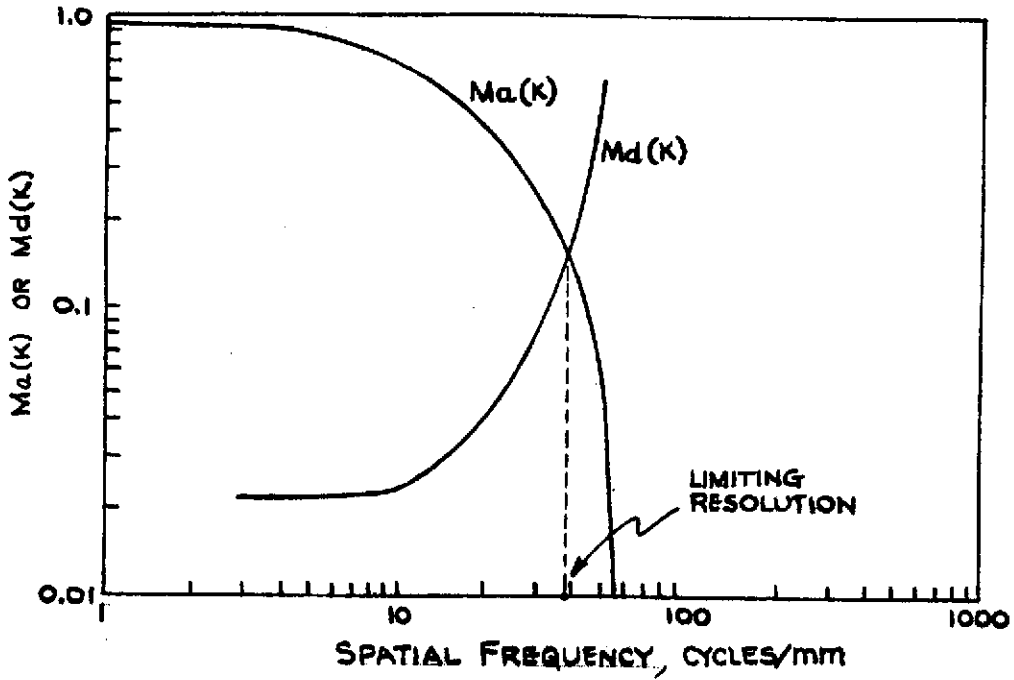
where

$SNR(K)$ = the signal-to-noise ratio of the camera system

SNR_L = the limiting threshold signal-to-noise ratio.
This value is generally set between 1.7 and 3.6 when testing a system depending on the type of target pattern used and if motion is present. A value of 3 was selected for the curves plotted in this study.

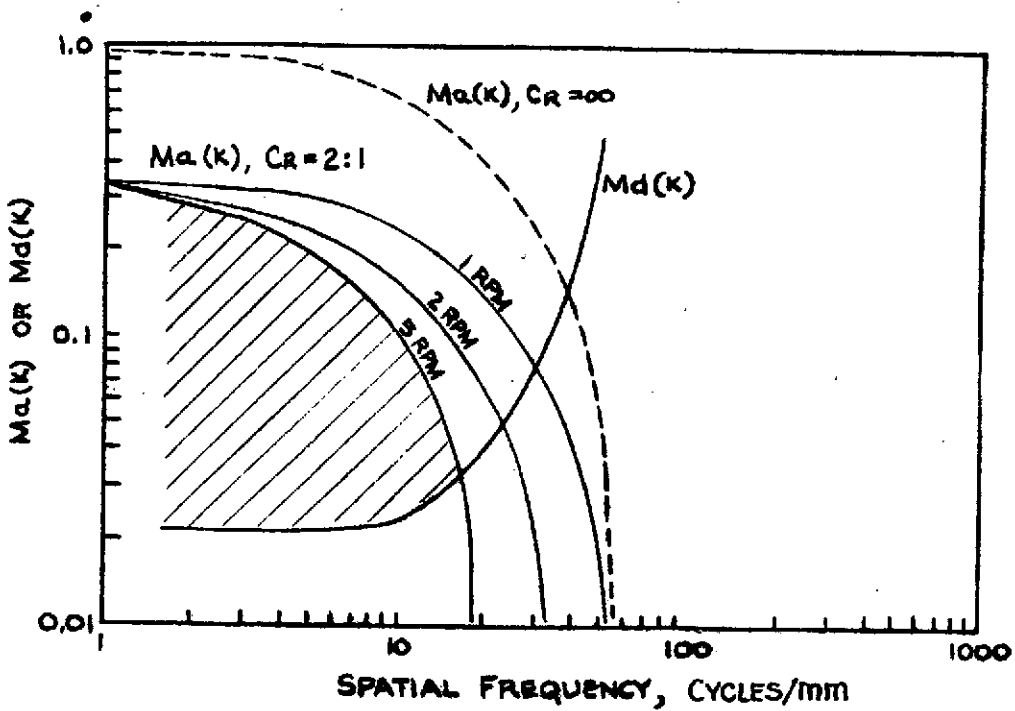
The modulation detectability curve $M_d(K)$, as shown in Figure 3-2, defines the locus of constant signal-to-noise ratio (at the threshold value of SNR_L). It also describes the minimum aerial image modulation at the sensor required to achieve the resolution corresponding to the intersection of the two curves.

Figure 3-2 illustrates the method of determining the resolving power of a camera system. Here, the available aerial image modulation and the modulation detectability curve of the camera are plotted as a function of spatial frequency. Note that the scene is resolved when $M_a \geq M_d(K)$ and that the limit of resolution occurs when $M_a = M_d(K)$. The limiting resolution of the system (at a threshold signal-to-noise ratio of 3) is indicated by the spatial frequency corresponding to the intersection of the two curves.



AIM CURVE (HYPOTHETICAL EXAMPLE)

FIGURE 3-2



AIM CURVE (HYPOTHETICAL EXAMPLE)

FIGURE 3-3

To find the resolution which would be obtained with a low-contrast target, we use the same modulation detectability curve. Only the available aerial image modulation is affected by the contrast change. For a contrast ratio of 2:1 ($M_o = 0.33$), the ordinate of the curve, $M_a(K)$, is multiplied by the scene modulation as shown in Equation (3-42).

The available image modulation can also be modified to show the effect of spin rate and other mission variables on system performance. At 5 rpm, for instance, the performance of the system would be limited to the shaded region shown in Figure 3-3.

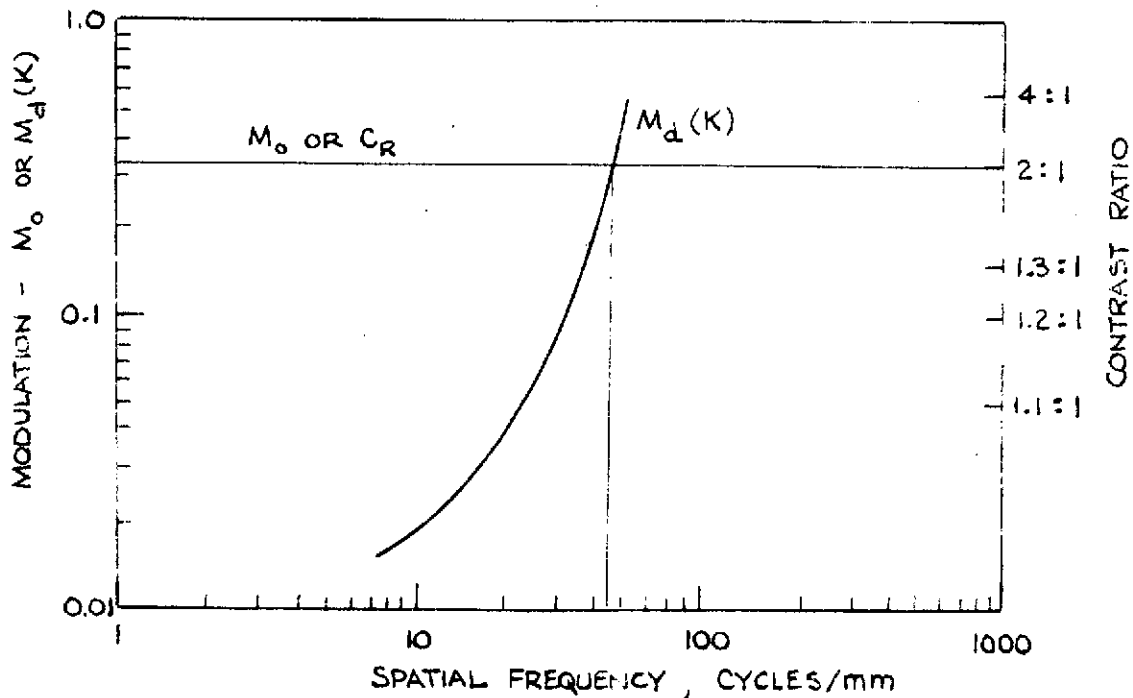
3.4.1 APPLICATION OF AIM CURVES

The AIM curve concept, described in Paragraph 3.4, will be applied in Section 7 to perform the worst-case analysis and to compare the performance of the candidate systems. The method is especially suited to comparing different sensors. Since the modulation, $M_a(K)$, is defined at the sensor faceplate, the performance of the sensor is thereby isolated from the lens and the effects of image motion. Consequently, only the sensor portions of the candidate systems are compared.

In Section 8, in which the analysis for a specific Jupiter orbiter mission is performed using the selected camera systems, a different method of plotting performance is employed. In Section 8, the performance of the entire system is of interest and we do not want to isolate the sensor from the rest

of the system. In this case, the available aerial image modulation is taken at the scene rather than at the sensor faceplate, and it is equivalent to the object modulation M_o . The MTFs of the lens and for image motion are now used in the calculation of the modulation detectability curve, $M_d(K)$.

Figure 3-4 illustrates the system modulation curve method of plotting performance. Note that the object modulation, M_o , is plotted on the ordinate. Referring to Equation (3-16) we see that the object modulation is only dependent on the contrast of the scene and is invariant with the spatial frequency. Consequently, the object modulation can be represented by a straight horizontal line, and a contrast ratio scale can be superimposed on the modulation scale.



SYSTEM MODULATION (HYPOTHETICAL EXAMPLE)

FIGURE 3-4

3.5 SIGNAL-TO-NOISE RATIO

The signal-to-noise ratios plotted in this study are calculated at two distinct locations along the image processing chain. First, the signal-to-noise ratio at the data link ($SNR_{\text{data link}}$) is given to characterize a camera's analog signal prior to encoding. Then the signal-to-noise ratio of the reconstructed picture ($SNR_{\text{reconstructed}}$) at the ground recorder is determined. The $SNR_{\text{reconstructed}}$, as used in this analysis, represents the ideal case where no additional noise is introduced by the digitizing and recording processes and where no MTF loss is associated with digitizing. The characteristics of the telemetry equipment and ground recorder must be known before the actual performance in terms of the reconstructed picture can be determined. Without this information, we can only establish the limits of performance and conclude that the actual SNR of the picture will be between the data link and reconstructed picture signal-to-noise ratios given.

3.5.1 SIGNAL-TO-NOISE RATIO AFTER RECONSTRUCTION

The analytical models developed in subsequent program tasks represent the SNR at the data link. In order to obtain the signal-to-noise ratio after reconstruction of the analog signal, the analytical models must be modified so that

$$SNR_{\text{reconstructed}} = \sqrt{\frac{A_k}{A_b}} \frac{\tau_{\text{rec}}(K)}{\beta_2(K)} SNR_{\text{data link}} \quad (3-44)$$

where

A_k is any arbitrary area defined in terms of a resolution element of spatial frequency K so that

$$A_k = \left(\frac{1}{2K}\right)^2,$$

A_b is the area of the recording beam (which in this analysis has been assumed to be the same as that of the scanning beam in the camera),

$\tau_{rec}(K)$ is the modulation transfer function of the recorder,

and β_2 is a noise correction factor given by O. Schade Sr. (15)

$$\beta_2 = \frac{\int_0^K \int_0^K \tau_{rec}(K)^2 dK_x dK_y}{\int_0^K \int_0^K dK_x dK_y} \quad (3-45)$$

Since the recording method has not been identified, in this analysis the recorder modulation transfer function will be set to unity. Consequently when $\tau_{rec}(K) = 1$, $\beta_2(K)$ is also unity and

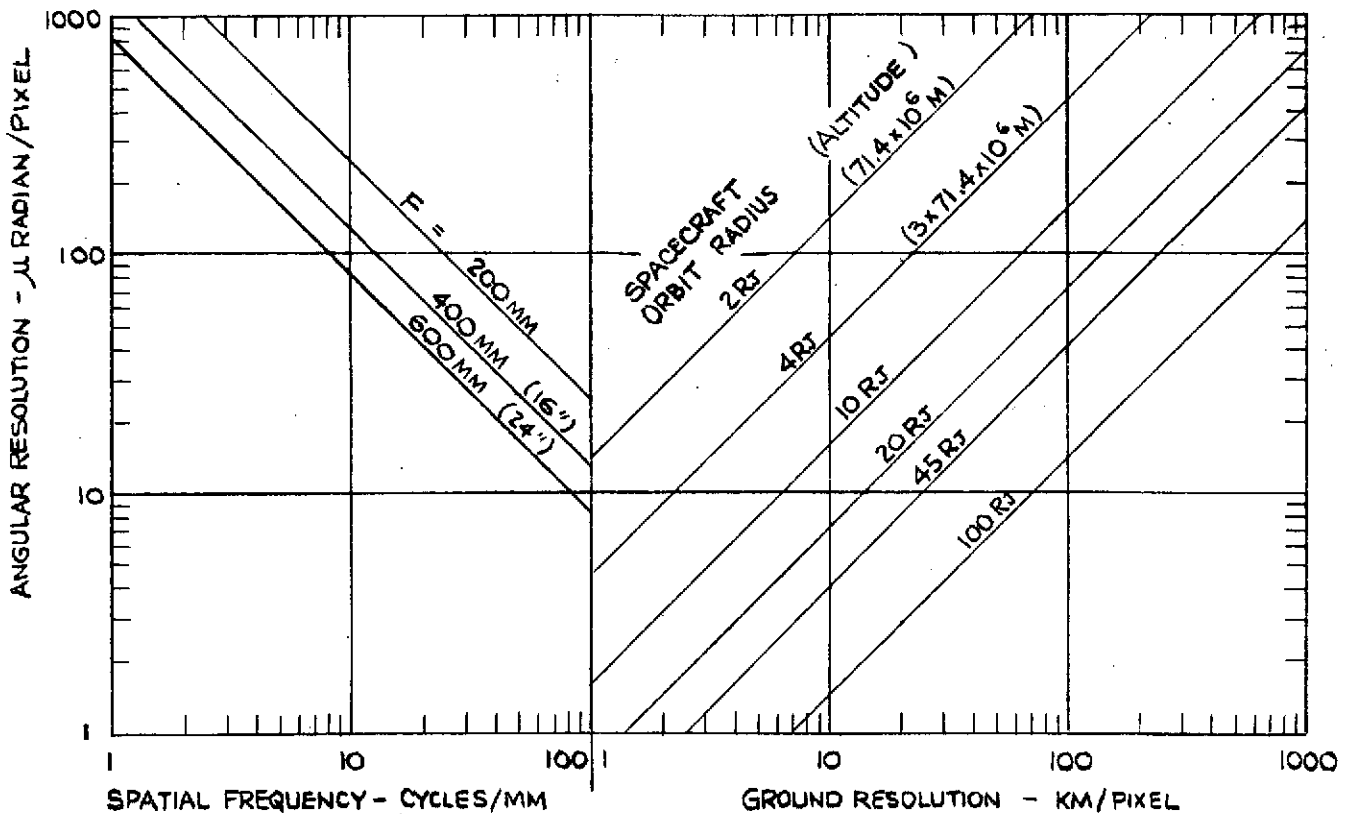
$$SNR_{reconstructed} = \sqrt{\frac{A_k}{A_b}} SNR_{data\ link} \quad (3-46)$$

This equation represents an upper bound to the signal-to-noise ratio of the reconstructed image on the recording medium. Knowledge of the characteristics of the encoding circuits and recorder equipment are required to increase the accuracy of the calculation.

3.6 RESOLUTION RELATIONSHIPS

The resolution relationships required to determine the ground resolution for a camera system orbiting Jupiter are of interest. The conversion from angular resolution subtended by one pixel to ground resolution at the planet Jupiter can be obtained from Figure 3-5 for vertically-oriented camera systems.

Starting with a known focal length, the angular resolution can be converted to spatial frequency in cycles/mm at the detector. Angular resolution can also be translated to ground resolution in km/pixel once the altitude of the spacecraft is known.



RESOLUTION RELATIONSHIPS

FIGURE 3-5

To convert directly from spatial frequency to ground resolution the following relationship may be used as a first-order approximation:

$$G = \frac{H}{2KF} \quad (3-47)$$

where

- G = ground resolution in km/pixel
- H = altitude of the spacecraft in km
- K = spatial frequency in cycles/mm or lp/mm
- F = focal length in mm

3.7 MAXIMUM SIGNAL-TO-NOISE RATIO

The maximum signal-to-noise ratio that a sensor can deliver is associated with quantum-noise-limited operation. The signal-to-noise ratio is limited by the fluctuations in the photon flux arriving at the photoemitter. If, during the exposure, the average number of photons per picture element is \bar{n} and the quantum efficiency of the photocathode is η , then an average of $\eta\bar{n}$ photoelectrons/picture element strike the target. If no other noise sources are present,

$$\text{SNR (photoelectrons)} = \frac{\eta\bar{n}}{\sqrt{\eta\bar{n}}} = \sqrt{\eta\bar{n}} \quad (3-48)$$

It is important to realize that no amount of noise-free amplification can improve the photoelectron signal-to-noise ratio. From this viewpoint, placing an intensifier stage in front of any quantum-noise-limited system would not improve performance.

SECTION IV
COMPUTER PROGRAMS

4.1 INTRODUCTION

Computer programs have been developed for the signal-to-noise ratio models for all of the candidate imaging systems. These programs were used in Sections 7 and 8 to perform the parametric analysis.

4.2 COMPUTER PROGRAMS

The analytical models for the camera systems have been programmed in FORTRAN IV computer language. A separate program exists for each sensor type. Detailed symbolic listings of the programs along with a line-by-line description are given in Appendix B. Computational flow diagrams and samples of a typical input/output worksheet are included.

SECTION V

RADIATION AND RELIABILITY FACTORS

5.1 INTRODUCTION

The objective of the radiation and reliability study is to evaluate each of the proposed sensors in order to help select the most suitable sensor for the Jupiter orbiter mission. First, the expected radiation environment is studied, then the effect of that radiation upon each of the various image tubes is discussed. Conclusions are then drawn on which tubes are the most reliable.

5.2 DISCUSSION OF RADIATION

5.2.1 MISSION DURATION

The Jupiter orbiter mission consists of the passage from Earth to Jupiter with a mission objective of at least 10 orbital passes. The interplanetary leg is expected to take from 750 to 900 days, and the orbital passes from 10 to 50 days each. ⁽²⁾ Although many different orbit shapes are being considered for the mission, the charged particle densities will be calculated for an orbit in the Jovian magnetic equatorial plane with a periapsis of $2.29 R_J$ and an apoapsis of $45.131 R_J$. The neutron and gamma fluences will be calculated based on a total operating time of 1100 days.

5.2.2 EXPECTED RADIATION DOSAGE

Several sources contribute to the sensor radiation environment: RTG radiation; terrestrial and Jovian trapped particle radiation; galactic and solar cosmic rays; and the solar wind. The RTGs have a neutron and gamma ray flux, while the other sources consist primarily of protons, electrons and gamma rays. However, the charged particle flux in the Jovian magnetosphere is so much greater than that encountered in interplanetary space that all other charged particle sources can be neglected.

5.2.3 RTG RADIATION

Estimates by TRW⁽²⁾ for the SNAP-19 RTGs indicate an average neutron flux of 3.5×10^3 neutrons/cm²-sec and an average gamma ray flux of 5×10^4 /cm²-sec at the science package. Other estimates are as low as 250 neutrons/cm²-sec and 8×10^3 gammas/cm²-sec, but the higher TRW measurements will be used for this report to establish worst-case results. Most of the neutron energy is in the 1-3 MeV range.

5.2.4 JOVIAN RADIATION BELTS

Several models have been developed for the Jovian radiation belts. The first, and most famous, is that developed by Neil Divine of JPL. Following the JPL Jupiter Radiation Workshop in July 1971, a new model was devised (BKTC model) which predicts significantly higher fluxes for both protons and electrons⁽¹⁶⁾. It should be pointed out, however, that both models rely on

analysis of the decametric radiation from Jupiter, which is only related to the electron flux. The proton flux has then been estimated from the electron flux. The graphs in Figure 5-1 depict the fluxes as a function of distance from the center of Jupiter in the equatorial plane. Using the BKTC model, the equatorial charged particle fluxes at 2.29 R_J are

	Nominal	Maximum
protons:	5×10^6	7×10^9 particles/cm ² -sec
electrons:	7×10^6	5×10^7 particles/cm ² -sec

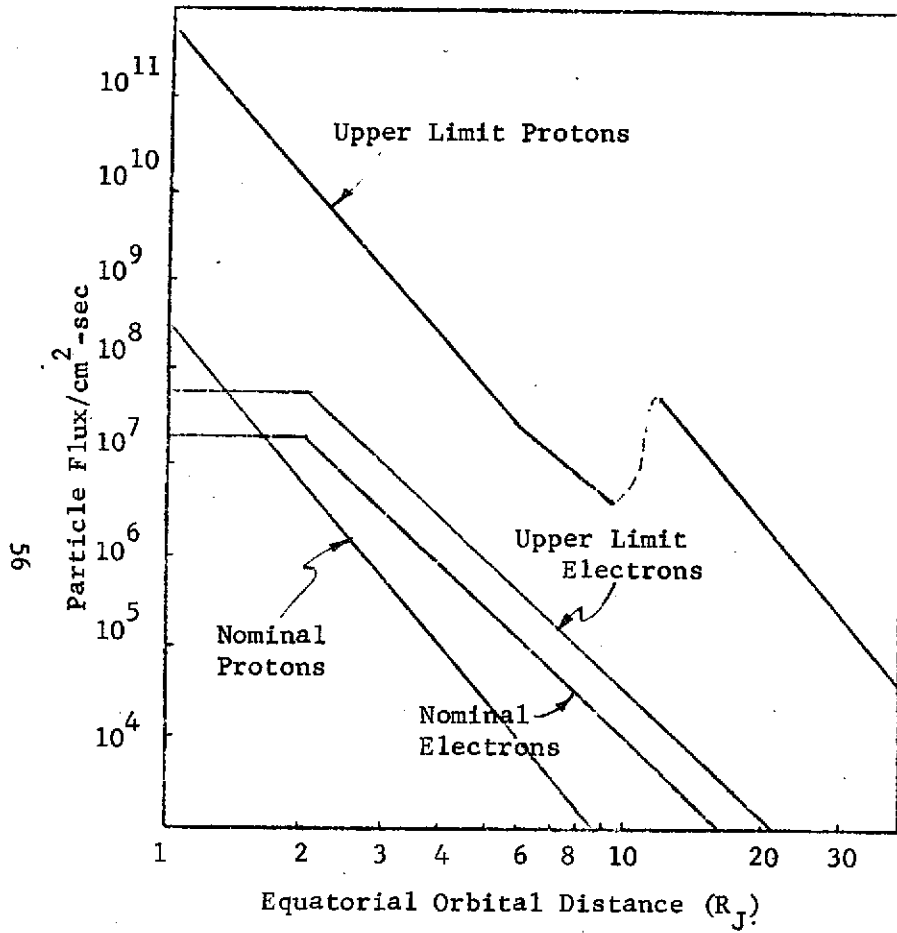
The maximum exposure occurs within a few hours of periapsis. For example, at $t = \pm 4$ hours, the spacecraft is beyond 5 R_J, which reduces the flux by two orders of magnitude for the BKTC model. The resulting integrated proton fluences are on the order of 4×10^{13} /cm² per orbit. Thus, for a ten-orbit lifetime, the total particle fluence would be:

	Max. Fluence/cm ²
protons	4×10^{14}
electrons	3×10^{12}
neutrons	3×10^{11}
gammas	5×10^{12}

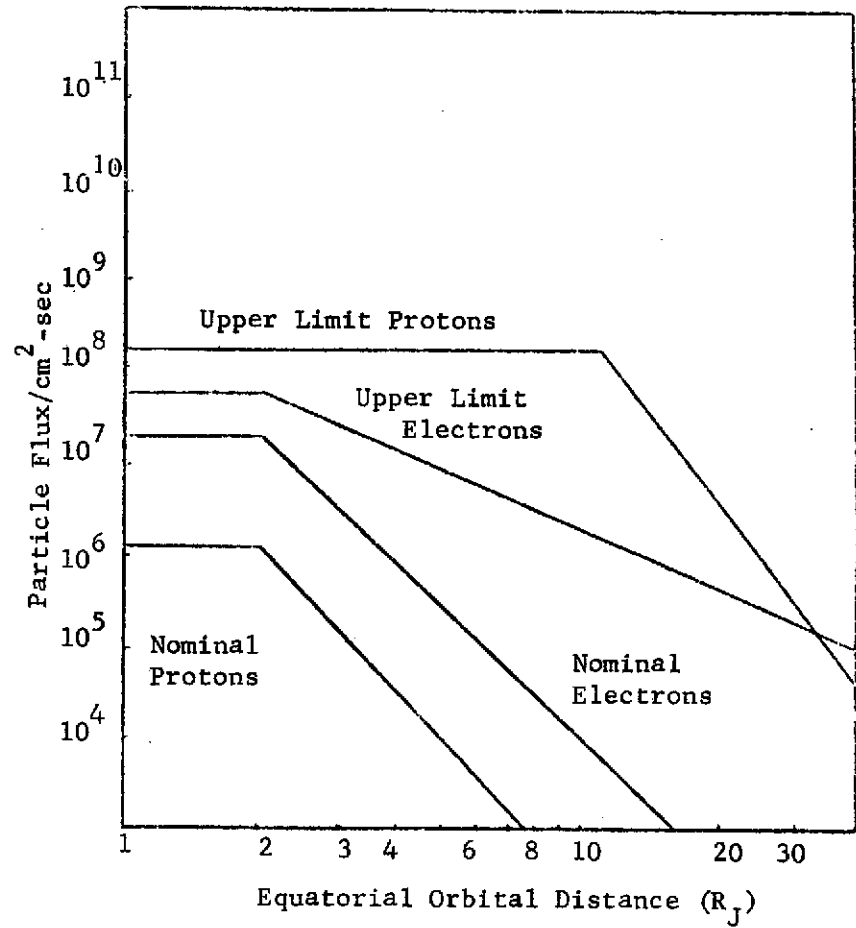
5.3 SENSOR RADIATION RESISTANCE DATA

Degradation of a sensor can occur in many ways. However, since all the parts of each sensor system except the target are identical from a first-order radiation damage standpoint, only the various targets will be discussed

RADIATION MODELS FOR JUPITER



BKTC model of charged particle fluxes in Jupiter's trapped radiation belts.
(Data from Beck)



Divine model of charged particle fluxes in Jupiter's trapped radiation belts. (Data from Beck)

Figure 5-1

in detail. For instance, each sensor will require a set of optics and electronic equipment. The radiation damage caused to each sensor system by degradation of these parts will be approximately equivalent. Only the relative radiation resistance of the sensor targets will cause significant differences.

Each of the candidate sensors will be subject to problems arising from radiation effects on the glass envelope. For instance, at proton dosages above $10^{10}/\text{cm}^2$, clear pyrex glass turns brown. In addition, luminescence can occur when particles collide with the glass. It is therefore recommended that fused silica or quartz be used for faceplates and that ceramic be used for the tube bodies. This would help to eliminate two important problem areas.

Detailed sensor data follows.

5.3.1 SEC TUBE

The target of the SEC tube is comprised of 500 \AA of Al_2O_3 deposited on a 500 \AA thick layer of Al. Deposited on the Al and facing the read gun is a porous layer of KCl. In operation, arriving photoelectrons from the photocathode generate secondary electrons in the KCl layer. These electrons are replaced by the read beam.

This tube is particularly gamma radiation resistant due to the excellent insulating properties of the KCl layer which holds the charge. Radiation studies⁽¹⁷⁾ done for the Apollo ATM program by Westinghouse showed that there

were no permanent irreversible effects on tube performance after gamma irradiation. This includes photoresponse, sensitivity and lag. When tubes were operated in a gamma ray flux, the only major problems were image washout and reduced storage time. At dosages of 1.8×10^7 gammas/cm²-sec, the washed-out picture was observable.

Using this as the maximum acceptable dose rate, the tube should be able to survive almost 2×10^{15} gammas/cm² over the length of the trip. This is far in excess of the 5×10^{12} gammas/cm² expected from the RTGs.

More data is needed on SEC tube operation in proton and electron environments before a complete assessment of its reliability can be made.

5.3.2 SIT TUBE/SILICON VIDICON

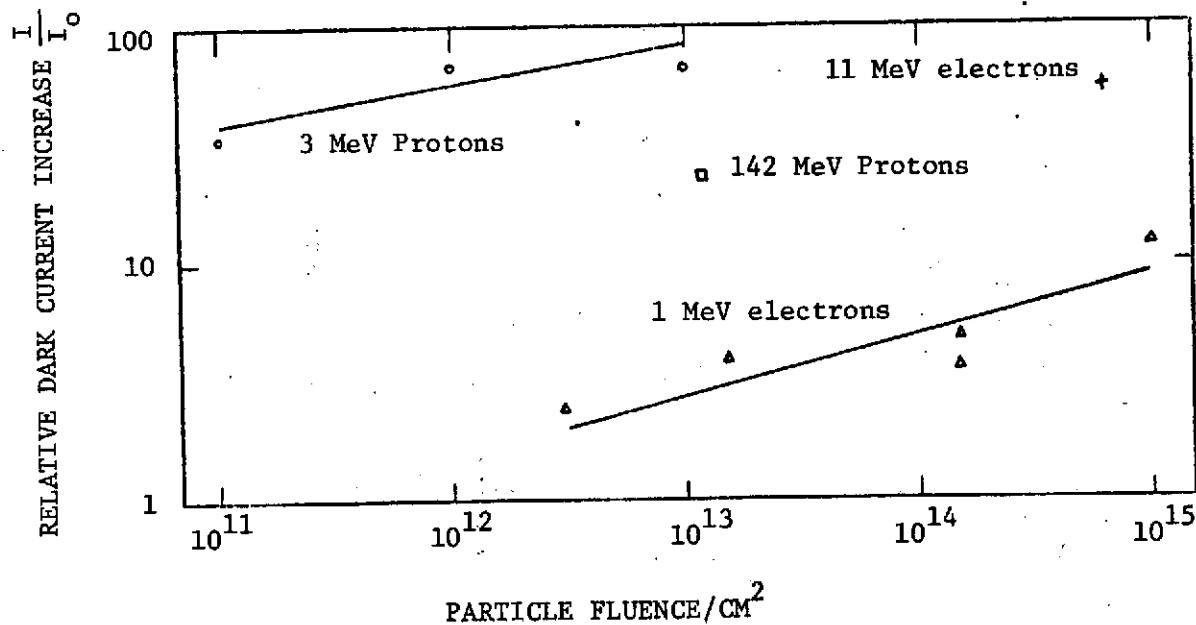
The targets of the SIT and silicon vidicon tubes consist of a silicon diode array on a 1/2 mil thick silicon wafer. In the silicon vidicon, incident light impinges directly on the diode target, whereas in the SIT tube, electrons from the photocathode strike the diodes. Electron-hole pairs are thus generated, and the free holes are stored in the diodes until read out.

Radiation studies performed by RCA Astro-Electronics⁽¹⁸⁾ show that the silicon diode array target is fairly sensitive to radiation. A neutron fluence of 10^{11} /cm² plus a 7×10^{13} /cm² gamma-ray fluence caused a doubling of the dark current, although the quantum efficiency was unchanged. No

structural damage was evident until the fluences approached $10^{12}/\text{cm}^2$ and $7 \times 10^{14}/\text{cm}^2$ respectively. Proton irradiation with low-energy protons (3 MeV) seemed to do the most damage, causing a 40-fold increase in dark current with a fluence of $10^{13}/\text{cm}^2$. The quantum efficiency of the target was also degraded by as much as a factor of 3. Electron bombardment at the same fluence level caused only a 3-fold increase in dark current and a slight decrease in quantum efficiency.

Studies done by JPL on silicon vidicons⁽¹⁹⁾ showed that for 2-MeV electron fluences of $4 \times 10^{12}/\text{cm}^2$, the only significant image degradation was caused by an increase in dark current. However, this was caused primarily by fluorescence in the 7056 faceplate. This effect declined after a period of hours and the vidicon performance returned to its original level.

The graph in Figure 5-2 shows how selected particle bombardments affected the dark current of silicon diode arrays.



Particle fluence versus relative increase in dark current for bare Silicon diode arrays. $V_T = 8$ volts. (From data in Brucker)

Figure 5-2

In summary, only the proton radiation appears to be potentially damaging. The threshold limit for good spectral response is $10^{10}/\text{cm}^2$. This fluence will be exceeded during the mission, so the SIT tubes will need careful hardening and shielding to survive. This shielding would increase the weight of the tube.

5.3.3 CHARGE-COUPLED DEVICES

The charge-coupled-device imager is basically an array of metal-insulator-semiconductor capacitors on a thin semiconductor substrate. When an image is projected onto the array, minority carriers accumulate in the potential well associated with each capacitor in proportion to the photon fluence. The resulting charge configuration can then be serially read out by utilizing the intrinsic shifting ability of the array. Thus, although a buffer or tape recorder would be needed (unless the target were cooled), the support electronics is otherwise limited to the shifting circuitry. No high-voltage or filament supplies are required.

No experimental work has yet been done on the radiation resistance of CCDs. Since these devices are similar to MOS transistors, some similar effects can be inferred. The major effects of ionizing radiation on MOS devices are the buildup of positive charge in the oxide and the generation of new interface states. However, the CCD is insensitive to the positive charge buildup, and the generation of new interface states can be minimized by using

the "buried channel" construction technique⁽²⁰⁾. The major remaining problem would then be the increase in dark current caused by the displacement damage due to heavy particles. This damage occurs in all materials.

Thus, although there is no data available on CCD radiation resistance, it is expected that these devices can survive at least as well as the silicon diode arrays.

5.3.4 ELECTROSTATIC STORAGE CAMERA

The ESC target consists of an SiO_2 film on a conductive substrate. In use, a flood of electrons first primes the surface to a uniform potential. Then the arriving photoelectrons penetrate the film and discharge the surface, causing the resultant surface charge distribution to be proportional to the input signal. Due to the high energy of the arriving electrons and the large electric field in the film, many conductive electrons are released by each photoelectron by the process of EBIC gain. Readout is accomplished by sampling the charge with an electron beam.

Recently, experiments have been performed by CBS Laboratories to determine the radiation sensitivity of the storage film⁽²¹⁾. Target samples stored in evacuated ampoules were exposed to varying amounts of proton and electron and Bremsstrahlung radiation. The irradiated samples were tested for discharge of the surface potential, EBIC gain, and long-term charge storage. Table 5-1 summarizes the maximum dosages involved.

TABLE 5-1

PARTICLE BOMBARDMENT OF ESC STORAGE TARGET

TEST RADIATION FLUENCES		EXPECTED MAXIMUM MISSION FLUENCE
ELECTRONS		
<u>energy</u>	<u>maximum fluence particles/cm²</u>	
.3 MeV	1.9×10^{14}	
1.0 MeV	6.3×10^{13}	
Total Fluence	2.53×10^{14}	3×10^{12} electrons/cm ²
PROTONS		
<u>energy</u>	<u>maximum fluence particles/cm²</u>	
2.0 MeV	2.0×10^{12}	
30 MeV	1.6×10^{12}	
48 MeV	2.0×10^{12}	
Total Fluence	5.6×10^{12}	4×10^{14} protons/cm ²

Results of the experiments show that no decrease in the EBIC gain or long-term charge storage properties was observed. Also, there was no measurable change in the surface potential of the film. This indicates that the ESC should have sufficient radiation resistance to survive the Jupiter orbits, although further radiation studies at larger proton fluences are needed to confirm this.

5.3.5 SLOW-SCAN VIDICON

Targets for these vidicons are made from a variety of materials, so no general results can be inferred.

One short study done by JPL⁽²²⁾ evaluated the radiation resistance of a GEC Selenium-Sulfur vidicon, a slow-scan vidicon used on Surveyor. Irradiations were performed at fluence levels of 2×10^{12} , 1×10^{14} , and 1×10^{15} electrons/cm². The electron energy was approximately 2 MeV. At the increasing fluences, there was increasing video distortion immediately after irradiation. However, this decreased with time, and even at the most severe level, all the electrical parameters and the video had returned to normal after two days. No permanent damage was observed until the final irradiation at 1×10^{15} /cm². The glass envelope (but not the quartz faceplate) exhibited some browning, and radiation-induced crystallization had caused some blemishes in the target.

Unfortunately, this study is not broad enough to draw any general conclusions. It uses only one test sample and does not study the effects of proton bombardment, which are expected to be more severe.

5.3.6 CONCLUSIONS

There is insufficient experimental evidence available to completely categorize the susceptibility of the various targets to radiation damage. This points out a need for more radiation studies on these devices, particularly in view of the increased proton fluences predicted near Jupiter by the BKTC model.

However, a general grouping of these devices in order of increasing susceptibility to radiation damage can be made on the basis of each mode of operation.

- Least Susceptible: SEC and SiO₂ vidicons, and ESC.
These devices use an insulating film to store the image until readout. The only degradation expected is due to the discharge of the target during long storage periods or in peak radiation environments.
- More Susceptible: SIT vidicon, ICCD.
These devices have semiconductor-array type targets with a photocathode. Since these targets have lower back resistance than the insulating films, they are more prone to discharge or increased dark current. Although they also suffer some loss of quantum efficiency during and immediately after exposure

to ionizing radiation, the quantum efficiency of the photocathode is unchanged and the overall sensitivity is not reduced.

- Insufficient Data: RBV and CCD.

Although there is no information on the performance of the RBV or CCD during and after exposure to radiation, these devices both have photoconducting targets which may be susceptible to increased dark current and loss of quantum efficiency. This effect has been reported in other vidicons with photoconductive targets, namely the SSV and the silicon vidicon.

5.4 DISCUSSION OF RELIABILITY

5.4.1 RELIABILITY ASSESSMENT

A complete reliability analysis of a large system requires large amounts of performance data, especially when nonstandard parts such as imaging tubes are used. Typically, such a system would be run for a long period of time, with careful count kept of the number of component failures. The mean time before failure (MTBF) of such a system can be calculated from

$$MTBF = \frac{2T_T}{\chi^2 [(2N_F + 1)(P_c)]} \quad (5-1)$$

where

- T_T = total system test time
- N_F = total number of failures
- P_c = desired confidence level of MTBF
- χ^2 = chi-square value of $2N_F + 1$ degrees of freedom at confidence level P_c .

A lower limit on the MTBF could be calculated by substituting $[1 - P_c]$ for P_c in the denominator.

The reliability of the system would then be calculated from

$$R = e^{-\frac{t_o}{MTBF}} \quad (5-2)$$

where t_o is the desired operating time of the system.

In a large system, the MTBF can be estimated using the known failure rates of standard electronic parts. To accomplish this, the system is broken successively into smaller subsystems for which the MTBF can be individually calculated. On nonstandard parts, an estimate is made based on the best available data. The estimated MTBF is then computed for each block, and its reciprocal, or failure rate, is calculated. The failure rates of the individual blocks are then summed, and the reciprocal of this sum is the estimated MTBF of the entire system.

The level of effort of this particular study is insufficient to cope with the large amounts of data needed to provide this information. A qualitative evaluation of each device will be made instead, followed by a breakdown of device types in order of overall expected reliability.

5.4.2 CANDIDATE CAMERA SYSTEM RELIABILITY

Good radiation resistance and long storage time can be expected from the SEC camera. No tape recorder or data buffer is needed, no special cooling equipment is required, and in some cases image motion compensation can be applied electronically. Space-qualified tubes are available and the sensor has flown on many missions. Target structures have been improved especially in the area of target burn resistance. The SEC tube should be quite reliable.

The SIT camera has only fair radiation resistance. This camera system will require either a tape recorder for image storage or a special cooling system for slow-scan operation. On the plus side, space-qualified tubes with ceramic envelopes are available. IMC can most likely be applied electronically. Even with the tape recorder option, the reliability should be good for a three-year mission.

The radiation resistance of the silicon vidicon is questionable, due to the loss of quantum efficiency and the increased dark current caused by irradiation that was reported in the JPL studies. It requires either a tape recorder or cooling apparatus. Also, it needs mechanical image motion compensation and a mechanical shutter since it has no photocathode. The overall reliability is fair.

An internal storage capability and long storage time is the big advantage of the ESC camera. It can expose and internally store many pictures in a short interval of time without a tape recorder. It does not require mechanical IMC or special cooling equipment. The basic tube will have a mechanical rotating drum to provide multiple frame storage. Although the basic tube has a higher parts count than most other image tubes, the reliability should be better than most other sensor/tape recorder combinations. Although the ESC is still in the development stage, the overall reliability should be good.

Since it is much less complex than any of the other cameras, the CCD camera needs much less instrumentation to operate and requires less power. A buffer or tape recorder is needed for storage, however, unless the device is cooled. The ICCD does not need mechanical IMC, while the CCD alone does. Both devices should have high reliability, but they are still in the experimental stage.

The radiation resistance of the SSV camera remains questionable, as no thorough studies have been made. Space-qualified tubes have been used on many missions. Mechanical IMC is needed, and the use of certain photoconductors would require cooling equipment. The reliability would be very good except that the factor of unknown radiation resistance reduces it to the fair-to-good level.

The return beam vidicon is space-qualified and is currently being flown on the Earth Resources Technology Satellite. The RBV's photoconductor may be susceptible to the radiation environment, however. A thermal control system or tape recorder, mechanical IMC, and mechanical shutter are required. While the reliability of the basic tube is good, the combined overall system reliability for this mission is reduced to the fair level.

The silicon dioxide vidicon is still being developed but should closely resemble the SEC vidicon from a reliability viewpoint when operational. The device should be quite reliable because of its good radiation resistance and simple construction. No tape recorder, cooling equipment, or mechanical IMC will be required.

5.4.3 CONCLUSIONS

Only a qualitative assessment relating the comparative reliability of the candidate sensors is possible until specific auxiliary hardware is selected. Items such as tape recorders, special thermal control, image motion compensation mechanisms and mechanical shutters can have a great impact on reliability figures. From a radiation and reliability standpoint, the SEC tube, silicon dioxide vidicon, and charge-coupled imagers should rate high. The SIT vidicon and ESC systems should have good reliability. The reliability of the RBV, silicon vidicon and slow-scan vidicon systems will range from good to fair, depending on the auxiliary equipment requirements and the amount of shielding provided.

SECTION VI
IMAGE MOTION ANALYSIS

6.1 INTRODUCTION

The purpose of this section is to determine the performance limitations of the candidate sensors resulting from the rotation of the spacecraft and to establish the extent to which the performance of these sensors can be improved through the use of image motion compensation.

The conclusion is that without image motion compensation, the peak-signal-to-RMS noise of all the selected sensors is too low for satisfactory performance on the Jupiter orbiter mission. With IMC, however, several of the sensors exhibit acceptable SNRs.

6.2 PERFORMANCE ANALYSIS OF IDEAL SENSORS

The output signal-to-noise ratio of any sensor is a function of many parameters. Due to differences in construction and operation, the output signal-to-noise ratios for various sensors under the same output conditions may be quite different. There is, however, an upper limit to the signal-to-noise ratio (SNR) value that can be obtained. This upper (quantum) limit is only a function of the irradiance from the scene, the sensor optics, the exposure time, the pixel size, and the responsivity of the sensor.

To derive an expression for the quantum-limited signal-to-noise ratio of an ideal camera, begin with the definition of the output signal of a camera as given in equation (3-23). There, the output signal is defined as $2M_o \tau_s(K) I_i$, where M_o is the scene modulation, I_i is the camera output current, and $\tau_s(K)$ is the camera system modulation transfer function. The ideal camera causes no signal degradation so $\tau_s(K) = 1$. The quantum

noise associated with this signal is defined as $\sqrt{I_i}$, so the signal-to-noise ratio of the ideal camera, in general terms, becomes $2M_o I_i / \sqrt{I_i}$, or $2M_o \sqrt{I_i}$.

This expression can now be expanded in terms of the camera parameters and the scene irradiance. The camera output current I_i , in amps, is equal to the product of the flux density at the photocathode F_{pc} times the responsivity R_D of the photocathode. The scene flux incident on the camera lens is related to the flux at the photocathode by $F_L = 4f^2 F_{pc}$, where f is the focal ratio of the camera lens. Since f is a pure number, the product $F_L R_D / 4f^2$ gives the current density (at the target) in amps/m². Since an ampere is a coulomb per second, multiplying by the exposure time t_e gives the total coulombs/m² per exposure. If the area of each resolution element is A square meters, multiplying the expression by this factor gives the coulombs/resolution element accumulated during the exposure. And finally, dividing by the electron charge e in coulombs gives the number of electrons available from each resolution element per exposure for an ideal camera.

The quantum-limited peak-signal-to-RMS-noise ratio (SNR) of an ideal camera then becomes:

$$SNR = 2M_o \left[\frac{AF_L R_D t_e}{4ef^2} \right]^{1/2} \quad (6-1)$$

In obtaining this expression, the assumption is made that there are no transmission losses within the optics, that there is no degradation in the signal due to the response of the sensor ($\tau_{SEN}(K) = 1$), and that there is no degradation in the signal due to image motion.

6.2.1 SNR DEGRADATION DUE TO IMAGE MOTION

Several types of image motion can reduce the performance of a sensor. Linear motion, random motion, sinusoidal vibrations, and parabolic movement all result in a "smearing" of the image during exposure. This smearing degrades the output signal of the sensor. The relative magnitude of the various motions are discussed below.

6.2.1.1 Motion of the Spacecraft Relative to Jupiter - The most obvious motion is that of the entire spacecraft with respect to the planet's surface. This is comprised of the rotational speed of the planet, the velocity of the spacecraft, and the inclination of the spacecraft orbit to the planet's equator. The worst case occurs when the spacecraft is in an equatorial orbit.

Using the $2.29 \times 45.13 R_J$ orbit as an example, the spacecraft orbit period is 14.222 days⁽²³⁾. The average spacecraft velocity over the elliptical orbit is given by

$$\bar{v} = \frac{4a_o E_o(e_o, \pi/2)}{T_o} \quad (6-2)$$

where a_o is the length of the semimajor axis, $E_o(e_o, \pi/2)$ is the value of the complete elliptic integral of the first order, and e_o is the eccentricity of the orbit. For the $2.29 \times 45.13 R_J$ orbit, the average velocity is 6.43 km/sec, while the velocity of the spacecraft at periapsis is

$$\begin{aligned} v_p &= 38.41 \text{ km/sec, or} \\ \omega_p &= 2.349 \times 10^{-4} \text{ rad/sec.} \end{aligned}$$

The planet Jupiter has a rotational period of 9 hours, 55 minutes and 30 seconds⁽²⁴⁾. This is equivalent to an angular velocity of 1.759×10^{-4} rad/sec. Since the spacecraft orbit is direct, the total relative angular

velocity of the spacecraft with respect to the planet Jupiter at periapsis is

$$\omega_{\text{tot}} = 5.9 \times 10^{-5} \text{ rad/sec.}$$

The image smear due to this relative angular velocity can now be calculated. Assuming a 400-mm focal length, a 1.0-msec exposure time, and a 17.5 x 17.5 mm target with 700 pixels on a side, the amount of image smear is given by

$$\text{smear} = \left(\frac{\omega_{\text{tot}} t_e}{\theta_v} \right) n_p \quad (6-3)$$

where

$$\theta_v = 2 \tan^{-1} \frac{\ell}{2F} \quad (6-4)$$

and

n_p = the number of resolution elements

θ_v = the field of view

ℓ = image format size

The amount of image smear is 1.35 μ rad, which is equivalent to 9.5×10^{-4} pixels. Since we can tolerate over 1/2 pixel smear, this amount of image smear can be neglected without compromising the resolution.

The motion of the entire spacecraft with respect to the planet's surface results in linear image motion. Linear image motion also arises whenever the relative movement between the object or scene and the viewing system is linear as a function of the exposure time.

6.2.1.2 Spacecraft Rotation - The spin-stabilized spacecraft will be rotating on axis at a fixed speed of 2 to 32 rpm. This is equivalent to angular velocities of 0.21 to 3.35 rad/sec respectively. Using the system parameters of the previous example, the corresponding angular smear values range from 0.21 to 3.35 mrad. For a 1.0 msec exposure time, the image

smear is from about 3.4 to 54 pixels. At a nominal spin rate of 5 rpm, a smear of approximately 8.4 pixels results if we do not compensate for the motion.

An image motion compensation system is needed to reduce the smear to a tolerable level (0.5 to 1.0 pixel). The effectiveness of the IMC system depends on many factors including the type of IMC system selected, the type of motion present, and the method of measuring the motion. Currently available IMC systems provide compensation for about 90% of the horizontal relative motion between the sensor system and the planetary scene⁽²⁵⁾. Additional development could result in IMC systems which would compensate for 99% of the relative motion. In this study, a 90%-effective IMC system has been assumed whenever IMC is employed.

With a 90%-effective IMC system, the uncompensated smear of 8.4 pixels, resulting from a spacecraft rotating at 5 rpm, will be reduced to 0.84 pixels. As spin rates increase, the smear soon becomes excessive. Either the exposure time must be shortened or a more effective IMC system must be utilized at the faster spin rates.

Both mechanical and electronic IMC systems are feasible. Generally the amount of smear is small compared to the size of the raster, so that compensation can be readily applied using electronic IMC techniques, provided that the amount of correction required is accurately known.

One of the simplest methods is to preprogram the IMC from the ground to compensate for the smear. However, this means that the speed of rotation has to be exactly that calculated. A more complex method would involve using a star tracker to check the speed of rotation. This could be accomplished with the image tube itself as it pointed away from Jupiter, or with the sensor currently employed on Pioneer for roll reference.

When the camera is pointed normal to the spin axis of the spacecraft (which is the condition assumed for calculations in this study), the image motion caused by spacecraft spin rate is essentially a linear function of the short exposure time required. A single-direction IMC system can generally compensate for this apparent motion. If the camera is pointed in a forward-oblique direction to the spin axis, the image motion becomes more complex⁽²⁶⁾. It is no longer linear because a rotary component of motion is added. The net image motion (or image velocity) is a quadratic function of the frame coordinates⁽²⁷⁾. A two-direction IMC system must be employed to compensate for this type of image motion.

6.2.1.3 Platform Motion - Another source of image motion is random vibrations of the sensor mounting platform. These are often due in part to the limit cycles in the IMC servo system and spacecraft attitude control. In addition, any moving part on the spacecraft will cause some jitter at the sensor. Typical values for the RMS platform unsteadiness are given as

between 50 and 500 arc-seconds per second⁽²⁸⁾, corresponding to 2.4×10^{-4} to 2.4×10^{-3} rad/sec. This larger value results in a 0.04 pixel smear for the conditions given in paragraph 6.2.1.1 above.

6.2.1.4 Conclusions - The spin motion of the spacecraft is the only significant component of image motion, and the only component that will cause any appreciable smear. For the nominal values given, 90%-effective IMC would reduce the smear to less than one pixel.

6.2.1.5 Image-Motion Transfer Functions - The reduction in output signal due to the linear image motion can be taken into account by introducing a transfer function, $\tau_{IM}(K)$, into the mathematical expression for the output signal of the sensor. This is

$$S_{\text{under image motion conditions}} = \tau_{IM}(K) S_{\text{under no image motion conditions}}$$

As discussed in the section on Camera Modeling, the transfer function for linear image motion can be expressed as

$$\tau_{IM} = \frac{\sin(\pi A_m K)}{\pi A_m K} \quad (6-5)$$

where A_m is the magnitude of image motion relative to the sensor's faceplate during the exposure time. It is assumed that the camera is pointed normal to the spin axis of the spacecraft for these analyses.

A_m is given by

$$A_m = F \omega_s t_e \quad (6-6)$$

where

F = focal length of the lens

ω_s = spin angular velocity

t_e = exposure time

As can be seen from Equation (6-5), increasing the spin rate, exposure time, focal length, and spatial frequency all result in decreasing values of τ_{IM} .

By combining equations (6-1), (6-5), and (6-6), the mathematical expression for the quantum-limited peak-signal-to-RMS noise ratio (SNR) under image motion conditions becomes

$$SNR = \frac{M_o \sin(\pi F \omega_s t_e K)}{\pi F \omega_s K f} \left[\frac{A F R L D}{e t_e} \right]^{1/2} \quad (6-7)$$

6.2.2 OPTIMIZATION OF EXPOSURE TIME

Equation (6-7) suggests that for a fixed spin rate, focal length, F-number and spatial frequency, an exposure time exists at which an optimum SNR (using no image motion compensation) can be obtained.

By taking the derivative of equation (6-7) with respect to t_e and setting it equal to zero, the value for this optimum exposure time can be determined. Setting the derivative equal to zero results in the following expression:

$$t_e^{\text{opt}} = \frac{\tan(\pi F \omega_s K t_e^{\text{opt}})}{2\pi F \omega_s K} \quad (6-8)$$

This equation is satisfied when

$$t_e^{\text{opt}} \approx \frac{0.371}{\omega_s F K} \text{ seconds}$$

The corresponding value for $\tau_{IM}(K)$ is 0.79 which in turn corresponds to a smear of 0.74 pixels.

6.2.3 PERFORMANCE OF "IDEAL SENSORS" UNDER NO-IMAGE-MOTION-COMPENSATION CONDITIONS

Using the results of the analysis described above, the optimum SNRs for three types of ideal sensors under no-IMC conditions were calculated as a function of spin rate. The three types of sensors were:

- Sensors using an S-20 photocathode
- Sensors using a silicon photoconductor
- Sensors using an ASOS photoconductor

In making these calculations, the "worst-case" conditions at Jupiter (1.3:1 input contrast, 60° phase angle) were used. Also, a lens with $f = 4$ and $F = 400$ mm was chosen.

The results of these calculations are presented in Figure 6-1. In this figure, the optimum SNRs of the three sensors are plotted as a function of spin rate for a resolution of 10 lp/mm. Some of the optimized exposure times used in obtaining these SNRs are also presented.

In order to obtain larger SNRs from these sensors under the conditions described above, image motion compensation must be used.

6.3 PERFORMANCE ANALYSIS OF SELECTED CANDIDATE SENSORS UNDER NO-IMAGE-MOTION-COMPENSATION CONDITIONS

An analysis similar to that described for ideal sensors was performed using the sensors which were selected for study in this program. Specifically, this analysis was performed using the detailed peak-signal-to-RMS-noise models developed for the

- SIT Vidicon
- SEC Vidicon
- SiO₂ Vidicon
- Intensified SEC Vidicon
- Silicon Vidicon
- Intensified Silicon Vidicon
- Slow Scan Vidicon
- Intensified Slow Scan Vidicon
- Return Beam Vidicon
- Electrostatic Storage Camera (ESC)
- Charge Coupled Device
- Intensified Charge Coupled Device

(See Appendix A for detailed descriptions of the signal-to-noise models)

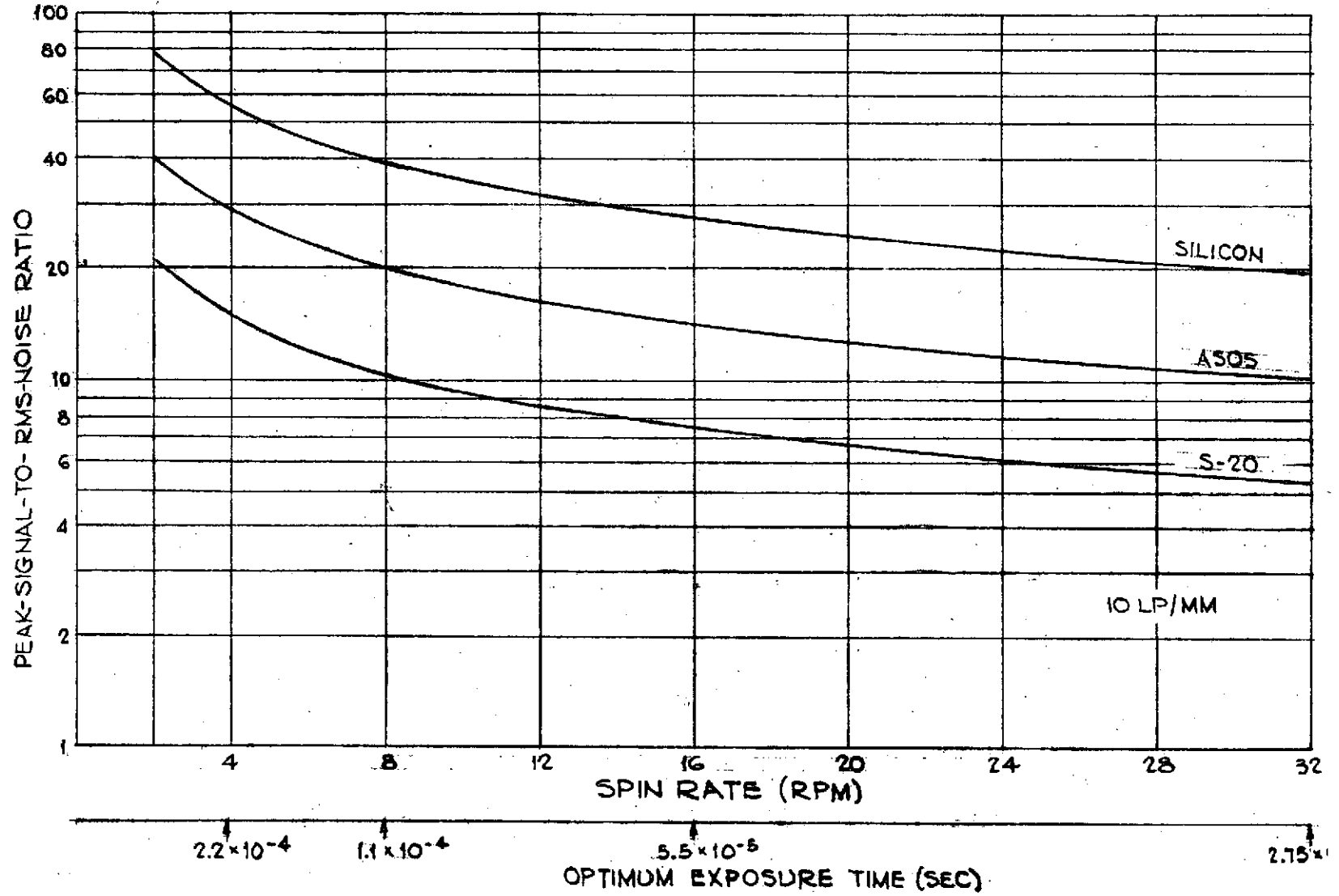


FIGURE 6-1 - PERFORMANCE OF IDEAL SENSORS UNDER NO-IMAGE-MOTION-COMPENSATION CONDITIONS

This analysis took into account such factors as:

- Modulation Transfer Functions of sensor components
- Readout Efficiencies
- Noise sources other than the quantum noise which contribute to the overall output noise of the sensors.
- Effect of image reconstruction on the signal-to-noise ratio.

6.3.1 OPTIMIZATION OF EXPOSURE TIME

As in the case of ideal sensors, there exist exposure times for these selected (real) sensors at which the output signal-to-noise ratios are maximum. To determine these optimum exposure times, an approach similar to that described in Section 6.2.2 was used.

All of the signal-to-noise models developed for the selected sensors take the general form

$$*SNR = \frac{A \left(\frac{\sin Bt_e}{Bt_e} \right) t_e}{[C + D \ln(Et_e) + Ft_e]^{\frac{1}{2}}} \quad (6-9)$$

where A, B, ... F are independent of the exposure time, t_e .

*Note that $D = 0$ for all sensors except the charge-coupled and intensified charge-coupled devices.

By taking the derivative of Equation (6-9) with respect to t_e and setting it equal to zero, the expression for the optimum exposure time takes the form

$$2Bt_e^{\text{opt}} [C + D \ln(Bt_e^{\text{opt}}) + Ft_e^{\text{opt}}] = [D + Ft_e^{\text{opt}}] [\tan(Bt_e^{\text{opt}})] \quad (6-10)$$

Having established values of B ... F, the optimum value for t_e is the value for which this equation is satisfied.

In many of the cases studied, it was found that (6-10) could be simplified. Of course, for all the sensors except the CCD and ICCD, (6-10) reduces to

$$2B[C + Ft_e^{\text{opt}}] = Ft_e^{\text{opt}} \tan(Bt_e^{\text{opt}}) \quad (D = 0) \quad (6-11)$$

In addition, for those cases where $Ft_e \gg C$, expression (6-11) can also be simplified to

$$t_e^{\text{opt}} = \frac{\tan(Bt_e^{\text{opt}})}{2B} \quad (6-12)$$

The quantity B is the constant multiplying the exposure time in the expression for the transfer function associated with image motion.

$$\text{i.e., } B = \pi \omega_s FK \quad (6-13)$$

This expression for t_e^{opt} , the same as that obtained for the ideal sensor [expression (6-8), Section 6.2.2], results in an optimum exposure time of $0.37/\omega_s \text{FK}$ seconds and a corresponding smear of 0.74 pixels.

In cases where those noise terms that are not a function of exposure time predominates ($C \gg D \ln(Et_e^{\text{opt}}) + Ft_e^{\text{opt}}$), expression (6-10) reduces to the form

$$\frac{2BCt_e^{\text{opt}}}{D + Ft_e^{\text{opt}}} = \tan Bt_e^{\text{opt}} \quad (6-14)$$

In those cases where C predominates, $2BCt_e^{\text{opt}}/(D+Ft_e^{\text{opt}})$ is generally much greater than 1. Under those conditions, Equation (6-14) is satisfied by values of Bt_e^{opt} approaching $\pi/2$. By substituting Equation (6-6) for A_m , and $Bt_e \rightarrow \pi/2$ into Equation (6-5), $\tau_{\text{IM}}(\text{K})$ becomes

$$\tau_{\text{IM}}(\text{K}) = \frac{\sin(\pi/2)}{\pi/2} = 0.64 \text{ (1 pixel smear)}. \quad (6-15)$$

6.3.2 RESULTS OF PERFORMANCE ANALYSIS OF SELECTED SENSORS UNDER NO-IMAGE-MOTION-COMPENSATION CONDITIONS

Using the detailed signal-to-noise models for the selected sensors and the corresponding optimum values for the exposure times, the performance of these sensors under no-IMC conditions was determined. As in the case of the ideal sensors, worst-case conditions of 1.3:1 contrast, 60° phase angle were used along with a lens with $f = 4$ and $F = 400$ mm.

C²

Figures 6-2 and 6-3 show the results of this analysis. In Figure 6-2, the optimum data link peak-signal-to-RMS noise-ratios are plotted as functions of spin rate for a resolution of 10 lp/mm. In Figure 6-3, the optimum peak-signal-to-RMS-noise ratios in the reconstructed images are plotted for the same set of conditions. Table 6-1 gives the optimum exposure times and the corresponding values of $\tau_{IM}(K)$ used in this analysis.

To obtain the plots in Figure 6-3, the following relationship was used:

$$SNR_{\text{Reconstructed}} = (A_k/A_b)^{1/2} (SNR_{\text{Data link}}) \quad (6-16)$$

where

A_k = area of resolution element

A_b = area of read beam and recording beam

$(\tau_{\text{rec}}(K) = 1)$

The encoding, transmitting and recording processes will result in somewhat lower SNRs in the reconstructed images. However, until the characteristics of the telemetry and recording equipment are known, the extent to which these SNRs are degraded cannot be determined.

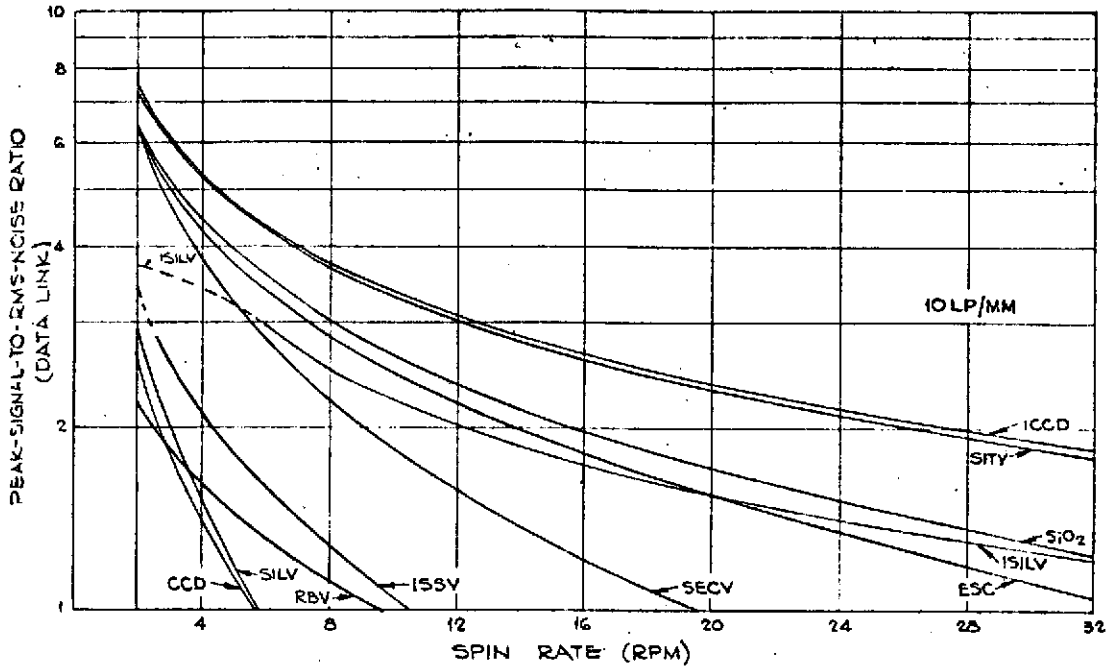


FIGURE 6-2 - PERFORMANCE OF SELECTED SENSORS UNDER NO-IMAGE-MOTION-COMPENSATION CONDITIONS

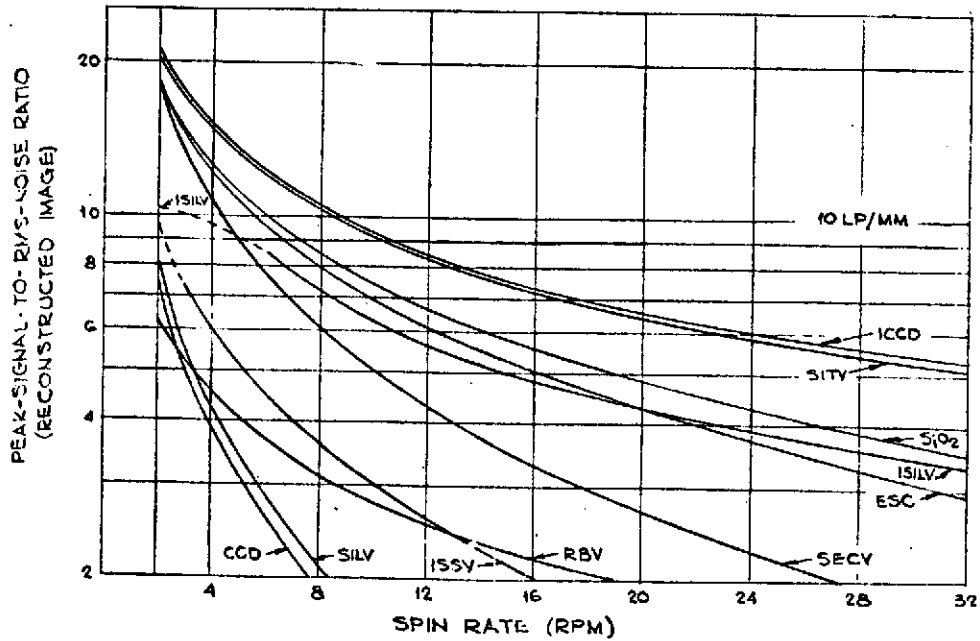


FIGURE 6-3 - PERFORMANCE OF SELECTED SENSORS UNDER NO-IMAGE-MOTION-COMPENSATION CONDITIONS

TABLE 6-1
OPTIMUM EXPOSURE TIMES AND CORRESPONDING
 τ_{IM} (K) VALUES USED IN PERFORMANCE ANALYSIS

Sensor	Spin Rate (rpm)	Exposure Time (sec x 10 ⁻⁴)	τ_{IM} (K)
SITV ICCD RBV	2	4.4	0.79
	4	2.2	0.79
	8	1.1	0.79
	16	0.55	0.79
	32	0.275	0.79
SiO ₂	2	4.4	0.79
	4	2.3	0.77
	8	1.18	0.76
	16	0.6	0.75
	32	0.32	0.72
SECV	2	5.1	0.72
	4	2.65	0.70
	8	1.4	0.67
	16	0.71	0.66
	32	0.363	0.65
ESC	2	4.6	0.77
	4	2.35	0.76
	8	1.2	0.75
	16	0.64	0.72
	32	0.33	0.70
CCD	2	5.93	0.64
	4	2.97	0.64
	8	1.48	0.64
SILV	2	5.9	0.64
	4	2.96	0.64
	8	1.47	0.64
ISILV	8	1.15	0.77
	16	0.58	0.77
	32	0.3	0.75
ISSV	4	2.6	0.71
	8	1.34	0.70
	16	0.7	0.67

In making this analysis, the capability of the various sensor targets to utilize the total charge delivered to them during these exposure times was also considered. In several cases, it was felt that if the total charge associated with a given optimum exposure time was delivered to a particular target, an unrealistic shift in target potential would result. Consequently, certain upper limits were placed on the exposure times of the candidate sensors. The maximum allowable exposure times for each sensor were

<u>Sensor</u>	<u>Maximum Exposure Time (sec)</u>
RBV, SSV	1×10^{-2}
SiO ₂ , ESC	5×10^{-3}
SILV, CCD	3×10^{-3}
SITV, ICCD	1×10^{-3}
SECV	6×10^{-4}
ISSV	4.5×10^{-4}
ISILV	1.5×10^{-4}
ISECV	2×10^{-5}

The dashed-line portion of the curves presented in Figures 6-2 and 6-3 indicate those regions where the maximum allowable exposure times (rather than the optimum exposure times) were used in determining the SNRs.

The low SNRs obtained for all the sensors in this analysis clearly point out the need for image motion compensation.

6.4 PERFORMANCE OF SELECTED CANDIDATE SENSORS UNDER COMPLETE-IMAGE-MOTION-COMPENSATION CONDITIONS

The smear due to image motion can be greatly reduced by using image motion compensation (IMC). Mechanical methods of IMC, toggling mirrors or image plane motion, can be used with any of the sensors being studied in this program. In those sensors having a photocathode and an image section, IMC can also be achieved by electronically shifting the "electron image" within the image section during exposure. Two-direction IMC can readily be supplied using the electronic method.

Regardless of the method used, IMC allows the use of longer exposure times. Where target capacitance permits, longer exposure times result in larger SNRs. This fact is illustrated in Figures 6-4 and 6-5. Here, the data link SNR and reconstructed SNR for the selected sensors are plotted as functions of exposure time for a resolution of 10 lp/mm. As in the case of the analysis performed under no-IMC conditions (Section 6.3.2), the worst-case conditions of 1.3:1 contrast, 60° phase angle and a lens with $f = 4$ and $F = 400$ mm were used. However, unlike the analysis described in Section 6.3.2, this analysis set $\tau_{IM}(K) = 1$ (complete image motion compensation). The maximum allowable exposure times, determined on the basis of target capacitance, are the points at which the plots for the various sensors end.

For a given exposure time, the amount of image motion compensation required for complete compensation is a function of spin rate and the focal length of the lens. Figure 6-6 shows the amount of IMC required as a function of exposure time for the resolution presented in Figures 6-4 and 6-5 and for various spin rates. As in all these analyses, a lens with $f = 4$, $F = 400$ mm was used.

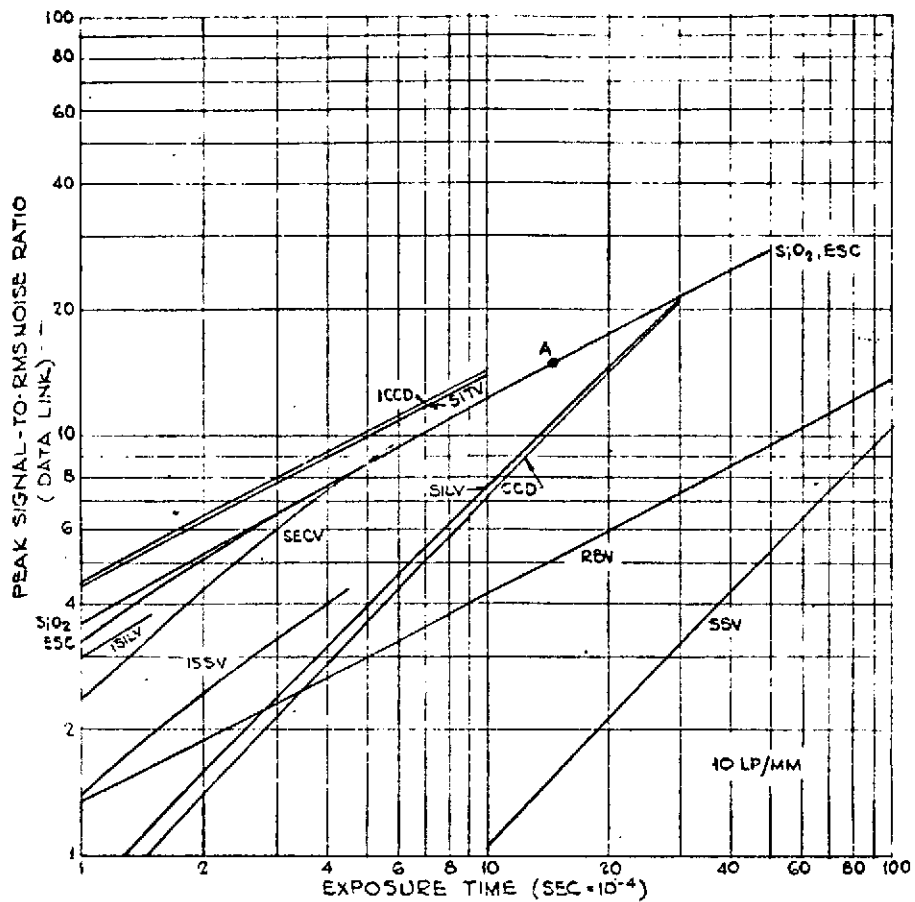


FIGURE 6-4- PERFORMANCE OF SELECTED SENSORS UNDER COMPLETE-IMAGE-MOTION-COMPENSATION CONDITIONS

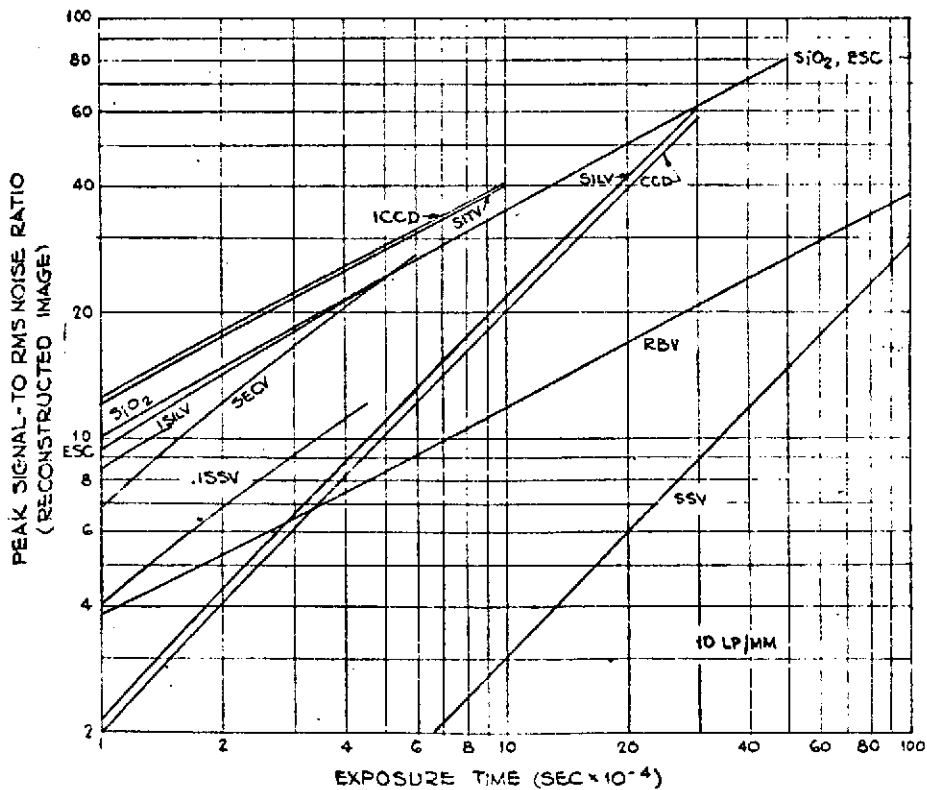


FIGURE 6-5- PERFORMANCE OF SELECTED SENSORS UNDER COMPLETE-IMAGE-MOTION-COMPENSATION CONDITIONS

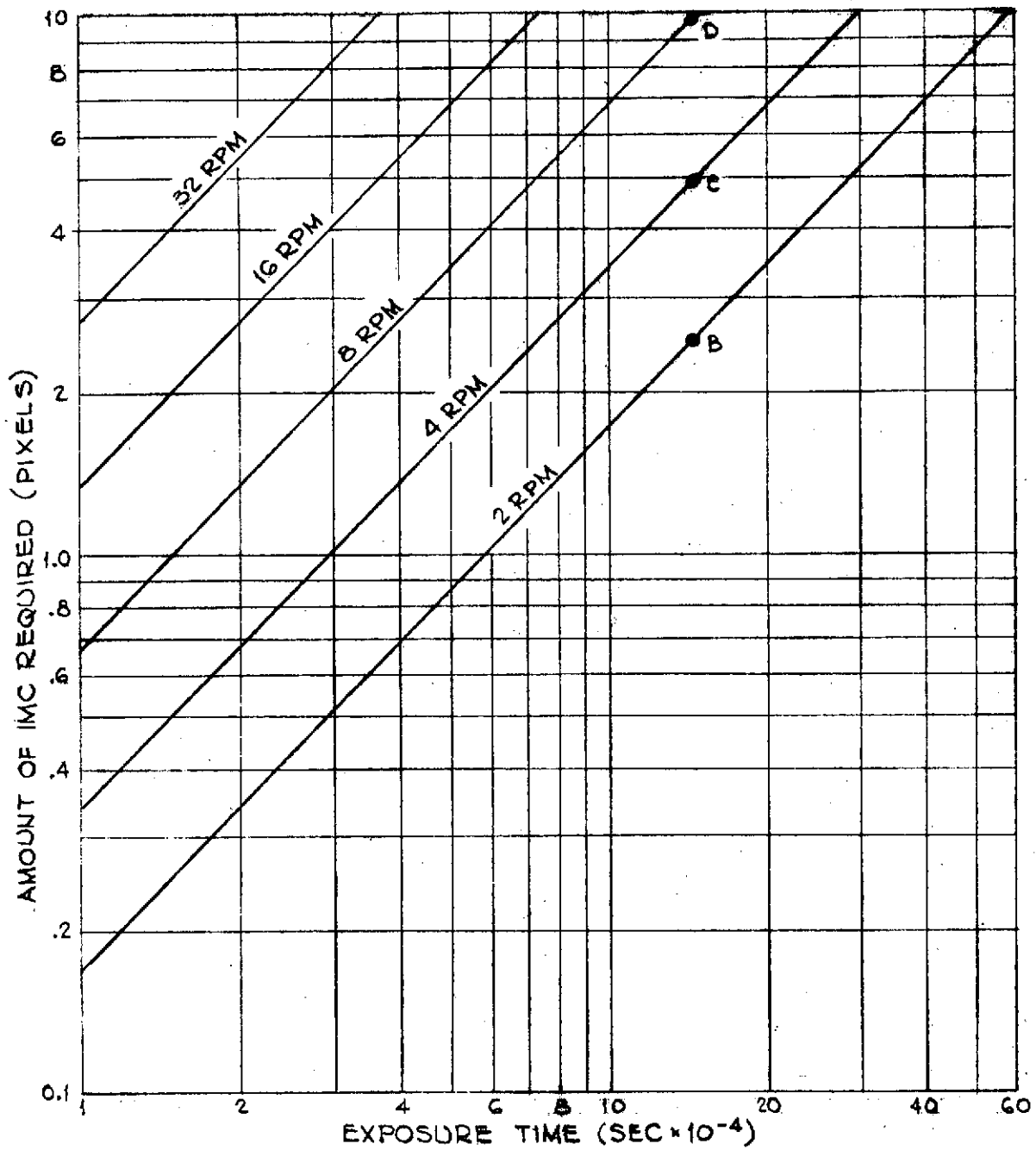


FIGURE 6-6 IMAGE-MOTION-COMPENSATION REQUIREMENTS

To illustrate the use of these graphs, consider a case where the following conditions and sensor specifications are given:

Input Contrast Ratio	1.3:1
Phase Angle	60°
Optics	f = 4, F = 400 mm
Resolution	10 lp/mm
Sensor	Electrostatic Camera (ESC)
IMC	yes
Required data-link SNR	15

Figure 6-4 shows that in order to achieve a data-link SNR of 15 under these conditions, an exposure time of approximately 1.45 milliseconds (pt. A) is required. Figure 6-6 indicates that the corresponding amount of IMC required is approximately

2.45 pixels if the spin rate is 2 rpm	(pt. B)
4.9 pixels if the spin rate is 4 rpm	(pt. C)
9.8 pixels if the spin rate is 8 rpm	(pt. D)

Many tradeoffs are possible that could be used to optimize camera system performance. Factors such as the spin rate, the effectiveness of the IMC, the resolution, the exposure time, and optical lens parameters may be weighed against each other. Therefore, considerable flexibility is available to minimize image motion when it is more pronounced, such as when the viewing angle is not normal to the spin axis.

SECTION VII
WORST-CASE ANALYSIS, COMPARISON OF
CAMERAS, AND SELECTION OF BEST SYSTEMS

7.1 INTRODUCTION

The objective of this task is to select from the candidate systems the most promising frame imaging systems to be used on spinning platforms for long-term space missions. The selection is based upon the results of all of the previous analyses.

In order to properly evaluate the candidates, more specific requirements and selection criteria must first be established. In this way systems are compared and measured against mission constraints and performance requirements.

The results of exercising the analytical models of the candidate systems using worst-case conditions are presented. Aerial image modulation (AIM) curves showing the different frame imaging systems under identical worst-case conditions are given with the effects of spin rate superimposed. The signal-to-noise ratios for the candidate systems at the data link and for reconstructed images are presented as a function of spatial frequency. Sensor resolution is shown as a function of exposure, and other relationships of interest are developed.

Finally, each candidate sensor system is examined in detail, and three systems are selected for additional analysis for the specific Jupiter orbiter in Section 8. The reasons for acceptance or rejection of each sensor have been identified. The systems selected for additional analysis are the SEC vidicon, the electrostatic storage camera, and the intensified charge-coupled device.

7.2 SELECTION CRITERIA AND REQUIREMENTS

In order to properly evaluate the candidate camera systems, specific mission requirements based on worst-case conditions and other study constraints will be established. The selection criteria will be based on these mission constraints and desired performance requirements.

7.2.1 STUDY CONSTRAINTS

The preliminary screening analysis to select the best camera systems will be based on the following constraints:

- The analysis is limited to the planet Jupiter,
- A worst-case phase angle of 60° is to be used,
- A worst-case contrast ratio of 1.3:1 is to be used,
- The mission duration is approximately 3 years,
- The study is limited to frame imagers, and

- A surface resolution at Jupiter is 100 - 300 km for full disk images, 10 - 15 km for nested frames with limited coverage, and 10 - 15 km for satellite images.

The constraints resulting from spacecraft limitations are:

- The weight of the imaging system is limited to 18 kg,
- Spin rates of from 2 to 32 rpm are to be considered for a spin-stabilized system as typified by Pioneer F/G,
- Imaging systems with long target storage are desirable so that data can be transmitted without ancillary storage equipment,
- Image-motion-compensation systems are undesirable because of reliability considerations, but will not be precluded from the study, and
- Data rates from Jupiter may be as low as 2048 bits/sec and as high as 83,220 bits/sec depending on spacecraft telecommunications equipment. A nominal value of 16,384 bits/sec is the most likely to be implemented.

7.2.2 PERFORMANCE REQUIREMENTS

The performance requirements to be used as study parameters have been established during a meeting between NASA and the contractor at the start of the study. The TRW Systems Group Report No. 20406-6004-R0-00, Study of Follow-On Pioneer Missions to Jupiter ⁽²⁾, was offered as a guide in establishing performance requirements and system parameters. A specific Jupiter orbiter with encounters with three satellites ($2.3 \times 45.1 R_J$ orbit) was selected as the mission to study in detail after completion of the worst-case parametric analysis and the camera selection.

7.2.2.1 Imaging Requirements - Specific requirements for an imaging experiment will vary substantially, depending on the actual objectives of the investigation being conducted. However, certain imaging requirements, such as the minimum desired resolution, the field of view, and the allowable smear, can be anticipated for the purpose of performing this study.

The surface resolution for viewing Jupiter is on the order of 10 km to 300 km. This fulfills the need for wide coverage over extended periods of time to view dynamic processes, as well as nested pictures showing full-disk coverage to close-ups at periapsis. A resolution of 200 km would require a camera system with a format of 700 elements to obtain full-disk coverage.

In viewing the satellites of Jupiter, the requirements differ. Static objects are to be observed at as high a resolution as possible. Surface resolution better than 10 km is required for viewing the satellites and only a narrow field of view is needed. Thus the desired field of view of the

imaging experiments range from about 0.1 to 5 degrees.

7.2.2.2 Image Smear Constraint - When imaging from a spin-stabilized spacecraft, the linear image motion caused by the spin rate generally predominates the other motions. The displacement of the image is linear as a function of time for the short exposure time required. For a three-axis stabilized system operating at longer exposures, random motion due to platform unsteadiness is generally the dominant angular motion. Linear motion due to the rapid rotational rate of Jupiter relative to the camera is also significant at lower altitudes.

From earlier discussions, we recall that the transfer function for linear motion is given by

$$\tau(K) = \frac{\sin(\pi A_m K)}{\pi A_m K} \quad (7-1)$$

where A_m is the magnitude of uncompensated image motion in the image plane, and K is the spatial frequency. This function was shown in Figure 3-1.

The TRW report suggests 60% of a resolution element (pixel) as a smear criterion. This is equivalent to a transfer function having a value of 0.85. Other reports suggest a scene motion of one pixel, which corresponds to a transfer function value of 0.64. An attempt was made in Section 6 to select a smear criterion based on the optimum exposure time required for each sensor. On this basis, a response of 0.79 was obtained, corresponding to smear of about 74% of a pixel.

In the worst-case parametric analysis, the degradation due to

image motion is handled more meaningfully as a modulation transfer function. It is combined with other transfer functions to form the available aerial image modulation curve which establishes the system performance limits (see Section 3.4).

7.2.2.3 Data Transmission Requirements - As stated, data rates for the mission will range from 2048 to 83,220 bits/sec, with 16,384 bits/sec used as the nominal rate for a framing camera at Jupiter. The telemetry rate impacts sensor design through the video bandwidth, B. This is given by

$$B = \frac{b_r}{2g}$$

where g is the digital encoding precision and b_r is the bit rate (bits/sec).

For a nominal 700-line picture with 6-bit encoding, about 3×10^6 bits of information must be transmitted. At the 16,384 bit/sec rate about three minutes per picture are required for transmission to Earth. In order to read out this quantity in real time, slow-scan techniques must be employed. The resulting video bandwidth is about 1300 Hz, which will be used in the subsequent parametric analysis for slow-scan operation.

For a selected digital encoding precision, it is desirable to maintain a signal-to-noise ratio which is efficient to encode and at the same time is not affected by the SNR of the encoder. In other words, if the SNR is lower than the number of gray levels, the result is a waste of encoding precision. However, if the SNR is greater than the number of gray levels, the encoding steps cause discrete contrast levels to be seen in the picture, resulting in "quantizing noise". Six-bit encoding has been used in this study as a compromise

between these two conflicting criteria. This is equivalent to a dynamic range of 64 gray levels.

7.2.3 PRACTICAL SYSTEM PARAMETERS

The practical limits for the optical system parameters are set by the total image system weight constraint of 18 kg (40 lb). Since the mass of the optical system varies roughly as the square of the aperture diameter, the weight becomes substantial for apertures of 150 mm (six inches) or larger, particularly as focal lengths increase. Estimated weights for typical catadioptric systems, based on the density of quartz, are given in Table 7-1. (2)

Although aperture diameters of up to 150 mm appear to be reasonable, a nominal diameter of 100 mm was selected for the worst-case parametric analysis. A focal length of 400 mm was selected, giving a nominal f-number of 4.0. Any aperture ratio between 2.0 and 8.0 could probably be used, depending on the spacecraft spin rate.

TABLE 7-1

WEIGHT OF CATADIOPTRIC SYSTEMS			
Focal Length	Aperture Dia.	f/#	Weight
400 mm	100 mm	4.0	2.3 kg
	150	2.6	5.4
	200	2.0	9.5
600 mm	75	8.0	3.6
	100	6.0	4.1
	150	4.0	8.6

7.2.4 OTHER REQUIREMENTS

The selection criteria for the best imaging systems must be based on other requirements in addition to those discussed in this section. The relative reliability and radiation resistance of the sensors must be considered. The technological problem areas and possible additional equipment needs, such as cooling apparatus, data storage equipment, and image motion compensation devices, will also influence the selection process.

7.3 WORST-CASE PARAMETRIC ANALYSIS

Models of the various sensors will be parametrically studied in this section using worst-case conditions. Because of the large number of parameters involved, it has been necessary to select nominal values for several variables to keep the study within reasonable bounds. For example, only a lens system of 400-mm focal length with a 100-mm aperture diameter was studied, and exposure times were limited to several reasonable values. Specific camera parameters such as the beam diameter and component MTFs were fixed. A beam

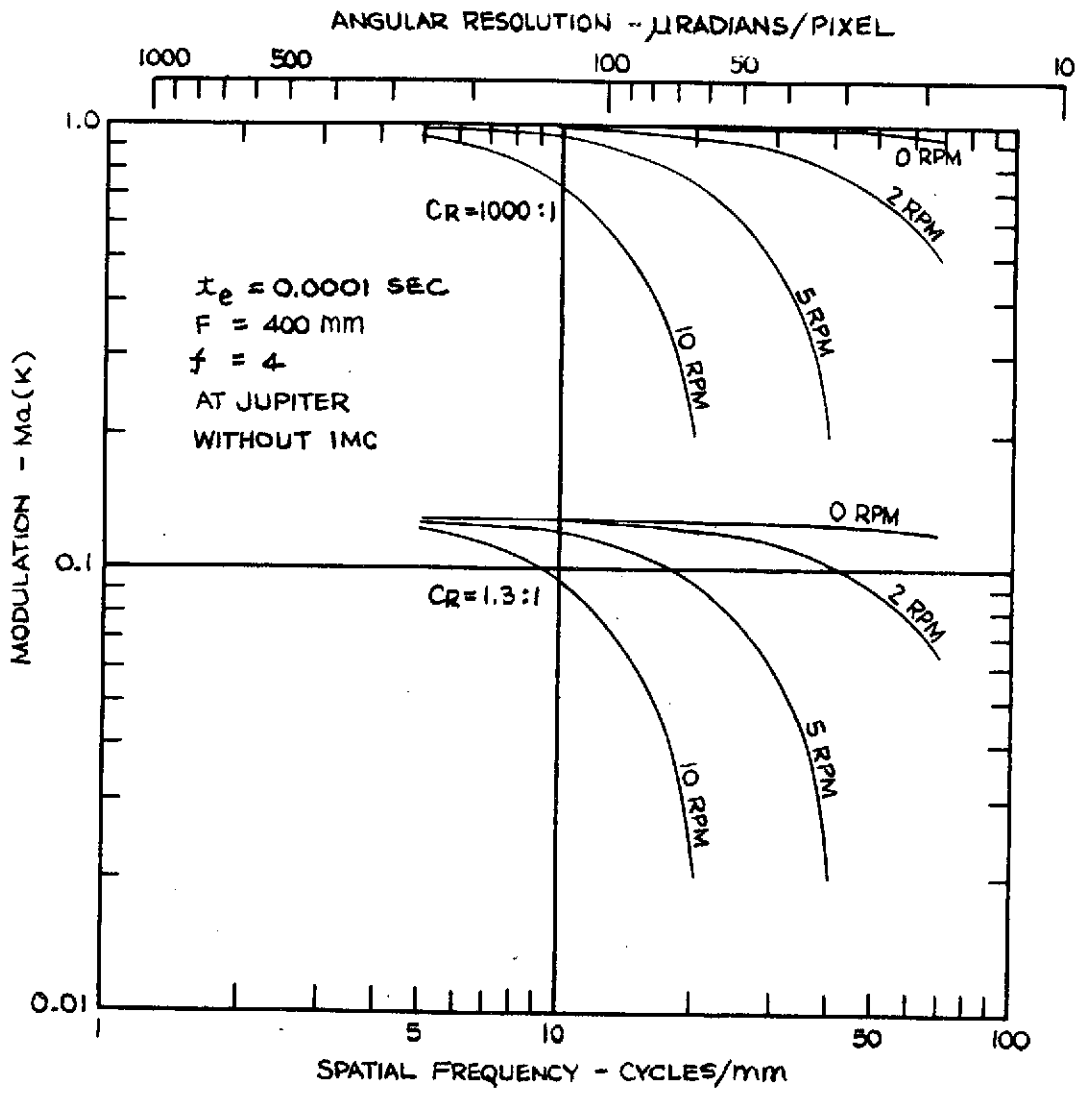
diameter of approximately 20 microns was selected for most devices to achieve performance results consistent with existing camera systems. The full visible spectrum was used, 0.3 μ to 0.95 μ . Electrostatic focusing was assumed wherever applicable. However, during the detailed analysis, electromagnetic focusing and additional camera variables will be considered.

7.3.1 AERIAL IMAGE MODULATION CURVES

The available aerial image modulation curves in Figure 7-1 show the effect of varying the spin rates at an exposure time of 0.0001 seconds for both high and worst-case contrast ratios (1.3:1). An optical system with a 400-mm focal length and an f/4 aperture ratio is used. The available aerial image response is plotted versus spatial frequency, as well as versus angular resolution.

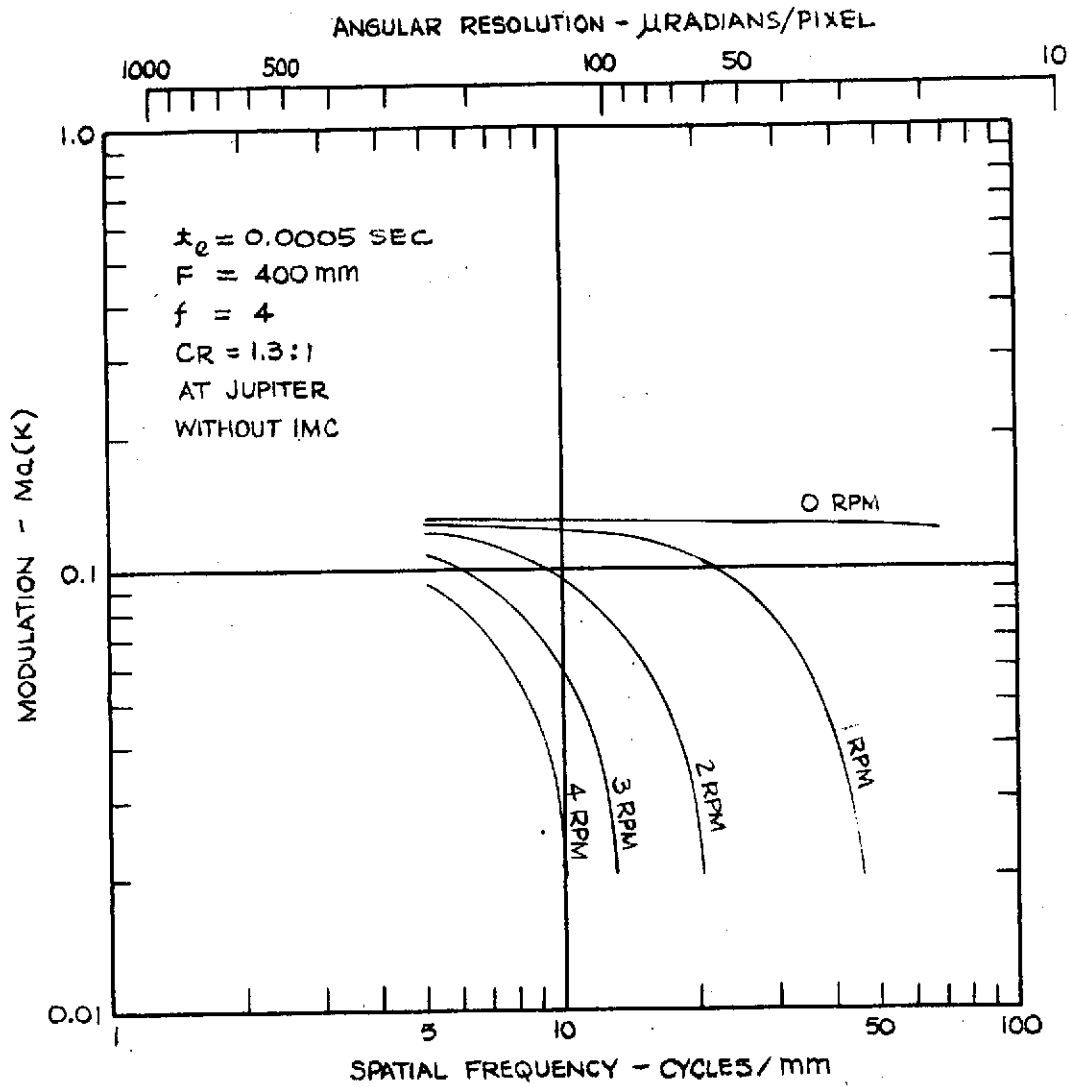
As indicated in Equation (3-42), the available aerial image modulation consists of the product of the modulation transfer functions of the lens system, the linear motion due to spacecraft spin, and the scene modulation (due to the contrast). These combine to establish the performance limit at which the camera system can operate. Note in Figure 7-1 that for a combination of a 5 rpm spin rate, a contrast ratio of 1.3:1 and a resolution of 20 cycles/mm, a maximum modulation of 0.094 is available. At 10 rpm, this modulation is reduced to 0.025, representing a substantial reduction in potential performance. The zero-rpm curve represents the maximum available aerial image modulation that can be obtained at any spin rate if a perfect image motion compensation system is employed.

Figure 7-2 shows a family of available aerial image modulation curves for 0.0005 sec exposure time. The effect of increasing the image



AVAILABLE AERIAL IMAGE MODULATION
 VERSUS RESOLUTION.

FIGURE 7-1



AVAILABLE AERIAL IMAGE MODULATION
 VERSUS RESOLUTION

FIGURE 7-2

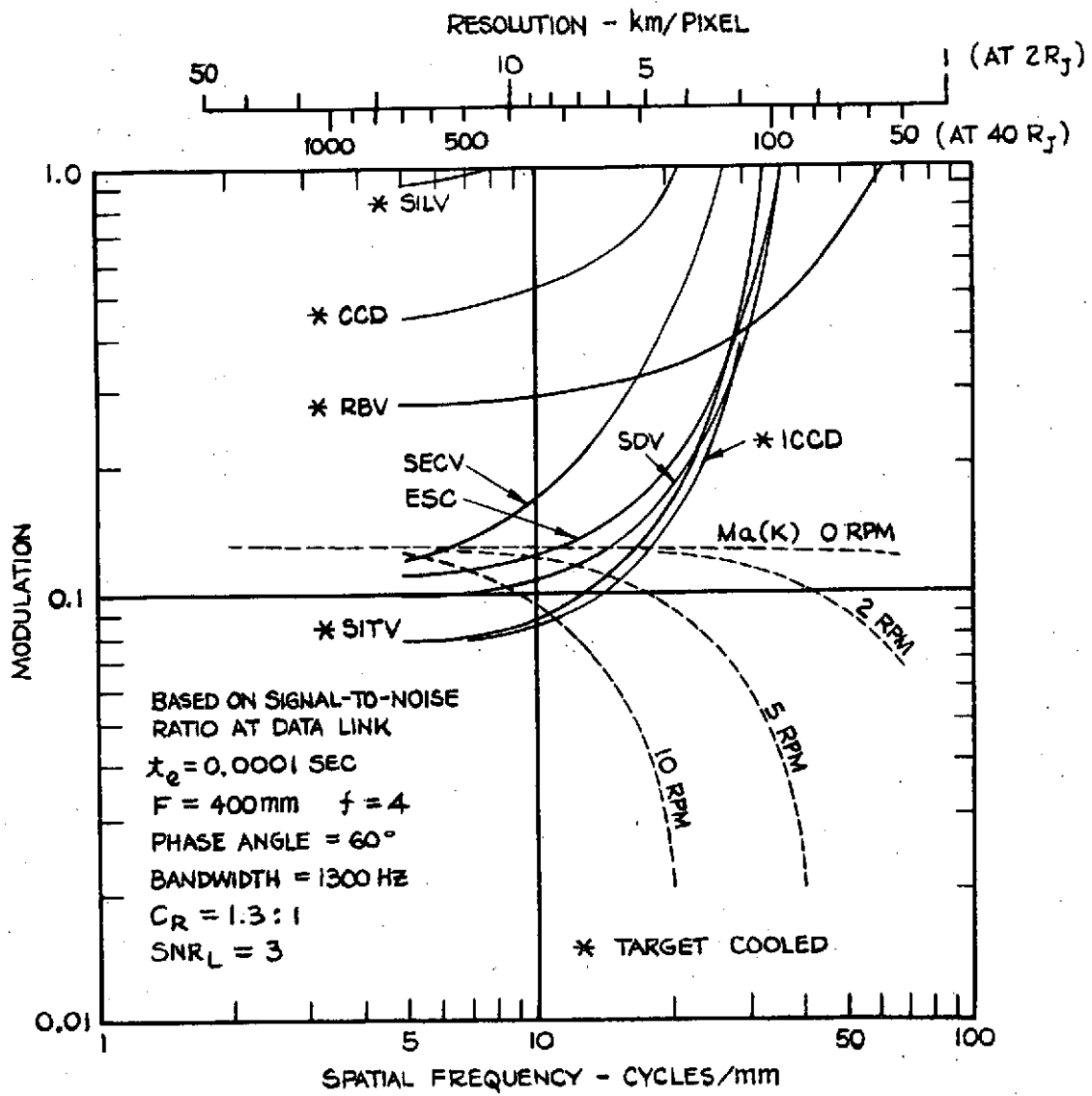
smear is apparent when the two graphs are compared. At 2 rpm, the response at 20 cycles/mm has already dropped to 0.025. Operation of the camera system at spin rates faster than 4 rpm without IMC would limit performance to 10 cycles/mm at this exposure.

Referring to the resolution relationships shown in Figure 3-5, we can determine the actual ground resolution from the spatial frequency. For example, at a spacecraft distance of $20 R_J$, a spatial frequency of 10 cycles/mm (using a 400-mm focal length system) can be translated into a ground resolution of 200 km/pixel.

7.3.2 CANDIDATE SENSOR AIM CURVES

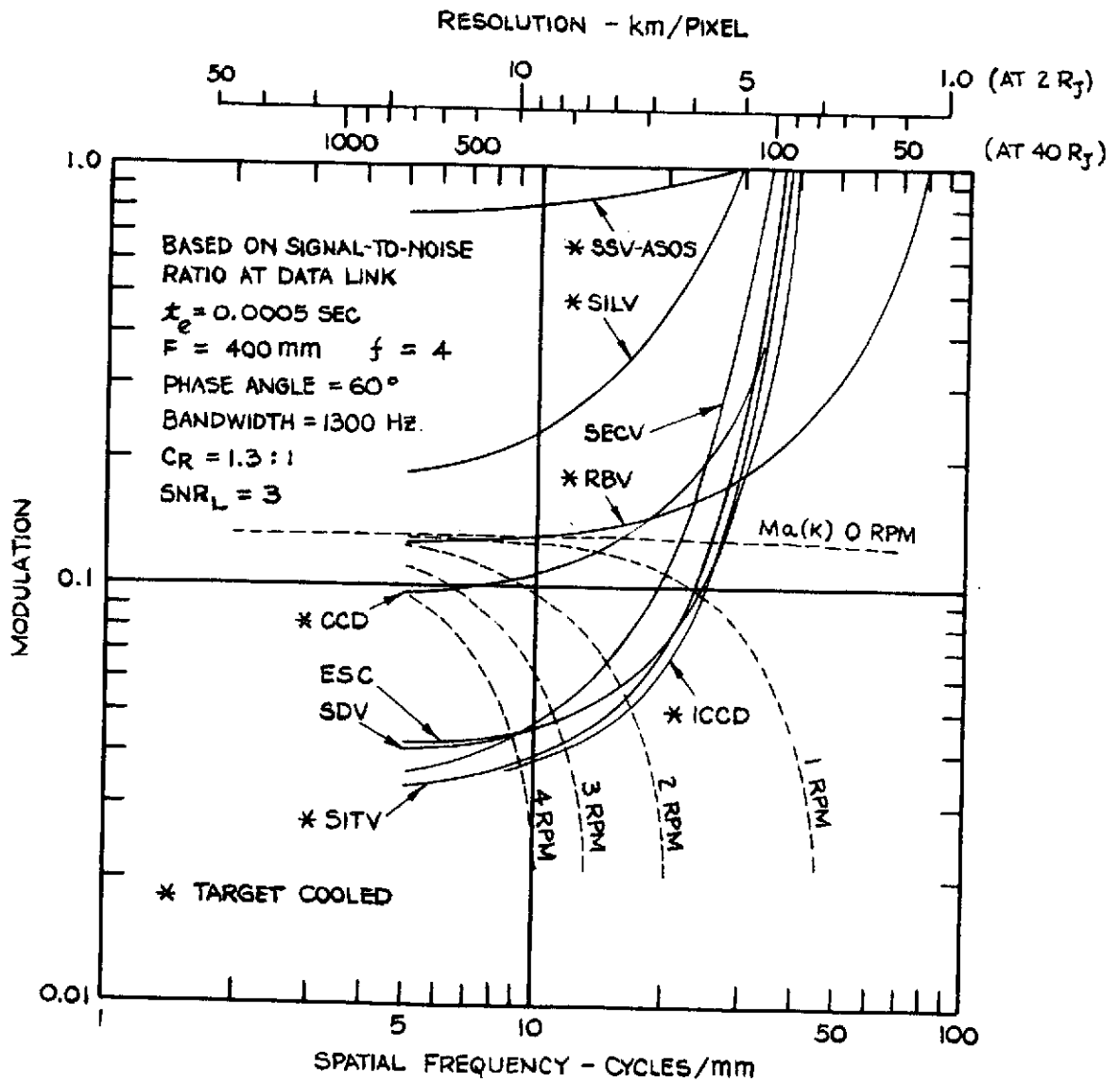
Threshold modulation curves for the candidate sensors based on the signal-to-noise ratio at the data link are given in Figures 7-3, 7-4, and 7-5 for different exposure times. Available aerial image modulation curves are superimposed. The bandwidth of 1300 Hz corresponds closely to the average data rate of 16,384 bits/sec. Actually, the data rate will range from about 2,048 to 83,220 bps. In order to compare the candidate sensors at the same bandwidth, it is necessary to cool the sensors indicated on these figures by asterisks to temperatures ranging down to -60°C . This reduces the dark current of the targets sufficiently to operate these devices at slow-scan rates. All of the sensors analyzed in this section employ electrostatic focusing.

AIM curves for an exposure time of 0.0001 second are plotted in Figure 7-3. At this low exposure level, sensors such as the silicon vidicon



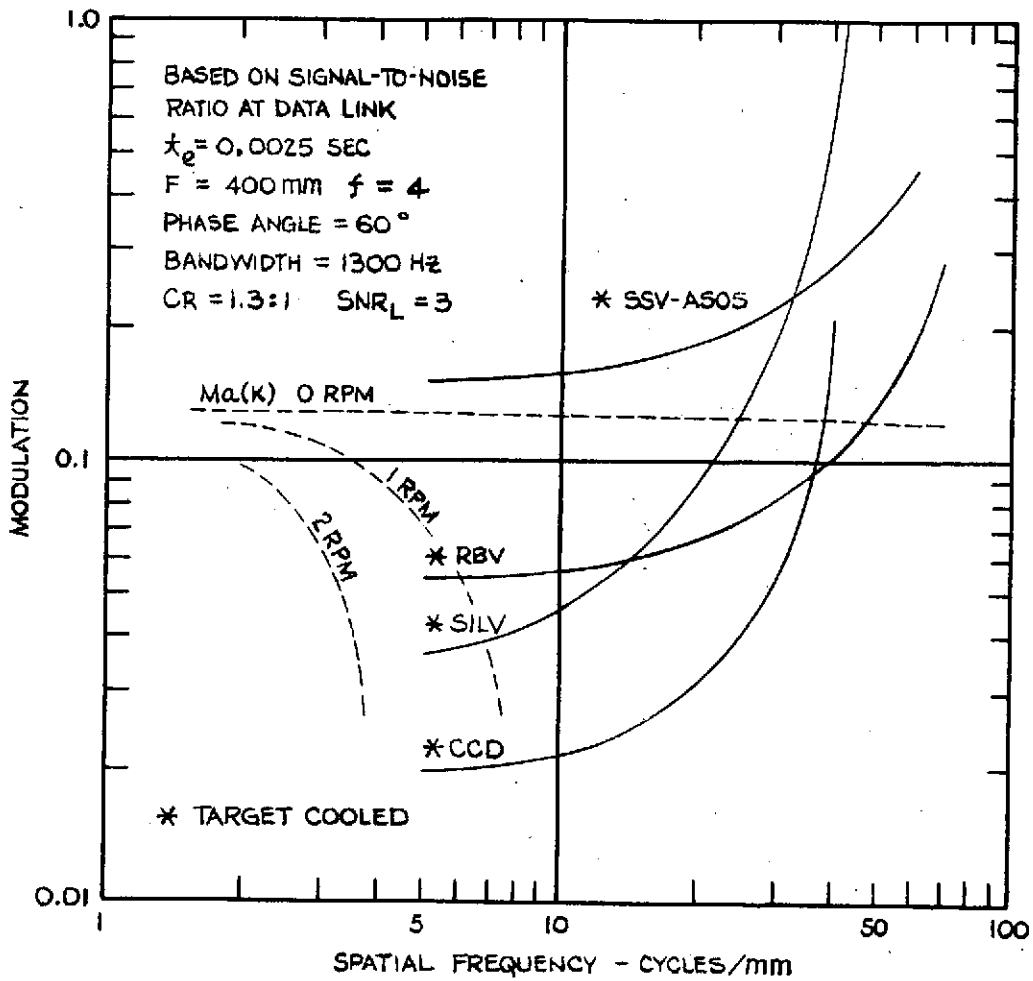
THRESHOLD MODULATION CURVES
FOR CANDIDATE FRAME IMAGERS

FIGURE 7-3



THRESHOLD MODULATION CURVES
FOR CANDIDATE FRAME IMAGERS

FIGURE 7-4



THRESHOLD MODULATION CURVES
 FOR CANDIDATE FRAME IMAGERS

FIGURE 7-5

(SILV), slow-scan vidicon (SSV), charge-coupled device (CCD), and return beam vidicon (RBV) are inadequate. They lack prestorage target gain, and consequently the preamplifier noise, or beam shot noise in the case of the RBV, dominates. Longer exposure times must be used. The SEC vidicon (SECV), electrostatic storage camera (ESC), silicon dioxide vidicon (SDV), SIT vidicon (SITV) and intensified charge-coupled device (ICCD), perform marginally at worst-case conditions for this exposure. An exposure time of 0.0001 sec is not adequate.

An exposure time of 0.0005 sec results in shifting the ESC, ICCD, SDV, and SECV into the region where good performance can be obtained. This is illustrated in Figure 7-4. However, resolution will be limited to about 10 cycles/mm at 4 rpm if image motion compensation is not used. At an exposure time of 0.0005 sec, image motion compensation will have to be used at the higher spin rates. With an ideal IMC system the region of possible performance will be extended to the intersection of the camera threshold modulation curves and $M_a(K)$ for no spin.

Figure 7-5 shows threshold modulation curves for an exposure time of 0.0025 second. This exposure time is impractical without a highly-effective IMC system. At a 2-rpm spin rate the limiting resolution is already degraded to about 4 cycles/mm because of excessive image smear. However, the graph shows that the CCD, RBV and SILV do become feasible with an ideal IMC system if sufficient exposure is provided.

Corresponding threshold modulation curves based on the signal-to-noise ratio of the reconstructed image for 0.0005 second exposure time are

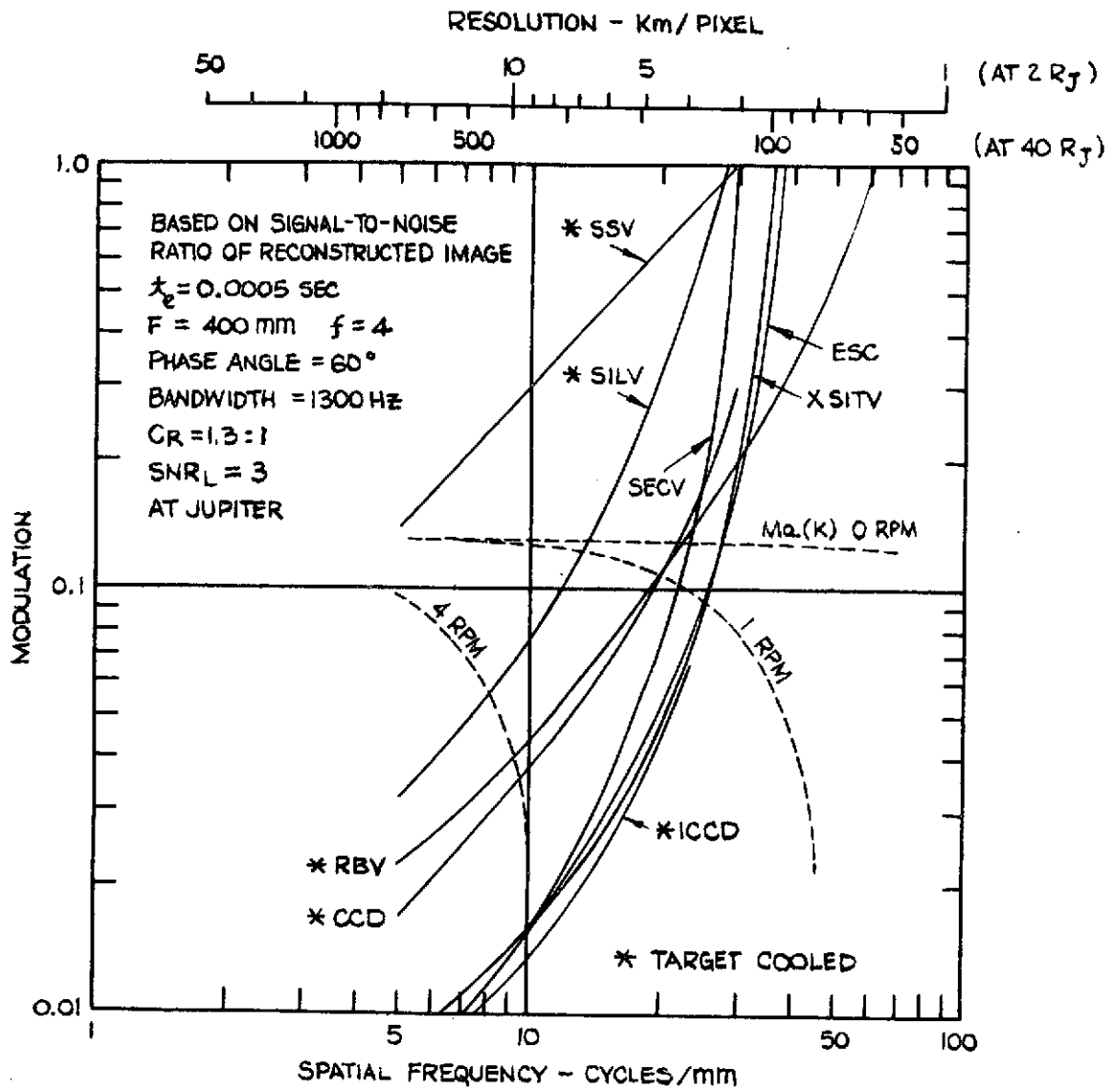
given in Figure 7-6. Comparing these curves to Figure 7-4, we see that after reconstruction the large-area signal-to-noise ratios have benefited from the integration over many pixels. This improvement can be explained by examining Equation (3-46). While the signal in a given reconstructed image area increases by the ratio of areas A_k/A_b , the noise only increases by the square root of this ratio. This results in better signal-to-noise ratios when A_k is greater than A_b .

7.3.3 SIGNAL-TO-NOISE RATIO VERSUS RESOLUTION

Another meaningful method of stating performance of a camera system is on the basis of signal-to-noise ratio versus spatial frequency. These curves form a good basis for comparing the sensitivity and resolution of various systems. The parameters used here correspond to the worst-case viewing conditions at Jupiter. The signal-to-noise ratios at the data link versus spatial frequency for exposure times of 0.0001 sec and 0.0005 sec are shown in Figures 7-7 and 7-8 respectively. Only the fully image-motion-compensated case (equivalent to zero-rpm spin rate) is shown.

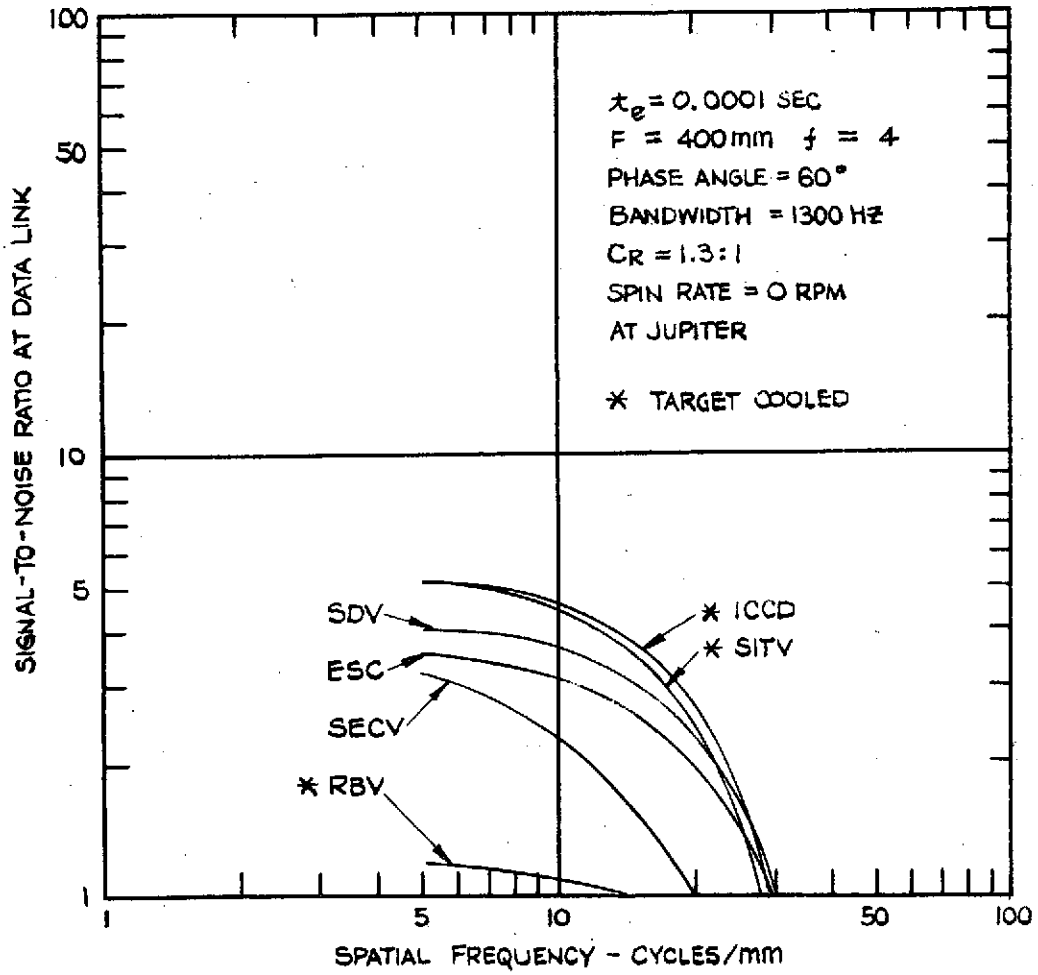
At $t_e = 0.0001$ sec (Figure 7-7), the maximum signal-to-noise ratio at the data link is about 6, at 10 cycles/mm for the ICCD. By increasing the exposure time to 0.0005 sec (Figure 7-8) the $SNR_{\text{data link}}$ increases to 12 at the same frequency. If a higher signal-to-noise ratio is required for an increased digitized bit rate/element, then these curves are helpful, because they present the maximum $SNR_{\text{data-link}}$ available.

The signal-to-noise ratio of the reconstructed image versus resolution for the candidate systems is given in Figure 7-9 for an exposure



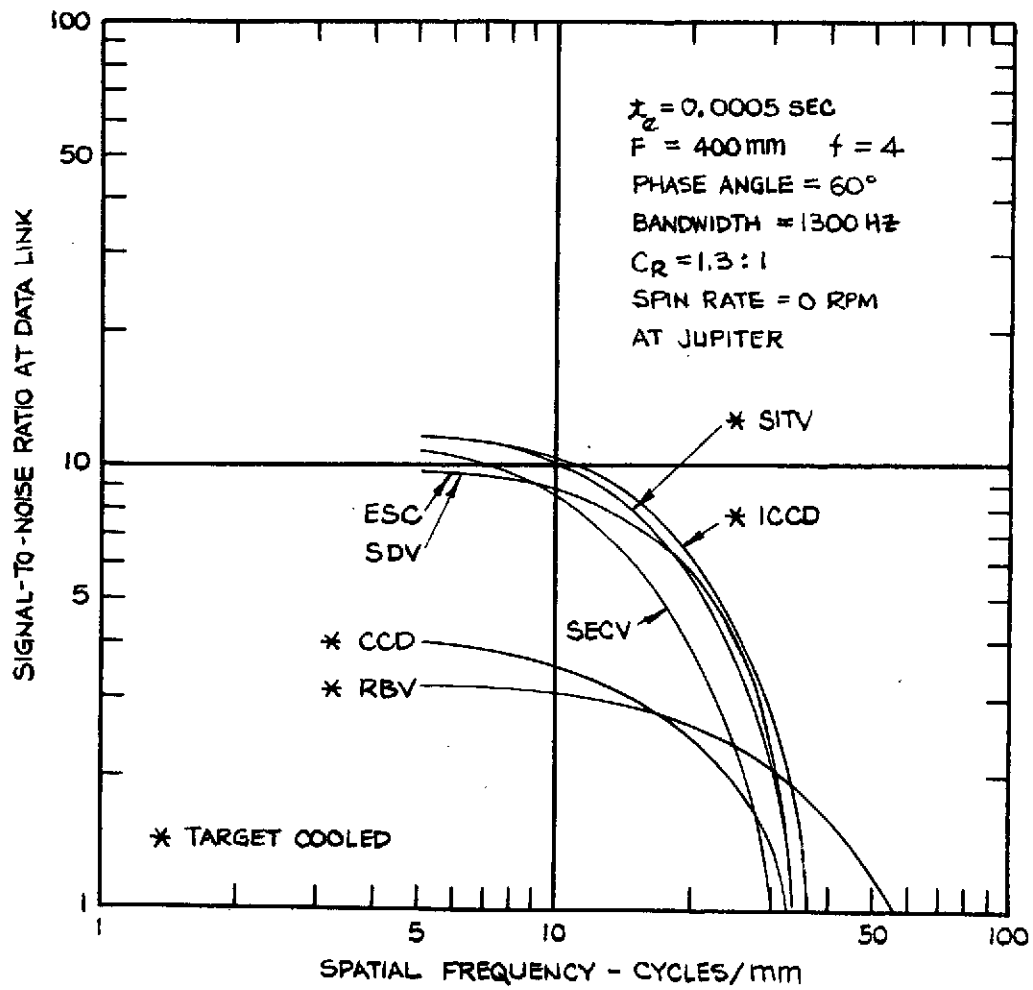
THRESHOLD MODULATION CURVES
FOR CANDIDATE FRAME IMAGERS

FIGURE 7-6



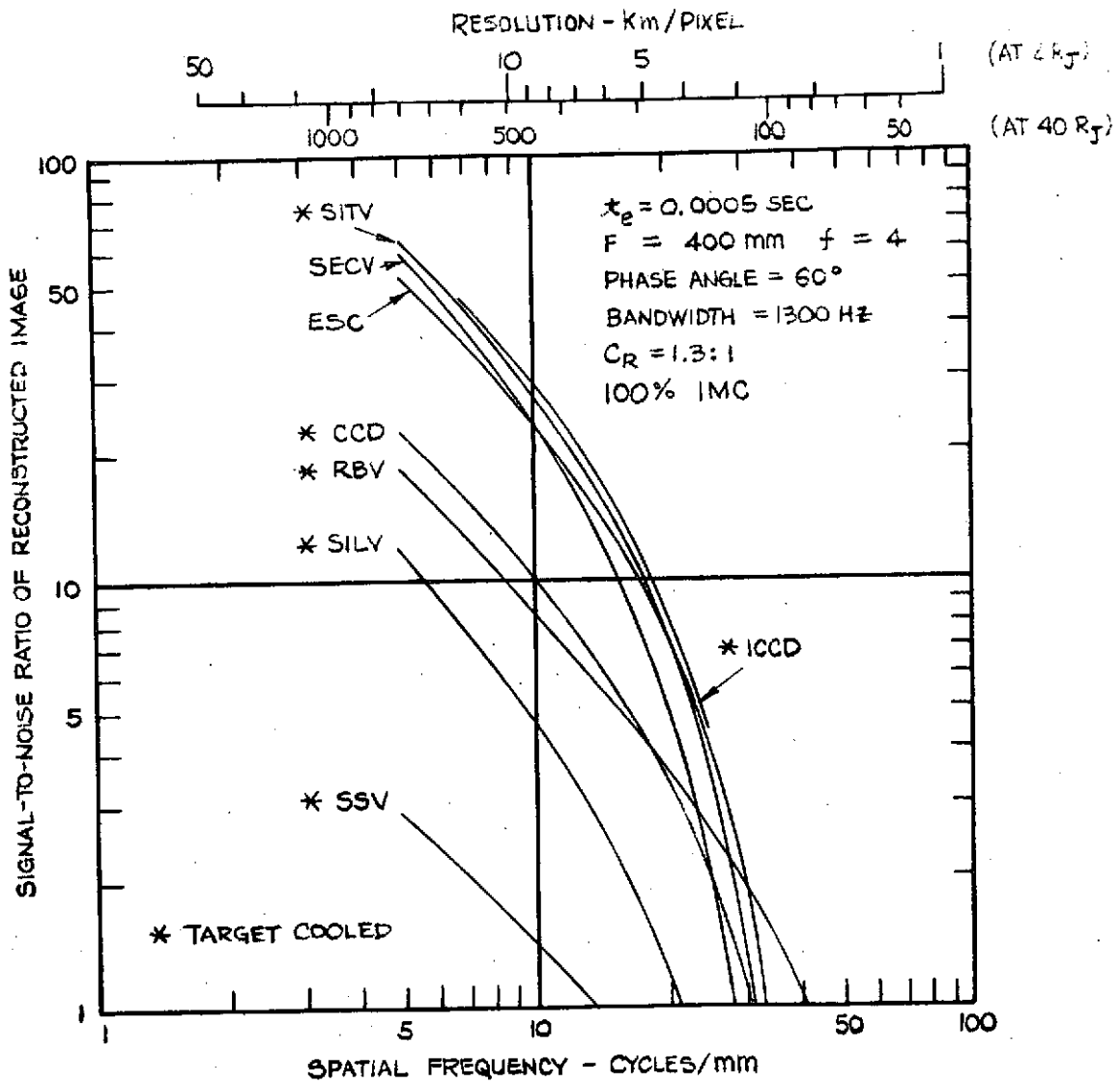
SIGNAL - TO - NOISE RATIO (DATA LINK)
 VERSUS RESOLUTION

FIGURE 7-7



SIGNAL - TO - NOISE RATIO (DATA LINK)
 VERSUS RESOLUTION

FIGURE 7-8



SIGNAL - TO - NOISE RATIO (RECONSTRUCTED IMAGE)
 VERSUS RESOLUTION

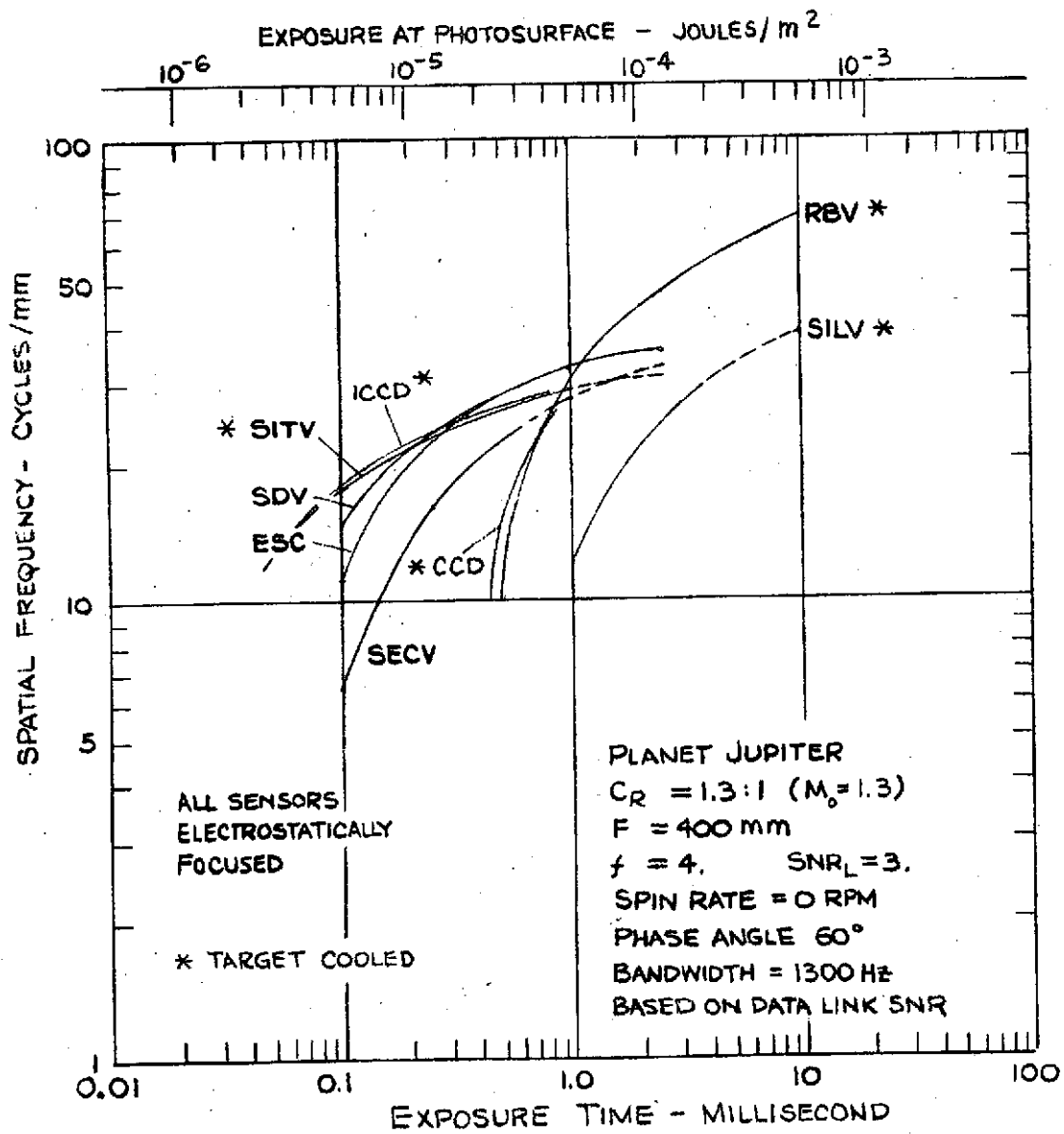
FIGURE 7-9

time of 0.0005 second. A comparison of Figures 7-8 and 7-9 illustrates the difference between the $SNR_{\text{data-link}}$ and $SNR_{\text{reconstructed}}$ under identical conditions.

7.3.4 RESOLVING POWER VERSUS EXPOSURE

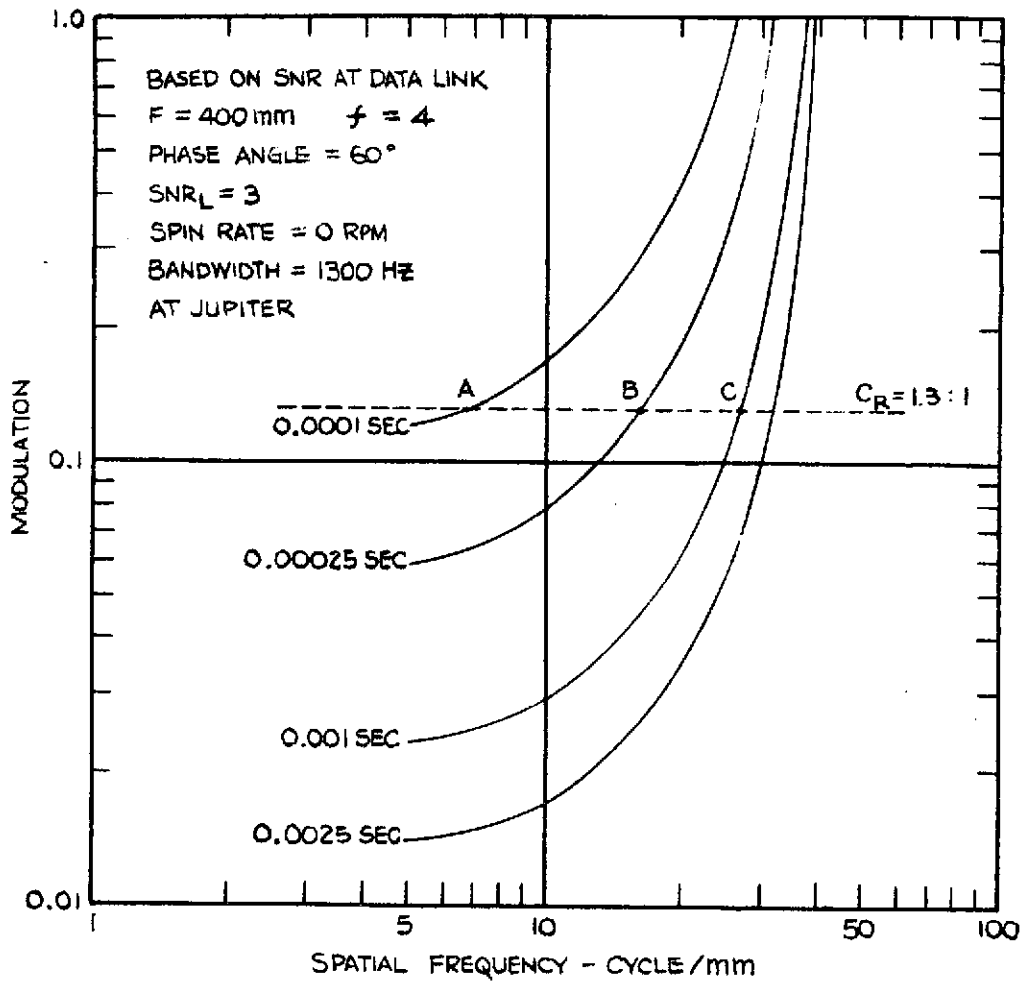
In this section, resolving power characteristics of the candidate sensors are presented as a function of exposure. The exposure E_x is the product of the input irradiance at the photosurface, F_{pc} , and the exposure time t_e . The resolving power (spatial frequency) is given in Figure 7-10 as a function of exposure as well as exposure time. Worst-case conditions at Jupiter are used, assuming zero spin rate. The sensor curves represent a constant data-link signal-to-noise ratio of 3 at a 1.3:1 contrast ratio. Due to the 1300-Hz bandwidth, the usual sensors must be cooled for slow-scan operation. Exposure times from 0.1 to 10 msec are used.

Since the basic SNR expressions necessary to obtain these curves are transcendental equations, the method of preparing Figure 7-10 may be of interest. Threshold modulation system curves, typified by Figures 7-11 and 7-12, were first established for different exposure times. The modulation of 0.13, corresponding to a 1.3:1 contrast ratio, was then identified. The spatial frequencies at the intersects of the threshold modulation curves and the 0.13 response line (points A, B, and C) were then used to construct Figure 7-10.



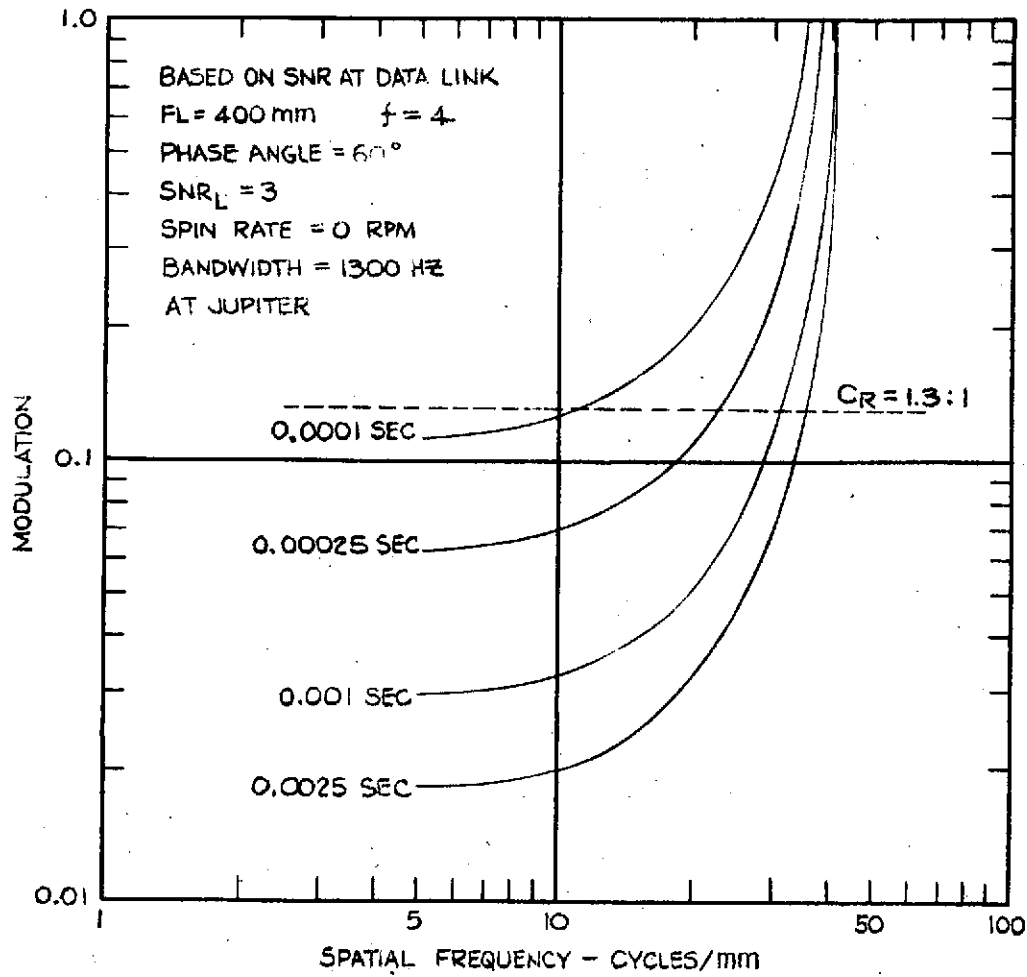
RESOLVING POWER VERSUS RESOLUTION

FIGURE 7-10



SEC VIDICON SYSTEM
 THRESHOLD MODULATION

FIGURE 7-11



ESC SYSTEM THRESHOLD MODULATION

FIGURE 7-12

7.4 SELECTION OF CAMERA SYSTEMS FOR DETAILED STUDY

Based upon an overall assessment of the candidate camera systems, applying the worst-case conditions for performance evaluation, and considering reliability, radiation, and other technological areas, several sensors have been selected for additional analysis. The initial list of candidates has been reduced to the SEC vidicon, the intensified charge-coupled device, and the electrostatic storage camera.

Table 7-2 summarizes the selection factors used in determining the best camera systems. Characteristics identified by a "Y" rating represent desirable features, while a "N" rating indicates an undesirable feature. Camera systems with several negative characteristics were rejected. Characteristics that rate consideration for rejection are circled on the summary chart.

Each of the initial list of candidate sensors will now be examined and the reasons for acceptance or rejection will be clearly identified.

7.4.1 SEC VIDICON

The SEC vidicon has been selected for detailed study for the following reasons:

- The SEC vidicon has a long-term integration capability and can store an image for many hours. It is capable of slow-scan operation at the slowest mission data rate. As a consequence, the data-handling and communications system can unload the data to Earth without an ancillary storage system such as a tape recorder. The resultant simplification of equipment will have a great impact on reliability, weight, and payload considerations.

TABLE 7-2

SUMMARY SENSOR SELECTION MATRIX

SENSOR	CHARACTERISTIC								SELECTION
	SLOW-SCAN CAPABILITY (W/O COOLING)	LONG TERM STORAGE (W/O COOLING)	PRE-STORAGE TARGET GAIN	HIGH SENSITIVITY	HIGH TARGET CAPACITANCE	DEVELOPED & SPACE QUALIFIED	ADEQUATE WORST CASE PERFORMANCE	GOOD RADIATION RESISTANCE	
SEC VIDICON	Y	Y	Y	Y	N	Y	Y	Y	Yes
ESC	Y	Y	Y	Y	Y	N	Y	Y	Yes
ICCD	(N)	N	Y	Y	N	N	Y	-	Yes
CCD	(N)	N	N	N	N	N	(N)	-	No
SIT VIDICON	(N)	N	Y	Y	Y	Y	Y	-	No
SILICON VIDICON	(N)	N	N	(N)	Y	Y	(N)	-	No
RBV	(N)	N	N	(N)	Y	Y	(N)	-	No
SiO ₂ VIDICON	Y	Y	Y	Y	Y	(N)	Y	Y	No
SSV-SELENIUM	Y	Y	N	(N)	N	Y	(N)	-	No
SSV-ASOS	(N)	N	N	(N)	Y	Y	(N)	-	No

CODE: Y YES

N NO

- INSUFFICIENT DATA

○ CONSIDERATION FOR REJECTION

- The SEC vidicon target gain is sufficient to make the preamplifier noise negligible at the expected exposure levels. Figure 7-4 illustrates the importance of target gain on worst-case performance for a 0.5-msec exposure time. Devices such as the SSV and SILV lack prestorage gain; consequently, they cannot achieve low modulation levels, such as in a quantum-noise-limited signal, due to preamplifier noise. All of the devices with prestorage target gain are capable of operating very close to the quantum noise limit. For this reason, the ISEC offers no advantage, since the intensifier cannot further improve the performance of a quantum-noise-limited system.
- The resolution capability of the SEC vidicon is acceptable. A standard Westinghouse WL-30893 has an aperture response of 20% at 16.4 lp/mm. The performance curves of Section 7.3.2 show the worst-case resolution that can be expected and relate it to the ground resolution for a Jupiter mission.
- The target capacitance is low. It is only sufficient to allow collection of several thousand photoelectrons per picture element before a "full target" is obtained (about 4×10^9 electrons per cm^2 for a standard target). Because of the low capacitance, the SECV cannot be utilized for large exposures and has limited low-contrast capability. However, for the mission being studied at a modulation of 0.13 (equivalent to a 1.3:1 contrast ratio), a signal-to-noise ratio of the reconstructed image of over 20 will be feasible at 10 lp/mm. This is illustrated in Figure 7-9.
- The SEC target does not require cooling, as the dark current is negligible.
- The SEC is fully developed and space qualified. It has been flown on many missions. A variety of configurations is available. For instance, performance of the electrostatically-focused version can be improved either by substituting electromagnetic focusing, by eliminating the collector mesh or by other changes. However, each increase in performance would result in some other tradeoff.
- Electronic image motion compensation is possible because the device contains an image section. Photoelectrons can be deflected in the imaging region before they land on the target to correct for linear motion during exposure. Electronic zooming and shuttering are also feasible when using other SEC vidicon configurations.

7.4.2 ELECTROSTATIC STORAGE CAMERA

The electrostatic storage camera (ESC) has been selected for further study. Although the ESC is presently being developed and is not yet ready for space missions, its future potential for planetary exploration is excellent because of its unique storage properties. The reasons for selecting the ESC are given below:

- The ESC has a storage medium with a long integration capability that can be scanned at the slowest mission data transmission rate. The storage target does not require cooling because of its negligible dark current. Images can be stored for weeks if required before being transmitted to Earth.
- The electrostatic storage camera can provide its own bulk storage in the form of a multifaceted storage drum. A number of pictures (typically two to thirty frames, 16mm on a side) can be exposed, stored, and transmitted at arbitrary times and data rates. This unique feature allows multiple pictures to be taken of Jupiter satellites during a single flyby, thereby providing extensive photographic coverage. The ESC would transmit the information at a convenient time after the sequence of exposures were taken. Other framing cameras would have to dump the data into a tape recorder or transmit it to Earth before the next frame could be exposed.
- The high prestorage gain associated with the target (adjustable from about 20 to 200) is sufficient to override the readout noise at the low exposure levels of interest. This results in quantum-noise-limited camera operation over a wide dynamic range.
- The ESC has a high target capacitance that can be adjusted during design to satisfy a particular application. For target thicknesses of 2000 to 5000 Å the capacitance ranges from 1.5×10^{-8} to 5.4×10^{-9} F/cm². Even at the lower capacitance value about 7×10^9 electrons per cm² can be stored at a 5-volt target potential, allowing operation over a wide dynamic range. In addition, an adequate target potential can be achieved at lower exposures than with sensors having lower target capacitance.

- The readout process is non-destructive. Repetitive scans are possible because the ESC uses a high-velocity read beam. The ESC essentially has a built-in data compression capability in that a cursory examination of pictures can be made at low resolution to identify areas of interest. These portions can be re-scanned at high resolution.
- The electrostatic storage camera is capable of high electro-optical resolution over a large format. The resolution can be improved by employing electromagnetic focusing, a thin storage target, and a smaller spot diameter. Although high performance is not required for the Jupiter orbiter, these improvements enhance the suitability of the ESC for other outer planet missions.
- The electrostatic storage camera system design is extremely flexible. The size of the image and storage sections can be adjusted to accommodate varying format requirements. Electromagnetic focusing can be provided for improved resolution. Electronic shuttering is possible, as well as electronic image motion compensation.

7.4.3 CHARGE-COUPLED IMAGERS

Charge coupling is a significant new concept in imaging. Although experimental devices are now quite crude and limited in format size, the potential attributes of excellent performance at low power, low weight, and good reliability are very appealing. Two devices in the sensor family based on the charge-coupled principle have been examined. The basic charge-coupled device is first considered as a frame imager, then the characteristics of an intensified charge-coupled device are summarized.

7.4.3.1 Charge-Coupled Device - The charge-coupled device (CCD) possesses many attractive characteristics. Despite the fact that it employs a new concept, it is based on well-developed semiconductor

technology. It has the attributes of silicon fabrication simplicity, high reliability, low power, and intrinsic low-noise analog signal processing. The extremely low-noise properties of the basic CCD impose demanding requirements for on-chip amplifiers in order to realize the full benefits of the technology. Using the best conventional preamplifiers, the thermal noise generated is excessive. By integrating the amplifier, the shunt capacitance can be reduced to approximately 0.2 pf. Novel amplification schemes should be possible which would take advantage of the low output capacitance and reduce the amplifier noise.

The high quantum efficiency of the CCD coupled with the low-noise properties of an on-chip amplifier provide excellent imaging results at high video bandwidths. However, for slow-scan operation, clock-related noise is excessive. Due to the presence of interface states within the target, the minority carriers in each potential well are subject to random capture and emission. This adds noise to the signal both during the integration time and during the readout periods. When the signal bandwidth and the clocking frequency are low, the readout interface noise becomes dominant. The interstate noise decreases with increasing clock frequency and with decreasing integration time.

Interface state trapping limits the performance of the basic CCD⁽³⁰⁾ at moderate and low frequencies. The amount of signal degradation can be influenced by the device parameters, dimensions, and clocking waveforms. Incomplete charge transfer due to interface state trapping can be reduced by increasing clock voltages, increasing the signal charge, or using special

"push" clocks to move the charge. Other CCD system approaches that utilize single-line storage can be used to overcome the interface state trapping limitation. For example, the CCD can be operated a line at a time by transferring the first line into an auxiliary storage unit at a high clocking frequency. The line in the auxiliary store can then be transmitted to Earth at the desired low frequency before the second line is transferred. The process is repeated until the entire frame is transmitted. This type of system will not be analyzed in this study because of the relative superiority of the intensified charge-coupled device.

There are several dark current sources associated with the CCDs: the depletion region, neutral bulk silicon, and the oxide-silicon interface. The dark current is typically several nanoamperes per square centimeter at room temperature. This limits the integration period to less than a second. If slow-scan operation is desired, cooling to about -60°C is essential.

Because of the newness of the CCD technology, only a few devices of limited size have been built. A useful device would consist of at least 500×500 elements, but a more suitable device might consist of 1000×1000 elements. This goal appears reasonable since 500-element buried channel linear imaging devices have been constructed.

Figure 7-4 shows the threshold modulation curve for the CCD for 0.5-millisecond exposure time. The readout interstate noise is responsible for the moderate performance displayed. The basic CCD device has not been selected for further study. In addition to its poor low-frequency performance, the CCD lacks an image section. Consequently, mechanical IMC must be employed

and some form of mechanical shuttering must be devised. An intensified charge-coupled device overcomes these limitations.

7.4.3.2 Intensified Charge-Coupled Device - The intensified charge-coupled device (ICCD) consists of a charge-coupled device preceded by a photocathode and an electrostatically-focused image section. The high prestorage target gain (2000) provides a quantum-noise-limited signal-to-noise ratio at very low exposures. At an exposure time of 0.1 millisecond (see Figure 7-3), the ICCD provides the best performance among all of the imagers. This is due to the low-noise properties of the integrated amplifier. The interstate noise is not a problem because of the high prestorage target gain.

Unlike the CCD, image motion compensation can be applied electronically. Electronic gating is also feasible. The ICCD requires less mechanical equipment if the IMC and shuttering functions are performed electronically. It operates well at low exposure levels. However, it will be bulkier and heavier than the CCD. The ICCD has been selected for further study.

7.4.4 SIT VIDICON

The SIT vidicon has not been selected for further study. The primary reason for rejection is the need for cooling to achieve slow-scan operation. The SIT vidicon would be an excellent choice for

many alternative planetary missions, particularly where ancillary storage equipment can be added because of reduced payload restrictions. Some of the SIT vidicon characteristics are listed below:

- Based on sensitivity alone, the SIT vidicon is superior to most camera systems. Its silicon target has a prestorage gain of 2000, which is considerably higher than other target types. The significance of the high target gain is that the preamplifier noise becomes negligible. Consequently, a quantum-noise-limited signal-to-noise ratio is achieved at lower exposure levels. Figure 7-10, which shows resolving power versus exposure, illustrates the superior performance of the SIT vidicon at low exposures.

At longer exposures, the high gain of the SIT vidicon does not offer as much of an advantage. This is because the maximum signal-to-noise ratio is determined by charge-storage considerations. If a target can store a maximum of b electronic charges per picture element because of its capacitance, the maximum number of photoelectrons that can be stored per picture element is b/G_t , where G_t is the target gain. Thus the signal-to-noise ratio set by charge storage considerations is:

$$\text{SNR (charge storage)} = \sqrt{\frac{b}{G_t}} \quad (7-2)$$

At the higher exposure levels, SNR (charge storage) imposes a limitation since it is independent of exposure for a given target gain. SIT vidicons have 20 to 25 times the gain of an SEC tube, and their charge storage capacity is about 10 to 20 times greater. As a result, the maximum signal-to-noise ratio set by charge storage considerations is about the same for both tubes. The performance of both tubes is quite similar at an exposure time of 0.0005 second, as shown in Figure 7-4.

- The resolution capability of the SIT vidicon is acceptable for this class of mission. Conventional silicon targets have a diode center-to-center spacing density of 72 per millimeter with a response of 20% at 25.5 lp/mm when used in a 16mm tube. Special silicon targets have been used in experimental tubes with spacing densities of up to 130 diodes per millimeter. The results of the parametric worst-case analysis (Figures 7-3 and 7-4) demonstrate adequate resolution.
- The slow-scan capability of the SIT tube is limited by the dark current of the silicon diodes. At room temperature the integration period must be limited to less than a second. Consequently, target cooling is required to read out directly at the expected data rates. For scan periods on the order of a few seconds, the target temperature must be held at approximately -20°C . Integration times of several hours may be obtained by cooling to -60°C . Implementing thermal control, however, can involve practical difficulties and the use of considerable power. The tradeoffs involved in using onboard storage at higher video bandwidths versus slow-scan operation requiring cooling equipment would have to be considered if an SIT vidicon were used.

It is of interest to calculate the limitation imposed by the dark current in a cooled silicon target. Consider a target at -40°C , where the dark current is 10^{-12} amperes per square millimeter. At a resolution of 20 cycles/mm, the number of dark-current electrons per picture element per second is approximately 3900.

The charge required for full target capacity for a practical target swing of 5 volts and a target capacitance of 40×10^{-12} F/mm is

$$Q = C*V = \frac{40 \times 10^{-12} \frac{F}{mm^2} \times \left(\frac{1}{40} mm\right)^2 \times 5v}{1.6 \times 10^{-19} \text{ coulomb/electron}} \quad (7-3)$$

$$= 7.8 \times 10^5 \text{ photoelectrons per picture element.}$$

The time required to fill the target is:

$$\text{time} = \frac{7.8 \times 10^5 \text{ photoelectrons}}{3.9 \times 10^3 \text{ photoelectrons/sec}} = 200 \text{ seconds}$$

So the dark current of 10^{-12} amperes per square centimeter at -40°C completely fills the target in 200 seconds. At the nominal data rate of 16,384 bits/sec, about 184 seconds will be required to transmit the data on a 700-x-700-element target. It is obvious that either onboard storage or cooling to about -60°C is essential, since rates as low as 2048 bits/sec may be used.

- The SIT vidicon is a relatively new device. So far a variety of tubes have been developed and space-qualified versions are available. High resolution, large image format, and slow-scan configurations of the SIT vidicon must still be developed.

7.4.5 SILICON VIDICON

The silicon vidicon tube will not be considered. It has little to offer on a mission of this type that could not be handled better by the SIT vidicon. It should be recalled that the SIT vidicon is actually a silicon vidicon with an intensifier front end added. However, the silicon vidicon does have better red response than the SIT vidicon.

The silicon vidicon has limited sensitivity because it lacks prestorage target gain. Thus, the preamplifier noise remains the dominant noise term at the exposure levels encountered at Jupiter. Another disadvantage is the requirement to cool the silicon vidicon to -60°C for slow-scan operation, or, in lieu of cooling, the need for auxiliary storage equipment. Finally, shielding would probably be required to prevent losses in quantum efficiency and increased dark current due to the radiation environment.

The performance levels that can be expected are best illustrated in Figures 7-4 and 7-5. At a half-millisecond exposure, the SILV is not sensitive enough. However, when the exposure is increased to 2.5 milliseconds the SILV performs nicely, providing that image motion compensation limits the smear. Its poor relative sensitivity is illustrated in Figure 7-10.

7.4.6 SLOW-SCAN VIDICON

The slow-scan vidicon has been rejected because of its low sensitivity. Since there is no target gain mechanism in this tube, the amplifier noise prevents its use at the expected exposure levels. The vidicon generally requires longer exposure times which cannot be used in this application due to the associated image smear.

A slow-scan vidicon utilizing an ASOS photoconductor with a peak quantum efficiency of 47% illustrates the lack of sensitivity. Figure 7-5 shows the threshold modulation curve at 2.5 milliseconds exposure time. Low-contrast images would have an SNR of less than three at the data link. The ASOS photoconductor also has the disadvantage of requiring cooling to limit the dark current and allow slow-scan operation.

The selenium vidicon, used in the Mariner series of space probes, offers good resolution and excellent slow-scan characteristics without cooling. The dark current is negligible. Unfortunately the sensitivity is also low, although high quantum efficiencies can be obtained.

7.4.7 SILICON DIOXIDE VIDICON

The silicon dioxide vidicon (SDV) has not been selected. Although the predicted performance of the SDV is excellent, the device must still be developed. Other candidates requiring development effort such as the electrostatic storage camera and intensified charge-coupled device offer greater advantages and have therefore been selected instead of the SDV. The ESC offers multiple-frame storage instead of a single picture, whereas the ICCD is smaller, weighs less, and consumes less power than the SDV.

The silicon dioxide vidicon has a storage medium with a long integration capability that can be scanned at the slowest mission data rates. The storage target does not require cooling as the dark current is negligible. In addition, the SDV has a high-capacitance target.

The SDV has the same configuration as the SEC vidicon, with the exception of the target. The high prestorage gain associated with the target is sufficient to override the preamplifier noise and results in a quantum-noise-limited SNR over a wide dynamic range. Figures 7-3 , 7-4, and 7-10 demonstrate the predicted performance levels and resolution.

7.4.8 RETURN BEAM VIDICON

The return beam vidicon (RBV) has not been selected. It lacks sufficient sensitivity and requires cooling to achieve slow-scan operation at the specified rates. The factors supporting this decision are summarized below.

- The return beam vidicon has only moderate sensitivity. The absence of prestorage gain in the target makes it impossible to achieve a quantum-noise-limited signal due to the beam shot noise associated with the return beam. The performance of the RBV at low contrast is inadequate at 0.5-millisecond exposure time, however, at 2.5 milliseconds the signal-to-noise ratio improves substantially. See Figure 7-4 and 7-5 for performance comparisons.
- The dark current of the photoconductor used in the RBV requires cooling to about -40°C to be compatible with the required slow-scan operation. Thermal control would be essential. The alternative use of short integration times with an auxiliary storage unit is undesirable from weight and reliability considerations.

- Because of the lack of an image section, electronic image motion compensation cannot be applied. Mechanical IMC must be used in addition to a mechanical shutter.
- The primary advantage of the return beam vidicon is its high resolution. It has an aperture response of 20% at 59 lp/mm. The RBV is a fully developed tube available in sizes up to 4-1/2 inches in diameter. It is space qualified and has flown on space missions.

7.5 CONCLUSION

The basic objective of this task was to select the most promising frame image systems based on a worst case parametric analysis. The SEC vidicon, the electrostatic storage camera, and the intensified charge-coupled device were found to be the best systems for the class of mission being studied. These three systems will now be analyzed for the specified Jupiter orbiter.

SECTION VIII
ANALYSIS FOR SPECIFIED JUPITER ORBITER MISSION
USING SELECTED CAMERA SYSTEMS

8.1 INTRODUCTION

The objective of this section is to determine the performance of the selected sensors for a specific Jupiter orbiter mission.

Performance curves are presented for the SEC vidicon, the electrostatic storage camera, and the intensified charge-coupled device for the specified Jupiter orbit including satellite encounters. Both electrostatically-focused and high performance, electromagnetically-focused configurations are analyzed.

The suitability of the selected sensors for other outer planet missions is discussed. Performance curves are given at Saturn and Uranus. Conclusions are then presented indicating the best systems for outer planet missions.

8.2 DISCUSSION

8.2.1 SPECIFIED JUPITER ORBITER MISSION

The mission selected by NASA for study by the contractor consists of a Jupiter orbiter which repeatedly encounters three satellites⁽³¹⁾. The selected 1976 orbit is equatorial with a $2.29 R_J$ periapsis, a $45.13 R_J$ apoapsis and a period of 14.22 days. From an interaction region orbit ($2.29 \times 100 R_J$),

the spacecraft is deboosted into the $2.29 \times 45.13 R_J$ orbit, where close encounters with the satellites occur for about three to five orbits.

Figure 8-1 shows the three-satellite encounter geometry of the Jupiter orbit. Three of the four Galilian satellites, Io, Europa, and Ganymede, are nearly commensurate (i.e., their orbital periods are near-multiples of each other). Syzygy occurs about every 7 days; however, the alignment drifts about 5.2° in a retrograde direction between one alignment and the next. The planned orbit therefore results in several encounters with the three satellites.

The characteristics of the encounter with Jupiter and the satellites are shown in Figure 8-2, where the distance from the center of Jupiter is plotted versus the phase angle. These characteristics will be used in determining the performance of the selected camera systems.

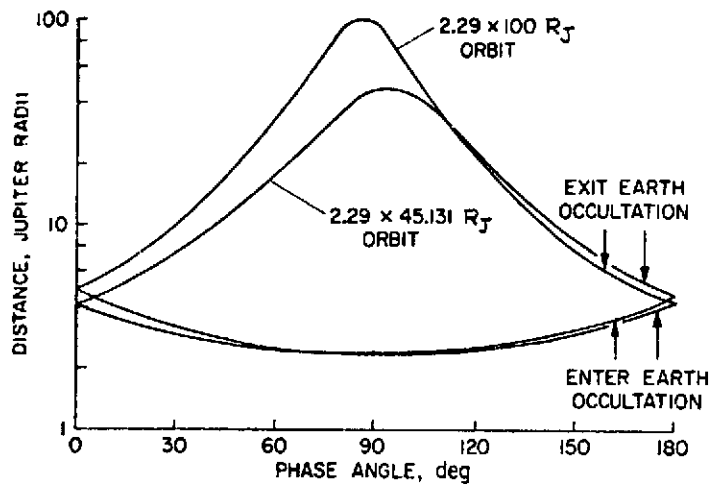
The following frame imagers will be examined for the specified Jupiter orbiter mission:

SEC Vidicon

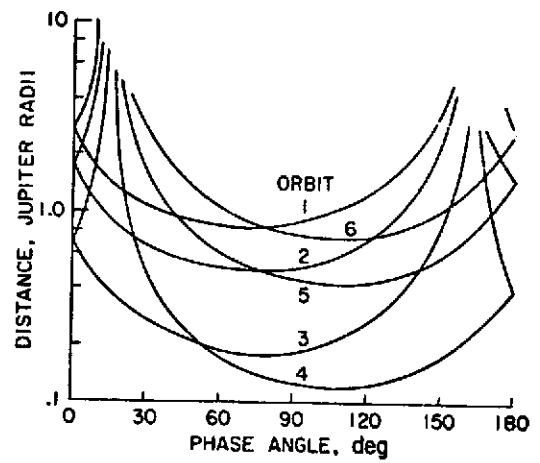
Intensified Charge-Coupled Imager

Electrostatic Storage Camera

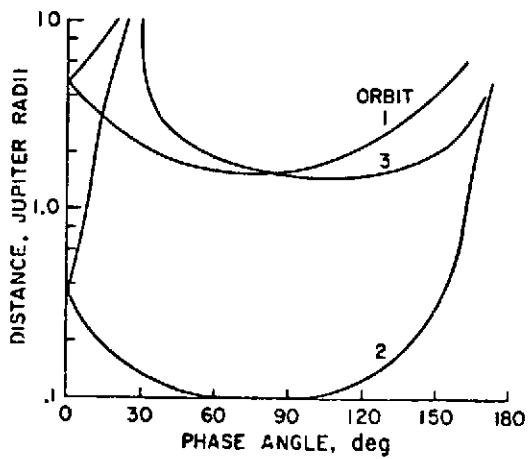
Performance curves will be given for both electrostatically- and electromagnetically-focused configurations for all three devices.



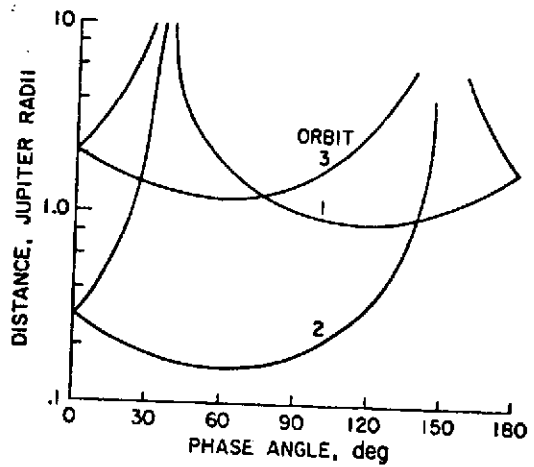
Jupiter.



Europa.



Io.



Ganymede.

1976 ENCOUNTER CHARACTERISTICS

Figure 8-2

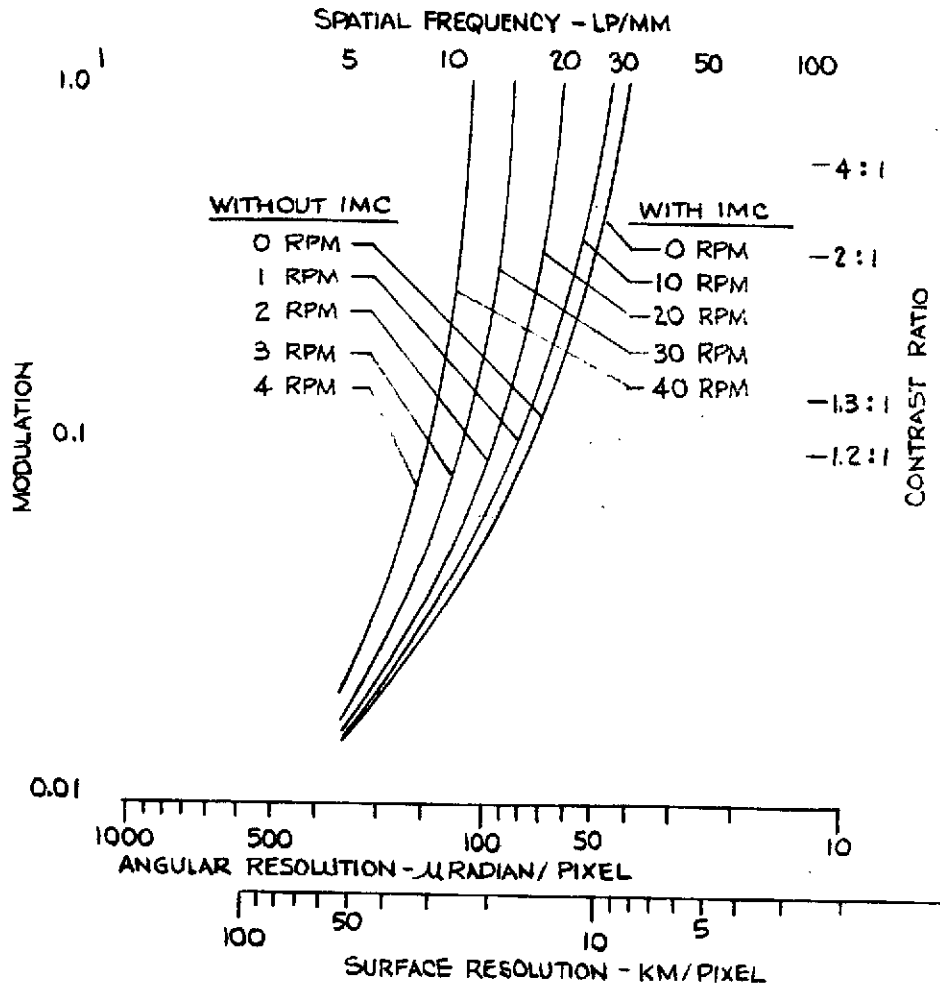
8.3 PERFORMANCE ANALYSIS

The analytical SNR models for the selected sensors have been used to prepare the performance curves for the Jupiter orbiter mission. As in the previous worst-case parametric analysis, it has been necessary to limit the number of variables and parameters involved to keep the analysis within reasonable bounds. In particular, specific camera parameters were fixed to reasonable values. Nominal values were selected for other system parameters. For example, a video bandwidth of 1300 Hz (corresponding to a 16,384-BPS data rate) was selected. Performance curves are based on a constant signal-to-noise ratio of 10 for the reconstructed image. In cases where image motion compensation (IMC) is used, a 90%-effective system is assumed. Spectral filtering is not included in the analysis.

8.3.1 EFFECT OF IMC ON PERFORMANCE

The effect of image motion compensation on performance is illustrated for the SEC vidicon in Figure 8-3. Modulation curves are given showing the contrast ratio versus resolution as a function of spin rate for cases both without and with 90%-effective IMC. Note that all of the modulation curves in this section are plotted using the scene modulation (and contrast ratio) as the ordinate as described in Paragraph 3.4.1.

$\lambda_e = 0.0005 \text{ SEC}$ BANDWIDTH = 1300 HZ
 $F = 400 \text{ MM}$ BASED ON RECONSTRUCTED IMAGE SNR
 $f = 4$ $2.29 \times 45.1 R_J$ JUPITER ORBITER
 $\text{SNR}_L = 10$ ALTITUDE = $4 R_J$
 PHASE ANGLE = 0° IMC IS 90% EFFECTIVE



SEC VIDICON SYSTEM MODULATION CURVES

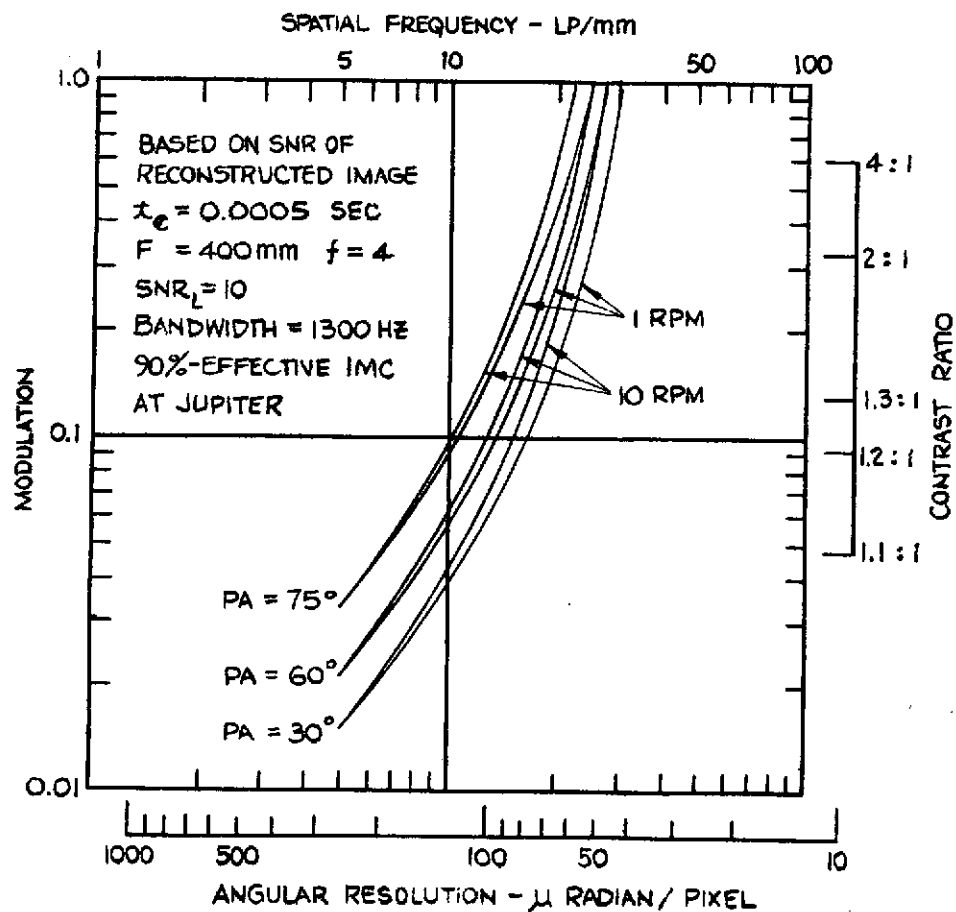
Figure 8-3

The need for image motion compensation has been established in Section 6. Consequently, all subsequent performance curves will be based on a 90%-effective IMC system. That is, only 10% of the image displacement relative to the sensor's faceplate that would result without IMC remains after IMC is applied. As an example, with 90%-effective IMC the performance at 10 rpm is identical to that at 1 rpm for the uncompensated case.

8.3.2 EFFECT OF VARYING PHASE ANGLE

The effect of varying phase angle on performance is shown for the SEC vidicon in Figure 8-4. Modulation curves giving the response (contrast ratio) as a function of angular resolution are shown at various phase angles and spin rates. For a constant angular resolution, we can see how the ability of the system to perform drops off at low contrast.

Angular resolution can be expressed as ground resolution by applying the 1976 encounter characteristics for Jupiter (Figure 8-2). This figure shows the distance from the center of the planet in units of Jupiter radii as a function of solar phase angle. The ground resolution for several spacecraft locations characterized by this orbit are tabulated in Figure 8-4 for an angular resolution of 125 μ radian/pixel.



GROUND RESOLUTION FOR JUPITER ORBITER 2.29 x 45.13 R _J ORBIT		
PHASE ANGLE	SPACECRAFT ORBIT RADIUS	GROUND RESOLUTION AT 10 LP/mm (125 μ R/PIX)
0°	4 R _J	26.8 km
± 30°	7	53.6
± 60°	3	17.8
± 75°	18	151.7
	2.4	12.6
	25	214.2
	2.3	11.6

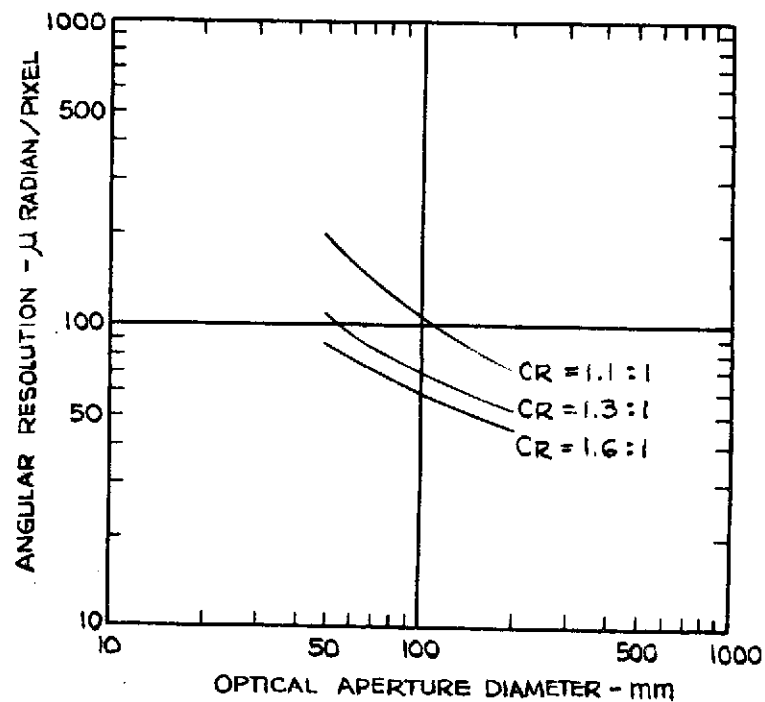
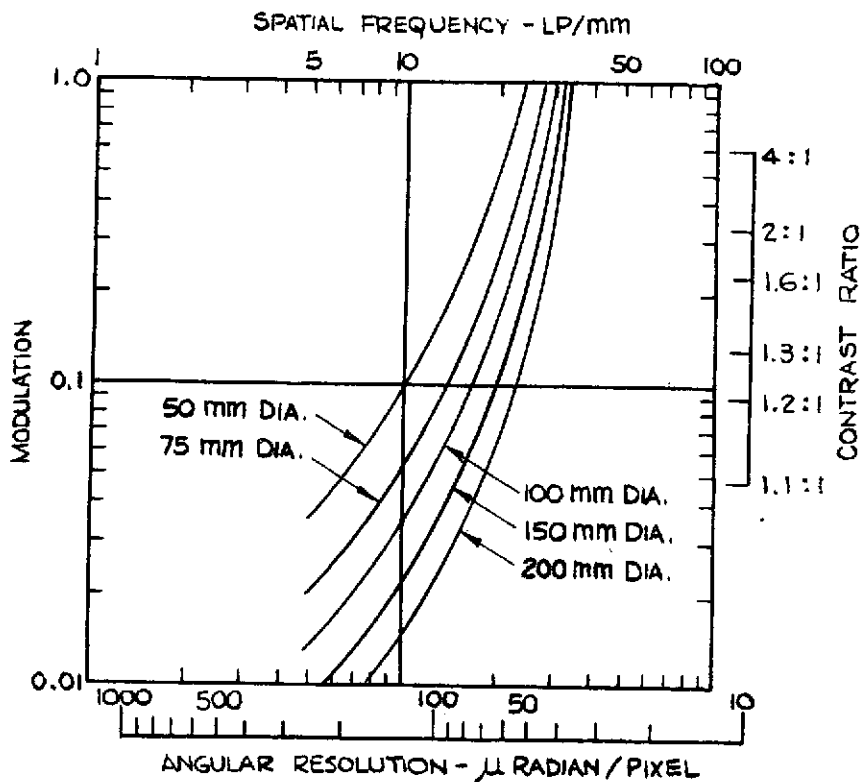
SEC VIDICON SYSTEM MODULATION CURVES
AS A FUNCTION OF PHASE ANGLE

Figure 8-4

8.3.3 EFFECT OF VARYING OPTICAL PARAMETERS

In the preceding analyses a nominal optical aperture of 100-mm diameter was assumed. Because of weight considerations, an aperture diameter of 150 mm was selected for the upper limit. In Figure 8-5, the performance of the SEC vidicon is shown as a function of optical aperture diameter covering the range of interest. As expected, the performance improves with larger aperture size because the light-gathering ability of the optical system increases by the square of the diameter (assuming a fixed focal length).

The effect of varying focal length is illustrated for the SEC vidicon in Figure 8-6, where the modulation (or contrast ratio) is given as a function of angular resolution. In the preceding analyses a nominal focal length of 400 mm was assumed. In this figure, the performance is given for focal lengths ranging from 200 mm to 1000 mm. The improvement in angular resolution at longer focal lengths is primarily due to the improved MTF of the image sensor at lower spatial frequencies. Figure 8-7 illustrates the field of view obtained versus focal length for several photocathode format sizes. A camera system with a 400-mm focal length has a field of view of approximately 28 milliradians for an 11.3 x 11.3 mm format. The distance required for a full-disc view of Jupiter and its satellites has been plotted as a function of focal length. Full-disc coverage of Jupiter occurs at about $70 R_J$ with a 400 mm focal length optical system.

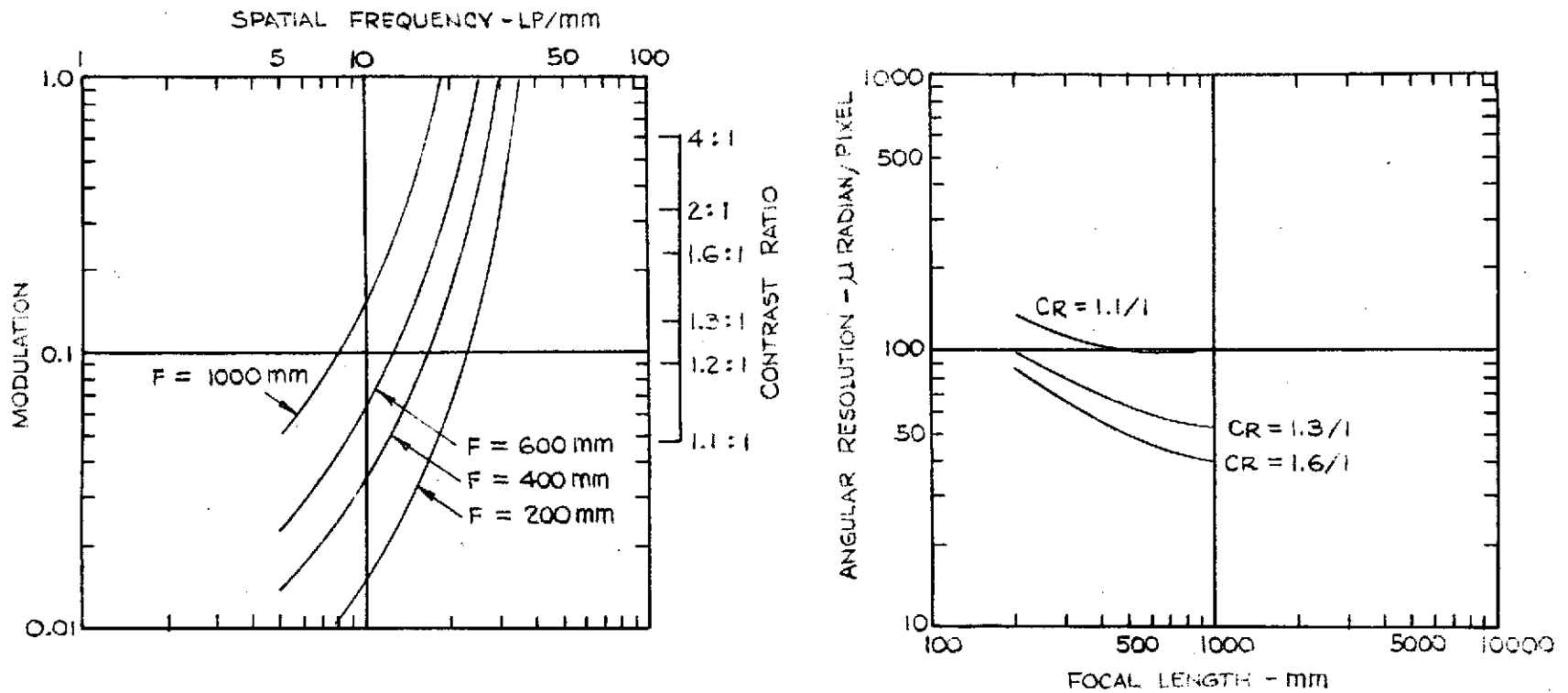


$t_e = 0.0005$ SEC
 $SNR_L = 10$
 PHASE ANGLE = 0°
 $F = 400$ mm
 ELECTROSTATICALLY FOCUSED

BANDWIDTH = 1300 HZ
 BASED ON RECONSTRUCTED IMAGE SNR
 WITH 90%-EFFECTIVE IMC
 AT JUPITER

SEC VIDICON PERFORMANCE AS A FUNCTION OF OPTICAL APERTURE DIAMETER

Figure 8-5

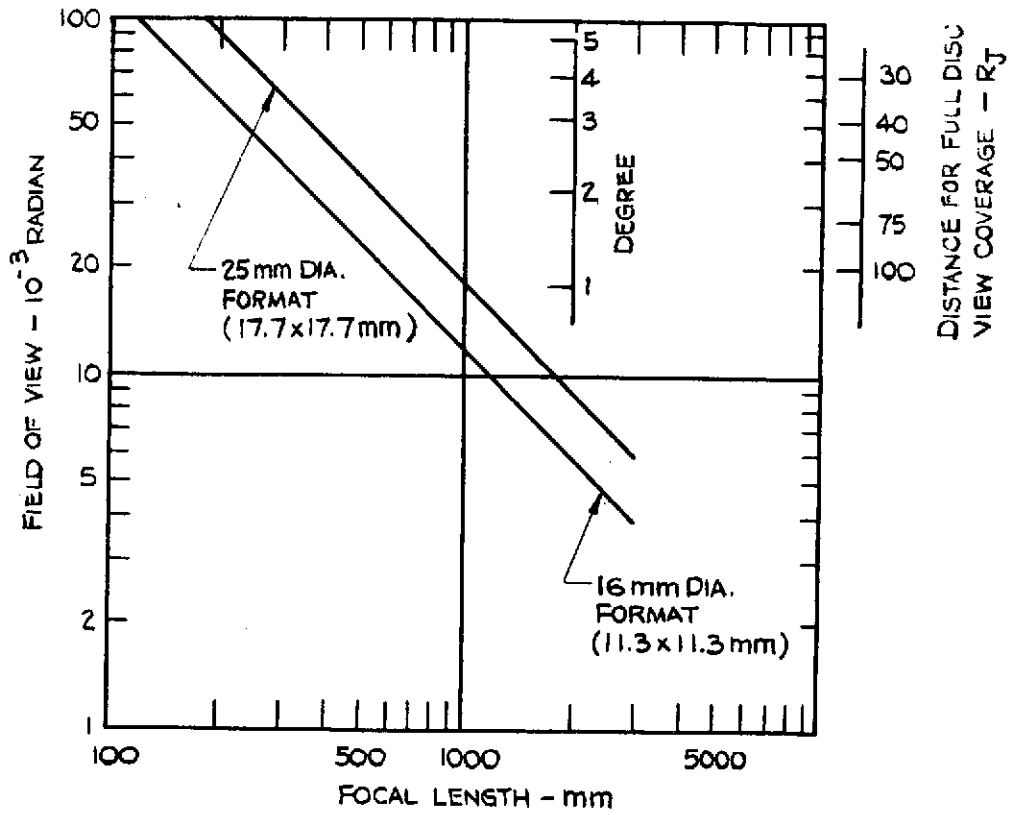


$\lambda_e = 0.0005$ SEC
 OPTICS DIA. = 100 mm
 $SNR_L = 10$
 PHASE ANGLE = 0°
 ELECTROSTATICALLY FOCUSED

BANDWIDTH = 1300 HZ
 BASED ON RECONSTRUCTED IMAGE
 WITH 90%-EFFECTIVE IMC
 AT JUPITER

SEC VIDICON PERFORMANCE AS A FUNCTION OF FOCAL LENGTH

Figure 8-6



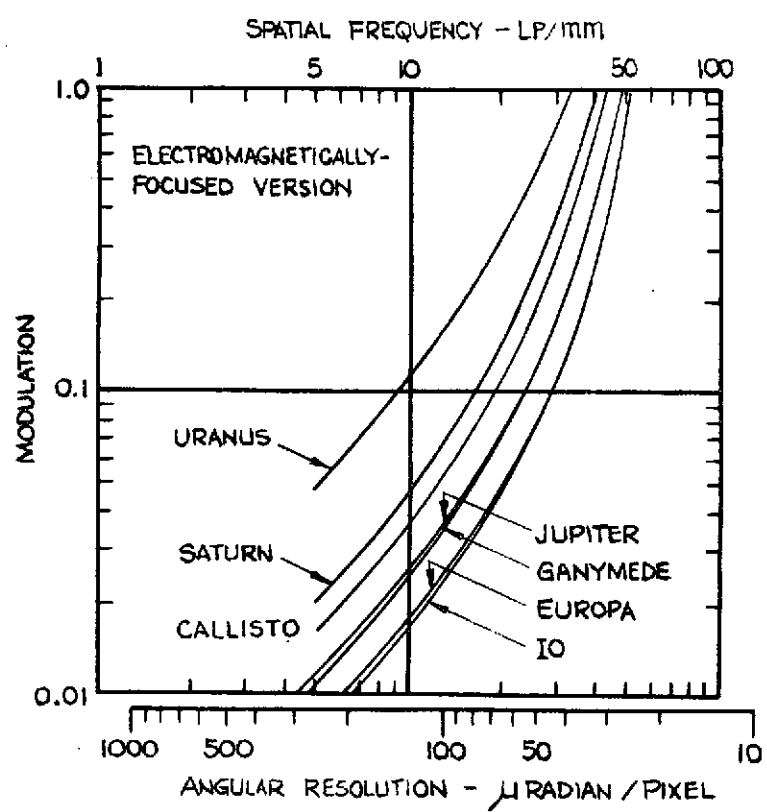
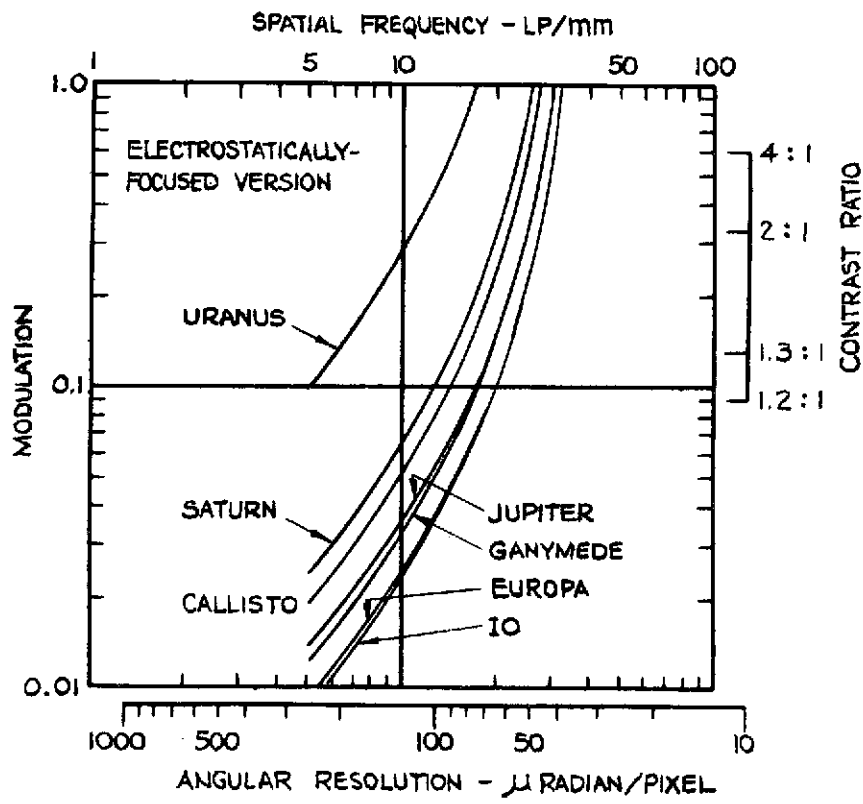
FIELD OF VIEW VERSUS FOCAL LENGTH
FOR DIFFERENT CAMERA FORMATS

Figure 8-7

8.3.4 PERFORMANCE AT JUPITER AND ITS SATELLITES

Performance curves are presented in this section for the selected camera systems at Jupiter and the Galilian satellites. The analysis is later extended to Saturn and Uranus to show the applicability of the systems to other outer planet missions.

Modulation curves for two versions of the SEC vidicon are shown in Figure 8-8. Performance curves are presented for the standard SEC vidicon with electrostatic focusing and also for a high-performance SEC vidicon with electromagnetic focusing and without a suppressor mesh. The suppressor mesh is a necessary component to prevent destruction of the SEC target when operating in a continuous mode. However, by operating the tube sequentially and keeping the scanning beam off when the photocathode is being exposed, the suppressor mesh can be eliminated. In Figure 8-8, the contrast ratio (and relative response) is plotted as a function of angular resolution for the various celestial bodies. Curves are plotted for a nominal spin rate of 5 rpm assuming a zero-degree phase angle, 90%-effective IMC, an exposure time of 0.0005 sec., an f/4 lens with a 400-mm focal length, a bandwidth of 1300 Hz and a constant SNR of 10 based on the reconstructed image. For a contrast ratio of 1.3:1 the electrostatically focused version of the SEC vidicon is shown to resolve about 68 μ radian/pixel at Jupiter. The electromagnetically-focused SEC vidicon configuration without suppressor mesh will resolve about 50 μ radian/pixel under identical conditions.



$t_e = 0.0005$ SEC
 $F = 400$ MM
 $f = 4$
 $SNR_L = 10$
 SPIN RATE = 5 RPM

PHASE ANGLE = 0°
 BANDWIDTH = 1300 HZ
 BASED ON RECONSTRUCTED IMAGE SNR
 WITH 90%-EFFECTIVE IMC

SEC VIDICON SYSTEM MODULATION CURVES

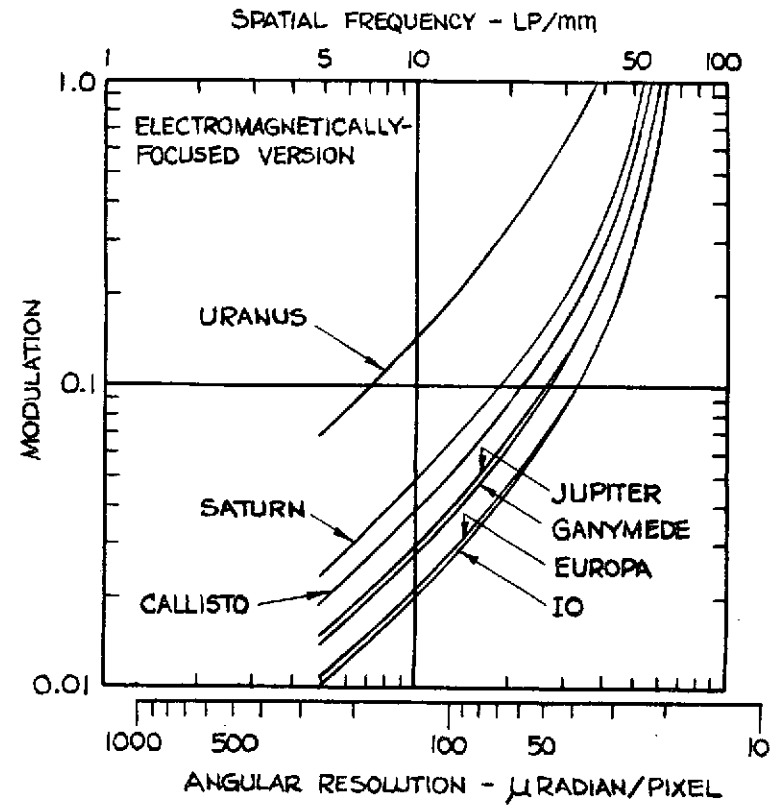
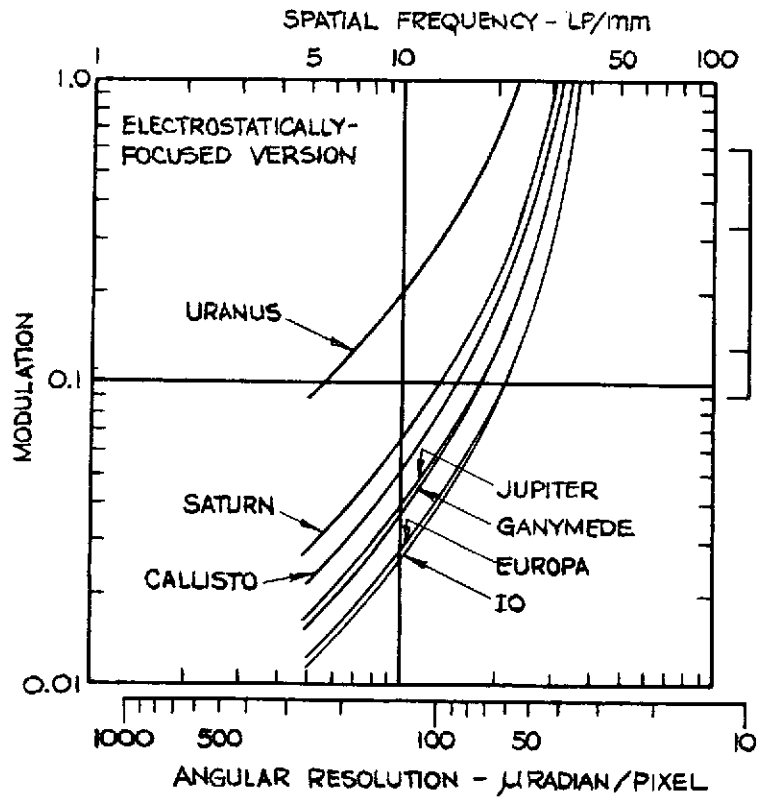
Figure 8-8

Note that the performance curves in Figure 8-8 can be modified for other values of constant SNR if desired. For example, if threshold modulation curves are desired for a SNR of 3, simply multiply the relative response curve by the ratio of the two SNRs (0.3).

Similar modulation curves for the electrostatic storage camera are shown in Figure 8-9. Both an electrostatically-focused configuration and a high-performance electromagnetically-focused version with a 10 μ diameter read beam are analyzed. For a contrast ratio of 1.3:1 the resolution at Jupiter is 54 μ radian/pixel and 41 μ radian/pixel for the electrostatically- and electromagnetically-focused versions respectively.

Figure 8-10 shows modulation curves under identical conditions for the intensified charge-coupled device with both types of focusing. A resolution of 62 μ radian is obtained at Jupiter for a contrast ratio of 1.3:1 using electrostatic focusing. Electromagnetic focusing improves the performance and results in a resolution of 45 μ radian/pixel.

It is interesting to note that, in these applications, performance is generally limited by system parameters external to the sensor, and therefore operation is limited to a narrow performance range. Factors such as the uncompensated image smear, the short exposure time, and the image contrast limit the performance of the sensors. A comparison of Figures 8-8 through 8-10 shows that the performance of the ICCD and ESC are quite similar. The SEC vidicon does not perform as well as the other two, although its performance is adequate for the mission being considered.

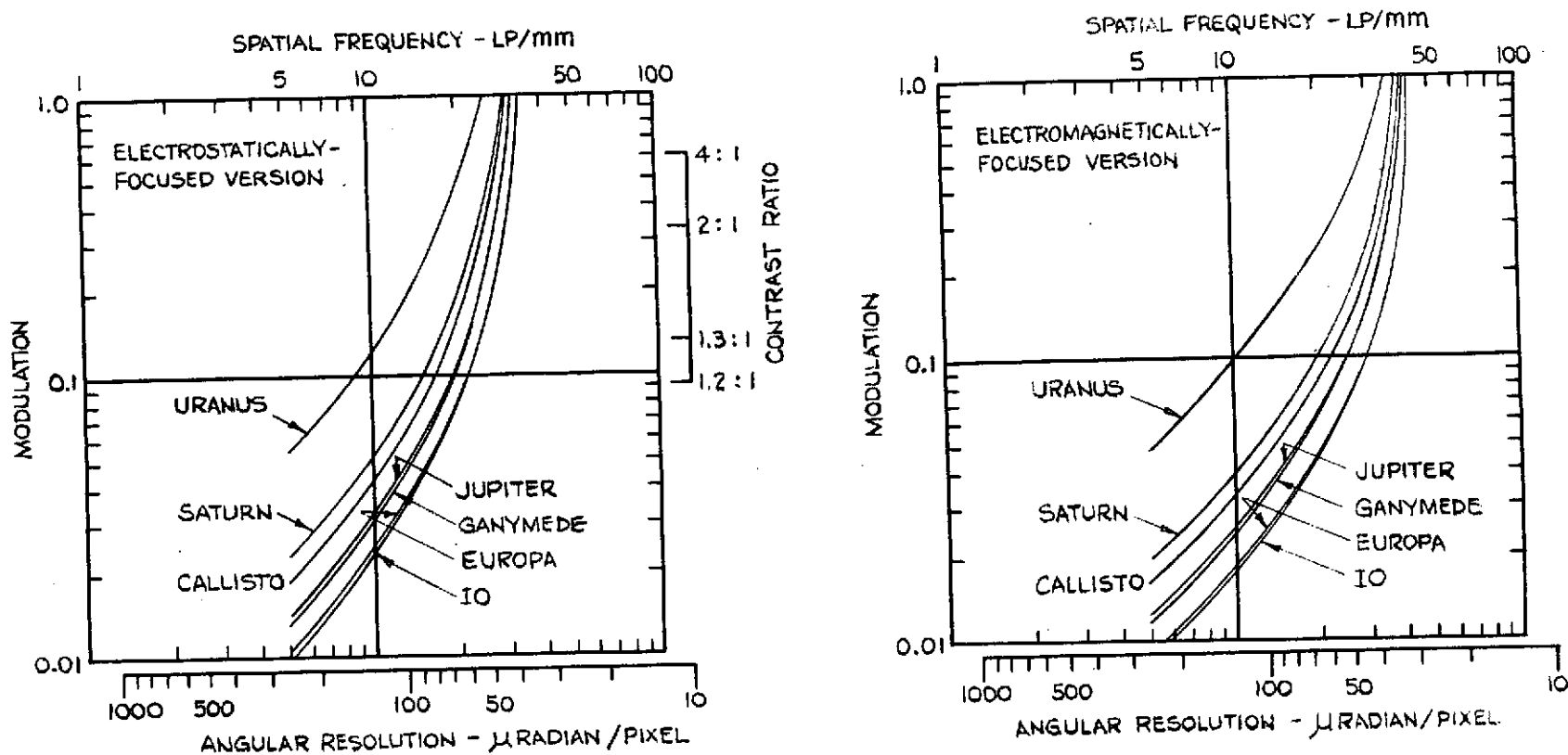


$t_e = 0.0005$ SEC
 $F = 400$ mm
 $f = 4$
 $SNR_L = 10$
 SPIN RATE = 5 RPM

PHASE ANGLE = 0°
 BANDWIDTH = 1300 HZ
 BASED ON RECONSTRUCTED IMAGE SNR
 WITH 90%-EFFECTIVE IMC

ELECTROSTATIC STORAGE CAMERA SYSTEM MODULATION CURVES

Figure 8-9



$\tau_e = 0.0005$ SEC
 $F = 400$ MM
 $f = 4$
 $SNR_L = 10$
 SPIN RATE = 5 RPM

PHASE ANGLE = 0°
 BANDWIDTH = 1300 HZ
 BASED ON RECONSTRUCTED IMAGE SNR
 WITH 90%-EFFECTIVE IMC
 TARGET COOLED

INTENSIFIED CHARGE - COUPLED DEVICE MODULATION CURVES

Figure 8-10

8.3.4.1 Satellite Encounters - Encounters with Jupiter's major satellites - Io, Ganymede, and Europa - have been considered, and camera performance at Callisto was also analyzed. Performance curves for the selected sensors at these satellites are shown in Figures 8-8 through 8-10. As we would expect, the performance at the satellites is quite similar to that at Jupiter. Differences are mainly the result of the different satellite albedos.

An important consideration in photographing the satellites of Jupiter is the amount of time available to take pictures due to the encounter trajectories involved. Let us look, for example, at the encounter with the satellite Io during the spacecraft's second orbit of Jupiter (after the phasing orbits). The spacecraft would be within $1.8 R_J$ of Io, the closest distance at which full-disk pictures can be obtained, for about 4 hours. Conditions satisfactory for photography (when the phase angle is less than 60°) would last for about 2 hours. During this period, all three of the selected camera systems are capable of satisfactorily photographing the satellites and producing a number of pictures. Approximately 30 to 40 photographs could be taken, assuming a 700 line x 700 pixel format and a 16,384-bit/sec telemetry rate.

When multispectral photographs of the satellite surface are to be taken, the ESC offers an advantage. Because of its unique bulk storage capability, it can expose a sequence of pictures in rapid succession, each at a different spectral band, and transmit them back to Earth afterwards. Contiguous ground coverage over several spectral bands can be achieved in this manner over a wide resolution range from close-up shots to full-disc

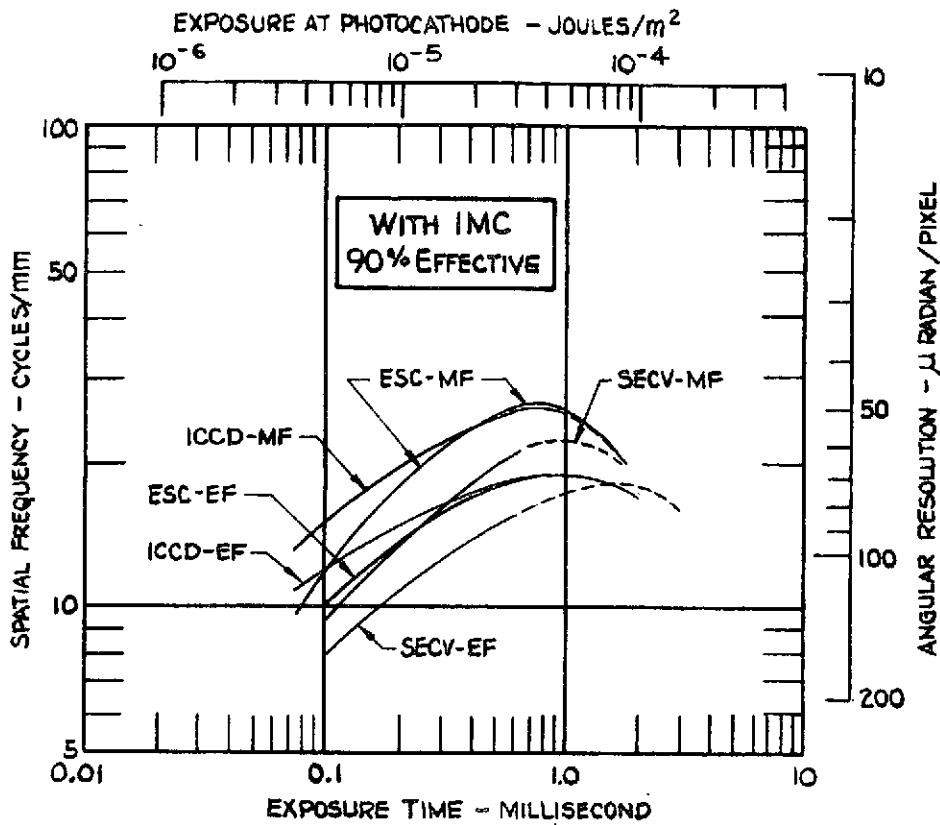
photographs. The ICCD and SEC vidicon, which must transmit each picture before another can be taken, would require a tape recorder to obtain similar coverage over several different spectral bands.

8.3.5 RESOLVING POWER VERSUS EXPOSURE

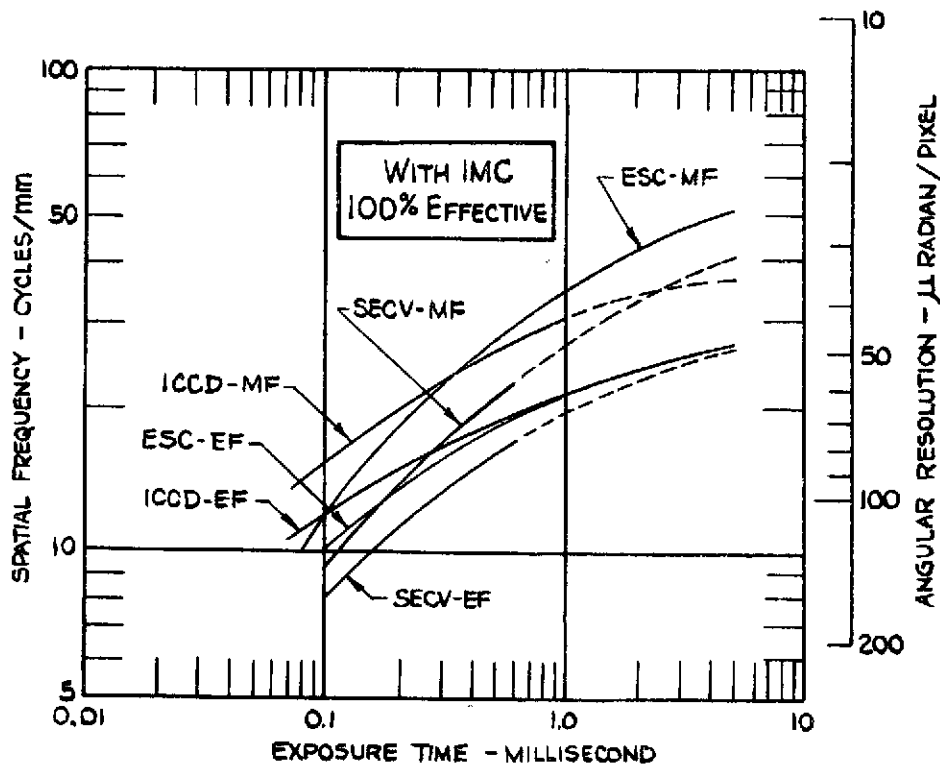
Performance curves are presented in Figure 8-11 showing resolution as a function of exposure time at Jupiter. Curves for the three selected camera systems are given for comparison. Electromagnetically-focused cameras are included. Currently-available IMC subsystems which provide compensation for ninety percent of the motion due to the spacecraft spin are used in Figure 8-11a. We see that as the exposure time is increased, each sensor reaches a point of maximum performance. The resolution then begins to drop off as the smear due to image motion becomes excessive. Both the ICCD and ESC perform better than the SEC vidicon. IMC systems can probably be developed for this mission which would compensate for up to 99% of the relative motion⁽²⁸⁾. For comparative purposes, Figure 8-11b shows the ideal, 100%-effective IMC case.

8.3.6 CAMERA PERFORMANCE VERSUS ORBITAL TIME BEFORE PERIAPSIS

Figure 8-12 shows the performance which may be achieved using systems designed around the selected sensors. Resolution is given in terms of the maximum ground resolution, assuming a contrast ratio of 1.3:1 at an SNR of ten. The resolution is shown as a function of approach time and phase angle, with the optical axis pointed toward the planet's center.

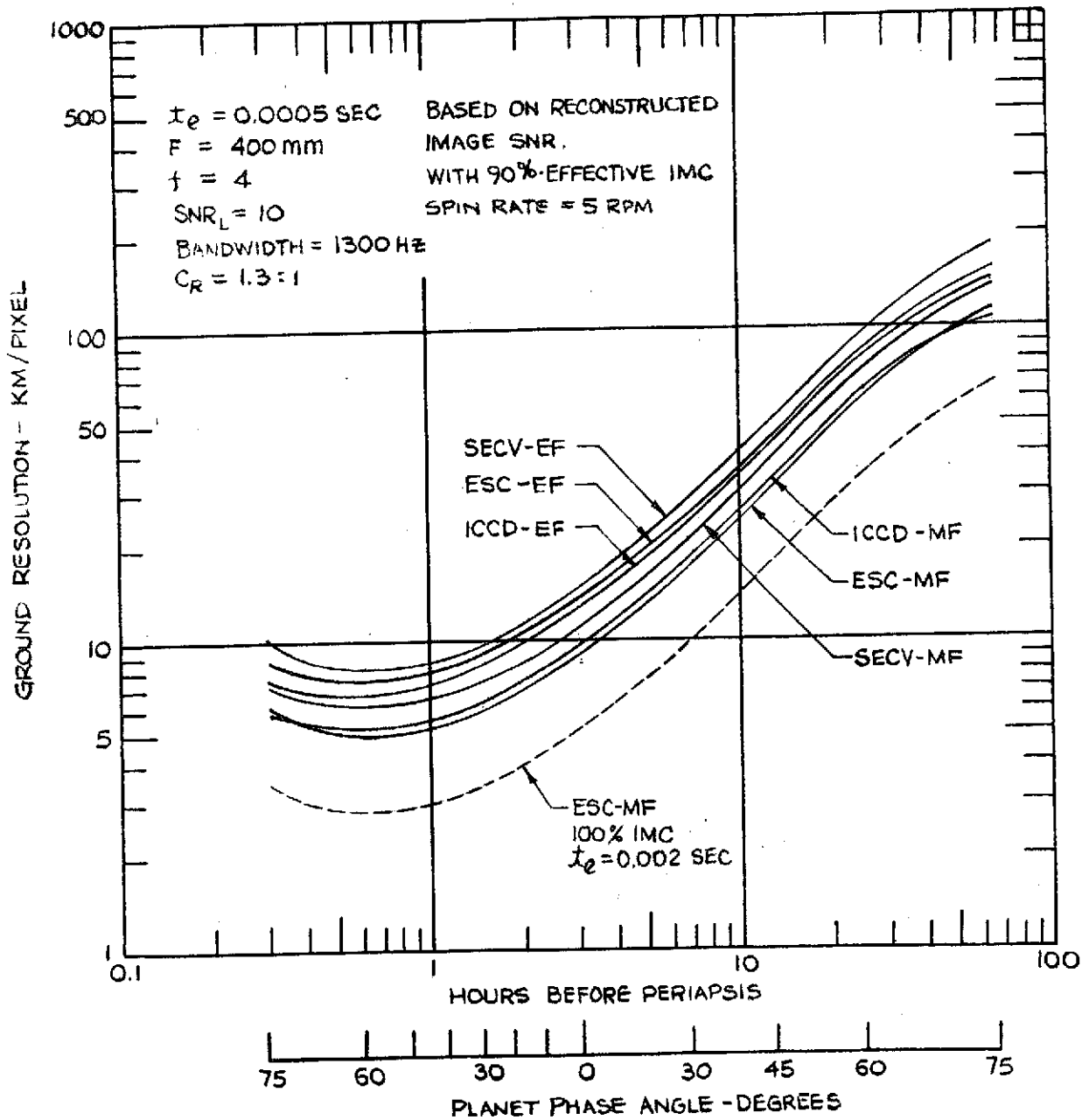


SPIN RATE = 5 RPM
 PLANET JUPITER
 $C_R = 3.1:1$
 $F = 400\text{mm } f = 4$
 $SNR_L = 10 \quad \theta = 60^\circ$
 BANDWIDTH = 1300 HZ
 BASED ON SNR OF RECONSTRUCTED IMAGE
 $\Delta\lambda = 0.3 - 0.95 \mu\text{m}$



RESOLVING POWER VERSUS EXPOSURE

Figure 8-11



CAMERA PERFORMANCE CHARACTERISTICS
 FOR 2.29 x 45.1 R_J JUPITER ORBITER

Figure 8-12

8.4 OTHER OUTER PLANET MISSIONS

8.4.1 SATURN AND URANUS

Although the scope of this analysis addresses a specific Jupiter orbiter mission, the suitability of the selected sensors for other outer planet missions is also an important consideration. Performance curves presented in Figures 8-8 through 8-10 include the planets Saturn and Uranus to illustrate the feasibility of using the selected sensors without changing the basic design. The analysis is applicable to both flyby and orbiter missions.

The planet Saturn is 9.54 AU from the sun and has an albedo of about 0.61. Compared to Jupiter, Saturn reflects approximately a third as much light. Even under these reduced lighting conditions, the performance of all the cameras is still adequate. Using the SEC vidicon with electrostatic focusing as an example (see Figure 8-8), a resolution of 90 μ radian/pixel is obtainable at a 1.3:1 contrast ratio. The other sensor configurations have better performance.

Uranus is twice as far from the sun as Saturn at a mean distance of 19.2 AU. Therefore, since its albedo is 0.42, or approximately the same as Jupiter, the planet reflects only about 7% as much light. Referring to the SEC vidicon with electrostatic focusing operating under the conditions of Figure 8-8, the low-contrast performance drops off rapidly. A scene contrast ratio of 4:1 (as compared to 1.3:1 at Saturn) is required to resolve

90 μ radian/pixel at an SNR of 10. Performance can be improved by increasing the exposure time to 1 millisecond, however, performance then decreases sharply because of image smear. The largest diameter optics that are practical within the mission weight constraints are preferred at Uranus to maximize the illumination at the image plane of the camera.

It is doubtful that pictures will be transmitted from Uranus using the same telemetry support equipment as the Jupiter mission. Even at X-band frequencies, with the inherent increase in communication-link gain, slower data-transmission rates will probably be required, depending on the transmitter power. However, the performance curves for Uranus are calculated using a video bandwidth of 1300 Hz to allow comparison with the performance at other planets.

8.4.2 BEYOND URANUS

Neptune and Pluto orbit beyond Uranus at mean distances of 30.1 and 39.4 AU respectively. The light reflected from Neptune is only 2.5% of that reflected from Jupiter, while that from Pluto is only about 0.005% as much. Communication distances are approximately 5.8 and 7.6 times longer than for Jupiter. It is apparent that missions to these planets will impose much more stringent demands on the camera and communications system than the Jupiter orbiter.

For these planets, camera systems with high quantum efficiency and high inherent target gain must be used to compensate for the limited illumination. This is essential because the maximum exposure time is limited by the image motion. By modifying camera parameters, both the electrostatic storage camera and the ICCD can probably produce modest results at Neptune. Obtaining good pictures of Pluto from a spinning spacecraft will be difficult, as much longer exposure times will be required.

Because of the vast distances and long data transmission time involved, the need for auxiliary storage increases as missions extend to the outermost planets. Camera systems with tape recorders, or imagers such as the ESC with integral bulk storage, become essential if a significant number of pictures are to be obtained.

8.4.3 FLYBY MISSIONS

Many other outer planet missions will be of the "flyby" type rather than planetary orbiters. These missions take advantage of favorable planetary alignments by using the gravity-assist flyby technique to explore two or more planets. For example, the Mariner Jupiter/Saturn Mission scheduled for 1977 uses this technique. The Pioneer type spin-stabilized spacecraft will also eventually be used for flyby missions to several planets. Undoubtedly, the same limited data transmission and storage capabilities of the Pioneer spacecraft that apply for the Jupiter orbiter will also impose limitations on the two-planet flybys. As communications distances lengthen and the available illumination at the distant planets

decreases, data storage and transmission limitations become more important. An auxiliary storage system becomes a necessity in order to insure sufficient data return.

Of all of the camera systems studied, only the electrostatic camera system contains a built-in storage capability to store more than one picture. It is capable of taking at least 30 pictures during a planetary flyby and then transmitting the sequence of pictures to Earth after the encounter. At the outer planets, other camera systems such as the SEC vidicon and ICCD would require an auxiliary storage system to achieve the same picture-gathering capability.

8.5 CONCLUSIONS

The three selected camera systems all perform satisfactorily when applied to the $2.29 \times 45.1 R_J$ Jupiter orbiter mission. Ground resolution of less than 10 km can be achieved at Jupiter near periapsis for the conditions selected.

When photographing the satellites of Jupiter, the three selected camera systems all perform satisfactorily. If multispectral pictures are to be taken with filters over several color bands, the ESC offers an advantage because of its multiframe storage capability.

The selected cameras appear suitable for missions to Saturn and Uranus without any major design changes. The low-contrast capability of the sensors begins to deteriorate when missions to Uranus are considered, more so with the SEC vidicon than the others.

Performance appears to be limited more by other system parameters than the sensors, particularly for the high-performance electromagnetic configurations. If the camera parameters were not dominated by factors such as image smear, even higher-performance versions could be constructed. However, the need for such systems is not required for the Jupiter orbiter mission.

SECTION IX
DESIGN STUDY AND TECHNOLOGICAL ASSESSMENT

9.1 SUMMARY

This task presents the preliminary design configurations for each of the three imaging systems chosen in Section 7. These systems are the SEC Vidicon Camera, the Electrostatic Storage Camera, and the Intensified Charge-Coupled Device. Sketches of each system are given with estimated dimensions. A functional block diagram of each system has also been prepared showing the interrelationship between the various parts. The weight and power requirements of each system are then presented as a function of the different performance options available for each system.

Specific equipment such as lenses, mechanical image motion compensation, heating and cooling equipment, and data storage equipment will not be specified due to the large number of choices available and the resulting changes in weight and power requirements. However, representative nominal weights and power consumption will be used to illustrate trade-off options and to calculate the total weight and power consumption of the camera system.

9.2 PERIPHERAL EQUIPMENT

This section will investigate the necessary equipment other than the imaging sensor and electronics. This includes optics, shutter, filter wheel, image motion compensation, thermal control, and data storage. Each of these items will be investigated to determine possible options and nominal weight, power and volume requirements.

9.2.1 OPTICS

The aperture diameter and focal length of the lens system are constrained by the field of view, the resolution desired, and the weight limitation. For the sensors and orbits being considered in the study, maximum and minimum sizes of the optics are given below:

	<u>Aperture Diameter</u>	<u>Focal Length</u>
Maximum:	150 mm	600 mm
Minimum:	100 mm	200 mm

These systems are both capable of giving diffraction-limited resolution over the proper field of view.

Weights and volumes for the optics can be found from studies done by Slater and Johnson⁽²⁹⁾ and Bashe and Kennedy⁽³²⁾. Slater and Johnson studied the

weights of a variety of space optical systems as a function of the collecting aperture diameter. With 21 datum points, the dependence was approximated by

$$M_c = 168 D_c^2 \quad (9-1)$$

where M_c is the mass of the optical system in kilograms, and D_c is the diameter of the collecting optics in meters.

This data can be verified by comparing it to that obtained by Bashe and Kennedy. Since this latter study is not confined to space-qualified optical systems, the weights are slightly higher than those found in the former study. The weights as a function of aperture size are given below.

	Bashe and Kennedy		Slater and Johnson
	<u>Refractive</u>	<u>Catadioptric</u>	<u>(all types)</u>
150 mm aperture	7.0 kg.	4.5 kg	3.8 kg
100 mm aperture	2.0 kg	1.5 kg	1.7 kg

Other data for optical system weights based on unknown sources have been used in reference 2. A portion of that table has been reproduced below for systems with 0.61-m (24-inch) focal lengths. (See Table 7-1 also)

150-mm aperture (catadioptric): 8.6 kg

100-mm aperture (catadioptric): 4.1 kg

These seem somewhat high compared to the system values found in Slater and Johnson. In the following analysis, the data of Slater and Johnson will be used.

The volume of the optics can be approximated by a right circular cylinder of diameter $1.1 D_s$ and length $1.1 F$, where D_s is the collecting lens diameter, and F is the focal length. The equation for the volume of the cylinder is then

$$\text{Volume} = 1.05 D_s^2 F \quad (9-2)$$

which yields the following volumes:

<u>Aperture</u>	<u>Focal Length</u>	<u>Volume</u>
150 mm	600 mm	0.014 m ³
100 mm	200 mm	0.002 m ³

9.2.2 SHUTTER AND FILTER WHEEL

Two types of shuttering will be investigated here. The first is conventional mechanical shuttering and the second is electronic shuttering within the sensor itself.

There are two basic types of mechanical shutters: leaf and focal plane. Both have been used in space missions, the main difference being that the focal plane shutter can achieve shorter exposure times, with a minimum of about one millisecond. A shutter of this type was used on the Mariner 6 and 7 narrow-angle TV camera. It weighed 140 grams, was 89 mm in diameter and 28 mm thick. (33)

The main disadvantage of mechanical shuttering is that, due to the rotational speed of the spacecraft, very short exposure times are needed to avoid halation and smear. Minimum exposure times of 0.1 millisecond are needed for fast rotation speeds if the pictures are to be smear-free, because even the image motion compensation systems are only 90% to 95% effective.

Electronic shuttering, or gating, has been demonstrated with electrostatic-focus SEC tubes.⁽³⁴⁾ A grid is installed ahead of the target in the image section of the tube. A small (15 - 20 volt) negative swing on this grid is sufficient to cut off the arriving photoelectrons from the photocathode. Gating speeds much faster than the one-millisecond limit for mechanical shutters can be attained using relatively simple circuitry. In addition, the gating mesh can be put into any sensor utilizing an intensifier, such as the ICCD or the ESC or the SEC vidicon, with very little loss of MTF.

Unfortunately, the electronic gating has two main disadvantages. First, it is impossible to stop all of the arriving photoelectrons, since the spaces in the gating mesh need to be big enough to cause very little transmission loss when the shutter is open. Consequently, the maximum attenuation possible with the electronic gating is on the order of 10^4 .⁽³⁵⁾ This could cause ghosting or smear with bright targets. The second

disadvantage is that the gating mesh has its own electric field when it is on, and hence could be a possible cause of distortion. At present, no SEC tubes with a gating electrode and magnetic lens have been made and tested, so further investigation is needed to realize the full value of electronic gating.

In summary, electronic shuttering development should be accelerated if the short exposure time necessary for the Jupiter orbiter mission is to be achieved. The fastest mechanical shutters still provide about twice the desired exposure. Perhaps a hybrid scheme would eliminate most of the ghosting while still allowing fast exposure times. Another all-electronic method might involve reducing the intensifier voltage between exposures.

A filter wheel is often included with a shutter for making color composites or multispectral pictures. It consists of a stepping motor and a wheel with several openings covered with glass color filters large enough to clear the light path from the lens to the sensor. The proper filter is stepped into position immediately before the exposure. The total weight of the filter wheel and stepping solenoid is about 100 grams.

Electrical power requirements for small accessories such as the shutter and filter wheel are estimated to be 0.1 watt each.

9.2.3 IMAGE MOTION COMPENSATION

Section 6 demonstrated that image motion compensation is necessary perpendicular to the spacecraft axis of rotation. The other components of image motion (e.g., due to the platform unsteadiness and the rotation of the planet) were shown to be negligible.

There are two separate aspects of the IMC problem. First, a device is needed to sense the rotational speed of the spacecraft. Second, another device is needed to translate the data from the IMC sensor into the proper amount of compensation and to apply that compensation to the image tube.

As mentioned in Section 6, the image motion sensor could be eliminated by preprogramming the correction into the image tube. For an orbiter close to the surface of the planet, where ground speed would also be a factor, a standard V/H sensor could be used. For the $2.29 \times 45.13 R_J$ orbit, however, the image tube could also be used in a star-tracker mode to sense the rotation speed.

The IMC could be applied to the image tube by means of a rotating or oscillating mirror, or in the case of a tube with an image intensifier section it could be applied electronically. Other methods involving rotating lenses and prisms⁽³⁶⁾ may offer significant savings in weight, power, and volume, but are not yet part of the state of the art. Design formulas for oscillating scanning mirrors are given in references 25 and 28. Multifaceted mirrors are unnecessary due to the slow rotation speed and are much too heavy.

Representative values of the mass, power, and volume required for an oscillating mirror have been calculated from these formulas as a function of aperture diameter.

Oscillating Mirror Only

	<u>Mass</u>	<u>Power</u>	<u>Volume</u>
100 mm aperture	.69 kg	3.4 watts	$5.7 \times 10^{-4} \text{ m}^3$
150 mm aperture	2.3 kg	25.9 watts	$1.9 \times 10^{-3} \text{ m}^3$

Klopp et al summarize weight and power data for several space-qualified IMC assemblies. They estimate that a complete single-direction mechanical IMC system with nodding mirror and V/H sensor should weigh 6.8 kg, occupy 0.013 m^3 , and consume 15 watts of power.

Since all of the sensors under consideration have an image section, fully electronic IMC may represent a feasible alternative. In this method, an electromagnetic deflection yoke or electrostatic deflection plates are mounted on the image section of the tube and are used to deflect the image in the proper direction as the spacecraft rotates. This system would utilize an angular velocity sensor, suitable electronics, and, in the electrostatic case, a modified image section.

Advantages of this system include fewer mechanical parts, simplified camera construction and alignment, and a much wider range of scanning speeds. Weight and power requirements should be much less than for the mechanical IMC, especially for large-diameter collecting optics.

The primary disadvantage of the electronic IMC is the lack of space-qualified systems, although similar systems have been used in aircraft camera systems. However, the electronic IMC has greater mechanical simplicity, along with savings in power, weight and volume over mechanical IMC. For this reason the electronic IMC is the best choice, in spite of the extra development needed. For this report, the weight, power and volume of an electronic IMC system in a star-tracker mode or using a V/H sensor are estimated to be 2 kg, 6 watts, and 0.05 m³.

9.2.4 THERMAL CONTROL

The ICCD camera has one significant drawback for the outer planet missions. Due to the slow data transmission rates and the relatively high dark current of the silicon, either the ICCD will have to be cooled to approximately -60°C, or else a tape recorder will have to be included in the system. This section will examine the weight and power impact of the thermal control.

Several different types of cooling apparatus are available, but few can be efficiently used to achieve such low temperatures. Thermoelectric cooling is feasible, but may require several stages. Other solutions utilize active fluid loops such as heat pipes or pumped, closed-loop systems.

A radiative cooler design proposed for Nimbus uses a radiative horn weighing one-half pound to dissipate 20 milliwatts. The horn size of 6 inches on a side gives a radiator area of 5 square meters per watt to cool to 135°K. For a radiative cooler capable of dissipating 300 mW, the Nimbus figures can be scaled up to:

Weight	3.4 kg
Volume	0.05 m ³

However, due to the spinning spacecraft, cooling efficiencies may be further reduced, since the radiator will be exposed to the sun during part of each revolution.

Reference 28 gives a table of IR Detector Cooling Scaling Coefficients for pumped, closed-loop coolers. By increasing the detector temperature from 80°K to 160°K, the scaling coefficients for 300 mW of sensor power dissipation become:

Electrical Power Consumption	10 watts
Weight	0.7 kg
Volume	0.007 m ³

Klopp et al give an approximate sensor power dissipation of $500 A_s$ milliwatts where A_s is the area of the sensor in m^2 . For a CCD one inch on a side, the power is 323 mW, which agrees with the values for the above tables. The power consumption and weight given in the table will be used for the cooler parameters in the trade offs.

The main problem with both the radiative horn and the closed-cycle systems is that they are still not part of the state of the art and need more development, although the radiative cooler seems to have more potential for the Jupiter orbiter mission. Due to the long distance from the sun, any effects of spacecraft rotation on the radiator efficiency will be minimized. The closed-loop system would have a much lower reliability than the radiator due to the presence of moving parts alone.

9.2.5 DATA STORAGE

The alternative to using a cooler for the ICCD is an onboard data storage medium capable of holding at least one frame of information. Since the ICCD would have at least 500 resolution elements on a side, the data storage must be able to handle about 300,000 pixels x 6 bits/pixel, or about 2 megabits of information per frame. This could be accomplished with a MOS read-write memory or a tape recorder.

The present state of the art in semiconductor memories corresponds to 4096 bits per chip, with each chip requiring about 400 mW⁽³⁷⁾. To store one frame, however, 488 chips would be required, which would consume almost 200 watts of power — far too much.

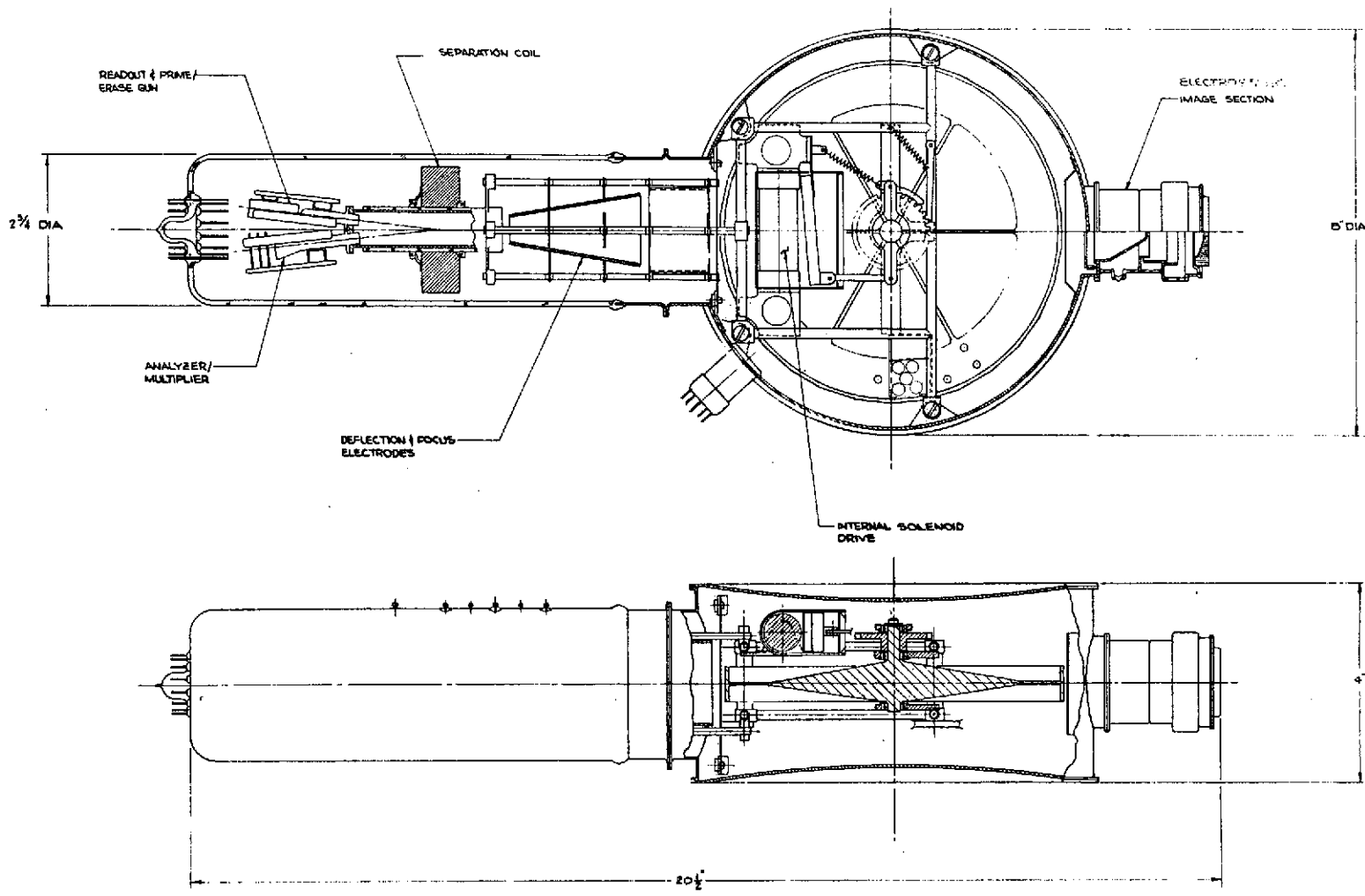
A study of tape recorders⁽²⁾, however, shows that several flight-qualified recorders are available with capacities as large as 10^8 bits. The weight of these recorders is about 4.5 kg, the volume is about $9.8 \times 10^{-3} \text{ m}^3$, and the total power requirement is about 10 watts. This is certainly the better data storage option.

9.3 BASIC SENSOR PARAMETERS

9.3.1 ELECTROSTATIC CAMERA SYSTEM⁽³⁸⁾

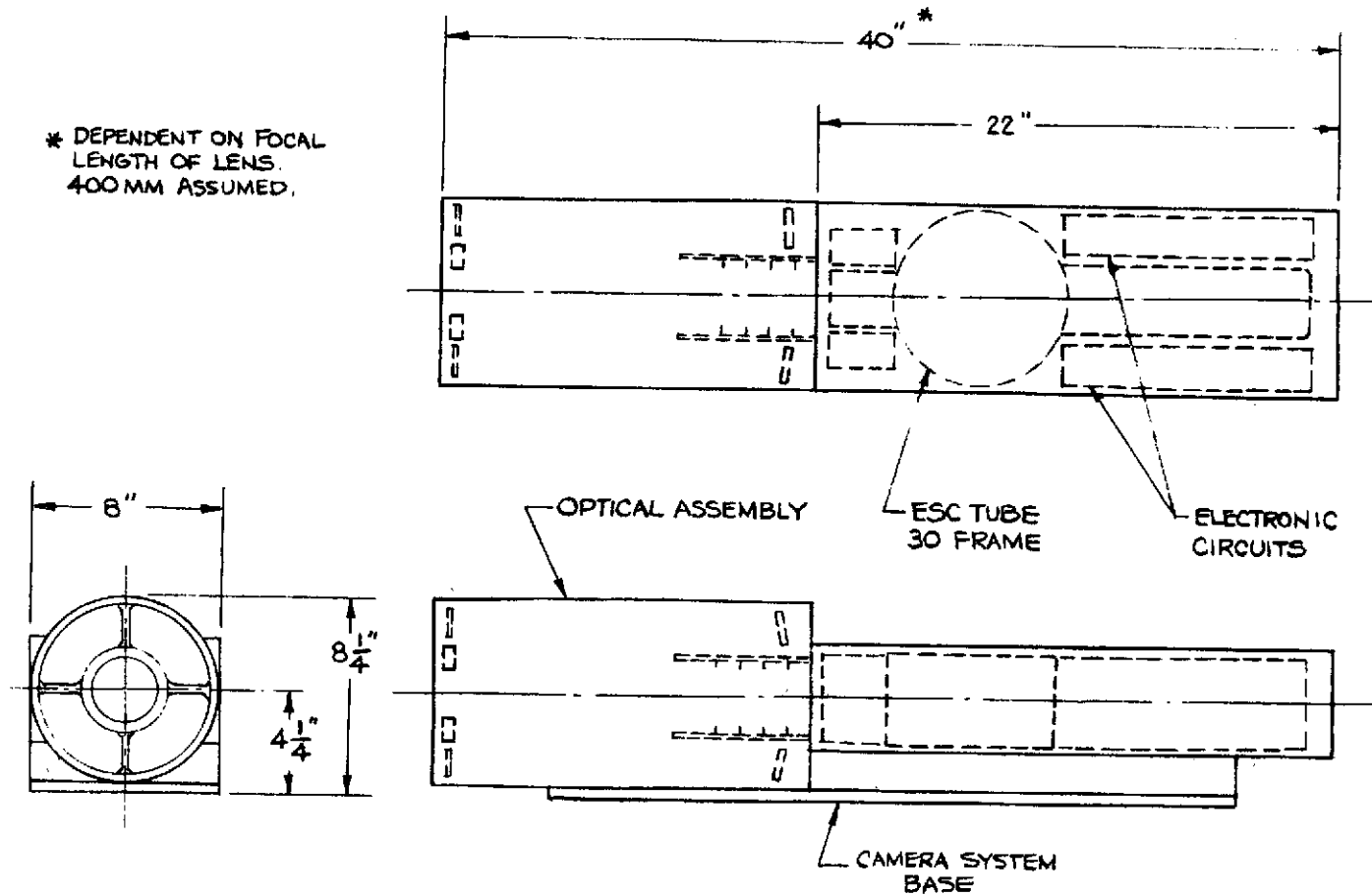
The basic camera tube for the Jupiter orbiter framing camera would utilize a multifaceted drum as the storage medium. Up to 30 frames 16 mm on a side could be stored at one time, and the time between exposures would be limited only by the stepping time of the target. A diagram of the ESC tube is shown in Figure 9-1, a possible camera packaging configuration is shown in Figure 9-2, and a block diagram of the system is shown in Figure 9-3.

System performance can be changed by substituting an electromagnetic-focus image section for the electrostatic one shown in Figure 9-1. This results in a weight and power decrease, which is shown in Table 9-1 along with the decrease in MTF. Both the electromagnetic- and electrostatic-focusing configurations are currently available technologies. An alternative which



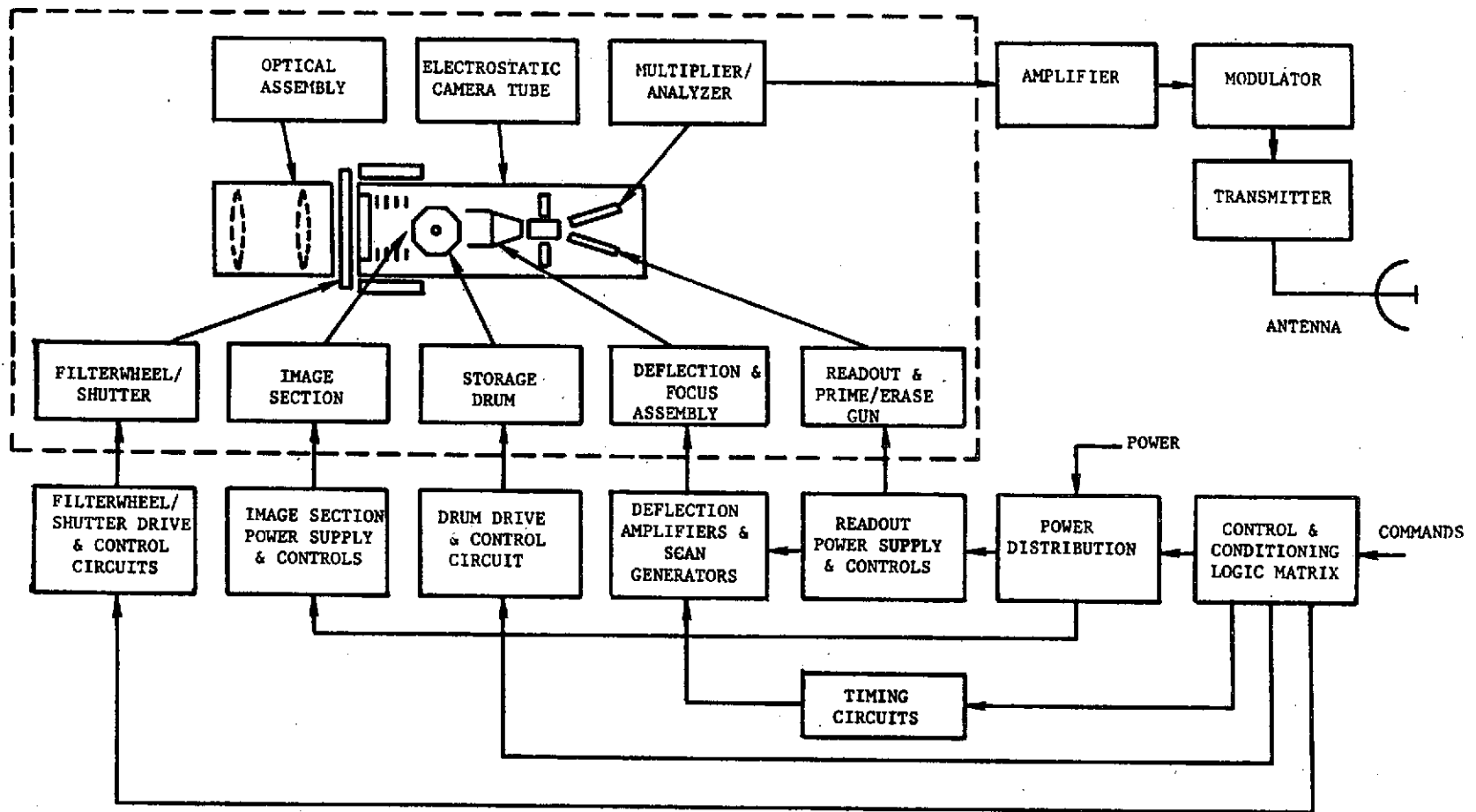
ELECTROSTATIC STORAGE CAMERA TUBE
30 FRAME STORAGE

Figure 9-1



ELECTROSTATIC STORAGE CAMERA PACKAGING CONFIGURATION

Figure 9-2



ELECTROSTATIC STORAGE CAMERA
SIMPLIFIED BLOCK DIAGRAM

Figure 9-3

TABLE 9-1

30 - FRAME ELECTROSTATIC CAMERA PARAMETERS

Parameter	Electrostatic Focus	Electromagnetic Focus	
		Aluminum Coil	Permanent Magnet
<u>Weight:</u>			
Camera Head	7.2 kg	8.4 kg	8.4 Kg
Cables & Electronics	3.0 kg	3.6 kg	3.0 kg
	10.2 kg	12.0 kg	11.4 kg
<u>Power:</u>			
Average*	18.6 watts	20.0 watts	18.5 watts
Peak	22.8 watts	34.6 watts	21.8 watts
<u>Advantages:</u>	Sensor MTF 20% at 30 lp/mm	Sensor MTF 20% at 68 lp/mm	

*10% duty cycle of the image section

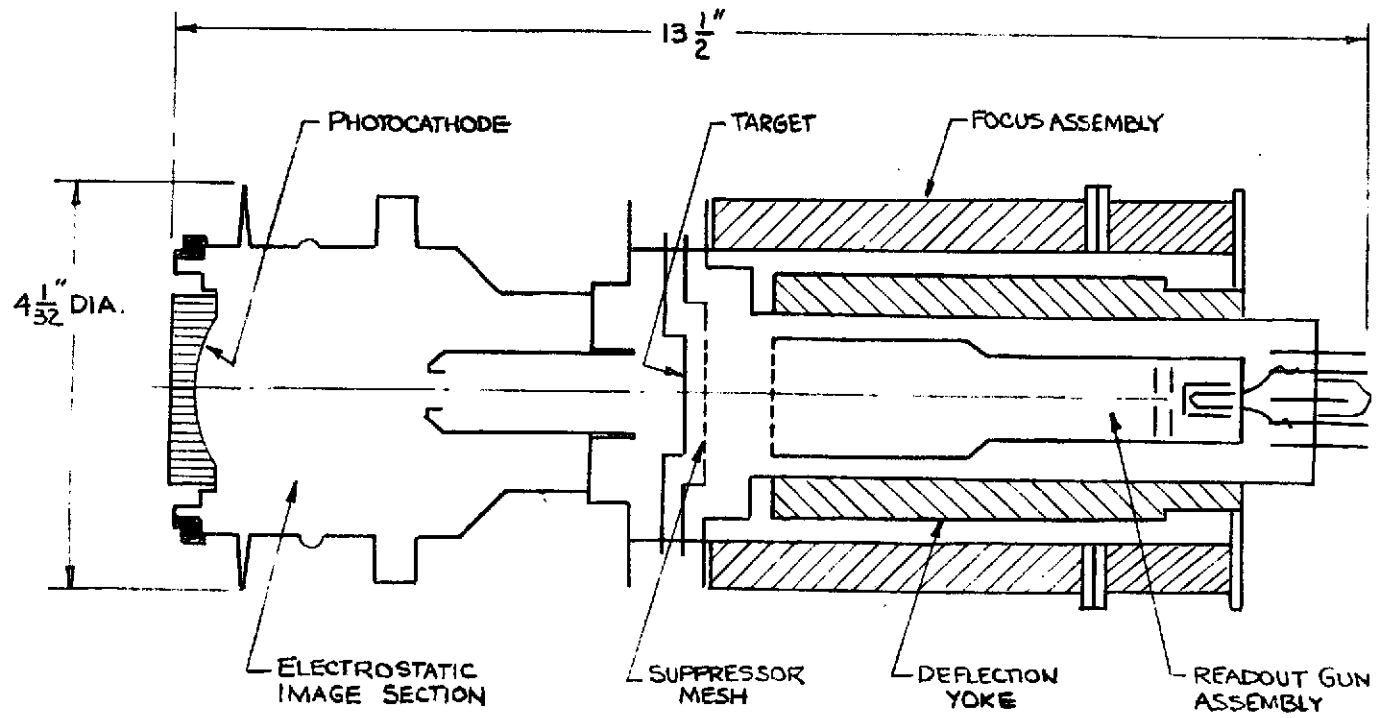
would decrease the weight and the power consumption of the electromagnetically-focused design but still retain the high MTF would be a permanent-magnet focusing section.

CBS Laboratories has constructed a permanent-magnet focusing module⁽³⁹⁾ that provides the proper field, yet uses no power. The weight and volume are less than that of an aluminum-wire coil used for electromagnetic focusing.

9.3.2 SEC VIDICON

A space-qualified SEC vidicon camera has been described previously⁽⁵⁾ and will form the basis of this study. In its original form, the camera utilized a one-inch-diagonal tube with an electrostatic image section. The basic system has been examined both with electrostatic - and electromagnetic-focus SEC tubes and with a permanent-magnet focus module. A picture of a typical SEC tube is shown in Figure 9-4, a proposed packaging configuration for the SEC vidicon camera is shown in Figure 9-5, and a simplified block diagram of the camera is shown in Figure 9-6. The various performance and weight trade-offs are shown in Table 9-2.

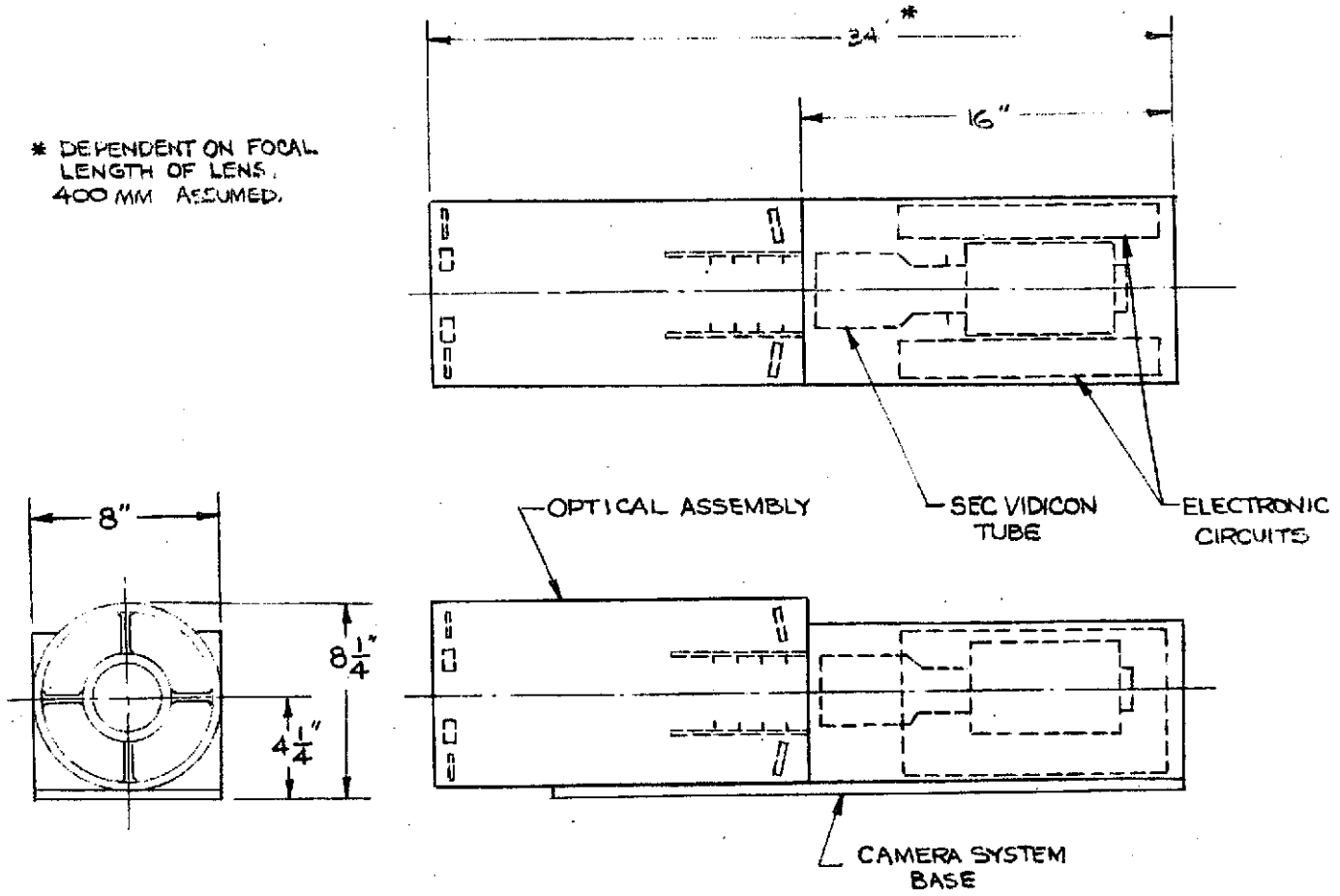
This tube is capable of storing one frame of information in slow-scan operation unless a tape recorder or memory unit is used. For this analysis, one-frame storage is assumed to obtain the minimum weight and power and maximum reliability.



SEC VIDICON CAMERA TUBE

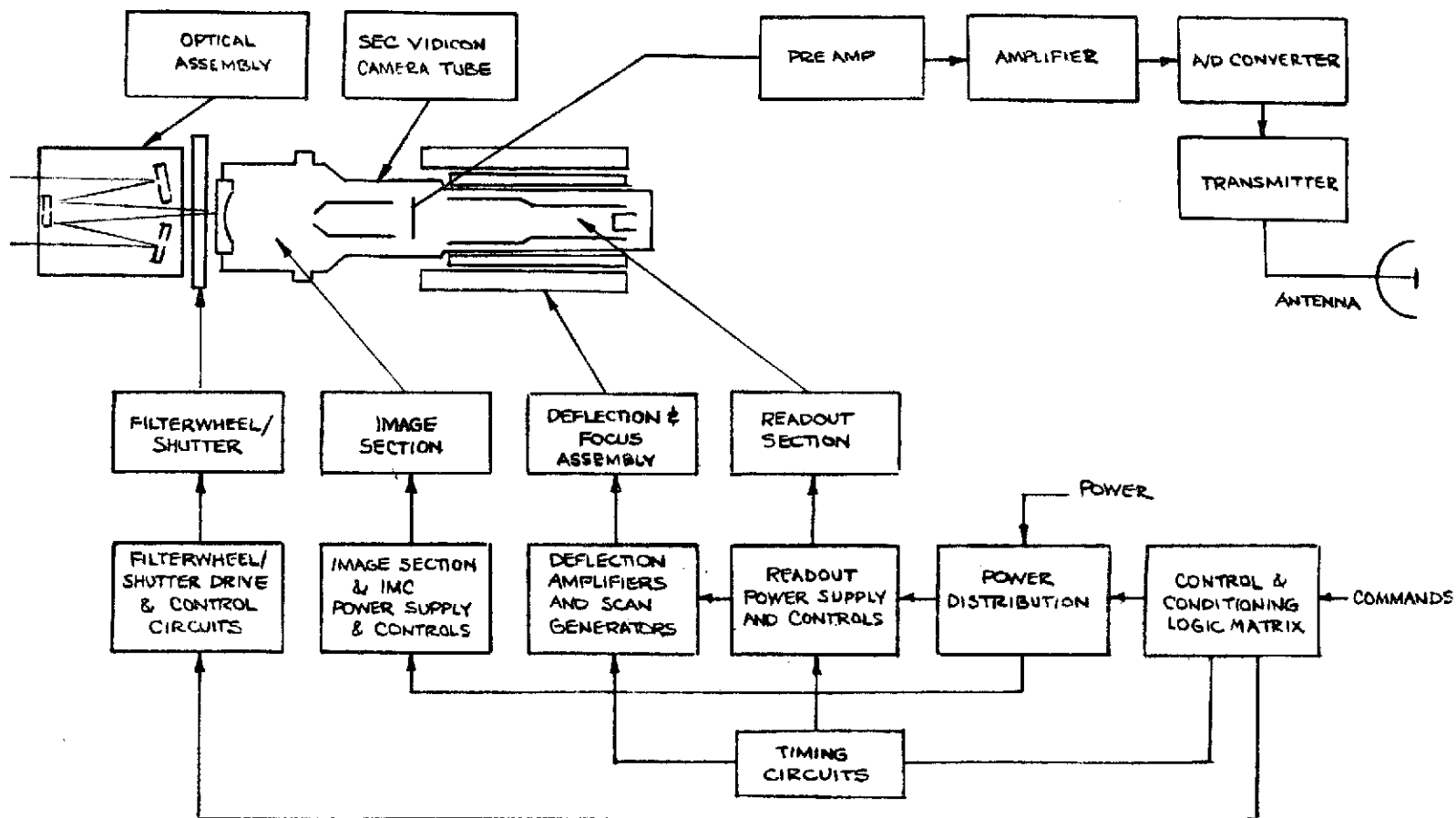
Figure 9-4

* DEPENDENT ON FOCAL LENGTH OF LENS, 400 MM ASSUMED.



SEC VIDICON CAMERA PACKAGING CONFIGURATION

Figure 9-5



SEC VIDICON CAMERA
SIMPLIFIED BLOCK DIAGRAM

Figure 9-6

TABLE 9-2

SEC VIDICON CAMERA PARAMETERS

Parameter	Electrostatic Focus	Electromagnetic Focus	
		Aluminum Coil	Permanent Magnet
<u>Weight:</u>	6.8 kg	8.6 kg	8.0 kg
<u>Power:</u>			
Average*	10.0 watts	11.2 watts	9.5 watts
Peak	10.0 watts	21.8 watts	9.5 watts
<u>Advantages:</u>	Sensor MTF 20% at 17 lp/mm	Sensor MTF 20% at 28 lp/mm	

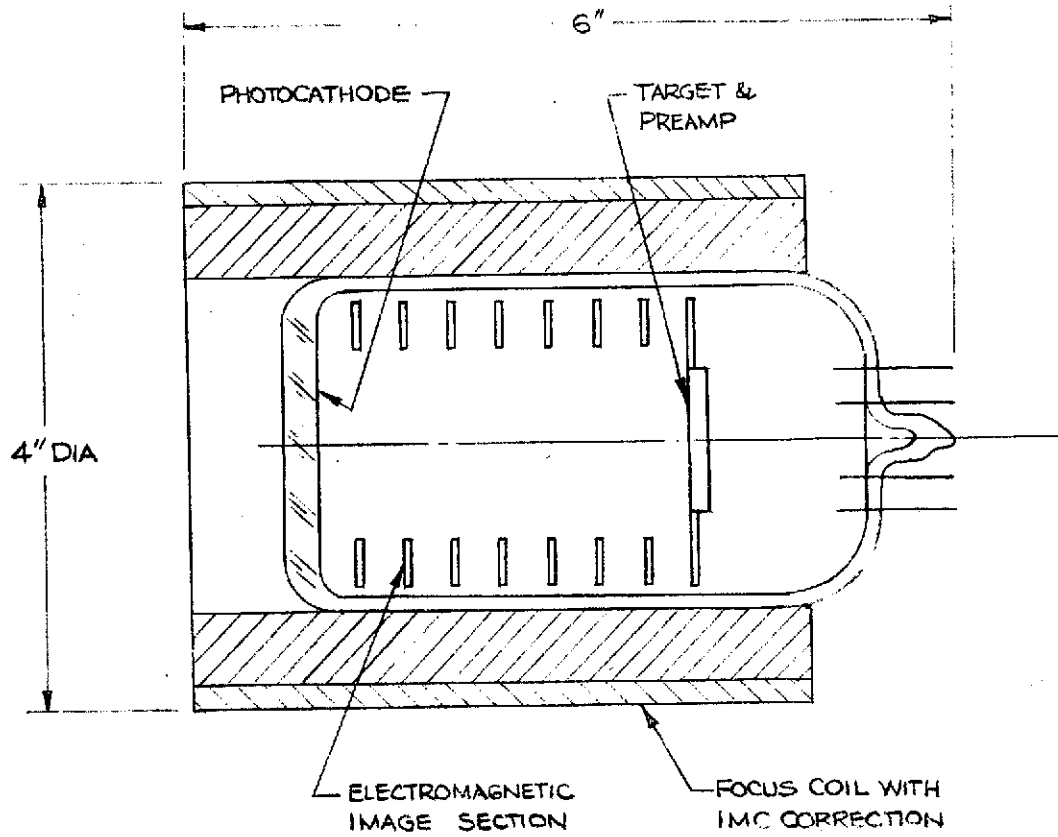
* 10% duty cycle of the image section.

9.3.3 INTENSIFIED CHARGE-COUPLED DEVICE CAMERA

The ICCD camera is significantly smaller and less complicated than either of the other two systems. Its main drawback is that it must be cooled for slow-scan operation or have a memory unit. Both the control electronics and the high voltage supplies are simpler than those for the other camera systems. No filament supply is needed, and high voltages are needed for the intensifier only. A schematic of the device is shown in Figure 9-7, a proposed packaging configuration in Figure 9-8, and a simplified block diagram in Figure 9-9.

As in the other cameras, the ICCD image section can be focused electrostatically, electromagnetically, or with a permanent magnet module. Table 9-3 shows the weight and performance tradeoffs anticipated using each of these options. These figures are probably more conservative and have a larger probability of error than those for the other two cameras. This is because the ICCD, even more than the CCD, is still in the laboratory experiment stage, and the circuitry is still being developed. The MTFs given in the table were obtained from the camera models and represent the resolution expected for an array with 20 μm element spacing.

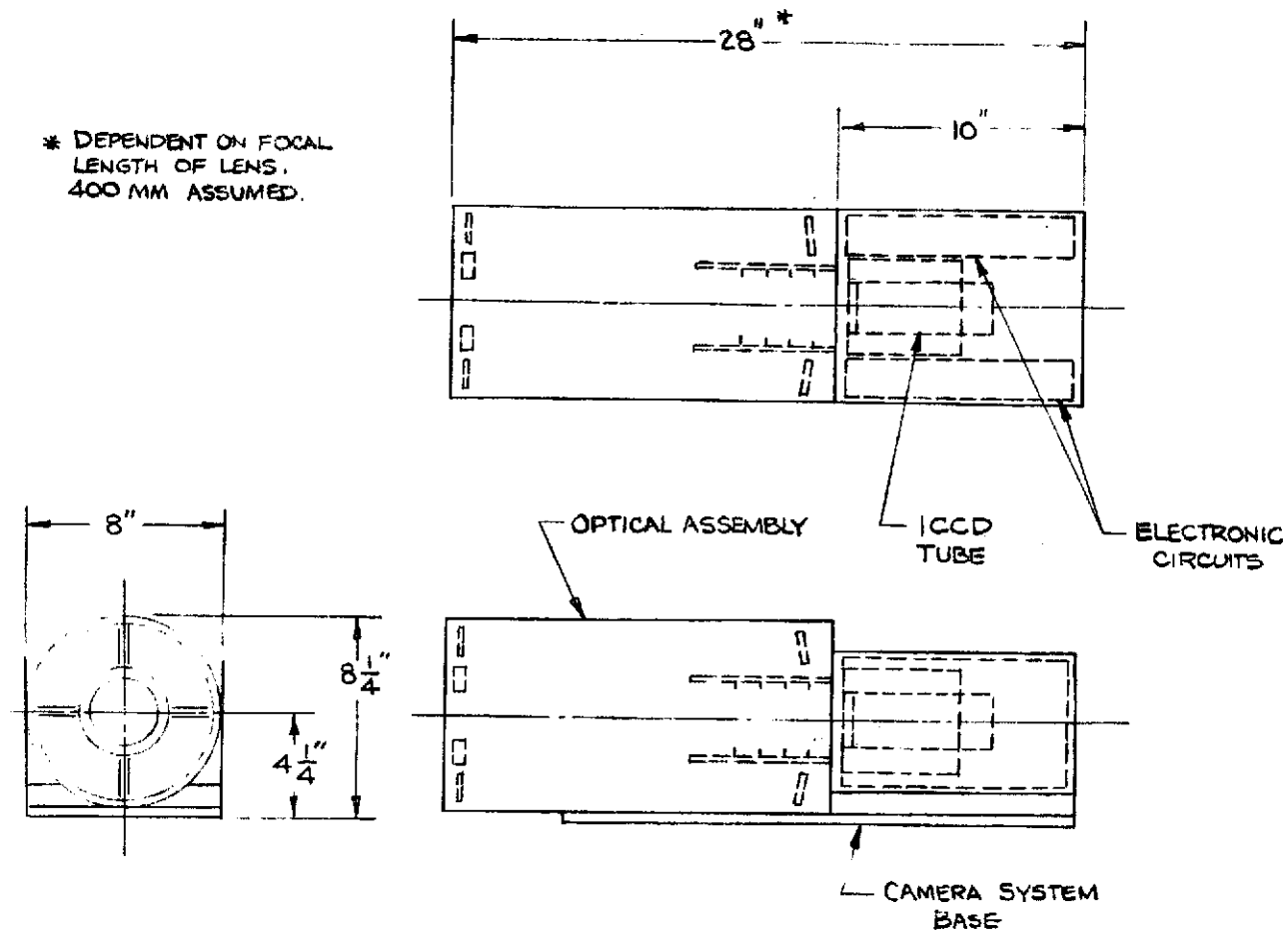
181



INTENSIFIED CHARGE - COUPLED DEVICE

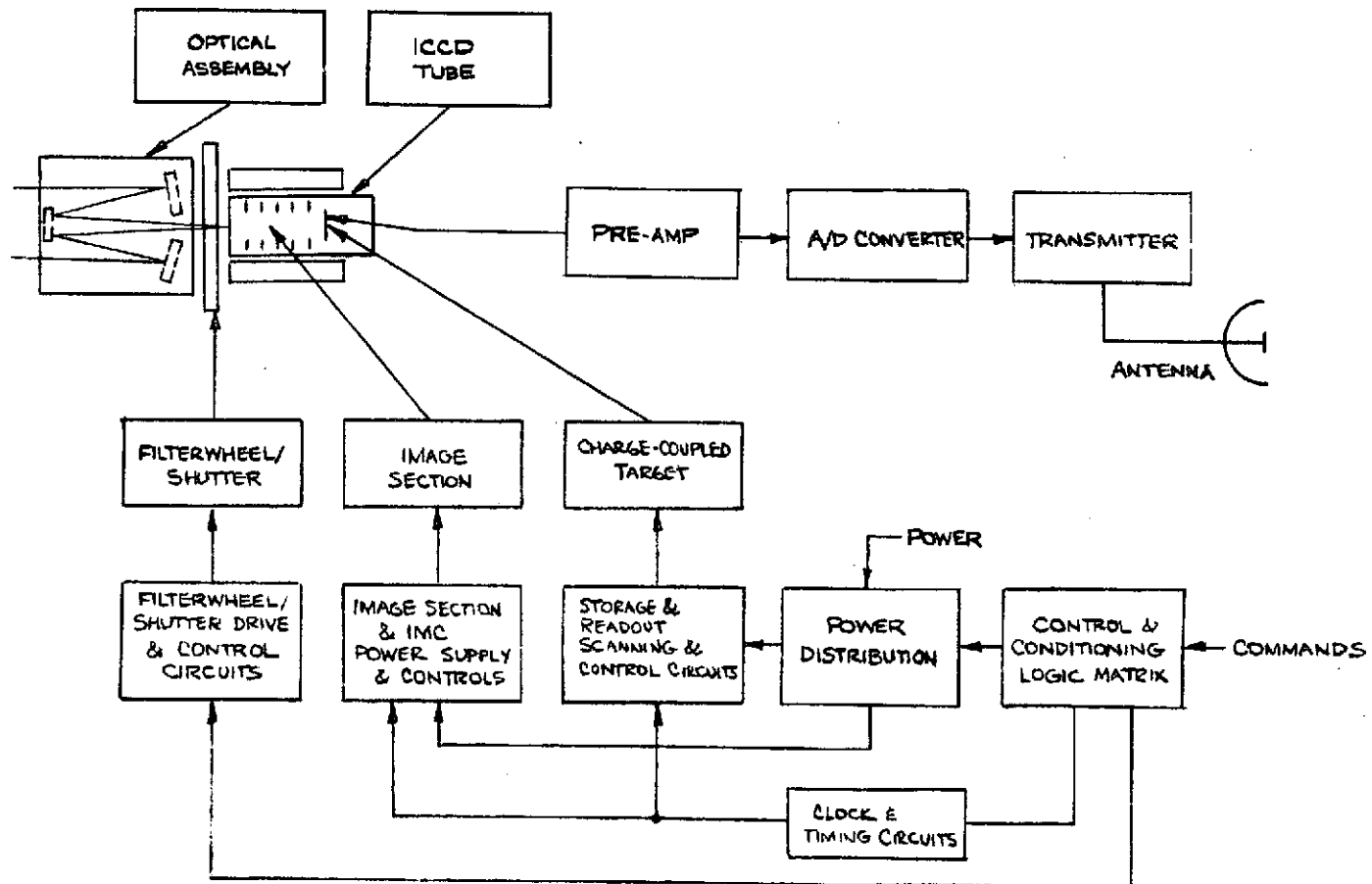
Figure 9-7

3



INTENSIFIED CHARGE - COUPLED CAMERA PACKAGING CONFIGURATION

Figure 9-8



INTENSIFIED CHARGE - COUPLED CAMERA
SIMPLIFIED BLOCK DIAGRAM

Figure 9-9

TABLE 9-3

ICCD CAMERA PARAMETERS

Parameter	Electrostatic Focus	Electromagnetic Focus	
		Aluminum Coil	Permanent Magnet
<u>Weight:</u>	2.7 kg	3.9 kg	3.2 kg
<u>Power:</u>			
Average*	5.0 watts	6.4 watts	5.0 watts
Peak	5.0 watts	16.8 watts	5.0 watts
<u>Advantages:</u>	Sensor MTF 20% at 24 lp/mm	Sensor MTF 20% at 34 lp/mm	

*10% duty cycle of the image section.

9.4 CAMERA SYSTEM TECHNOLOGICAL ASSESSMENT

9.4.1 SENSOR DEVELOPMENT: STATE OF THE ART

The three sensors chosen for the Jupiter orbiter mission are in various stages of development. Only the Westinghouse-manufactured SEC vidicon is currently a production item. Several models of these tubes are space qualified, and they have been flown on many missions.

The electrostatic storage camera is still in the developmental stage. Over the past several years, CBS Laboratories has funded several in-house research and development programs to test the basic image sensing and storage concepts. As a result, all of the basic components have been successfully built and debugged, and a complete camera tube is now being assembled to demonstrate system performance.

Although the basic charge-coupled device is currently being sold in sample quantities, it is not yet in a form suitable for space qualification. Several companies, notably General Electric and Fairchild, are manufacturing row arrays and small area arrays. However, more development work is needed in several problem areas, namely increased array size, elimination of blemishes, uniformity of photoresponse, and increased transfer efficiency. Adequate sensitivity, once a problem, has been accomplished by placing a low-noise preamplifier directly on the sensor substrate. It appears to be only a matter of time before the rest of these problems are satisfactorily resolved.

9.4.2 MISSION PARAMETERS

Each sensor can have many possible combinations of the peripheral equipment discussed in Section 9.2. However, it is important to carefully define the mission requirements so that the different systems can be compared. Whatever the mission, each camera needs a shutter, filter wheel, diffraction-limited optics, and associated electronics. For the Jupiter orbiter mission, the need for IMC has been established.

In Tables 9.4 through 9.6, each sensor is presented in several possible configurations, together with weight and power requirements. The items necessary for the Jupiter orbiter mission requirement listed above have been selected, and the total weight and power of that system has been calculated. A section describing each of the systems follows the tables. Tradeoff charts are then given for various entire systems.

9.4.2.1 Electrostatic Camera System - The components picked for the ESC system are shown in Table 9.4. The total estimated system weight is 17.45 kg (38.44 lbs.). The average power usage is 24.8 watts. If it is necessary to further cut the weight, the 100-mm lens can be used, reducing the total weight to 15.35 kg (31.81 lbs.). Both lenses are diffraction-limited, but the larger lens would be best suited for high-resolution photographs in the low incident light.

TABLE 9-4

ELECTROSTATIC STORAGE CAMERA SYSTEM CONFIGURATIONS

OPTION LIST			
Alternative Configurations	Approx. Weight	Average Power	Benefit
①. Basic 30 Frame ESC Tube and Electronics (Electrostatic Focus)	10.2 Kg	18.6 W	Additional ground coverage at satellites and during flyby missions.
a. Electromagnetic Focus with Focus Coil	+1.8 Kg	+1.4 W	Higher resolution than with Electrostatic Focus. See Figure 8-9.
b. Electromagnetic Focus with Permanent Magnet	+1.2 Kg	-	High resolution with some additional weight and no power penalty. Needs development.
2. 100 mm Optics	1.7 Kg	-	
③. 150 mm Optics	3.8 Kg	-	Larger diameter optics have greater light gathering ability and improved SNR. Penalty of added weight and volume.
4. Mechanical Shutter	.14 Kg	0.1 W	
⑤. Electronic Shutter	.15 Kg	0.1 W	Both shutters require development. Electronic shutter will be more reliable and will provide shorter exposures.
6. Mechanical IMC	6.8 Kg	15 W	
⑦. Electronic IMC	2.0 Kg	6.0 W	Electronic IMC will be more reliable and will weigh less. However, it must be developed.
⑧. Filter Wheel	0.1 Kg	0.1 W	
SYSTEM TOTAL: (Circled Options)	17.45 Kg	24.8 W	

Several parts of the ESC system in addition to the basic tube need some further development before they are flight-qualified. Most important is the electronic shutter for the electromagnetic image section. A mechanical shutter is just too slow to take non-smearing pictures from a spinning spacecraft. In addition, an electronic shutter would probably have higher reliability. So far the electronic shutter has only been used on tubes with electrostatic image sections.

The permanent-magnet image section is attractive because of its high reliability, low weight and zero power consumption. Although prototypes of this device have been made and tested, further development work is needed before a space-qualified version is ready.

The most attractive feature of the ESC is its internal storage capability. Instead of utilizing a 4.5 kg, 10 watt tape recorder with its many moving parts and subsequently low reliability, the ESC employs an integral, silicon-dioxide coated drum rotated by a stepping motor.

9.4.2.2 SEC Camera System - The components picked for the SEC camera system are shown in Table 9.5. The total estimated system weight is 14.05 kg (30.95 lbs.). The average power usage is 16.2 watts.

All the comments relating to the lens, shutter, and image section of the ESC system in Section 9.4.2 also apply here. The basic difference is that the SEC camera does not have a multiframe internal storage capability (a tape recorder would be required to store more than one picture).

SEC VIDICON CAMERA SYSTEM CONFIGURATIONS

OPTION LIST			
Alternative Configurations	Approx. Weight	Average Power	Benefit
①. Basic Tube and Electronics (Electrostatic Focus)	6.8 Kg	10 W	Basic tube already developed and space qualified.
a. Electromagnetic Focus with Focus Coil.	+1.8 Kg	+1.4 W	Higher resolution than with Electrostatic Focus. See Figure 8-9.
b. Electromagnetic Focus with Permanent Magnet.	+1.2 Kg	-	High resolution with some additional weight and no power penalty. Needs development.
2. 100 mm Optics	1.7 Kg	-	
③. 150 mm Optics	3.8 Kg	-	Larger diameter optics, greater light gathering ability and improved SNR. Penalty of added weight and volume.
4. Mechanical Shutter	.14 Kg	0.1 W	
⑤. Electronic Shutter	.15 Kg	0.1 W	Both shutters require development. Electronic shutter will be more reliable and will provide shorter exposures.
6. Mechanical IMC	6.8 Kg	15 W	
⑦. Electronic IMC	2.0 Kg	6.0 W	Electronic IMC will be more reliable and will weigh less. However, it must be developed.
⑧. Filter Wheel	0.1 Kg	0.1 W	
9. Tape Recorder	4.5 Kg	10 W	
SYSTEM TOTAL: (Circled Options)	14.05 Kg	16.2 W	

The advantage of the SEC is that it has been successfully used a number of times in flight hardware. Thus there would be less unknowns in this approach than in the other two.

9.4.2.3 ICCD Camera System - Due to the integrated-circuit-type sensor, the ICCD is the lowest-weight and lowest-power system of the group. The components of the system are shown in Table 9.6, and the weight and power are 13.35 kg (29.41 lbs.) and 11.2 watts, respectively.

All the comments in Section 9.4.2 concerning the development of the basic device, the electronic shutter, optics, and image section apply here also. The main problem in using the ICCD is the method of data storage. Even for one-frame storage, either a radiative cooler or thermal control is needed. Thus, if multi-frame storage is anticipated, it is much more convenient to use a tape recorder and quickly read out the sensor after each exposure.

The big advantage of the ICCD system is its low complexity. Compared to either of the tube systems, it has fewer moving parts and less electronic equipment. Its main drawback is the short storage time of the silicon necessitating thermal control or a tape recorder.

ICCD CAMERA SYSTEM CONFIGURATIONS

OPTION LIST			
Alternative Configurations	Approx. Weight	Average Power	Benefit
①. Basic ICCD with Electronics (Electrostatic Focus)	2.7 Kg	5.0 W	Light weight, low power system.
a. Electromagnetic Focus with Focus Coil	+1.8 Kg	1.4 W	Higher resolution than with Electrostatic Focus. See Figure 8-9.
b. Electromagnetic Focus with Permanent Magnet	+1.2 Kg	-	High resolution with some additional weight and no power penalty. Needs development.
2. 100 mm Optics	1.7 Kg	-	
3. 150 mm Optics	3.8 Kg	-	Larger diameter optics have greater light gathering ability and improved SNR. Penalty of added weight and volume.
4. Mechanical Shutter	.14 Kg	0.1 W	
5. Electronic Shutter	.15 Kg	0.1 W	Both shutters require development. Electronic shutter will be more reliable and will provide shorter exposures.
6. Mechanical IMC	6.8 Kg	15 W	
⑦. Electronic IMC	2.0 Kg	6.0 W	Electronic IMC will be more reliable and will weigh less. However, it must be developed.
⑧. Filter Wheel	0.1 Kg	0.1 W	
9. Tape Recorder	4.5 Kg	10 W	
⑩. Radiative Cooler	3.4 Kg	-	
11. Closed-cycle Cooler	.7 Kg	10 W	
SYSTEM TOTAL: (Circled Options)	13.35 Kg	11.2 W	

9.5 CAMERA SYSTEM TRADEOFFS

In previous sections, different camera types were evaluated, along with necessary peripheral equipment for the mission under consideration. The only remaining task is to examine the three complete camera systems chosen and to choose the system that best fits the mission. In this case the systems picked out in Tables 9-4 to 9-6 will be rated, with a choice of either electrostatic or electromagnetic focus. This is because the Jupiter orbiter mission does not require extremely high resolution, and therefore the lower-weight electrostatic system may be more appropriate.

Table 9-7 shows the weight, power, and resolution of the three camera systems chosen for the Jupiter orbiter mission. With the exception of the ESC system, each camera must transmit the previous frame to Earth before the next picture is taken. There is very little difference in resolution between the three systems because they are all performance-limited by the spacecraft spin.

It would be useful if the camera system used on the Jupiter orbiter mission could also be used for other similar missions. Such missions would include outer planet flybys and missions with satellite encounters where multispectral pictures are required. For these missions, it would be important to have some sort of onboard data storage to obtain the desired photographic coverage.

TABLE 9-7

PERFORMANCE TRADEOFFS FOR SELECTED JUPITER ORBITER MISSION

CAMERA	FOCUS	SYSTEM RESOLUTION* (μ rad/pixel)	WEIGHT (kg)	POWER (W)
ESC (30 frames available)	Electrostatic (ES)	72	16.2	24.8
	Electromagnetic (EM)	46	18.0	26.2
	Permanent Magnet (PM)	46	17.4	24.8
SEC	ES	76	12.8	16.2
	EM	59	14.6	17.6
	PM	59	14.0	16.2
ICCD	ES	68	12.1	11.2
	EM	50	13.9	12.4
	PM	50	13.3	11.2

TABLE 9-8

PERFORMANCE TRADEOFFS FOR OTHER OUTER PLANET MISSIONS
REQUIRING MULTIFRAME STORAGE

CAMERA	FOCUS	SYSTEM RESOLUTION* (μ rad/pixel)	WEIGHT (kg)	POWER (W)
ESC (30 Frames available)	Electrostatic (ES)	72	16.2	24.8
	Electromagnetic (EM)	46	18.0	26.2
	Permanent Magnet (PM)	46	17.4	24.8
SEC (With Recorder)	ES	76	17.3	26.2
	EM	59	19.1	27.6
	PM	59	18.5	26.2
ICCD (With Recorder)	ES	68	16.6	21.2
	EM	50	18.4	22.4
	PM	50	17.8	21.2

*For 150-mm lens diameter, 400-mm focal length, 0.25-msec exposure, SNR = 10,
60° phase angle, 1.3:1 contrast, 5-RPM spin rate with 90%-IMC, 1300-Hz bandwidth.

In Table 9-8, each of the Jupiter orbiter cameras is presented, including a data storage capacity of at least 30 frames. For the SEC and ICCD cameras this is accomplished by adding a tape recorder, while the ESC utilizes its internal recording drum. The resolution of each system is again presented, along with the weight and power requirements.

9.6 RECOMMENDED TECHNOLOGY IMPROVEMENTS

Based on the results of this study, a number of suggestions are tendered for further work associated with the camera systems.

- New camera concepts are now being actively investigated by industry. The electrostatic storage camera and charge-coupled imagers are two systems that should be adapted to future outer planet missions. NASA support in funding the development of the ESC and ICCD is clearly indicated by this study. Active support by NASA is recommended in order to speed up the availability of these systems.
- There is a need for additional radiation studies, especially involving low-energy protons, at irradiation levels approximating those expected at Jupiter. There is insufficient experimental evidence available on the susceptibility of the various camera systems to radiation damage.

- Even existing camera systems may require additional developmental work to function adequately on a Jupiter orbiter mission. In particular, the development of new shutters may be required in order to achieve the short exposure times necessary to limit image smear. The need for shutter design improvement will depend on the type of shuttering used, the effectiveness of the IMC system, the type of sensor and other factors. Existing mechanical shutters do not operate well in the required range of 0.0005 to 0.002 seconds and will have to be improved if they are to be used. An electronic shutter incorporated into the image section of the sensor is recommended from a reliability viewpoint. While electronic shutters have been satisfactorily applied to electrostatically-focused sensors, additional work will be required to implement electronic shuttering in electromagnetic-image sections.
- An image motion compensation system is mandatory. Although mechanical image motion compensation systems and associated angular velocity sensors currently used are satisfactory, they are heavy.

Alternative methods of IMC should be investigated, particularly electronic IMC where compensation takes place within the image section of the tube. Alternative methods of sensing the amount of angular compensation required, including pre-programming for fixed amounts of correction, should be analyzed.

SECTION X

COSTS AND DEVELOPMENT SCHEDULES

10.1 INTRODUCTION

This part of the study will investigate the costs and development times associated with the three types of sensors chosen in Section 7. Both an overall cost estimate and a relative cost comparison between the three systems will be supplied. Data on mission operations and data processing will not be included in the cost study. All cost figures should be taken as approximate.

10.2 HISTORIC COST ESTIMATES

Two cost models developed by Goddard Space Flight Center will be used to estimate the system costs. Neither one covers television imaging specifically, but both used together should give a good indication of the magnitude of costs that will be involved. The earliest study,⁽⁴⁰⁾ made in 1966, utilized a data base of 15 optical experiments which were flown on unmanned satellites. The experiments were not mentioned by name, but were defined as requiring "...significant optical elements..."

The second study⁽⁴¹⁾, completed in 1971, covers the costs of "optical, infrared, line scanning (Imaging) radiometer experiments for unmanned satellite missions..." A data base of 12 experiments was used, including the ERTS-A and -B multi-spectral scanners.

Both studies, or cost estimating relationships (CERs), as they are called, use versions of a multiple linear regression program developed by the Health Sciences Computing Facility at UCLA.

10.2.1 INPUTS

The cost data in the models cover the design, development and fabrication of the complete experiment, one prototype and one flight model. The estimating relationships use combinations of parameters that are readily available, such as weight, power, volume, lens size, and data rate. The inputs for each of the systems used are given in Table 10-1 below.

TABLE 10-1
INPUTS USED IN COST ESTIMATING RELATIONSHIPS

ITEM	ESC	SECV	ICCD
Field of view	33.7 mrad	33.7 mrad	33.7 mrad
Data Rate (6 bits/word, 1 channel)	16384 BPS	16384 BPS	16384 BPS
Average Power	33.3 watts	24.2 watts	30.2 watts
Lens Diam.	100 mm	100 mm	100 mm
Focal Length	400 mm	400 mm	400 mm
Path Tolerance	25 μ	25 μ	25 μ
Scan Mirror Area	450 mm ²	450 mm ²	450 mm ²
Weight	17.8 kg	15.9 kg	16.3 kg
Volume	0.028 m ³	0.026 m ³	0.031 m ^{3*}

*Includes tape recorder since the model does not specifically provide for cooling.

10.2.2 CER RESULTS

The 1966 study produced much higher costs than the 1971 study, probably due to its emphasis on optical components. The only such components on the three imagers discussed here are the lens system and scan mirror. For these CERs, the mechanical IMC described in Section 9.2.3 is used since there is no provision for electronic IMC. The estimated costs for the three systems are given below:

	AVERAGE COST	<u>67% CONFIDENCE BAND</u>	
		HIGH	LOW
ESC	\$4.6M	\$6.2M	\$3.4M
SEC	\$4.3M	\$5.7M	\$3.2M
ICCD	\$4.4M	\$6.0M	\$3.3M

The 1971 study used a slightly different method of estimation and, as stated earlier, based the results on more analogous types of equipment. The average and high and low costs from this study were:

	AVERAGE COST	HIGH	LOW
ESC	\$1.4M	\$2.7M	\$0.7M
SEC	\$1.3M	\$2.1M	\$0.7M
ICCD	\$1.4M	\$2.5M	\$0.7M

10.2.3 MAXIMUM CER INPUTS

To get an idea of what the maximum cost of a camera system might be, the CERs were exercised again using the largest values of the parameters, even though each of these systems would be far too heavy for the Jupiter orbiter mission.

TABLE 10-2: MAXIMUM INPUTS TO THE CERS

ITEM	ESC	SEC	ICCD
Field of View	50 mrad	50 mrad	50 mrad
Data Rate	16384 BPS	16384 BPS	16384 BPS
Average Power**	35.2 W.	26.4 W.	31.4 W.
Lens Diam.	150 mm	150 mm	150 mm
Focal Length	600 mm	600 mm	600 mm
Path Tolerance	25 μ	25 μ	25 μ
Scan Mirror Area	1000 mm ²	1000 mm ²	1000 mm ²
Weight**	21.4 kg	19.5 kg	19.1 kg
Volume	0.039 m ³	0.038 m ³	0.043 m ³

*includes tape recorder for the ICCD since the model does not specifically provide for cooling.

**electromagnetic image section with focus coil.

10.2.4 MAXIMUM CER RESULTS

Again, the 1966 report gave much higher values than the 1971 report.

The estimated costs were

	AVG. COST	67% CONF. BAND	
		HIGH	LOW
ESC	\$6.4M	\$10.0M	\$4.7M
SEC	\$6.3M	\$ 8.5M	\$4.7M
ICCD	\$6.2M	\$ 8.4M	\$4.6M

The 1971 study results were

	AVG. COST	HIGH	LOW
ESC	\$1.62M	\$2.96M	\$.82M
SEC	\$1.55M	\$2.81M	\$.75M
ICCD	\$1.56M	\$2.81M	\$.79M

10.3 ENGINEERING COST ESTIMATES

To amplify the results of Section 10.2, engineering estimates of the cost of each camera system have been made⁽⁴²⁾. Included in the breakdown are costs of the design and breadboarding, engineering model, prototype model, bench test equipment, and one flight model. Mission operations and data processing are not included in the cost figures. Tables 10-3 to 10-5 show the expected costs for the ESC camera, SEC camera, and ICCD camera, respectively.

It should be emphasized that these figures are merely engineering estimates. However, they agree in order of magnitude with cost figures given by people who have managed similar programs for various companies. They do seem more realistic than the results of the CERS.

10.4 COST COMPARISONS

As a quantitative check, the average costs obtained in Section 10.2 from the CERS should be compared with the engineering estimates from Section 10.3. Table 10-6 below summarizes this comparison:

TABLE 10-3
ESC CAMERA COSTS

	Engineering Model	Prototype Model	First Flight Model
Sensor D&D	\$ 450 K	\$ 300 K	-
Sensor Fabrication	\$ 350 K	\$ 200 K	\$ 200 K
Sensor Evaluation	\$ 200 K	\$ 400 K	\$ 200 K
Sensor Equipment	\$ 200 K	\$ 100 K	-
Sensor Mgt. & Q.C.	\$ 150 K	\$ 400 K	\$ 400 K
Electronics D&D	\$ 150 K	\$ 50 K	-
Electronics Fabrication	\$ 100 K	\$ 250 K	\$ 250 K
Electronics Test & Q.C.	\$ 40 K	\$ 100 K	\$ 150 K
IMC & Elec. Shutter	\$ 300 K	\$ 150 K	\$ 50 K
Optics Des. & Proc.	\$ 40 K	\$ 30 K	\$ 30 K
Customer Interface	\$ 200 K	\$ 100 K	\$ 100 K
Subtotals:	\$ 2.18 M	\$ 2.08 M	\$ 1.38 M
TOTAL SYSTEM COST:		\$ 5.64 M	

TABLE 10-4

SEC CAMERA COSTS

	Engineering Model	Prototype Model	First Flight Model
Sensor D&D	-	-	-
Sensor Fabrication	\$ 200 K	\$ 100 K	\$ 50 K
Sensor Evaluation	\$ 50 K	\$ 100 K	\$ 50 K
Sensor Equipment	\$ 100 K	\$ 50 K	-
Sensor Mgt. & Q.C.	\$ 100 K	\$ 200 K	\$ 200 K
Electronics D&D	\$ 100 K	\$ 30 K	-
Electronics Fabrication	\$ 80 K	\$ 150 K	\$ 150 K
Electronics Test & Q.C.	\$ 40 K	\$ 100 K	\$ 100 K
IMC & Elec. Shutter	\$ 300 K	\$ 150 K	\$ 50 K
Optics Des. & Proc.	\$ 40 K	\$ 30 K	\$ 30 K
Customer Interface	\$ 200 K	\$ 100 K	\$ 100 K
	<hr/>	<hr/>	<hr/>
Subtotals:	\$ 1.21 M	\$ 1.01 M	\$.73 M
	<hr/> <hr/>	<hr/> <hr/>	<hr/> <hr/>
TOTAL SYSTEM COST		\$ 2.95 M	

TABLE 10-5

ICCD CAMERA COSTS

	Engineering Model	Prototype Model	First Flight Model
Sensor D&D	\$ 600 K	\$ 400 K	-
Sensor Fabrication	\$ 200 K	\$ 100 K	\$ 50 K
Sensor Evaluation	\$ 200 K	\$ 400 K	-
Sensor Equipment	\$ 400 K	\$ 100 K	-
Sensor Mgt. & Q.C.	\$ 150 K	\$ 200 K	\$ 200 K
Electronics D&D	\$ 100 K	\$ 30 K	-
Electronics Fabrication	\$ 80 K	\$ 150 K	\$ 150 K
Electronics Test & Q.C.	\$ 40 K	\$ 100 K	\$ 100 K
IMC & Elec. Shutter	\$ 300 K	\$ 150 K	\$ 50 K
Optics Des. & Proc.	\$ 40 K	\$ 30 K	\$ 30 K
Customer Interface	\$ 200 K	\$ 100 K	\$ 100 K
Subtotals:	<u>\$ 2.31 M</u>	<u>\$ 1.76 M</u>	<u>\$.73 M</u>
TOTAL SYSTEM COST:	<u><u> </u></u>	<u><u>\$ 4.8 M</u></u>	<u><u> </u></u>

TABLE 10-6

MODEL COST COMPARISONS

	1966 Study		Engineering Estimates	1971 Study	
	Avg. Inputs	Max. Inputs		Avg. Inputs	Max. Inputs
ESC	\$ 4.6 M	\$ 6.4 M	\$ 5.6 M	\$ 1.4 M	\$ 1.6 M
SEC	\$ 4.3 M	\$ 6.3 M	\$ 3.0 M	\$ 1.3 M	\$ 1.6 M
ICCD	\$ 4.4 M	\$ 6.2 M	\$ 4.8 M	\$ 1.4 M	\$ 1.6 M

The reasons for the large variations are, in part, due to the fact that the models only took into account the average costs of previous systems. Thus, the small cost needed to further develop the SEC was not accurately differentiated from the large research and development costs needed for the ESC and ICCD cameras. The reason for the low results of the 1971 Study is not known. This examination of the cost data indicates that the engineering cost estimates should be more accurate than the CER results.

10.5 DEVELOPMENT SCHEDULES

Listed below are approximate development schedules for the three cameras. These cover the period from the initial contract date to the delivery of the flight model to the spacecraft contractor, and also allow for six months of customer interface after delivery. The ESC system schedule is shown in Table 10-7, the SEC vidicon in Table 10-8, and the ICCD in Table 10-9. The SEC camera would require approximately 20 months to deliver; the ESC and ICCD systems about 36 months.

TABLE 10-7

ESC CAMERA DEVELOPMENT SCHEDULE

EVENTS	MONTHS						
	6	12	18	24	30	36	42
CONTRACT AWARD	□						
ENGINEERING MODEL:							
DESIGN & DEVELOPMENT	■	■					
FABRICATION		■	■				
TESTING			■	■			
SYSTEM OPERATIONAL			▽				
PROTOTYPE MODEL:							
DESIGN & DEVELOPMENT			■	■			
FABRICATION				■	■		
TESTING				■	■	■	
DELIVERY					▽		
FLIGHT MODEL:							
FABRICATION					■	■	
TESTING						■	■
DELIVERY							▽
CUSTOMER INTERFACE							■

TABLE 10-8

SEC VIDICON CAMERA DEVELOPMENT SCHEDULE

EVENTS	MONTHS						
	6	12	18	24	30	36	42
CONTRACT AWARD	□						
ENGINEERING MODEL:							
DESIGN & DEVELOPMENT	■						
FABRICATION	■	■					
TESTING		■	■				
SYSTEM OPERATIONAL		▽					
PROTOTYPE MODEL:							
DESIGN & DEVELOPMENT		■					
FABRICATION			■				
TESTING			■	■			
DELIVERY			▽				
FLIGHT MODEL:							
FABRICATION			■	■			
TESTING				■	■		
DELIVERY				▽			
CUSTOMER INTERFACE				■	■		

APPENDIX A
CAMERA MODELING

A.1 INTRODUCTION

Detailed analytical models for the candidate camera systems are developed in this appendix using the basic relationships established in Section 3. The analytical signal-to-noise-ratio models for all of the candidate camera systems are shown.

A.2 DEVELOPMENT OF ANALYTICAL PEAK-SIGNAL-TO-RMS-NOISE MODELS FOR SELECTED CANDIDATE SENSORS

A.2.1 ANALYTICAL PEAK-SIGNAL-TO-RMS-NOISE MODEL FOR SIT-SEC-SiO₂ VIDICONS

These vidicons incorporate a photocathode and a target exhibiting a charge gain mechanism. Light imaged onto the photocathode generates electrons which in turn are accelerated toward the target. Upon striking the target, they initiate a gain mechanism which causes the primed surface of the target elements on the read beam side to discharge by an amount equal to the charge delivered to that target element times the gain of the target.

During readout, the surface of the target facing the read electron gun is primed to the cathode potential of the gun. This repriming process generates a modulated current in the target (output) circuit which is proportional to the charge pattern established on the target.

A.2.1.1 Output Signal Current - As discussed in Section 3.2.1.1, Equation (3-5), the current density leaving the photocathode of the camera, can be determined from the integral of the product of the spectral response of the detector, the input flux at the image plane, and the spectral transmission of the detector optics. For a given exposure time, t_e , the charge density, Q_{in} , delivered to the target from the photocathode is given by the expression

$$Q_{in} = \frac{t_e W S t_e \cos\theta}{4r^2 f^2} \int_0^\infty W_\lambda P_\lambda t_{o\lambda} \sigma_\lambda d\lambda \quad (A-1)$$

The amount, Q_d , by which a resolution element on the target is discharged is equal to

$$Q_d = G_t A Q_{in} \text{ (couls/res. ele.)} \quad (A-2)$$

or

$$Q_d = \frac{G_t A t_e W S t_e \cos\theta}{4r^2 f^2} \int_0^\infty W_\lambda P_\lambda t_{o\lambda} \sigma_\lambda d\lambda \quad (A-3)$$

where

G_t = gain of the target

A = area of a resolution element (meters²)

For the case where the area of the read beam is equal to the area of a resolution element, a fraction, n_c , of this charge is replaced during readout in a time, Δt , where Δt is approximately equal to $\frac{1}{2B}$ (B = video bandwidth).

The current, I_i , generated in the target circuit by this readout process is given by the expression

$$I_i = \frac{Q_d}{\Delta t} = \frac{Bn G A_t W S t_L \cos \theta}{2r^2 f^2} \int_0^\infty W_{\lambda} P_{\lambda} t_{o\lambda} \sigma_{\lambda} d\lambda \quad (A-4)$$

The signal, S , corresponding to this output current (Equation 3-23) is then

$$S(K) = 2M_o \tau_s (K) I_i \quad (A-5)$$

or

$$S(K) = \frac{M_o \tau_s (K) Bn G A_t W S t_L \cos \theta}{r^2 f^2} \int_0^\infty W_{\lambda} P_{\lambda} t_{o\lambda} \sigma_{\lambda} d\lambda \quad (A-6)$$

A.2.1.2 Output Noise Current - The noise sources associated with these image tubes are

- Quantum (image) noise
- Noise associated with the gain mechanism of the target
- Shot noise in the read beam
- Shot noise in the target dark current
- Thermal noise of the load impedance
- Shot noise in channel current of the preamp field effect transistor (FET)

Each source of noise will now be discussed in detail.

NOTE: In discussing the development of the analytical models, the assumption has been made that the area of the read beam, A_b , is equal to the area of the resolution element, A . When $A_b \neq A$, A must be replaced by A_b in the analytical models.

A.2.1.2.1 Quantum (Image) and Target Noise Terms - The charge density delivered to the target from the photocathode is given by equation (A-1) above.

The number of electrons striking a resolution element is then

$$\frac{AQ_d}{e} = \frac{At W S t_c \cos\theta}{4er^2 f^2} \int_0^\infty W_\lambda P_\lambda t_{o\lambda} \sigma_\lambda d\lambda \quad (\text{electrons/res. ele.}) \quad (\text{A-7})$$

where

e = electronic charge.

Assuming Poisson statistics, the RMS fluctuations in this number of electrons is the noise, which is associated with the image. As in the case of the signal, these noise electrons are multiplied by the gain of the target.

In addition, the target contributes its own noise. If the assumption is made that the randomness of the gain process can best be described in terms of a Poisson distribution, then this noise contribution can be taken into account by multiplying the image noise by the factor F_G where

$$F_G = \left(\frac{G_t + 1}{G_t} \right)^{\frac{1}{2}} \quad (\text{A-8})$$

Thus, the number of noise electrons, N_d , associated with the discharging of a resolution element on the target is given by the expression

$$N_d = G_t \left[\left(\frac{G_t + 1}{G_t} \right) \frac{At W S t_c \cos\theta}{4er^2 f^2} \int_0^\infty W_\lambda P_\lambda t_{o\lambda} \sigma_\lambda d\lambda \right]^{\frac{1}{2}} \quad (\text{A-9})$$

= (noise electrons/res. ele.)

or, expressed in terms of a noise charge, Q_{nd} ,

$$Q_{nd} = \left[\frac{e(G_t+1)G_t A t_e W S t_e \cos \theta}{4r^2 F^2} \int_0^\infty W_\lambda P_\lambda t_{o\lambda} \sigma_\lambda d\lambda \right]^{1/2} \quad (A-10)$$

= (couls/res. ele.)

As with the signal, a fraction, n_c , of this noise charge is replaced during readout in a time, $\Delta t = 1/2B$, assuming that the area of the read beam is equal to the area of a resolution element.

Therefore, the noise current associated with the input signal is

$$\frac{Q_{nd}}{\Delta t} = B n_c \left[\frac{(G_t+1)G_t A t_e W S t_e \cos \theta}{r^2 F^2} \int_0^\infty W_\lambda P_\lambda t_{o\lambda} \sigma_\lambda d\lambda \right]^{1/2} \quad (\text{amps}) \quad (A-11)$$

While the quantum noise is not reduced by the response of the entire imaging system, it is reduced by a correction factor, β , which is a measure of the equivalent noise bandwidth⁽⁴³⁾. This bandwidth is determined by the modulation transfer function of certain system components. In the above analysis, the MTFs of the target and read beam will result in a smaller noise current being observed at the output. The corresponding correction factor, β , is given by the expression

$$\beta = \frac{1}{K} \int_0^K |\tau_T(K) \tau_R(K)|^2 dK \quad (A-12)$$

where $\tau_T(K)$ and $\tau_R(K)$ are the responses of the target and readout section respectively and K is the spatial frequency at which the signal and noise is being observed.

Therefore, the output noise current, i_i , resulting from the input signal is

$$i_i = \beta B n_c \left[\frac{(G_t + 1) G_t e A t W S t \cos \theta}{r^2 f^2} \int_0^\infty W_{\lambda} P_{\lambda} t_{o\lambda} \sigma_{\lambda} d\lambda \right]^{1/2} \text{ (amps)} \quad (\text{A-13})$$

A.2.1.2.2 Readout Beam Shot Noise - The current I_i generated in the target (output) circuit by the read process is given by Equation (A-4) above. This current, originating from the read electron gun, has a shot noise component given by the expression

$$i_r = (2eI_i B)^{1/2} \quad (\text{A-14})$$

where i_r is the shot noise current due to the read beam.

By combining equations (A-4) and (A-14), the shot noise in the read beam can be expressed as

$$i_r = \left[\frac{e B^2 n_c G_t A t W S t \cos \theta}{r^2 f^2} \int_0^\infty W_{\lambda} P_{\lambda} t_{o\lambda} \sigma_{\lambda} d\lambda \right]^{1/2} \text{ (amps)} \quad (\text{A-15})$$

A.2.1.2.3 Target Dark Current Shot Noise - During the read process a second current, I_D , is observed in the output. This current is the result of the dark current in the target. While this current does not contribute to the output signal, it does contribute to the noise in the signal. Its noise current i_d is equal to $(2eI_D B)^{1/2}$.

A.2.1.2.4 Thermal Noise of Load Impedance - The thermal noise current, i_t , generated by the output load impedance of the device is given by the expression

$$i_t = \left(\frac{4kTB}{R_L} \right)^{1/2} \quad (\text{amps}) \quad (\text{A-16})$$

where

k = Boltzmann's constant

T = absolute temperature

R_L = load impedance

A.2.1.2.5 Shot Noise in Channel Current of Preamp Field Effect Transistor (FET) - The preamp chosen for this model utilizes a low noise junction field effect transistor. The shot noise current, i_s , due to the channel current of the FET is given by the expression

$$i_s = \left(\frac{8eI_F B^3 C^2}{g_m^2} \right)^{1/2} \quad (\text{amps}) \quad (\text{A-17})$$

where

I_F = FET channel current

C = total shunt capacitance to ground

g_m = FET transconductance

A.2.2 ANALYTICAL PEAK-SIGNAL-TO-RMS-NOISE MODEL FOR THE SEC VIDICON WITH AN IMAGE INTENSIFIER

When an image intensifier having an effective gain, G_I , (see Section A.2.10) is used on this image tube, the following modification must be made to the corresponding signal-to-noise model:

- The output signal S is increased by the gain of the intensifier and decreased by the MTF, $\tau_1(K)$, of the intensifier.

$$* S(K) = \frac{G_M \tau_1(K) B_n G A t W S t_L \cos \theta}{I_0 S \frac{c t}{r^2 f^2} e p p L} \int_0^\infty W_\lambda P_\lambda t_{o\lambda} \sigma_\lambda d\lambda \text{ (amps)} \quad (A-18)$$

*NOTE: $\tau_s(K)$ now includes the MTF of the intensifier.

- The output noise current, i_1 , associated with the input signal (quantum noise) is modified as follows:

In a manner similar to that discussed in Section A.2.1.2.1, the noise associated with the signal photoelectrons generated by the photocathode of the image intensifier can be given by the expression

$$N_d = \left[\frac{A t W S' t_L \cos \theta}{4 e r^2 f^2} \int_0^\infty W_\lambda P_\lambda t_{o\lambda}'' \sigma_\lambda' d\lambda \right]^{1/2} \quad (A-19)$$

in units of noise electrons/resolution element

where $t_{o\lambda}''$ = transmission of image intensifier (II) fiber optic faceplate.

S_p' = II photocathode sensitivity (couls/joule)

σ_λ' = the relative spectral II photocathode response

Expressed in terms of noise charge, Q_{nd} , the noise associated with this signal is

$$Q_{nd} = \left[\frac{e A t W S' t_L \cos \theta}{4 r^2 f^2} \int_0^\infty W_\lambda P_\lambda t_{o\lambda}'' \sigma_\lambda' d\lambda \right]^{1/2} \quad (A-20)$$

(couls/res. ele.)

This noise charge is amplified by the intensifier in the same manner as the signal. When it is accelerated across a potential difference of V_a within the image section of the intensifier, it has an energy of $Q_{nd}(V_a - V_d)$ joules at the phosphor surface, since $Q_{nd}V_d$ joules of energy were lost in penetrating the conductive coating on the phosphor.

The resulting energy (light) output of the phosphor then passes through the fiber optic endplate of the intensifier and the fiber optic faceplate of the vidicon, and reaches the photocathode. At the photocathode of the vidicon, this light energy, which is associated with the noise charge generated at the photocathode of the image intensifier, (quantum noise), is converted back into an electronic charge, Q_{qn} .

This amplified noise charge is given by the expression:

$$Q_{qn} = Q_{nd}(V_a - V_d)L_p S_p \int_0^\infty \sigma_\lambda \phi_\lambda t'_{o\lambda} t_{o\lambda} d\lambda \quad (A-21)$$

where

L_p = peak monochromatic output of the phosphor (joules/
joule/nm)

ϕ_λ = relative spectral output of the phosphor

$t'_{o\lambda}$ = spectral transmission of the intensifier fiber
optic faceplate

$t_{o\lambda}$ = spectral transmission of the vidicon faceplate.

Substituting expression (A-20) for Q_{nd} , this amplified quantum noise charge is equal to

$$Q_{qn} = \left[\frac{eAt W t S' \cos \theta}{4r^2 f^2} \int_0^\infty W_\lambda P_\lambda t''_{o\lambda} \sigma'_\lambda d\lambda \right]^{1/2} \\ \times (V_a - V_d)L_p S_p \int_0^\infty \sigma_\lambda \phi_\lambda t'_{o\lambda} t_{o\lambda} d\lambda \quad \text{couls/res. ele.} \quad (A-22)$$

This quantum noise charge can be traced through the camera in a manner identical to that described in Section A.2.1.2.1. The resulting output noise current, i_i , associated with the input signal is given by the expression

$$i_i = \beta 2Bn_c [G_t (G_t + 1)]^{1/2} (V_a - V_d) L_p S_p' \int_0^\infty \sigma_\lambda \phi_\lambda t'_{o\lambda} t_{o\lambda} d\lambda$$

$$\times \left[\frac{eAt W t_p S' \cos\theta}{4r^2 f^2} \int_0^\infty W_\lambda P_\lambda t''_{o\lambda} \sigma_\lambda' d\lambda \right]^{1/2} \quad (A-23)$$

Only in the case where $S_p = S_p'$, $\sigma_\lambda = \sigma_\lambda'$ and $t_{o\lambda} = t'_{o\lambda} = t''_{o\lambda}$, does equation (A-23) reduce to

$$i_i = \beta 2Bn_c [(G_t + 1)(G_t)]^{1/2} G_I \left[\frac{eAt W t_p S \cos\theta}{4r^2 f^2} \int_0^\infty W_\lambda P_\lambda t_{o\lambda} \sigma_\lambda d\lambda \right]^{1/2} \quad (A-24)$$

where $G_I =$ effective gain of the image intensifier.

- The amount of read beam current required for readout is increased by the factor G_I . This increases the shot noise current i_r in the read beam by a factor of $(G_I)^{1/2}$.

$$i_r = \left[\frac{G_I e B^2 n_c G A t W S t_p \cos\theta}{r^2 f^2} \int_0^\infty W_\lambda P_\lambda t_{o\lambda} \sigma_\lambda d\lambda \right]^{1/2} \text{ (amps)} \quad (A-25)$$

- The remaining noise terms described in Section A.2.1.2 remain the same.

The complete analytical peak-signal-to-RMS noise expression for the SIT-SEC-SiO₂ vidicons and the SEC vidicon with an image intensifier is presented in Section A.2.12.

A.2.3 ANALYTICAL PEAK-SIGNAL-TO-RMS-NOISE MODEL FOR SILICON AND SLOW-SCAN VIDICONS

The signal-to-noise model of the silicon vidicon and slow-scan vidicons are obtained in the same way as the SIT-SEC-SiO₂ vidicon model discussed above. However, since a photoconductor is used in these image tubes (replacing the photocathode and target), the expressions for the

signal and the signal-related noise take a somewhat different form.

For a given exposure time, the photoconductor is discharged by the amount, Q_d , where

$$Q_d = \frac{e t A W_p t_{\cos\theta}}{4 h c r^2 f^2} \int_0^\infty \lambda W_\lambda P_\lambda t_{o\lambda} \eta_\lambda d\lambda \quad (\text{couls/res. ele.}) \quad (\text{A-26})$$

Having converted the image into a charge pattern on the photoconductor, the expressions for the output signal and noise currents associated with these image tubes are developed in a manner identical to the development of the SIT-SEC-SiO₂ vidicon signal-to-noise model described in Section A.2.1.

The complete analytical peak-signal-to-RMS noise expression for the silicon and slow-scan vidicon is presented in Section A.2.12.

A.2.4 ANALYTICAL PEAK-SIGNAL-TO-RMS-NOISE MODEL FOR SILICON AND SLOW-SCAN VIDICONS WITH IMAGE INTENSIFIERS

When an image intensifier having an effective gain, G_I , is used on the silicon and slow-scan vidicons, modifications similar to those discussed in Section A.2.2 must be made to the corresponding signal-to-noise model:

- Using the definition of G_I presented in Section A.2.11, the output signal of the intensified vidicon is equal to the output signal of the unintensified vidicon multiplied by G_I and the response of the intensifier:

$$S(K) = \frac{G_I t M \tau_s(K) B n_c e A W_p t_{\cos\theta}}{h c r^2 f^2} \int_0^\infty \lambda W_\lambda P_\lambda t_{o\lambda} \eta_\lambda d\lambda \quad (\text{A-27})$$

where, $\tau_s(K)$, now includes the response of the intensifier.

- The output noise current, i_i , associated with the input signal (quantum noise) is modified in a manner similar to that described in Section A.2.2. However, since both a photocathode and a photoconductor are being used, the expression for the output noise current takes the form

$$i_i = \beta 2 B n_c (\eta + 1)^{\frac{1}{2}} \frac{e L (V_a - V_d)}{h c} \int_0^\infty \phi_\lambda t'_{o\lambda} t_{o\lambda} \lambda \eta_\lambda d\lambda$$

$$\times \left[\frac{e A t W t_p S' \cos \theta}{4 r^2 f^2} \int_0^\infty W_\lambda P_\lambda t''_{o\lambda} \sigma_\lambda d\lambda \right]^{\frac{1}{2}} \quad (A-28)$$

- The amount of read beam current required for readout is increased by the factor, G_I . This increases the shot noise current, i_r , in the read beam by a factor, $(G_I)^{\frac{1}{2}}$.

$$i_r = \left[\frac{G_I t B^2 n_c e^2 A W t_p \cos \theta}{h c r^2 f^2} \int_0^\infty \lambda W_\lambda P_\lambda t_{o\lambda} \eta_\lambda d\lambda \right]^{\frac{1}{2}} \quad (A-29)$$

- The remaining noise terms for the intensified silicon and slow-scan vidicons are the same as those presented in the signal-to-noise model for the unintensified silicon and slow-scan vidicons.

A.2.5 ANALYTICAL PEAK-SIGNAL-TO-RMS-NOISE MODEL FOR RETURN BEAM VIDICON

In a return beam vidicon, that portion of the read beam that does not go into charging the target elements follows a return path to the read gun where it is collected by an electron multiplier. This method of obtaining the video signal results in the following modifications to the signal-to-noise model presented for the silicon and slow-scan vidicons.

A.2.5.1 Output Signal Current - A fraction of the signal from the target is lost due to the presence of a field mesh in the readout section of the tube. The remaining portion of the signal is multiplied by the gain, G_M , of the electron multiplier. The mathematical expression for the signal of the return beam vidicon is

$$S(K) = \frac{G_M t_e M_o \tau_s (K) t_f B_n e A W t_L \cos \theta}{h c r^2 f^2} \int_0^\infty \lambda W_\lambda P_\lambda t_{o\lambda} \eta_\lambda d\lambda \quad (\text{amps}) \quad (\text{A-30})$$

where t_f is the transmission of the field mesh.

A.2.5.2 Output Noise Current

A.2.5.2.1 Quantum (Image) Noise - The field mesh and electron multiplier have the same effects on the quantum noise current as they do on the signal current. As with the signal, the expression for the quantum noise current of the silicon and slow-scan vidicons is multiplied by the transmission of the field mesh and the gain of the electron multiplier. The expression for the quantum noise current, i_{qn} , thus becomes:

$$i_{qn} = [G_M^2 t_f^2 \beta^2 (n+1) \frac{t_e B_n^2 n_c^2 e^2 A W t_L \cos \theta}{h c r^2 f^2} \int_0^\infty \lambda W_\lambda P_\lambda t_{o\lambda} \eta_\lambda d\lambda]^{1/2} \quad (\text{amps}) \quad (\text{A-31})$$

A.2.5.2.2 Read Beam Shot Noise - Due to the dark current in the photoconductor and the reflection of a portion of the readout beam at the surface of the photoconductor, a current somewhat greater than the signal current must be used in a return beam vidicon. The required read beam current, (as measured at the plane of the photoconductor), must be larger, by a factor of $1/m$, than the

signal current, I_s , being read out. The quantity, m_b , is defined to be the "beam modulation factor". The corresponding noise current in this read beam is therefore equal to

$$\left[\frac{2eI_s B}{m_b} \right]^{1/2} \text{ (amps)} \quad (\text{A-32})$$

Since the return beam current, $\left[\frac{1-m_b}{m_b} \right] I_s$, passes through the field mesh of the readout section, a partition noise term must also be added. The resulting expression for the noise current, i_r , associated with the read beam thus becomes:

$$\begin{aligned} i_r^2 &= G_M^2 \left[\left(\frac{2eI_s B}{m_b} \right) t_f^2 + 2e t_f (1-t_f) \left(\frac{1-m_b}{m_b} \right) I_s B \right] \\ &= G_M^2 \left(\frac{2e t_f I_s B}{m_b} \right) (1-m_b + m_b t_f) \quad (\text{amps}^2) \end{aligned} \quad (\text{A-33})$$

or

$$i_r^2 = \frac{G_M^2 (1-m_b + m_b t_f) t_f e^2 B^2 n_c t AW_p L \cos \theta}{m_b h c r^2 f^2} \int_0^\infty \lambda W_\lambda P_\lambda t_{o\lambda} \eta_\lambda d\lambda \quad (\text{amps}^2) \quad (\text{A-34})$$

A.2.5.2.3 Noise due to Electron Multiplier - The electron multiplier in the return beam vidicon also contributes to the noise current. For a return beam current equal to $\frac{t_f(1-m)I_s}{m}$, the noise current, i_e , associated with the electron multiplier is given by the expression

$$i_e^2 = G_M^2 \left[\frac{2et_f(1-m_b)I_s B}{m_b(\delta_m - 1)} \right]$$

$$= \frac{G_M^2 t_f(1-m_b)e^2 B^2 n_c t_e A W_p t_L \cos\theta}{m_b(\delta_m - 1) h c r^2 f^2} \int_0^\infty \lambda W_\lambda P_\lambda t_{o\lambda} \eta_\lambda d\lambda \quad (\text{amps}^2) \quad (\text{A-35})$$

where δ_m = secondary emission yield of the first dynode of the electron multiplier.

The expression for the thermal noise of the load impedance and the shot noise in the channel current of the preamp FET are the same as in the analytical models already discussed.

The complete analytical peak-signal-to-RMS-noise expression for the return beam vidicon is presented in Section A.2.12.

A.2.6 ANALYTICAL PEAK-SIGNAL-TO-RMS-NOISE MODEL FOR THE IMAGE ORTHICON

The image orthicon is similar in operation to the return beam vidicon. The significant difference is that instead of a photoconductor, the image orthicon has a photocathode, an image section with a collector mesh of transmission

coefficient, t_m , and a thin insulating target. Secondary emission at the target is the pre-readout gain mechanism employed in this type of tube. The complete analytical peak-signal-to-RMS-noise expression for the image orthicon is presented in Section A.2.12.

Most of the terms in the signal-to-noise model for the image orthicon (IO) have been developed in detail in either Section A.2.1 (SIT-SEC-SiO₂ Vidicon Model) or Section A.2.5 (Return Beam Vidicon Model) and consequently will not be repeated here. The secondary emission noise at the target, however, has not been previously discussed.

A.2.6.1 Noise due to the Secondary Electron Emission of the Target - For a charge density, Q_d , striking the target from the photocathode, an amount of charge, Q_d' , is removed from each resolution element. This Q_d' is equal to

$$Q_d' = A\delta_t Q_d \text{ (coults/res. ele.)} \quad (\text{A-36})$$

or

$$Q_d' = \frac{A\delta_t Q_d}{e} \text{ (electrons/res. ele.)} \quad (\text{A-37})$$

where

$$\delta_t = \text{secondary emission ratio of the target.}$$

If Poisson statistics are assumed, the rms fluctuation in this number of electrons, q_s , is equal to

$$q_s = \left(\frac{A\delta_t Q_d}{e} \right)^{\frac{1}{2}} \text{ (electrons/res. ele.)} \quad (\text{A-38})$$

However, for some materials, the fluctuation in the secondary electron emission cannot be described using Poisson statistics. A more general expression for the rms fluctuations in the secondary electrons emitted from the target is

$$q_s = [(\kappa - \delta_t) \left(\frac{A \delta_t Q_d}{e} \right)^{\frac{1}{2}}] \quad (\text{electrons/res. ele.}) \quad (\text{A-39})$$

where, κ , defined by Timm and Van der Ziel⁽⁴⁴⁾, is a characteristic of the target.

These noise electrons can be expressed in the form of an output noise current contribution in the same manner as the noise associated with the image (quantum noise).

A.2.7 ANALYTICAL PEAK-SIGNAL-TO-RMS-NOISE MODEL FOR THE IMAGE ISOCON

Since the image isocon is very similar in operation to the image orthicon, its signal-to-noise model is also quite similar. However, the ability of the image isocon's readout section to separate the scattered and reflected portions of the return beam requires the introduction of certain factors into the model.

- The factor, α_s , is defined to be the "scatter gain" of the isocon readout.⁽⁴⁵⁾ The scatter gain is the ratio of that portion of the read beam current scattered during readout to that portion of the read beam current collected by charging the target.

- The factor, K_S , is a signal reduction factor.⁽⁴⁵⁾ This factor takes into account the effect of the field mesh in the readout section and the reduction in signal due to the incomplete separation of the scattered electrons from the reflected electrons.
- The factor, K_D , takes into account the fact that a certain portion of the reflected beam is not separated out from the scattered beam⁽⁴⁵⁾. As a result, a "dark current" is observed at the output of the image isocon. The noise in this dark current contributes to the overall tube noise. Measurements have shown the dark current I_D to be proportional to the signal on the target, i.e.,

$$I_D = \frac{K_D (\delta_t - 1) B A t_e W S t_L \cos \theta}{2 r^2 f^2} \int_0^\infty W_\lambda P_\lambda t_{o\lambda} \sigma_\lambda d\lambda \text{ (amps)} \quad (\text{A-40})$$

Using these additional factors, the development of the analytical signal-to-noise model for the image isocon is similar to the development of the signal-to-noise model for the image orthicon. The complete model is presented in Section A.2.12.

A.2.8 ANALYTICAL PEAK-SIGNAL-TO-RMS-NOISE MODEL FOR THE ELECTROSTATIC STORAGE CAMERA

The electrostatic storage camera differs significantly from the other sensors being considered. From the standpoint of developing a signal-to-noise model, the principal difference is the method by which the output signal is obtained. While the other sensors use charge replacement or charge transfer to obtain an output signal, the output signal in the electrostatic camera is obtained by analyzing the energy of secondary electrons generated at the dielectric storage surface by a high-energy read beam. Since the energy of these secondaries is a function of the surface

potential of the target elements from which they originate, the output signal corresponds to the potential variations on the storage target produced by the input (photoelectron) signal.

A.2.8.1 Output Signal Current - As in the case of the SIT-SEC-SiO₂ vidicons, a charge density, Q_d, is delivered to the storage target from the photocathode. The charge density is proportional to the exposure, i.e.,

$$Q_d = \frac{t_e W S t_p \cos\theta}{4r^2 f^2} \int_0^\infty W_\lambda P_\lambda t_{o\lambda} \sigma_\lambda d\lambda \quad (\text{couls/meter}^2) \quad (\text{A-41})$$

The amount, ΔQ_d, by which the surface of the storage target is discharged is

$$\Delta Q_d = G_t Q_d \quad (\text{couls/meter}^2) \quad (\text{A-42})$$

The corresponding change in surface potential, ΔV, is equal to ΔQ/C*, or

$$\Delta V = \frac{G_t t_e W S t_p \cos\theta}{C^* 4r^2 f^2} \int_0^\infty W_\lambda P_\lambda t_{o\lambda} \sigma_\lambda d\lambda \quad (\text{A-43})$$

where C* is the capacitance per square meter of the target.

When the read beam having a forward current, I_b, scans the storage target, a return beam of magnitude δ_tI_b is obtained (δ_t = secondary emission ratio of the target). Variations in the amount of this return beam current, ΔI, passing through the energy analyzer are related to variations in the target

potential, ΔV , by the readout characteristic slope. That is,

$$\Delta I = I_{\text{signal}} = m \delta \frac{I_b \Delta V}{t_b} \quad (\text{A-44})$$

where m is the slope of readout characteristic.

The electron multiplier then amplifies this signal by the multiplier gain factor, G_M .

After taking into account the reduction in signal due to the MTF of the system, $\tau_s(K)$, and the input modulation, M_o , the signal in the electrostatic camera is given by the expression:

$$I_{\text{signal}} = 2M_o \tau_s(K) (G_M m \delta \frac{I_b \Delta V}{t_b})$$

$$= \frac{M_o \tau_s(K) G_M m \delta \frac{I_b G_t A W S t_e \cos \theta}{2C * r^2 f^2}}{2C * r^2 f^2} \int_0^\infty W_\lambda P_\lambda t_{o\lambda} \sigma_\lambda d\lambda \quad (\text{amps}) \quad (\text{A-45})$$

A.2.8.2 Output Noise Current - The noise sources associated with the electrostatic storage camera are:

- Quantum (image) and target noise
- Dielectric target charging noise
- Read beam shot noise
- Secondary emission noise of dielectric target
- Energy analyzer partition noise
- Electron multiplier secondary emission noise
- Thermal noise of the load impedance
- Shot noise in the channel current of the preamp FET

A.2.8.2.1 Quantum (Image) and Target Noise Terms - For a given exposure the amount of noise charge Q_{nd} stored on one resolution element of the target is given by

$$Q_{nd} = \left[\frac{(G_t + 1) G_t e A t W S t_c \cos \theta}{4 r^2 f^2} \int_0^\infty W_{\lambda} P_{\lambda} t_{o\lambda} \sigma_{\lambda} d\lambda \right]^{1/2} \quad (\text{A-46})$$

(couls/res.ele.)

This equation, which takes into account the noise contribution of the target, is developed in the discussion of the SIT-SEC-SiO₂ vidicon signal-to-noise model (Section A.2.1.2.1).

This noise charge corresponds to a noise voltage, V_{nd} , where

$$V_{nd} = \frac{Q_{nd}}{C * A} \quad (\text{volts}) \quad (\text{A-47})$$

This noise voltage is converted into an output noise current, i_{nd} , in the same manner as the signal voltage on the target is converted into an output signal current, i.e.,

$$i_{nd} = \frac{G_m \delta}{M_t b} I_{bnd} V_{nd} \quad (\text{A-48})$$

or

$$i_{nd} = \frac{G_m \delta}{C * A} \frac{I_{bnd}}{C * A} \left[\frac{(G_t + 1) G_t e A t W S t_c \cos \theta}{4 r^2 f^2} \int_0^\infty W_{\lambda} P_{\lambda} t_{o\lambda} \sigma_{\lambda} d\lambda \right]^{1/2} \quad (\text{amps}) \quad (\text{A-49})$$

As was discussed in Section A.2.1.2.1, a correction factor, β , must be included in the quantum noise expression. This factor takes into account the fact that the quantum noise contribution to the overall noise of the sensor will be reduced due to the MTFs of the target and readout section.

A.2.8.2.2 Dielectric Charging Noise during Readout - During readout, the surface potential of the target is shifted to a more positive value (assuming $\delta_t > 1$). This causes additional fluctuation or noise in the surface potential of each resolution element. These voltage fluctuations are the result of current fluctuations in the primary read beam and in the return beam.

Since the noise in these two currents is fully correlated, the resulting fluctuation, V_{nc} , in the surface potential of a resolution element is given by the equation

$$V_{nc} = \frac{1}{C*A} \{ \Delta t [2eI_b (\delta_t - 1)^2 B + 2e(\kappa - \delta_t) \delta_t I_b B] \}^{1/2} \quad (A-50)$$

where κ is defined in Section A.2.6.1 and Δt is the dwell time of the read beam on a resolution element.

If the video bandwidth, B , is selected so that the dwell time of the read beam on a resolution element is equal to $1/2B$, then

$$\begin{aligned} V_{nc} &= \frac{1}{C*A} \left[\frac{eI_b (\delta_t - 1)^2 + eI_b (\kappa - \delta_t) \delta_t}{2B} \right]^{1/2} \\ &= \frac{1}{C*A} \left\{ \frac{eI_b [1 + (\kappa - 2) \delta_t]}{2B} \right\}^{1/2} \quad (\text{volts}) \end{aligned} \quad (A-51)$$

As with the quantum noise voltage, the noise voltage due to target charging is converted into an output noise current:

$$i_{nc} = \frac{G_M m \delta_t I_b}{C * A} \left\{ \frac{e I_b [1 + (\kappa - 2) \delta_t]}{2B} \right\}^{1/2} \quad (\text{amps}) \quad (\text{A-52})$$

A.2.8.2.3 Read Beam Shot Noise - The shot noise in the read beam is amplified by the secondary emission yield at the target. The shot noise current in the return beam is therefore equal to $\delta_t (2e I_b B)^{1/2}$. Since the energy analyzer permits only a fraction, a , of the return beam to enter the electron multiplier, the output noise current, i_r , due to the shot noise in the read beam can be expressed as

$$i_r = G_M a \delta_t (2e I_b B)^{1/2} \quad (\text{amps}) \quad (\text{A-53})$$

A.2.8.2.4 Secondary Emission Noise of Dielectric Target - The rms fluctuations in the secondary emission current, $\delta_t I_b$, would be equal to $(2e \delta_t I_b B)^{1/2}$ provided Poisson statistics could be assumed. Since, however, the fluctuations in the secondary electron emission of some materials cannot be described using Poisson statistics, a more general expression for the noise current associated with the secondary emission current takes the form $[2e(\kappa - \delta_t) \delta_t I_b B]^{1/2}$. As with the read beam shot noise current, a fraction, a , of this noise current enters the electron multiplier. The output noise current, i_s , due to secondary emission at the dielectric target can thus be expressed

as

$$i_s = G_M a [2e(\kappa - \delta_t) \delta_t I_b B]^{1/2} \quad (\text{amps}) \quad (\text{A-54})$$

A.2.8.2.5 Energy Analyzer Partition Noise - At the energy analyzer, a portion, a , of the return beam passes through the energy analyzer while the remaining portion, $1-a$, is rejected. The value of a is determined by the potential of the target element where the return (secondary) beam was generated. This return beam separation results in a partition noise current, i_p , at the sensor output, where

$$i_p = G_M [2e(1-a)a\delta_t I_b B]^{1/2} \quad (\text{amps}) \quad (\text{A-55})$$

A.2.8.2.6 Electron Multiplier Secondary Emission Noise - The development of the expression for the noise contribution of the electron multiplier is the same as that described in Section A.2.5.2.3, with the current entering the electron multiplier as $a\delta_t I_b$.

The complete peak-signal-to-RMS-noise model for the electrostatic camera system is presented in Section A.2.12.

A.2.9 ANALYTICAL-PEAK-SIGNAL-TO-RMS-NOISE MODEL FOR THE CHARGE-COUPLED IMAGER AND INTENSIFIED (PHOTOEMITTER) CHARGE-COUPLED DEVICE

Both the charge-coupled device target⁽²⁰⁾ and the intensified charge-coupled device target consist of arrays of closely-spaced metal electrodes that overlap an insulator deposited on a uniformly-doped semiconductor substrate. Silicon is normally used as the substrate.

Light from the scene results in a corresponding pattern of charge being collected in potential wells under the electrodes. In the case of the CCD, this charge pattern is generated directly by photons at the silicon target (photoconductivity). In the ICCD, a photocathode converts the light into photoelectrons which generate electron-hole pairs within the silicon. These "charge packets" are collected under each electrode and are transferred during readout by manipulation of the voltages that constrain them. When they reach one end of the device, an output shift register removes them sequentially from the silicon.

A.2.9.1 Output Signal Charge - As in the other sensors that have been discussed, the amount of charge, Q , generated at each target resolution element is given by

$$Q = \frac{t_e e A W_p t_L \cos \theta}{4 h c r^2 f^2} \int_0^\infty \lambda W_\lambda P_\lambda \eta_\lambda d\lambda \quad \text{couls/res. ele. (for the CCD)} \quad (\text{A-56})$$

and

$$Q = \frac{G t_e t A W_p S t_L \cos \theta}{4 r^2 f^2} \int_0^\infty W_\lambda P_\lambda t_{o\lambda} \sigma_\lambda d\lambda \quad \text{couls/res. ele. (for the ICCD)} \quad (\text{A-57})$$

If all the charge in each packet reached the output of the device, the output signal Q_s would be

$$Q_s = 2M_o \tau_s (K) Q \quad (\text{couls/res. ele.}) \quad (\text{A-58})$$

However, a certain fraction, ϵ_c , of this charge is lost during each transfer. If n transfers are required in order for a particular charge packet to reach the output, the output signal in that charge packet will have been reduced to:

$$Q_s = (1 - n\epsilon_c) \frac{M_{os} \tau_s (K) A e W_p t_L t_e \cos\theta}{2 h c r^2 f^2} \int_0^\infty \lambda W_{\lambda} P_{\lambda} \eta_{\lambda} d\lambda \quad (A-59)$$

couls/res. ele. (for the CCD)

and

$$Q_s = (1 - n\epsilon_c) \frac{M_{os} \tau_s (K) A G t W S t_L \cos\theta}{2 r^2 f^2} \int_0^\infty W_{\lambda} P_{\lambda} t_{ol} \sigma_{\lambda} d\lambda \quad (A-60)$$

couls/res. ele. (for the ICCD)

A.2.9.2 Output Noise Charge - The noise sources associated with the CCD and ICCD are:

- Quantum (image) and target noise
- Dark current noise
- Interface state noise
- Shot noise in channel current of preamp FET
- Thermal noise of preamp input impedance

A.2.9.2.1 Quantum (Image) and Target Noise - The expressions for the quantum target noise are very similar to those presented in other signal-to-noise models. In the case of the CCD and ICCD however, the signal and noise terms are being expressed in terms of charge rather than currents.

The expressions for the quantum target noise, Q_{qn} , thus becomes:

$$Q_{qn} = \left[\frac{\beta^2 (n+1) e^2 A W_p t_L e \cos \theta}{4 h c r^2 f^2} \int_0^\infty \lambda W_\lambda P_\lambda \eta_\lambda d\lambda \right]^{1/2} \quad (\text{A-61})$$

coul/res. ele. (for the CCD)

and

$$Q_{qn} = \left[\frac{\beta^2 (G_t+1) G_t t_e e A W_s t_L \cos \theta}{4 r^2 f^2} \int_0^\infty W_\lambda P_\lambda t_{o\lambda} \sigma_\lambda d\lambda \right]^{1/2} \quad (\text{A-62})$$

coul/res. ele. (for the ICCD)

A.2.9.2.2 Dark Current Noise - In both the CCD and ICCD, the dark current across a resolution element of the target adds shot noise to the signal. Noise charge resulting from this dark current is added to a signal charge packet both during the integration (exposure) time and during the time required to read out a given signal charge packet.

For an integration time, T_{integ} , the amount of noise charge added to a signal charge packet is equal to $(2eI_D T_{integ})^{1/2}$ couls, where I_D is the dark current per resolution element.

If the time required to transfer a signal charge packet from its original location to the output p-n junction is $\frac{n}{B_c}$, where n is the number of transfers required and B_c is the clocking (transfer) frequency, then the amount of shot noise charge added to a signal charge packet during the readout time is $\left(\frac{2enI_D}{B_c}\right)^{1/2}$ couls.

A.2.9.2.3 Interface State Noise - Due to the presence of interface states within the target, minority carriers in a potential well are subject to random capture and emission. The spectral density of the mean-square minority carrier charge density fluctuation $S_q(\omega)$ is given by the expression

$$S_q(\omega) = \frac{4kTN_t(E)A_c e^2}{\alpha_p \omega} [\tan^{-1}(\omega\tau_y e^{\alpha_p t_i}) - \tan^{-1}(\omega\tau_y)] \quad (\text{A-63})$$

where

$N_t(E)$ = number of interface states per unit volume per unit energy as a function of energy.

A_c = area of the MIS capacitor formed by the metal electrode-insulator-silicon overlap

ω = radian frequency

α_p = parameter characterizing the tunneling probability (i.e., $P(y) = e^{-\alpha_p y}$, where y is the distance from silicon into transition region)

t_i = thickness of the interface transition region

τ_y = time constant of interface state at $y = 0$

For $(e^{-\alpha_p t_i})/\tau_y < \omega < 1/\tau_y$, $S_q(\omega)$ varies as ω^{-1} . For $\omega > 1/\tau_y$, $S_q(\omega)$ varies as ω^{-2} .

As with the dark current, the interface states add noise to the signal both during the integration period and during the readout period. Integrating $S_q(\omega)$ over the appropriate frequency intervals results in the following expressions for noise charge contributions, q_n , due to the interface

states:

$$q_n(\text{integration}) = \left[\frac{kTN_t(\omega_{\text{integ}})A_c e^2}{\alpha_p} \ln \left(\frac{1}{\omega_{\text{integ}} \tau_y} \right) + \frac{4kTN_t(\omega_{\text{integ}})A_c e^2}{\alpha_p} \right]^{1/2} \quad (\text{A-64})$$

$$q_n(\text{readout}) = \left[\frac{kTN_t(\omega_c)A_c e^{2n}}{\alpha_p} \ln \left(\frac{1}{\omega_c \tau_y} \right) + \frac{4kTN_t(\omega_c)A_c e^{2n}}{\alpha_p} \right]^{1/2} \quad \text{if } \omega_c < \frac{1}{\tau_y} \quad (\text{A-65})$$

$$q_n(\text{readout}) = \left[\frac{4kTN_t(\omega_c)A_c e^{2n}}{\alpha_p \omega_c \tau_y} \right]^{1/2} \quad \text{if } \omega_c > \frac{1}{\tau_y} \quad (\text{A-66})$$

A.2.9.2.4 Shot Noise in Channel Current of Preamp FET - As in the other sensors discussed, the channel current of the preamp FET will contribute shot noise charge, q_{nFET} , equal to

$$q_{\text{nFET}} = \frac{i_{\text{FET}}}{2B} = \left(\frac{8eI_F B^3 C^2}{4B^2 g_m^2} \right)^{1/2} = \left(\frac{2eI_F B C^2}{g_m^2} \right)^{1/2} \quad (\text{couls}) \quad (\text{A-67})$$

where

$$i_{\text{FET}} = \text{shot noise current in } I_F$$

A.2.9.2.5 Thermal Noise of Preamp Input Impedance - Since the output of the CCD and ICCD has an impedance of the reverse-biased output diode (generally $\sim 10^{15}$ ohms), the thermal noise due to this load impedance is insignificant. However, the input resistor of the preamp, in parallel with the load impedance, will contribute a thermally-generated noise charge. This noise charge is equal to $(kT/R_i B)^{1/2}$ couls, where R_i is the impedance of the input resistor.

The complete analytical peak-signal-to-RMS noise models for both the CCD and ICCD are presented in Section A.2.12.

A.2.10 GAIN CALCULATION OF IMAGE INTENSIFIERS FOR USE IN ANALYTICAL MODELS

A.2.10.1 Determination of Gain of Image Intensifier to be used with the SEC Vidicon - The image intensifier consists of a fiber optic faceplate, photocathode, image (accelerating) section, phosphor, and fiber optic endplate. The photoelectron current density, I , resulting from the image plane irradiance is equal to

$$I = \frac{W_p L_p S' \cos \theta}{4r^2 f^2} \int_0^\infty W_{\lambda} P_{\lambda} t''_{o\lambda} \sigma'_{\lambda} d\lambda \quad (A-68)$$

These photoelectrons are accelerated across a potential difference, V_a , within the image section. At the phosphor surface, they have an energy of $e(V_a - V_d)$ electron volts. That is, the input power density to the phosphor is equal to $I(V_a - V_d)$ watts where $I V_d$ represents the energy lost by the electrons in penetrating the conductive coating of the phosphor.

The light output of the phosphor reaches the photocathode of the SEC vidicon after passing through the fiber optic endplate of the intensifier and the fiber optic faceplate of the vidicon. The resulting photoelectron current density, I_t , reaching the SEC target is thus

$$I_t = I(v_a - v_d) L_p S_p \int_0^\infty \phi_\lambda t'_{o\lambda} t_{o\lambda} \sigma_\lambda d\lambda \quad (A-69)$$

Substituting Equation (A-68) for photoelectron current density in the above equation gives

$$I_t = \left[\frac{W t S' \cos\theta}{4r^2 f^2} \int_0^\infty W_\lambda P_\lambda t''_{o\lambda} \sigma'_\lambda d\lambda \right] [(v_a - v_d) L_p S_p \int_0^\infty \phi_\lambda t'_{o\lambda} t_{o\lambda} \sigma_\lambda d\lambda] \quad (A-70)$$

Without the image intensifier, the photoelectron current density, I'_t , would be equal to

$$I'_t = \frac{W t S \cos\theta}{4r^2 f^2} \int_0^\infty W_\lambda P_\lambda t_{o\lambda} \sigma_\lambda d\lambda \quad (A-71)$$

The gain, G_I , of the image intensifier is, therefore, defined to be

$$G_I = \frac{I_t}{I'_t} = \frac{S' L (v_a - v_d) \int_0^\infty W_\lambda P_\lambda t''_{o\lambda} \sigma'_\lambda d\lambda \int_0^\infty \phi_\lambda t'_{o\lambda} t_{o\lambda} \sigma_\lambda d\lambda}{\int_0^\infty W_\lambda P_\lambda t_{o\lambda} \sigma_\lambda d\lambda} \quad (A-72)$$

If we assume that $S_p = S_p'$, $\sigma_\lambda = \sigma_\lambda'$ and $t_{o\lambda} = t'_{o\lambda} = t''_{o\lambda}$, then the gain becomes

$$G_I = (V_a - V_d) S_p L_p \int_0^\infty \phi_\lambda t_{o\lambda}^2 \sigma_\lambda d\lambda \quad (A-73)$$

A.2.11 DETERMINATION OF THE GAIN OF THE IMAGE INTENSIFIER TO BE USED WITH THE SILICON VIDICON AND SLOW-SCAN VIDICON

A derivation similar to that discussed in Section A.2.10.1, leads to an expression for the gain of an image intensifier used with a vidicon having a photoconductor.

Since a fiber optic faceplate must be added to the vidicon, the spectral light intensity striking the photoconductor is similar to the case for the photocathode device. If monochromatic quantum efficiencies, η_λ , are used to express the efficiency of the photoconductor, this spectral light intensity (generally expressed in watts/m²/nanometer) must first be converted into photons/nanometer. The corresponding current, I_{pc} , generated in the photoconductor is therefore equal to

$$I_{pc} = \frac{I(V_a - V_d) L_p e}{hc} \int_0^\infty \phi_\lambda t'_{o\lambda} t_{o\lambda} \eta_\lambda d\lambda \quad (A-74)$$

By substituting Equation (A-70) for, I, we obtain

$$I_{pc} = \left[\frac{W t S' \cos \theta}{4 r^2 f^2} \int_0^{\infty} W_{\lambda} P_{\lambda} t''_{o\lambda} \sigma_{\lambda} ' d\lambda \right] \left[\frac{(v_a - v_d) L e}{hc} \int_0^{\infty} \phi_{\lambda} t'_{o\lambda} t_{o\lambda} \lambda \eta_{\lambda} d\lambda \right] \quad (A-75)$$

In a silicon or slow-scan vidicon tube having no intensifier, the current I'_{pc} generated in the photoconductor would be equal to

$$I'_{pc} = \frac{W t e \cos \theta}{4 hc r^2 f^2} \int_0^{\infty} W_{\lambda} P_{\lambda} \lambda \eta_{\lambda} d\lambda \quad (A-76)$$

The effective gain, G_I , of the image intensifier is then defined to be

$$G_I = \frac{I_{pc}}{I'_{pc}} = \frac{S' L (v_a - v_d) \int_0^{\infty} W_{\lambda} P_{\lambda} t''_{o\lambda} \sigma_{\lambda} ' d\lambda \int_0^{\infty} \phi_{\lambda} t'_{o\lambda} t_{o\lambda} \lambda \eta_{\lambda} d\lambda}{\int_0^{\infty} W_{\lambda} P_{\lambda} \lambda \eta_{\lambda} d\lambda} \quad (A-77)$$

A.2.12 ANALYTICAL PEAK-SIGNAL-TO-RMS-NOISE MODELS FOR SELECTED CANDIDATE SENSORS

The analytical peak-signal-to-RMS-noise models developed in this section are presented in Equations (A-78) through (A-87).

A.2.13 ANALYTICAL MODEL PARAMETERS

Definitions of the parameters used in these models and in the development of these models, and the Fortran symbols which are used in Appendix B, are presented.

SIT VIDICON - SEC VIDICON - SiO₂ VIDICON

$$SNR = \frac{\frac{M_o \tau (K) B n_c G A t W S t_c \cos \theta}{r^2 f^2} \int_0^\infty W_\lambda P_\lambda t_{o\lambda} d\lambda}{\left[\frac{8eI_F B^3 C^2}{S_m^2} + \frac{4kTB}{R_L} + 2eI_D B + \frac{B^2 n_c e G A t W S t_c \cos \theta}{r^2 f^2} \int_0^\infty W_\lambda P_\lambda t_{o\lambda} d\lambda + \beta^2 (G_t + 1) \left(\frac{B^2 n_c^2 e G A t W S t_c \cos \theta}{r^2 f^2} \int_0^\infty W_\lambda P_\lambda t_{o\lambda} d\lambda \right) \right]^{1/2}} \quad (A-78)$$

Preamp FET Shot Noise	Load Imped- ance Thermal Noise	Target Dark Current Shot Noise	Read Beam Shot Noise	Quantum (Image) Noise
-----------------------------	--	--	-------------------------	--------------------------

SILICON VIDICON - SLOW SCAN VIDICON

$$SNR = \frac{\frac{M_o \tau (K) B n_c e A t W t_c \cos \theta}{h c r^2 f^2} \int_0^\infty \lambda W_\lambda P_\lambda t_{o\lambda} \eta_\lambda d\lambda}{\left[\frac{8eI_F B^3 C^2}{S_m^2} + \frac{4kTB}{R_L} + 2eI_D B + \frac{B^2 n_c e^2 A t W t_c \cos \theta}{h c r^2 f^2} \int_0^\infty \lambda W_\lambda P_\lambda t_{o\lambda} \eta_\lambda d\lambda + \beta^2 (\eta + 1) \left(\frac{B^2 n_c^2 e^2 A t W t_c \cos \theta}{h c r^2 f^2} \int_0^\infty \lambda W_\lambda P_\lambda t_{o\lambda} \eta_\lambda d\lambda \right) \right]^{1/2}} \quad (A-79)$$

Preamp FET Shot Noise	Load Imped- ance Thermal Noise	Target Dark Current Shot Noise	Read Beam Shot Noise	Quantum (Image) Noise
-----------------------------	--	--	-------------------------	--------------------------

INTENSIFIED SEC VIDICON

(A-80)

$$SNR = \frac{\frac{M_o \tau_s (K) B n_c G_t G_e A t W S t_i \cos \theta}{r^2 f^2} \int_0^\infty W_\lambda P_\lambda t_{o\lambda} d\lambda}{\left[\frac{8eI_F B^3 C^2}{g_m^2} + \frac{4kTB}{R_L} + 2eI_D B + \frac{B^2 n_c e G_t G_e A t W S t_i \cos \theta}{r^2 f^2} \int_0^\infty W_\lambda P_\lambda t_{o\lambda} d\lambda + [(G_t + 1) G_e] [2B B n_c L S_p (V_a - V_d) \int_0^\infty \sigma_\lambda \phi_\lambda t'_{o\lambda} t_{o\lambda} d\lambda]^2 \left(\frac{e A t W t_i S' \cos \theta}{4r^2 f^2} \int_0^\infty W_\lambda P_\lambda t''_{o\lambda} \sigma_\lambda d\lambda \right) \right]^{1/2}}$$

Preamp FET Shot Noise	Load Imped- ance Thermal Noise	Target Dark Current Shot Noise	Read Beam Shot Noise	Quantum (Image) Noise
-----------------------------	--	--	-------------------------	--------------------------

243

INTENSIFIED SILICON VIDICON - INTENSIFIED SLOW-SCAN VIDICON

(A-81)

$$SNR = \frac{\frac{M_o \tau_s (K) B n_c e A t W t_i \cos \theta}{h c r^2 f^2} \int_0^\infty \lambda W_\lambda P_\lambda t_{o\lambda} \eta_\lambda d\lambda}{\left[\frac{8eI_F B^3 C^2}{g_m^2} + \frac{4kTB}{R_L} + 2eI_D B + \frac{G_t t B^2 n_c e^2 A W t_i \cos \theta}{h c r^2 f^2} \int_0^\infty \lambda W_\lambda P_\lambda t_{o\lambda} \eta_\lambda d\lambda + (\eta + 1) \left(\frac{2B B n_c e L_p (V_a - V_d)}{h c} \int_0^\infty \phi_\lambda t'_{o\lambda} t_{o\lambda} \lambda \eta_\lambda d\lambda \right)^2 \left(\frac{e A t W t_i S' \cos \theta}{4r^2 f^2} \int_0^\infty W_\lambda P_\lambda t''_{o\lambda} \sigma_\lambda d\lambda \right) \right]^{1/2}}$$

Preamp FET Shot Noise	Load Imped- ance Thermal Noise	Target Dark Current Shot Noise	Read Beam Shot Noise	Quantum (Image) Noise
-----------------------------	--	--	-------------------------	--------------------------

RETURN BEAM VIDICON

$$SNR = \frac{M_{os} \tau_s (K) G_M B t_f n_e A t W t_c \cos \theta}{h c r^2 f^2} \int_0^\infty \lambda W_\lambda P_\lambda t_{o\lambda} n_\lambda d\lambda \quad (A-82)$$

$$\left[\frac{8eI_F B^3 C^2}{g_m^2} + \frac{4kTB}{R_L} + 2G_M^2 eB \left[\frac{t_f n_c (1-m_b)}{m_b (\delta_m - 1)} + \frac{t_f n_c}{m_b} + \beta^2 t_f^2 n_c^2 (\eta + 1) \right] \left(\frac{B e A t W t_c \cos \theta}{2 h c r^2 f^2} \int_0^\infty \lambda W_\lambda P_\lambda t_{o\lambda} n_\lambda d\lambda \right) \right]^{1/2}$$

Preamp FET Shot Noise	Load Imped- ance Thermal Noise	Electron Multiplier	Read Beam Shot Noise	Quantum (Image) Noise
-----------------------------	--	------------------------	-------------------------------	-----------------------------

IMAGE ORTHICON

$$SNR = \frac{M_{os} \tau_s (K) G_M B t_f (\delta_t - 1) A t W t_c \cos \theta}{r^2 f^2} \int_0^\infty W_\lambda P_\lambda t_{o\lambda} d\lambda \quad (A-83)$$

$$\left[\frac{8eI_F B^3 C^2}{g_m^2} + \frac{4kTB}{R_L} + 2G_M^2 eB \left(\frac{t_f (\delta_t - 1) (1-m_b)}{m_b (\delta_m - 1)} + \frac{t_f (\delta_t - 1)}{m_b} + \beta^2 t_f^2 (\kappa - \delta_t) \delta_t + \beta^2 t_f^2 (\delta_t - 1)^2 \right) \left(\frac{B A t W S t_c \cos \theta}{2 r^2 f^2} \int_0^\infty W_\lambda P_\lambda t_{o\lambda} d\lambda \right) \right]^{1/2}$$

Preamp FET Shot Noise	Load Imped- ance Thermal Noise	Electron Multiplier	Read Beam Shot Noise	Secondary Emission Noise at Target	Quantum (Image) Noise
-----------------------------	--	------------------------	-------------------------	---------------------------------------	-----------------------------

IMAGE ISOCON

$$\frac{M_o \tau_s (K) G_M B K_s \alpha (\delta_t - 1) A_t t_m W S t_e \cos \theta}{r^2 f^2} \int_0^\infty W_\lambda P_\lambda t_{o\lambda} \sigma_\lambda d\lambda \quad (A-84)$$

$$SNR = \left[\frac{8eI_F B^3 C^2}{g_m^2} + \frac{4kTB}{R_L} + 2G_M^2 eB \left[K_s \alpha_s \frac{\delta_t - 1}{\delta_m - 1} + K_s K_D (\delta_t - 1) + K_s \alpha_s (\delta_t - 1) + \beta^2 K_s^2 \alpha_s^2 (\kappa - \delta_t) \delta_t + \beta^2 K_s^2 \alpha_s^2 (\delta_t - 1)^2 \right] \left(\frac{B A t_m t_e W S t_e \cos \theta}{2r^2 f^2} \int_0^\infty W_\lambda P_\lambda t_{o\lambda} \sigma_\lambda d\lambda \right) \right]^{1/2}$$

Preamp FET Shot Noise	Load Imped- ance Thermal Noise	Electron Multiplier	Separation Dark Current	Read Beam Shot Noise	Secondary Emission Noise at Target	Quantum (Image) Noise
-----------------------------	--	------------------------	----------------------------	-------------------------------	---------------------------------------	-----------------------------

245

ELECTROSTATIC CAMERA SYSTEM

$$\frac{M_o \tau_s (K) G_M m \delta I_b G_t t_e W S \cos \theta}{2C * r^2 f^2} \int_0^\infty W_\lambda P_\lambda t_{o\lambda} \sigma_\lambda d\lambda \quad (A-85)$$

$$SNR = \left[\frac{8eI_F B^3 C^2}{g_m^2} + \frac{4kTB}{R_L} + G_M^2 \left(2eI_b B \left(\frac{a \delta_t}{\delta_m - 1} + a^2 \delta_t^2 + a^2 [\kappa - \delta_t] \delta_t + a[1-a] \delta_t \right) + \left[\frac{m \delta I_b}{C * A} \right]^2 \left(\frac{eI_b [1 + (\kappa - 2) \delta_t]}{2B} + \beta^2 [G_t + 1] \left[\frac{eG A t_e t_m W S \cos \theta}{4r^2 f^2} \int_0^\infty W_\lambda P_\lambda t_{o\lambda} \sigma_\lambda d\lambda \right] \right) \right) \right]^{1/2}$$

Preamp FET Shot Noise	Load Imped- ance Thermal Noise	Read Beam Shot Noise	Modified By Electron Mult. Noise	Mult. at Read- Out Dielectric	Secondary Emission Noise of Dielectric	Energy Analyzer Partition Noise	Dielectric Charging Noise during Readout	Quantum (Image) Noise
-----------------------------	--	-------------------------------	---	---	--	--	---	--------------------------

CHARGE COUPLED IMAGER

$$SNR = \frac{(1-n\epsilon_c) \frac{M_o \tau_s (K) e A t W t_{oL} \cos \theta}{2 h c r^2 f^2} \int_0^\infty \lambda W_\lambda P_\lambda t_{oL} \eta_\lambda d\lambda}{\left[\frac{kT}{R_1 B} + \frac{2eI_{FBC}^2}{g_m^2} + X + Y + 2eI_{Dint} + \frac{2enI_D}{B_c} + \beta^2 (\eta+1) \left(\frac{e^2 A t W t_{oL} \cos \theta}{4 h c r^2 f^2} \int_0^\infty \lambda W_\lambda P_\lambda t_{oL} \eta_\lambda d\lambda \right) \right]^{1/2}} \quad (A-86)$$

Preamp Input Imped- ance Thermal Noise	Preamp FET Shot Noise	Interface State Noise	Target Current Noise	Dark Current Noise	Quantum (Image) Noise
---	--------------------------------	-----------------------------	----------------------------	--------------------------	--------------------------

INTENSIFIED (PHOTOEMITTER) CHARGE COUPLED IMAGER

$$SNR = \frac{(1-n\epsilon_c) \frac{M_o \tau_s (K) G A t W S t_{oL} \cos \theta}{2 r^2 f^2} \int_0^\infty W_\lambda P_\lambda t_{oL} \sigma_\lambda d\lambda}{\left[\frac{kT}{R_1 B} + \frac{2eI_{FBC}^2}{g_m^2} + X + Y + 2eI_{Dint} + \frac{2enI_D}{B_c} + \beta^2 (G_t+1) \left(\frac{e G A t W S t_{oL} \cos \theta}{4 r^2 f^2} \int_0^\infty W_\lambda P_\lambda t_{oL} \sigma_\lambda d\lambda \right) \right]^{1/2}} \quad (A-87)$$

Preamp Input Imped- ance Thermal Noise	Preamp FET Shot Noise	Interface State Noise	Target Current Noise	Dark Current Noise	Quantum (Image) Noise
---	--------------------------------	-----------------------------	----------------------------	--------------------------	--------------------------

$$X = \left(\frac{kTN_t (\omega_{integ}) A_c e^2}{\alpha_p} \right) \ln \left(\frac{1}{\omega_{integ} \tau_y} \right) + \frac{4kTN_t (\omega_{integ}) A_c e^2}{\alpha_p}$$

$$Y = \left(\frac{kTN_t (\omega_c) A_c e^{2n}}{\alpha_p} \right) \ln \left(\frac{1}{\omega_c \tau_y} \right) + \frac{4kTN_t (\omega_c) A_c e^{2n}}{\alpha_p} \quad \left(\text{For } \omega_c < \frac{1}{\tau_y} \right)$$

$$Y = \frac{4kTN_t (\omega_c) A_c e^{2n}}{\alpha_p \omega_c \tau_y} \quad \left(\text{For } \omega_c > \frac{1}{\tau_y} \right)$$

LIST OF ANALYTICAL MODEL PARAMETERS

<u>TEXT SYMBOL</u>	<u>PROGRAM SYMBOL</u>	<u>DESCRIPTION</u>	<u>UNITS</u>
A	AELEM	AREA OF ELEMENT	m ²
A _c	AELEM	AREA OF CCD MIS CAPACITOR	m ²
A _b	ABEAM	AREA OF READ BEAM	m ²
A _k		RESOLUTION ELEMENT AREA	m ²
A _m	SMEAR	SMEAR IN IMAGE PLANE	m ²
a	A	FRACTION OF RETURN BEAM PASSING THROUGH ENERGY ANALYZER	
a _o		LENGTH OF THE SEMIMAJOR AXIS	m
α _s		SCATTER GAIN OF IMAGE ISOCON TARGET	
α _p		PARAMETER CHARACTERIZING TUNNELING PROBABILITY	
α	ALP	SILICON ABSORPTION COEFFICIENT AT WAVELENGTH OF INTEREST	m ⁻¹
B	BAND	VIDEO BANDWIDTH	hertz
B _C	BC	CLOCK (TRANSFER) FREQUENCY	sec ⁻¹
b _r		BIT RATE	bits/sec
b		TARGET STORAGE CHARGE	electrons/ res. ele.
β	BB	NOISE BANDWIDTH CORRECTION FACTOR	
β ₂		NOISE CORRECTION FACTOR	
C	CS	CAPACITANCE (PREAMP SHUNT CAPACITANCE)	Farads
C*	C	CAPACITANCE PER UNIT AREA (TARGET)	Farads/m ²
C _R	CR	CONTRAST RATIO	
c	C	VELOCITY OF LIGHT	3 x 10 ⁸ m/sec
D		OPTICAL LENS DIAMETER	m

<u>TEXT SYMBOL</u>	<u>PROGRAM SYMBOL</u>	<u>DESCRIPTION</u>	<u>UNITS</u>
D_h	D	HOLE DIFFUSION CONSTANT IN n-TYPE SILICON	m^2/sec
D_s		DIAMETER OF RIGHT CIRCULAR CYLINDER	m
d	D	DIAMETER OF ELECTRON BEAM	m
d_p	DP	ONE HALF CENTER TO CENTER SPACING OF DIODES	m
δ_t	SET	SECONDARY EMISSION YIELD OF TARGET	
δ_m	SEM	SECONDARY EMISSION YIELD OF FIRST DYNODE OF ELECTRON MULTIPLIER	
E		THE AVERAGE LEVEL OF LIGHT INTENSITY	W/m^2
E_{max}		MAXIMUM INTENSITY OF LIGHT	W/m^2
E_{min}		MINIMUM INTENSITY OF LIGHT	W/m^2
ΔE		DIFFERENCE OF MAXIMUM AND MINIMUM LIGHT INTENSITY	W/m^2
E_o		ELLIPTIC INTEGRAL OF THE FIRST ORDER	
e	Q	ELECTRONIC CHARGE	1.6×10^{-19} coul
ϵ_c	EC	FRACTION OF CHARGE CAPTURED FROM ONE PACKET AND EMITTED INTO TRAILING PACKET	
e_o		ECCENTRICITY OF THE ORBIT	
η_λ		MONOCHROMATIC QUANTUM EFFICIENCY	electrons/ proton
η	QE	INTEGRAL QUANTUM EFFICIENCY	electrons/ proton
	QEP	QUANTUM EFFICIENCY PEAK	electrons/ proton
	QEPC	RELATIVE QUANTUM EFFICIENCY OF PHOTOCONDUCTOR	

<u>TEXT SYMBOL</u>	<u>PROGRAM SYMBOL</u>	<u>DESCRIPTION</u>	<u>UNITS</u>
F	FOC	FOCAL LENGTH	m
F _G	FT	SCENE NOISE FACTOR	
F _O		INPUT FLUX DENSITY AT IMAGE PLANE	W/m ²
F _L		INPUT FLUX (OR FLUX DENSITY)	W (or W/m ²)
F _{pc}	FLUX	INPUT FLUX (OR FLUX DENSITY) AT PHOTOCATHODE	W (or W/m ²)
F _v	FLUX	RATE OF FLUX OF PHOTONS	photons/sec
f	FNUM	F-NUMBER OF OPTICAL SYSTEM	
φ _λ	AP20	RELATIVE SPECTRAL OUTPUT OF PHOSPHOR	
G _I	GS20	IMAGE INTENSIFIER CURRENT GAIN WHEN COUPLED TO AN S-20 PHOTOCATHODE	
G _I	GSSV	IMAGE INTENSIFIER CURRENT GAIN WHEN COUPLED TO A SLOW SCAN VIDICON	
G _I	GSV	IMAGE INTENSIFIER CURRENT GAIN WHEN COUPLED TO A SILICON VIDICON	
G _I	GI	IMAGE INTENSIFIER CURRENT GAIN	
G _M	GM	GAIN OF ELECTRON MULTIPLIER	
	GR	SPATIAL FREQUENCY EQUIVALENT TO ONE PIXEL SMEAR	lp/mm
G		GROUND RESOLUTION	m
	GRS	SMEAR IN GROUND PLANE	m
G _t	GT	GAIN OF TARGET	
g		ENCODING PRECISION	bits/pixel
g _m	GMFET	FET TRANSCONDUCTANCE	amp/volt
H	ALT	SPACECRAFT ALTITUDE ABOVE PLANET SURFACE	m
h	H	PLANCK'S CONSTANT	6.62 x 10 ⁻³⁴ J·sec
I	CURD	DETECTOR OUTPUT CURRENT DENSITY	amps/m ²

<u>TEXT SYMBOL</u>	<u>PROGRAM SYMBOL</u>	<u>DESCRIPTION</u>	<u>UNITS</u>
I_i		CURRENT FROM TARGET	amps
I_b	BEAM	READOUT BEAM CURRENT	amps
I_D	IDARK	DARK CURRENT	amps or amp/m ²
I_F	IFET	FET CHANNEL CURRENT	amps
I_S	SIGSYS	SIGNAL CURRENT	amps
I_{pc}		PHOTOCONDUCTOR CURRENT WITH IMAGE INTENSIFIER	amps
I'_{pc}		PHOTOCONDUCTOR CURRENT WITHOUT IMAGE INTENSIFIER	amps
i_d	UDARK	TARGET DARK CURRENT SHOT NOISE	amps
i_e	UMULT	NOISE CURRENT ASSOCIATED WITH ELECTRON MULTIPLIER	amps
i_i		OUTPUT NOISE CURRENT ASSOCIATED WITH INPUT SIGNAL	amps
i_{nc}		OUTPUT NOISE CURRENT DUE TO V_{nc}	amps
i_{nd}		OUTPUT NOISE CURRENT DUE TO V_{nd}	amps
i_r	UREAD	SHOT NOISE IN READ BEAM	amps
i_s		SECONDARY EMISSION NOISE CURRENT	amps
i_t	UAMPL	THERMAL NOISE CURRENT	amps
i_p		PARTITION NOISE CURRENT	amps
	UBEAM	READ BEAM SHOT NOISE (ESC)	amps
	UANAL	ENERGY ANALYZER PARTITION NOISE (ESC)	amps
	UDIEL	DIELECTRIC CHARGING NOISE DURING READOUT (ESC)	amps
	UQUANT	QUANTUM (IMAGE) NOISE	amps
	ULOAD	PREAMPLIFIER FET SHOT NOISE	amps
	USCENE	QUANTUM (IMAGE) NOISE	amps
K	SPAT	SPATIAL FREQUENCY	lp/mm or cycle/mm

<u>TEXT SYMBOL</u>	<u>PROGRAM SYMBOL</u>	<u>DESCRIPTION</u>	<u>UNITS</u>
K_s		SIGNAL REDUCTION FACTOR	
K_D		IMAGE ISOCON INCOMPLETE SEPARATION FACTOR	
k	BK	BOLTZMANN'S CONSTANT	$1.38 \times 10^{-23} \text{ J/}^\circ\text{K}$
k_t	DK	DIELECTRIC CONSTANT	
κ		VAN DER ZEIL'S CORRECTION FACTOR	
l		FORMAT SIZE	mm
L_a	LA	THICKNESS OF UNDEPLETED REGION	m
L_b	LB	THICKNESS OF THE N-TYPE REGION PLUS WIDTH OF DEPLETED REGION	m
L_o	LO	DIFFUSION LENGTH	m
L_p	PP20	PEAK MONOCHROMATIC OUTPUT OF PHOSPHOR	W/W/m
λ	WAVE	WAVELENGTH	m
m	M	SLOPE OF READOUT CHARACTERISTIC	amp/amp/volt
m_b	M	BEAM MODULATION FACTOR	
MTBF		MEAN TIME BETWEEN FAILURES	sec
MTF		MODULATION TRANSFER FUNCTION	
$M_a(K)$	TAVA	AVAILABLE AERIAL IMAGE MODULATION	
$M_i(K)$		IMAGE MODULATION	
M_o	TSCENE	OBJECT MODULATION (SCENE)	
$M_d(K)$	TMA	THRESHOLD MODULATION (EXCLUDES AVAILABLE IMAGE MODULATION FROM SNR CALCULATION)	
N_d		NOISE ELECTRONS ASSOCIATED WITH DISCHARGING A RESOLUTION ELEMENT	ele/res. ele.
N_F		TOTAL NUMBER OF FAILURES	
$N_t(E)$		NUMBER OF INTERFACE STATES PER UNIT VOLUME PER UNIT ENERGY AS A FUNCTION OF ENERGY	$\text{m}^{-3} \text{joule}^{-1}$

<u>TEXT SYMBOL</u>	<u>PROGRAM SYMBOL</u>	<u>DESCRIPTION</u>	<u>UNITS</u>
$N_t(W_{\text{integ}})$	NIL	NUMBER OF INTERFACE STATES ASSOCIATED WITH W_{integ}	$m^{-3} \text{joule}^{-1}$
$N_t(W_c)$	NTCL	NUMBER OF INTERFACE STATES ASSOCIATED WITH W_c	$m^{-3} \text{joule}^{-1}$
\bar{n}		AVERAGE NUMBER OF PHOTONS/RESOLUTION ELEMENT	photons/res.ele
n	TN	NUMBER OF TRANSFERS OF CHARGE PACKET	
n_c	RE	READOUT CONVERSION EFFICIENCY	
n_p		NUMBER OF RESOLUTION ELEMENTS	
ν		FREQUENCY OF LIGHT FROM SCENE	sec^{-1}
	PA	PHASE ANGLE	radians
P_λ	AJUP	GEOMETRIC ALBEDO (JUPITER)	
	PIX	PIXEL	m
P_c		DESIRED CONFIDENCE LEVEL OF MTBF	
Q_d		CHARGE DENSITY	couls/res.ele
Q'_d		CHARGE REMOVED FROM EACH RES. ELEMENT	couls
Q		CHARGE FOR FULL TARGET CAPACITY	couls/res.ele
Q_{in}	Q	INPUT CHARGE DENSITY FROM PHOTOCATHODE	couls/m^2
Q_{nd}		NOISE CHARGE ASSOCIATED WITH THE INPUT SIGNAL	couls/res. ele
Q_{qn}		NOISE CHARGE AT PHOTOCATHODE OF THE IMAGE INTENSIFIER	couls/res. ele
Q_s		OUTPUT CCD SIGNAL CHARGE	couls
q_n		NOISE CHARGE	couls
q_{nFET}		NOISE CHARGE DUE TO FET CHANNEL CURRENT	couls

<u>TEXT SYMBOL</u>	<u>PROGRAM SYMBOL</u>	<u>DESCRIPTION</u>	<u>UNITS</u>
q_s		NOISE ELECTRONS FROM EACH RESOLUTION ELEMENT	electrons/ res. ele
R	R	SILICON REFLECTIVITY AT WAVELENGTH OF INTENSITY	
R_e		RELIABILITY	
R_D	RESP	RESPONSIVITY OF DETECTOR	amp/W
R_i	RI	INPUT IMPEDANCE OF PREAMPLIFIER	ohms
R_J	RJ	RADIUS OF PLANET	m
R_L	RL	OUTPUT LOAD IMPEDANCE	ohms
R_s	SPIN	SPACECRAFT SPIN RATE	rpm
r	AUJ	SUN-PLANET DISTANCE IN ASTRONOMICAL UNITS (JUPITER)	A.U.
S(K)	SIGSYS	OUTPUT SIGNAL	amps
S_v	S	SURFACE RECOMBINATION VELOCITY HOLES AT THE ILLUMINATED SURFACE	m^2/sec
smear		IMAGE SMEAR	m
SNR(K)	SNR	SIGNAL-TO-NOISE RATIO	
SNR_L	SNRL	LIMITING THRESHOLD SIGNAL-TO-NOISE RATIO	
S_p	S20P	PEAK MONOCHROMATIC RESPONSIVITY OF THE DETECTOR (S-20)	amp/W
S_p'		INTENSIFIER PHOTOCATHODE SENSITIVITY	coul/J
$S_q(W)$		SPECTRAL DENSITY OF THE MEAN-SQUARE MINORITY CARRIER CHARGE DENSITY FLUCTUATIONS	coul ²
S_o		OPTICAL SIGNAL	W/m^2
	SNRAIM	SIGNAL-TO-NOISE RATIO (EXCLUDES AVAILABLE AERIAL IMAGE MODULATION FROM SNR CALCULATION)	

<u>TEXT SYMBOL</u>	<u>PROGRAM SYMBOL</u>	<u>DESCRIPTION</u>	<u>UNITS</u>
	SIGAVA	SIGNAL (EXCLUDES AVAILABLE AERIAL IMAGE MODULATION FROM SIGNAL CALCULATION)	amps
σ		STANDARD DEVIATION	
σ_{λ}	RS20	RELATIVE SPECTRAL DISTRIBUTION OF DETECTOR S-20	
σ_{λ}'		RELATIVE SPECTRAL RESPONSE OF INTENSIFIER PHOTOCATHODE	
T_{integ}		INTEGRATION (EXPOSURE) TIME	sec
T	TEMP	TEMPERATURE (KELVIN)	$^{\circ}\text{K}$
T_T		TOTAL SYSTEM TEST TIME	sec
	TM	THRESHOLD MODULATION	
T_o		SPACECRAFT ORBITAL PERIOD	sec
t_L	TL	TRANSMISSION OF OPTICAL SYSTEM	
t_m		TRANSMISSION OF COLLECTOR MESH	
t_e	EXPT	EXPOSURE TIME	sec
t_e^{opt}		OPTIMUM EXPOSURE TIME	sec
t_1	T1	TARGET THICKNESS	m
t_2	T2	TARGET-TO-MESH SPACING	m
t_i	L	THICKNESS OF INTERFACE TRANSITION REGION	m
t_f	TF	TRANSMISSION OF FIELD MESH	
$t_{o\lambda}$		SPECTRAL TRANSMISSION OF SENSOR FACEPLATE	
$t'_{o\lambda}$		SPECTRAL TRANSMISSION OF INTENSIFIER ENDPLATE	
$t''_{o\lambda}$		SPECTRAL TRANSMISSION OF INTENSIFIER FIBER OPTICS FACEPLATE	
Δt		READOUT TIME	sec

<u>TEXT SYMBOL</u>	<u>PROGRAM SYMBOL</u>	<u>DESCRIPTION</u>	<u>UNITS</u>
$\tau(K)$		RESPONSE FOR SINE WAVE OF K CYCLES/MM	
$\tau_{sen}(K)$	TCAM	MTF OF SENSOR	
$\tau_s(K)$	TSYS	MTF OF SYSTEM	
$\tau_{lens}(K)$	TLEN	MTF OF LENS	
$\tau_{IM}(K)$	TMOT	MTF DUE TO IMAGE MOTION	
$\tau_T(K)$	TTAR	MTF OF TARGET	
$\tau_{is}(K)$	TIS	MTF OF IMAGE SECTION	
$\tau_R(K)$	TELB	MTF OF READOUT BEAM	
$\tau_{rec}(K)$		MTF OF RECORDER	
$\tau_i(K)$	TII	MTF OF INTENSIFIER	
	TFIB	MTF OF FIBER OPTICS	
	TMES	MTF OF TRANSMISSION MESH	
θ	PAD	PHASE ANGLE	degrees
θ_v		FIELD OF VIEW	radians
$\tau_H(K)$	TLD	MTF OF SILICON TARGET DUE TO LATERAL HOLE DIFFUSION	
$\tau_D(K)$	TDS	MTF OF SILICON TARGET DUE TO DIODE SPACING	
$\tau_E(K)$	TFS	MTF OF SILICON TARGET DUE TO FIRST SCAN EFFECT	
τ_y	TS	TIME CONSTANT OF INTERFACE STATE FOR Y=0 SEC (WHERE Y= DISTANCE FROM SILICON INTO TRANSITION REGION)	
V_a	V	IMAGE INTENSIFIER ACCELERATING VOLTAGE	volts
V_d	VP	DEAD VOLTAGE LOST IN PENETRATING PHOSPHOR	volts

<u>TEXT SYMBOL</u>	<u>PROGRAM SYMBOL</u>	<u>DESCRIPTION</u>	<u>UNITS</u>
\bar{v}		AVERAGE SPACECRAFT VELOCITY	km/sec
ΔV		CHANGE IN TARGET SURFACE POTENTIAL	volts
v_s		VELOCITY OF IMAGE WITH RESPECT TO OBJECT	m/sec
v_{nd}		NOISE TARGET VOLTAGE CORRESPONDING TO NOISE CHARGE, Q_{nd}	volts
v_{nc}		CHARGING NOISE VOLTAGE DUE TO TARGET	volts
v_p		VELOCITY OF SPACECRAFT AT PERIAPSIS	km/sec
w_p	SIRP	PEAK SPECTRAL DENSITY OF INPUT FLUX	$W/m^2/nm$
w_λ	RSIR	RELATIVE SPECTRAL DISTRIBUTION OF THE INPUT FLUX	
ω		RADIAN FREQUENCY	rad/sec
ω_p		ANGULAR VELOCITY OF SPACECRAFT AT PERIAPSIS	rad/sec
ω_c	WC	CLOCK (TRANSFER) RADIAN FREQUENCY	rad/sec
ω_{integ}		INTEGRATION RADIAN FREQUENCY	rad/sec
ω_s		SPIN ANGULAR VELOCITY	rad/sec
ω_{tot}		RELATIVE ANGULAR VELOCITY OF THE SPACECRAFT WITH RESPECT TO JUPITER AT PERIAPSIS	rad/sec
X	X	INTERFACE STATE NOISE CONTRIBUTION DURING INTEGRATION TIME (CCD)	couls ²
χ^2		CHI-SQUARE VALUE OF $2N_F + 1$ DEGREES OF FREEDOM OF CONFIDENCE LEVEL P_c .	
x	H	SECONDARY EMISSION NOISE FACTOR	
Y	Y	INTERFACE STATE NOISE CONTRIBUTION DURING CHARGE TRANSFER (CCD)	couls ²

APPENDIX B

PREPARATION OF COMPUTER PROGRAMS

B.1 INTRODUCTION

Computer programs have been developed for the signal-to-noise-ratio models of the candidate imaging systems and were used to perform the parametric analysis in Sections 7 and 8. These programs were written in FORTRAN IV for interactive use on the Computer Sciences Corporation Univac 1108 computer timesharing system.

This appendix presents the computer programs. First, the SIT vidicon model is used as a representative example to illustrate how the models have been structured. Computational flow diagrams for the SIT vidicon main program and subroutines are shown along with a line-by-line description of the program. Samples of the input and output are included, as well as a symbolic listing of the programs for all of the camera systems. A symbol list showing both text and FORTRAN symbols is given in Appendix A.

B.2 COMPUTER PROGRAMS

The analytical models for the camera systems have been written in FORTRAN IV computer language. A separate main program exists for each sensor type. Subroutines common to several camera models were used whenever possible to simplify the programming task. A list of the main programs and subroutines along with a brief statement of the purpose of each is shown in the Computer Program Summary Matrix, Figure B-1.

COMPUTER PROGRAMS SUMMARY MATRIX

		SUBROUTINES							PURPOSE
		VTAR	IRWATT	MTFAYA	SDTAR	IRWATM			
MAIN PROGRAMS	NAME	NAME							
	SECV (2)	X	X	X		X			SEC VIDICON CAMERA (1) ANALYTICAL MODEL
	SITV		X	X					SIT VIDICON CAMERA ANALYTICAL MODEL
	RBV	X		X					RETURN BEAM VIDICON ANALYTICAL MODEL
	SILV			X					SILICON VIDICON (1) ANALYTICAL MODEL
	SSV	X		X					SLOW SCAN VIDICON (1) ANALYTICAL MODEL
	ESC (2)		X	X	X	X			ELECTROSTATIC CAMERA ANALYTICAL MODEL
	SDV		X	X	X				SILICON DIOXIDE VIDICON ANALYTICAL MODEL
	CCD			X					CHARGE-COUPLED DEVICE ANALYTICAL MODEL
	ICCD (2)			X		X			INTENSIFIED CHARGE-COUPLED DEVICE ANALYTICAL MODEL
PURPOSE	<div style="display: flex; justify-content: space-between;"> <div style="width: 45%;"> <p style="font-size: small; margin: 0;">CALCULATES MTF OF TARGET FOR SECV, SSV AND RBV</p> <p style="font-size: small; margin: 0;">CALCULATES INPUT FLUX, CURRENT DENSITY, & RESPONSIVITY</p> <p style="font-size: small; margin: 0;">CALCULATES AVAILABLE MTF DUE TO CONTRAST, MOTION & LENS</p> <p style="font-size: small; margin: 0;">CALCULATES MTF OF SILICON DIOXIDE AND ASOS TARGET</p> <p style="font-size: small; margin: 0;">CALCULATES FLUX, CURRENT DENSITY & RESPONSIVITY (MAGNETIC FOCUS)</p> </div> <div style="width: 45%;"> <p style="font-size: small; margin: 0;">(1) WITH OR WITHOUT IMAGE INTENSIFIER STAGE</p> <p style="font-size: small; margin: 0;">(2) MAGNETICALLY FOCUSED CAMERA PROGRAMS :</p> <p style="font-size: small; margin: 0;">ESC MF</p> <p style="font-size: small; margin: 0;">SEC MF</p> <p style="font-size: small; margin: 0;">ICCD</p> </div> </div>								

FIGURE B-1

Most of the programs representing models of the camera systems are quite similar in structure. Therefore, in order to avoid repetition, only the SIT vidicon model will be discussed in detail.

B.3 SIT VIDICON COMPUTER PROGRAM

A description of the SIT vidicon program includes the main program SITV and the associated subroutines IRWATT and MTFAVA. The signal-to-RMS-noise expression for the SIT vidicon, Equation (B-1), illustrates how the subroutines are used to calculate the various terms.

Calculated by
Main Program
SITV

Calculated by
Subroutine
IRWATT

$$\text{SNR} = \left[\frac{8\sigma_I^2 B^3 C^2}{g_m^2} + \frac{4kTB}{R_L} + 2\sigma_{ID}^2 + \frac{B^2 n_c e C A t W S t_c \cos \theta}{r^2 f^2} \int_0^{\infty} W_{\lambda} P_{\lambda} t_{o\lambda} d\lambda + \beta^2 (G_t + 1) \left(\frac{B^2 n_c^2 e C A t W S t_c \cos \theta}{r^2 f^2} \int_0^{\infty} W_{\lambda} P_{\lambda} t_{o\lambda} d\lambda \right) \right]^{1/2}$$

$$M_{OS}(K) \frac{B n_c e C A t W S t_c \cos \theta}{r^2 f^2} \int_0^{\infty} W_{\lambda} P_{\lambda} t_{o\lambda} d\lambda$$

$$\frac{B^2 n_c^2 e C A t W S t_c \cos \theta}{r^2 f^2} \int_0^{\infty} W_{\lambda} P_{\lambda} t_{o\lambda} d\lambda$$

SIT VIDICON MODEL

where,

$$M_{OS}(K) = M_{OIM}(K) \tau_{LENS}(K) \tau_{IS}(K) \tau_T(K) \tau_R(K)$$

Calculated by
Subroutine
MTFAVA

SITV is the call name of the main program for the SIT vidicon.

It controls the bulk of the input/output statements and performs the signal-to-noise ratio and threshold modulation calculations. The subroutine IRWATT, which is common to all camera programs that utilize photoemissive cathodes, calculates the integral expression shown in equation (B-1).

Actual computation requires taking the integral of the product of several wavelength-dependent factors, including the input flux at the image plane, the geometric albedo of the planet, the transmission of the fiber optics, and the detector spectral response. MTFAVA calculates the available aerial image modulation transfer function, which combines the MTFs due to the lens assembly, image motion, and the image modulation.

B.3.1 SIT VIDICON FLOW DIAGRAMS

Computational Flow Diagrams for SITV and subroutines IRWATT and MTFAVA are shown in Figures B-2 and B-3.

B.3.2 SIT VIDICON PROGRAM DESCRIPTION

A symbolic listing of SITV and its subroutines are given.

A brief line-by-line description for SITV and its subroutines will clarify the construction of the program.

FLOWCHART - SITV PROGRAM

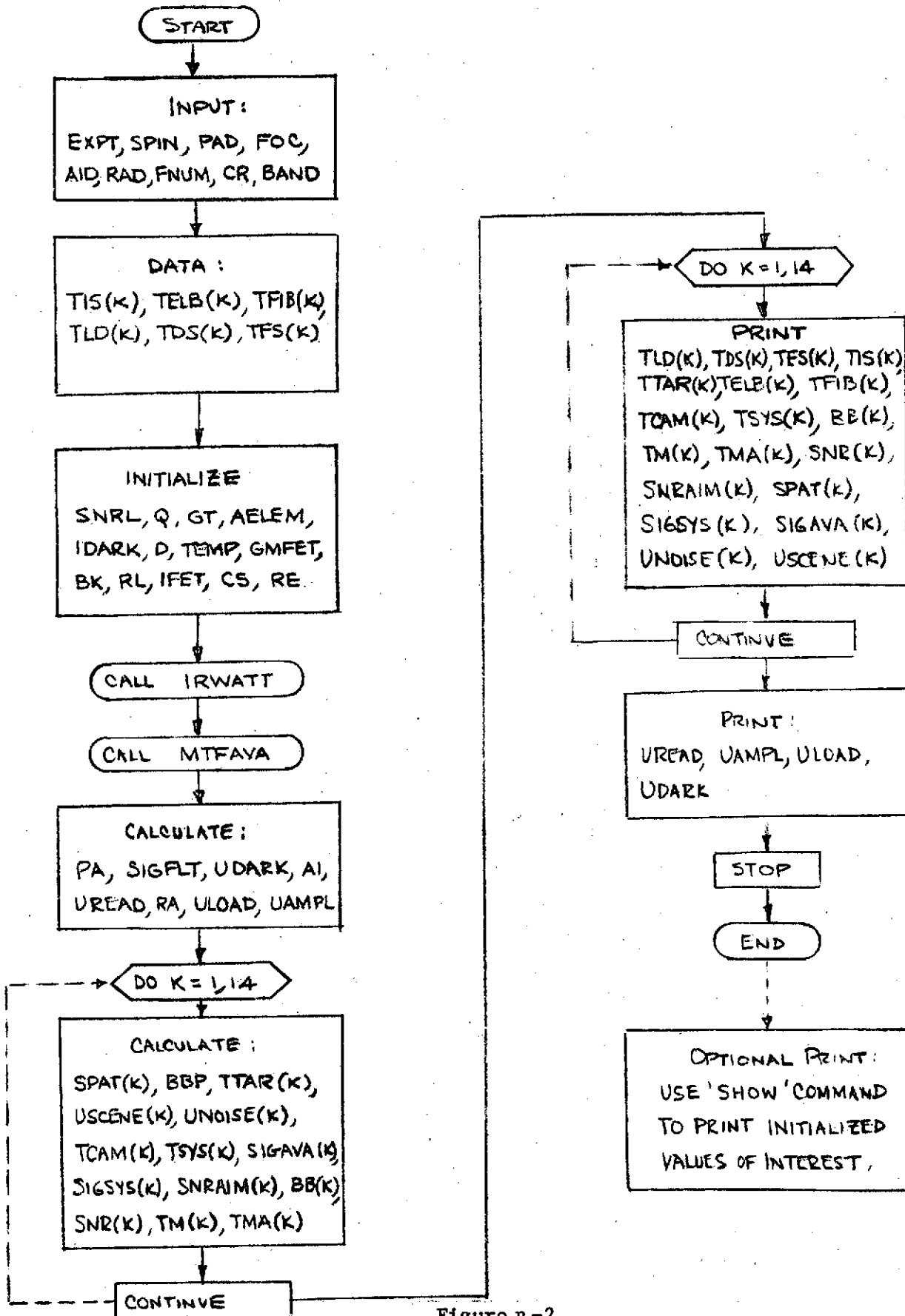


Figure B-2
261

FLOWCHART - SUBROUTINE RWATT

FLOWCHART - SUBROUTINE MTFAYA

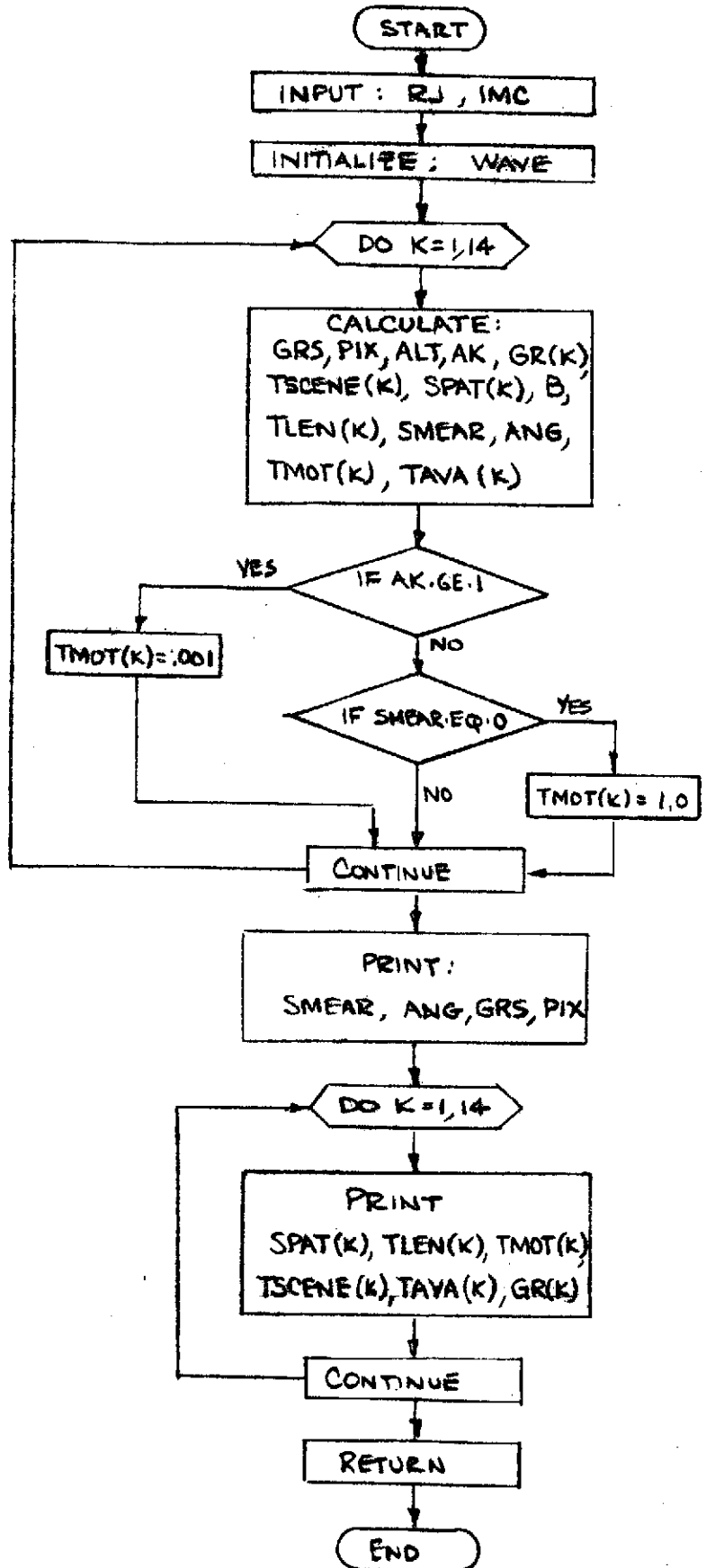
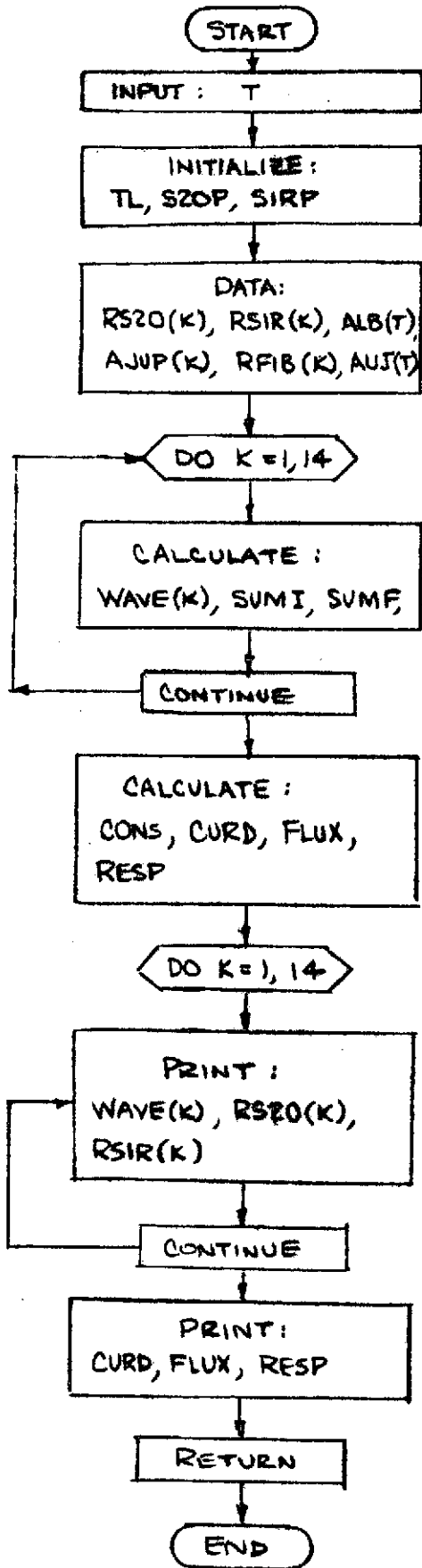


Figure B-3

SITV PROGRAM LIST

```

100 PRINT*, 'ANALYTICAL MODEL OF SIT VIDICON CAMERA
105 PRINT*, 'WITH ELECTROSTATIC IMAGE SECTION'
110 DIMENSION SNRAIM(14), SNR(14), TM(14), TCAM(14)
115 DIMENSION TSYS(14), TIS(14), TELB(14), TFI(14), SPAT(14)
120 DIMENSION BB(14), USCENE(14), UNOISE(14), SIGAVA(14)
125 DIMENSION TFAR(14), TLD(14), TDS(14), TFS(14)
130 DIMENSION SIGSYS(14), TMA(14)
135 COMMON CURD, FLUX, RESP, TAVA(14)
140 REAL IDARK, IFET
145 DATA TIS/.98,.9,.79,.65,.51,.36,.22,.08,.001,.001,*
150 .001,.001,.001,.001/
155 DATA TELB/.98,.965,.94,.905,.855,.78,.72,.66,.61,.56,*
160 .52,.46,.41,.36/
165 DATA TFI/.995,.98,.95,.9,.83,.75,.67,.62,.54,.5,.45,*
170 .4,.35,.3/
175 10 READ(5,*, PROMPT='EXPOSURE(SEC), SPIN RATE(RPM), %
180 BANDWIDTH (:') EXPT, SPIN, BAND
185 20 READ(5,*, PROMPT='FOCAL LENGTH(M), F NUMBER, CONTRAST %
190 RATIO (:') FOC, FNUM, CR
195 30 READ(5,*, PROMPT='PHASE ANGLE, INCIDENCE ANGLE, %
200 REFLECTION ANGLE (DEGREES) (:') PAI, AID, RAD
205 PA=PAI/57.2958
210 AI=AID/57.2958
215 RA=RAD/57.2958
220 Q=1.602E-19
225 GI=2000.
230 D=20.E-6
235 AELEM=(3.1416/4.)*D**2
240 IDARK=1.E-9
245 SNRL=3.
250 TEMP=233.
255 BK=1.38E-23
260 RL=2.E8
265 IFET=7.E-3
270 GMFET=13.4E-3
275 CS=20.E-12
280 RE=.9
285 CALL IRWATE(PA, AI, RA, FNUM)
290 CALL MIFAVA(FNUM, SPIN, EXPT, FOC, CR)
295 DATA TLD/.98,.926,.851,.772,.704,.64,.59,.55,.51,.47,.001,.001,
.001,.001/
300 DATA TDS/.99,.958,.908,.84,.757,.662,.568,.45,.341,.234,.133,
.042,.011,.011/
305 DATA TFS/.911,.833,.764,.702,.648,.599,.555,.516,.481,.45,
.42,.396,.373,.352/
308 DO 290 K=1,14
310 TFAR(K)=TLD(K)*TDS(K)*TFS(K)
312 290 CONTINUE
315 PRINT 305, (TLD(I), I=1,14)
320 PRINT 310, (TDS(I), I=1,14)
325 PRINT 315, (TFS(I), I=1,14)
330 PRINT 320, (TFAR(I), I=1,14)

```

```

335      305 FORMAT(' TLD      ',3X,14F6.3)
340      310 FORMAT(' TDS      ',3X,14F6.3)
345      315 FORMAT(' TFS      ',3X,14F6.3)
350      320 FORMAT(' TIAR     ',3X,14F6.3)
355      DO 30 K=1,14
360      SPAT(K)=K*5.E3
365      HBP=HBP+TIAR(K)**2+TELB(K)**2
370      BB(K)=(HBP*5000.)/SPAT(K)
375      300 CONTINUE
380      SIGFLT=4.*BAND)*GT+AFLEM*CRD*EXPT*RE
385      DDARK=SQRT(2.*I)*DDARK*BAND)
390      JREAD=SQRT(HAND*Q)*SIGFLT)
395      JLOAD=SQRT(4.*BK*TEMP*BAND)/RL)
400      JAMPL=SQRT(8.*Q)*IFFT*BAND* 3*CS**2)/GMFET**2)
405      DO 400 K=1,10
410      JSCENE(K)=SQRT(BB(K)**2+(GT+1.)*HAND*Q)*SIGFLT*RE)
415      JNOISE(K)=SQRT(JLOAD)**2+JAMPL**2+DDARK**2+JREAD**2*%
420      +JSCENE(K)**2)
425      TCAM(K)=TIAR(K)*TIS(K)*TFIB(K)*TELB(K)
430      TSCENE=(CR-1.)/(CR+1.)
435      TSYS(K)=TCAM(K)*TAVA(K)
440      SIGAVA(K)=SIGFLT*TCAM(K)
445      SIGSYS(K)=SIGFLT*TSYS(K)
450      SNRAIM(K)=SIGAVA(K)/JNOISE(K)
455      SNR(K)=SIGSYS(K)/JNOISE(K)
460      TMA(K)=SNRL/SNRAIM(K)
465      TM(K)=SNRL/SNR(K)
470      400 CONTINUE
475      PRINT 620,(TIS(I),I=1,14)
480      PRINT 625,(TELB(I),I=1,14)
485      PRINT 630,(TFIB(I),I=1,14)
490      PRINT 680,(TCAM(I),I=1,14)
495      PRINT 695,(TSYS(I),I=1,14)
500      PRINT 700,(BB(I),I=1,14)
505      PRINT 702,(TMA(I),I=1,14)
510      PRINT 705,(TM(I),I=1,14)
515      PRINT 715,(SNR(I),I=1,14)
520      PRINT 720,(SNRAIM(I),I=1,14)
525      PRINT*, ' '
530      PRINT 72 , (SPAT(I)/1000.,I=1,10)
535      PRINT 725,(SIGSYS(I),I=1,10)
540      PRINT 730,(SIGAVA(I),I=1,10)
545      PRINT 735,(JNOISE(I),I=1,10)
550      PRINT 740,(JSCENE(I),I=1,10)
555      PRINT*, ' '
560      PRINT 745, JREAD
565      PRINT 750, JLOAD
570      PRINT 755, JAMPL
575      PRINT 760, DDARK
580      620 FORMAT(' TIS      ',3X,14F6.3)
585      625 FORMAT(' TELB     ',3X,14F6.3)
590      630 FORMAT(' TFIB     ',3X,14F6.3)
595      680 FORMAT(' TCAM     ',3X,14F6.3)

```

```

600      695 FORMAT (' TSYS  ',3X,14F6.3)
605      700 FORMAT (' HB    ',3X,14F6.3)
610      702 FORMAT (' TMA   ',3X,14F6.3)
615      705 FORMAT (' TM    ',3X,14F6.3)
620      715 FORMAT (' SNR   ',3X,14F6.1)
625      720 FORMAT (' SNRAIM',3X,14F6.1)
630      722 FORMAT (' SPAT  ',1X,10I9)
635      725 FORMAT (' SIGSYS',3X,10E9.3)
640      730 FORMAT (' SIGAVE',3X,10E9.3)
645      735 FORMAT (' UNOISE',3X,10E9.3)
650      740 FORMAT (' USCENE',3X,10E9.3)
655      745 FORMAT (' READ NOISE =',E10.2,' AMPS')
660      750 FORMAT (' THERMAL NOISE =',E10.2,' AMPS')
665      755 FORMAT (' FET SHOT NOISE =',E10.2,' AMPS')
670      760 FORMAT (' DARK CURRENT =',E10.2,' AMPS')
675      STOP
680      END

```

IRWATT SUBROUTINE LIST

```

1000     SUBROUTINE IRWATT(PA, AI, RA, FNJM)
1005     DIMENSION RS20(14), RSIR(14), AJUP(14), RFIB(14), WAVE(14)
1006     DIMENSION ALB(9), AUJ(9)
1010     COMMON CURD, FLUX, RESP
1015     TL=.6
1020     10 READ(5,*,PROMPT='BODY NUMBER :') T
1021     DATA ALB/.1, .92, .85, .49, .26, .61, .42, .42, .14/
1022     DATA AUJ/5.2, 5.2, 5.2, 5.2, 5.2, 9.54, 19.18, 30.1, 39.44/
1025     S20P=.0626
1030     SIRP=.2006
1035     DATA RS20/.14, .68, .96, .952, .791, .645, .501, .356, .211, %
1040     .085, .019, .001, .001, .001/
1045     DATA RSIR/.256, .545, .712, 1., .968, .859, .831, .753, .682, %
1050     .615, .552, .493, .443, .416/
1055     DATA AJUP/.25, .31, .36, .42, .5, .5, .49, .49, .47, .44, %
1060     .39, .34, .33, .32/
1065     DATA RFIB/.001, .38, .71, .8, .8, .8, .8, .8, .8, .8, .8, %
1070     .8, .8, .8/
1071     IF(T.EQ.1.) GO TO 150
1072     DO 10 K=1,14
1073     AJUP(K)=1.
1074     10 CONTINUE
1075     150 CONTINUE
1076     DO 200 K=1,14
1080     WAVE(K)=250.+K*50.
1085     SUMI=SUMI+RSIR(K)*AJUP(K)*RFIB(K)*RS20(K)*ALB(T)
1090     SUMF=SUMF+RSIR(K)*AJUP(K)*RFIB(K)*ALB(T)
1095     200 CONTINUE

```

```

1100     CONS=(SIRP*TL*COS(AI)*COS(RA))/(4.*AUJ(T)**2*FN:JM**2)
1105     CURD=S20P*CONS*SJMI*500.
1110     FLUX=CONS*SJMF*500.
1115     RESP=CURD/FLUX
1120     PRINT*,' '
1125     PRINT*,' '
1130     PRINT 635,(WAVE(I),I=1,14)
1135     PRINT 640,(RS20(I),I=1,14)
1140     PRINT 645,(RSIR(I),I=1,14)
1145     PRINT*,' '
1150     PRINT 800, CURD
1155     PRINT 805, FLUX
1160     PRINT 810, RESP
1165     635 FORMAT(' WAVE ',3X,14I6)
1170     640 FORMAT(' RS20 ',3X,14F6.3)
1175     645 FORMAT(' RSIR ',3X,14F6.3)
1180     800 FORMAT(' CURRENT DENSITY= ',E10.2,' AMPS/SQ.METER')
1185     805 FORMAT(' FLUX= ',E10.2,' WATT/SQ.METER')
1190     810 FORMAT(' RESPONSIVITY= ',E10.2,' AMPS/WATT')
1195     RETURN
1200     END

```

MTFAVA SUBROUTINE LIST

```

1000     SUBROUTINE MTFAVA(FNUM, SPIN, EXPT, FOC, CR)
1005     DIMENSION TSCENE(14), SPAT(14), TLEN(14), TMOT(14), GR(14)
1010     COMMON DIM(3), TAVA(14)
1015     WAVE=500.E-9
1020     10 READ(5,*,PROMPT='ALTITUDE (RJ) :')RJ
1021     READ(5,*,PROMPT='IMC? YES=1, NO=0')COMP
1025     ALT=(RJ*71.4E6)-71.4E6
1030     DO 252 K=1,14
1035     TSCENE(K)=(CR-1.)/(CR+1.)
1040     SPAT(K)=K*5.E3
1045     B=(3.1416)/(FNUM*WAVE)
1050     TLEN(K)=(2./3.1416)*(ARCOS(SPAT(K)/B)-(SPAT(K)/B)*%
1055     SQR(1.0-(SPAT(K)/B)**2)
1060     IF(COMP.EQ.1) GO TO 90
1065     SMEAR=(2.*3.1416*SPIN*EXPT*FOC/60.)
1066     ANG=(2.*3.1416*SPIN*EXPT*1.E6)/60.
1067     GO TO 95
1068     90 SMEAR=(.2*3.1416*SPIN*EXPT*FOC/60.)
1069     ANG=(.2*3.1416*SPIN*EXPT*1.E6)/60.
1070     95 CONTINUE
1075     GRS=ALT*ANG*1.E-6
1080     IF(GRS.EQ.0) GO TO 100
1085     PIX=ALT/(FOC*GRS*2.)
1090     100 CONTINUE

```

```

1090 GR(K)=ALT/(FOC*SPAT(K)*2.)
1095 IF (SMEAR.EQ.0) GO TO 249
1100 AK=SPAT(K)*SMEAR
1105 IF (AK.GE.1.0) GO TO 250
1110 TMOT(K)=(SIN(3.1416*SMEAR*SPAT(K)))/(3.1416*SMEAR*SPAT(K))
1115 GO TO 251
1120 249 TMOT(K)=1.0
1125 GO TO 251
1130 250 TMOT(K)=.001
1135 251 CONTINUE
1140 TAVA(K)=TSCENE(K)*TLEN(K)*TMOT(K)
1145 252 CONTINUE
1150 PRINT 690,SMEAR
1155 PRINT 692,GRS
1160 PRINT 696,PIX/1000.
1165 PRINT 695,ANG
1170 PRINT*,' '
1175 PRINT 650,(GR(I),I=1,14)
1180 PRINT 660,(SPAT(I)/1000.,I=1,14)
1185 PRINT 665,(TLEN(I),I=1,14)
1190 PRINT 670,(TMOT(I),I=1,14)
1195 PRINT 675,(TSCENE(I),I=1,14)
1200 PRINT 680,(TAVA(I),I=1,14)
1205 650 FORMAT(' GR RES',3X,14I6)
1210 660 FORMAT(' SPAT ',1X,14I6)
1215 665 FORMAT(' TLEN ',3X,14F6.3)
1220 670 FORMAT(' TMOT ',3X,14F6.3)
1225 675 FORMAT(' TSCENE',3X,14F6.3)
1230 680 FORMAT(' TAVA ',3X,14F6.3)
1235 690 FORMAT(' SMEAR (IMAGE PLANE)=' ,E10.2,' METER')
1240 692 FORMAT(' SMEAR (GROUND)=' ,E10.2,' METER')
1245 695 FORMAT(' ANGULAR SMEAR =' ,F6.1,' MICRORADIANS')
1250 696 FORMAT(' SPATIAL FREQ. EQUIV. TO 1 PIXEL SMEAR =' ,%
1255 I6,' LP/MM')
1260 RETURN
1265 END

```

B.3.2.1

SITV Line Description

LINE	100-105	Prints out the identity of the camera model and any distinguishing features.
	110-140	Type and dimension statements for the variables and arrays used in the program.
	145-170	A list of the input data constants used in the signal-to-noise ratio calculations. MTF values for the image section (TIS), the electron beam (TELB), and fiber optics faceplate (TFIB) are given.
	175-200	These statements prompt for the input variables including the exposure, spin rate, phase angle, incidence angle, reflection angle, focal length, f number, contrast ratio, and video bandwidth.
	205-215	Calculates the phase angle, the angle of incidence, and the reflection angle in radians from input values which are in degrees.
	220-280	Initializes input data and constants such as: electron charge, the target gain, the beam diameter, the read-out efficiency, the temperature, Boltzmann's constant, FET leakage current and transconductance, the shunt capacitance, and load resistance. The limiting SNR is initialized for threshold modulation calculations.

LINE 405 Entry point to the DO loop 400 in which lines 405 to 470 are cycled 10 times. This varies the spatial frequency in 5 lp/mm increments over the range 5 to 50 lp/mm.

410 The quantum (image) noise term (USCENE) is calculated for each spatial frequency (SPAT).

415-420 The RMS noise (UNOISE) is calculated for each spatial frequency.

425-435 The MTF of the camera (TCAM) is calculated at each spatial frequency. The input modulation (TSCENE), and system MTF (TSYS) are also determined.

440-445 The signal terms are determined for the range of spatial frequencies. The system signal term (SIGSYS) is calculated using the system MTF (TSYS), whereas SIGAVA is computed using only the camera MTF (TCAM).

450-455 The signal-to-noise ratio expressions are calculated for the range of spatial frequencies. SNRAIM is determined using SIGAVA while SNRSYS employs SIGSYS.

460-465 The threshold modulation expressions (TM and TMA) are calculated for the range of spatial frequencies. TMA is used in plotting AIM curves. It is determined by taking the ratio of $SNRL/SNRAVA(K)$, where SNRL is the threshold signal-to-noise ratio (assumed to be 3.) TM is the threshold modulation (using the system MTF) determined by taking $SNRL/SNRSYS(K)$.

LINE	475-575	These lines control the output data. They instruct the computer to print out 14 values of TIS, TELB, TFIB, TCAM, TSYS, BB, TMA, TM, SNR and SNRAIM for spatial frequencies 5 to 70 lp/mm. Ten values of SPAT, SIGSYS, SIGAVA, UNOISE and USCENE are printed for 5 to 50 lp/mm. UREAD, ULOAD, UAMPL and UDARK are also printed.
	580-670	These are the format statements that control the print statements.
	675-680	Stop command and end of program.

R 3.2.2 IRWATT Subroutine Line Description -- IRWATT is a subroutine used for camera systems containing photoemissive cathodes to calculate the input flux in the image plane, the current density, and the photocathode responsivity.

LINE	1000	Subroutine name and dummy arguments.
	1005-1010	Dimension and common statements for variables and arrays.
	1015	Initializes the lens transmission (TL).

LINE 1020 This statement prompts for a body number (T) which corresponds to the planet or satellite of interest. The body number code used is:

<u>Body Number</u>	<u>Object</u>
1	Jupiter
2	Io
3	Europa
4	Ganymede
5	Callisto
6	Saturn
7	Uranus
8	Neptune
9	Pluto

1021-1070 Initializes input data and constants such as the sun-planet distance in astronomical units (AUJ(T)), and the albedo (ALB(T)) of the selected object. Values for the input flux, detector spectral response, and fiber optics faceplate transmission are given for different wavelengths ranging from 300 to 950 nm.

LINE 1076 Line 1076 is the entry point of DO loop 200 in which lines 1080 to 1095 are cycled 14 times. On each cycle of the loop the variable K is incremented until it equals 14.

1080 The wavelength (WAVE) is established from 300 nm to 950 nm in 50 nm steps as the program loops.

1085-1090 The integral product of terms required to calculate the current density (CURD) and flux at the photocathode (FLUX) are formed. On each cycle of the DO loop the terms $(\int \sigma_{p\lambda} W_{o\lambda} t_{\lambda} P_{\lambda} d\lambda)$ and $(\int W_{\lambda} P_{\lambda} d\lambda)$ are calculated for a specific wavelength interval and added onto the accumulated sums SUMI and SUMF.

1100-1115 The current density (CURD), input flux at the photocathode (FLUX), and detector responsivity (RESP) are calculated for use in the main program.

1130-1190 These lines control the printing of the output data. They cause the outputs WAVE, RS20 and RSIR to be printed for wavelengths between 300 and 950 nm. The terms CURD, FLUX, and RESP are also printed as directed by the format statements.

1195-1200 Returns control to the main program and ends the subroutine.

B.3.2.3 MTFAVA Subroutine Line Description - MTFAVA calculates the available aerial image modulation (TAVA). This term represents the available aerial image modulation incident on the faceplate of the camera system. It consists of the product of the image modulation due to contrast, the MTF due to image motion, and MTF of the lens assembly. TAVA is useful in plotting AIM curves.

LINE	1000	Subroutine name and dummy argument.
	1020	This line prompts for the altitude in units of the planet radius. The altitude is later used to convert spatial frequencies to ground resolution.
	1021	This line prompts for a reply indicating whether or not image-motion compensation is to be applied. By typing a "1", 90%-effective-image-motion compensation will be applied. A "0" response will result in no IMC.
	1025	The altitude (ALT) is determined.
	1030	DO loop 252 loops through line 1145 incrementing K and establishes 14 values for the spatial frequency.
	1035	Calculates the input modulation due to the image contrast (TSCENE).
	1050	Calculates the MTF for a diffraction-limited lens (TLEN) as a function of spatial frequency.

LINE 1060-1090 This group of statements calculates the image plane smear (SMEAR), angular smear (ANG), the ground smear (GRS), the ground resolution per pixel (GR) equivalent to the spatial frequency, and the spatial frequency equivalent to one pixel smear (PIX).

1105-1135 Calculates the MTF due to image motion (TMOT) as a function of spatial frequency. Several IF and GO TO statements are used to test the value of TMOT to insure that division by zero will not later result. If TMOT equals zero, it will be set to .001 for future computations.

1140 Calculates the available aerial image modulation expression (TAVA) for spatial frequencies 5 lp/mm to 70 lp/mm.

1150-1255 These print and format statements control the output data. The outputs GR, SPAT, TLEN, TMOT, TSCENE and TAVA are printed for spatial frequencies 5 lp/mm to 70 lp/mm. SMEAR, GRS, PIX and ANG are also printed.

1195-1200 Returns control to the main program and ends the subroutine.

B.3.3 SIT VIDICON INPUT/OUTPUT FORMAT

The input/output format for the SIT vidicon program is typical of all of the camera models. An example of the SITV program output is shown in Figure B-4.

During program execution, the program will prompt for inputs representing a number of mission variables as shown below. Underlined values are typed in using the keyboard.

```
SITV
ANALYTICAL MODEL OF SIT VIDICON CAMERA
WITH ELECTROSTATIC IMAGE SECTION
EXPOSURE(SEC), SPIN RATE(RPM), BANDWIDTH :.0005 2. 1300.
FOCAL LENGTH(M), F NUMBER, CONTRAST RATIO : .4 4. 1.3
PHASE ANGLE, INCIDENCE ANGLE, REFLECTION ANGLE (DEGREES) :60. 60. 0
BODY NUMBER :1.
ALTITUDE (RJ) :4.
IMCP? YES=1, NO=01.
```

The program continues execution and responses with the data listed in Figure B-4. Note that many of the program data arrays are displayed as well as the calculated parameters. This facilitates plotting the output data in various forms.

In general, the output is arranged to present several arrays that vary as a function of wavelength. Wavelengths are taken at 50 nm intervals from 300 to 950 nm. Numerous arrays of data are also presented as a function of spatial frequency and ground resolution. Signal-to-noise ratios, MTF data, and threshold modulations are generally given for spatial frequencies ranging

SITV
 ANALYTICAL MODEL OF SIT VIDICON CAMERA
 WITH ELECTROSTATIC IMAGE SECTION
 EXPOSURE(SEC), SPIN RATE(RPM), BANDWIDTH :.0005 2. 1300.
 FOCAL LENGTH(M), F NUMBER, CONTRAST RATIO :.4 4. 1.3
 PHASE ANGLE, INCIDENCE ANGLE, REFLECTION ANGLE (DEGREES) :60. 60. 0
 BODY NUMBER :1.

WAVE	300	350	400	450	500	550	600	650	700	750	800	850	900	950	NM
RS20	.140	.680	.960	.952	.791	.645	.501	.356	.211	.085	.019	.001	.001	.001	
RS1R	.256	.545	.712	1.000	.968	.859	.831	.753	.682	.615	.552	.493	.443	.416	

CURRENT DENSITY = .15E-02 AMPS/SQ.METER
 FLUXE = .51E-01 WATT/SQ.METER
 RESPONSIVITY = .30E-01 AMPS/WATT
 ALTITUDE (RU) :4.
 IMCP YES=1, NO=01.
 SMEAR (IMAGE PLANE) = .42E-05 METER
 SMEAR (GROUND) = .22E+04 METER
 SPATIAL FREQ. EQUIV. TO 1 PIXEL SMEAR = .119 LP/MM
 ANGULAR SMEAR = 10.5 MICRORADIANS

GR RES.	53550	26775	17850	13387	10710	8925	7650	6693	5950	5355	4864	4462	4119	3825	KM/PIX
SPAT	5	10	15	20	25	30	35	40	45	50	55	60	65	70	LP/MM
TLEN	.996	.991	.987	.982	.978	.973	.969	.964	.960	.955	.951	.947	.942	.938	
FMOT	.997	.997	.994	.988	.982	.974	.965	.954	.943	.929	.915	.899	.882	.864	
TSCENE	.130	.130	.130	.130	.130	.130	.130	.130	.130	.130	.130	.130	.130	.130	
FAVA	.130	.129	.128	.127	.125	.124	.122	.120	.118	.116	.113	.111	.109	.106	
TLD	.980	.926	.851	.772	.704	.640	.590	.550	.510	.470	.001	.001	.001	.001	
TDS	.990	.958	.908	.840	.757	.662	.558	.450	.341	.234	.133	.042	.001	.001	
TFS	.911	.833	.764	.702	.648	.599	.555	.516	.481	.450	.422	.396	.373	.352	
T1AR	.884	.739	.590	.455	.345	.254	.183	.128	.084	.049	.000	.000	.000	.000	
TIS	.980	.900	.790	.650	.510	.360	.220	.080	.001	.001	.001	.001	.001	.001	
TELH	.980	.965	.940	.905	.855	.780	.720	.660	.610	.560	.520	.460	.410	.360	
TEIB	.995	.980	.950	.900	.830	.750	.670	.590	.540	.500	.450	.400	.350	.300	
TCAM	.845	.629	.415	.241	.125	.053	.019	.004	.000	.000	0.	0.	0.	0.	
TSYS	.110	.081	.053	.031	.016	.007	.002	.001	.000	.000	0.	0.	0.	0.	
BI	.750	.629	.522	.434	.365	.310	.269	.236	.210	.184	.172	.158	.145	.135	
TMA	.034	.039	.049	.070	.113	.226	.540	2.204	***	*****	*****	*****	*****	*****	
TM	.265	.301	.380	.502	.905	1.827	4.327	18.361	*****	*****	*****	*****	*****	*****	
SNR	11.3	10.0	7.9	5.4	3.3	1.6	.7	.2	.0	.0	0.	0.	0.	0.	
SNRATM	87.2	77.4	61.7	42.9	26.5	13.3	5.6	1.4	.0	.0	0.	0.	0.	0.	

SPAT	5	10	15	20	25	30	35	40	45	50	LP/MM
SIGSYS	.247E-09	.183E-09	.120E-09	.689E-10	.353E-10	.149E-10	.534E-11	.113E-11	.734E-14	.362E-14	AMPS
SIGAVE	.191E-08	.142E-08	.949E-09	.544E-09	.282E-09	.121E-09	.430E-10	.944E-11	.622E-13	.313E-13	AMPS
NOISE	.219E-10	.183E-10	.152E-10	.127E-10	.107E-10	.909E-11	.784E-11	.693E-11	.619E-11	.509E-11	AMPS
USCFHE	.218E-10	.183E-10	.152E-10	.125E-10	.106E-10	.903E-11	.782E-11	.690E-11	.611E-11	.500E-11	AMPS

READ NOISE = .69E-12 AMPS
 THERMAL NOISE = .29E-12 AMPS
 FET SHOT NOISE = .66E-14 AMPS
 DARK CURRENT = .65E-12 AMPS
 STOP

SITV PROGRAM INPUT/OUTPUT FORMAT

FIGURE B-4

from 5 to 70 lp/mm. The output signal and several spatial-frequency-dependent noise terms are also printed in array form.

A number of parameters of interest are displayed and identified, however not all of the program constants are listed. These can be displayed if required by using the system "SHOW" command for the specific computer used.

Although only the most important mission variables are prompted as input, we may wish to vary other parameters as well. This may be achieved by using the computer system command features, or rewriting the statements that require modifications.

B.4 LISTING OF COMPUTER PROGRAMS

A symbolic listing of the candidate camera system main programs and subroutines is presented in this section (excluding those already listed).

B.4.1 SECV PROGRAM LIST - ELECTROSTATIC FOCUS

```

100 PRINT*, 'ANALYTICAL MODEL OF SEC VIDICON CAMERA '
105 PRINT *, 'WITH SUPPRESSOR MESH AND ELECTROSTATIC IMAGE SECTION'
110 DIMENSION SNRAIM(14), SNR(14), TM(14), TCAM(14)
115 DIMENSION TSYS(14), TIS(14), TELB(14), TFIB(14), SPAT(14)
120 DIMENSION HB(14), USCENE(14), UNOISE(14), SIGAVA(14)
125 DIMENSION SIGSYS(14), TMA(14), TII(14), TMES(14)
130 COMMON CIRD, FLUX, RESP, TAVA(14), TTAR(14)
135 REAL IFFT
140 DATA TIS/.98,.9,.79,.65,.51,.36,.22,.08,.001,.011,%
145 .011,.001,.001,.01/
150 DATA TELB/.98,.965,.94,.905,.85,.78,.72,.66,.61,.56,%
155 .52,.46,.41,.36/
160 DATA TFIB/.995,.98,.95,.9,.83,.75,.67,.62,.54,.5,.45,%
165 .4,.35,.3/
170 DATA TII/.87,.7,.55,.4,.29,.21,.16,.12,.08,.06,.05,.04,.03,.02/
175 DATA TMES/.99,.97,.937,.889,.836,.771,.702,.629,.557,.486,%
180 .417,.354,.295,.243/
185 10 READ(5,*,PROMPT='EXPOSURE(SEC), SPIN RATE(RPM), %
190 BANDWIDTH :') EXPT, SPIN, BAND
195 20 READ(5,*,PROMPT='FOCAL LENGTH(M), F NUMBER, CONTRAST %
200 RATIO :') FOC, FNUM, CR
205 30 READ(5,*,PROMPT='PHASE ANGLE, INCIDENCE ANGLE, %
210 REFLECTION ANGLE (DEGREES):') PAD, AID, RAD
215 40 READ(5,*,PROMPT='INTENSIFIER STAGE? YES=1., NO=0 :') STAGE
220 PA=PAD/57.2958
225 AI=AID/57.2958
230 RA=RAD/57.2958
235 Q=1.602E-19
240 GI=32.
245 GT=70.
250 RE=.8
255 D=20.E-6
260 AELFM=(3.1416/4.)*D**2
265 TEMP=300.
270 BK=1.38E-23
275 RL=2.E8
280 IFET=7.E-3
285 GMFET=13.4E-3
290 CS=35.E-12
295 T1=10.E-6
300 SNRL=10.
305 CALL IRWATT(PA, AI, RA, FNUM)
310 CALL MTFAVA(FNUM, SPIN, EXPT, FOC, CR)
315 CALL VTAR(T1)
320 DO 300 K=1,14
325 SPAT(K)=K*5.E3
330 BHP=BHP+TTAR(K)**2*TELB(K)**2*TMES(K)**2
335 BQ(K)=(BHP*5000.)/SPAT(K)
340 IF(STAGE)250,250,300
345 250 GI=1.
350 TII(K)=1.
355 320 CONTINUE

```

```

360      300 CONTINUE
365      SIGFLT=4.*BAND*GI*GT*AELEM*CIRO*EXPT*RE
370      UREAD=SQRT(BAND*Q*SIGFLT)
375      ULOAD=SQRT((4.*BK*TEMP*BAND)/RL)
380      UAMPL=SQRT((8.*Q*IFET*BAND**3*CS**2)/GMFET**2)
385      DO 400 K=1,14
390      USCENE(K)=SQRT(BB(K)**2*(GT+1.)*BAND*Q*SIGFLT*RE*GI)
395      UNOISE(K)=SQRT(ULOAD**2+UAMPL**2+UREAD**2%
400      +USCENE(K)**2)
405      TCAM(K)=TTAR(K)*TIS(K)*TFIB(K)*TELB(K)*TMES(K)*TII(K)
410      TSCENE=(CR-1.)/(CR+1.)
415      TSYS(K)=TCAM(K)*TAVA(K)
420      SIGAVA(K)=SIGFLT*TCAM(K)
425      SIGSYS(K)=SIGFLT*TSYS(K)
430      SNRAIM(K)=SIGAVA(K)/UNOISE(K)
435      SNR(K)=SIGSYS(K)/UNOISE(K)
440      TMA(K)=SNRL/SNRAIM(K)
445      TM(K)=SNRL/SNR(K)
450      400 CONTINUE
455      PRINT 620,(TIS(I),I=1,14)
460      PRINT 625,(TELB(I),I=1,14)
465      PRINT 630,(TFIB(I),I=1,14)
470      PRINT 635,(TMES(I),I=1,14)
475      PRINT 640,(TII(I),I=1,14)
480      PRINT 680,(TCAM(I),I=1,14)
485      PRINT 695,(TSYS(I),I=1,14)
490      PRINT 700,(BB(I),I=1,14)
495      PRINT 702,(TMA(I),I=1,14)
500      PRINT 705,(TM(I),I=1,14)
505      PRINT 715,(SNR(I),I=1,14)
510      PRINT 720,(SNRAIM(I),I=1,14)
515      PRINT 722,(SPAT(I)/1000.,I=1,10)
520      PRINT 725,(SIGSYS(I),I=1,10)
525      PRINT 730,(SIGAVA(I),I=1,10)
530      PRINT 735,(UNOISE(I),I=1,10)
535      PRINT 740,(USCENE(I),I=1,10)
540      PRINT*,', '
545      PRINT 745,UREAD)
550      PRINT 750,ULOAD)
555      PRINT 755,UAMPL)
560      620 FORMAT(' TIS      ',3X,14F6.3)
565      625 FORMAT(' TELB     ',3X,14F6.3)
570      630 FORMAT(' TFIB     ',3X,14F6.3)
575      635 FORMAT(' TMES     ',3X,14F6.3)
580      640 FORMAT(' TII      ',3X,14F6.3)
585      680 FORMAT(' TCAM     ',3X,14F6.3)
590      695 FORMAT(' TSYS     ',3X,14F6.3)
595      700 FORMAT(' BB       ',3X,14F6.3)
600      702 FORMAT(' TMA      ',3X,14F6.3)
605      705 FORMAT(' TM       ',3X,14F6.3)
610      715 FORMAT(' SNR      ',3X,14F6.1)

```

```

610 702 FORMAT (' TMA      ',3X,14F6.3)
615 705 FORMAT (' TM       ',3X,14F6.3)
620 715 FORMAT (' SNR      ',3X,14F6.1)
625 720 FORMAT (' SNRAIM',3X,14F6.1)
630 722 FORMAT (' SPAT     ',1X,10I9)
635 725 FORMAT (' SIGSYS',3X,10E9.3)
640 730 FORMAT (' SIGAVE',3X,10E9.3)
645 735 FORMAT (' UNOISE',3X,10E9.3)
650 740 FORMAT (' USCENE',3X,10E9.3)
655 745 FORMAT (' READ NOISE =',E10.2,' AMPS')
660 746 FORMAT (' DIELECTRIC NOISE =',E10.2,' AMPS')
665 750 FORMAT (' THERMAL NOISE =',E10.2,' AMPS')
670 75  FORMAT (' FET SHOT NOISE =',E10.2,' AMPS')
675 STOP
680 END

```

B.4.2

SECV PROGRAM LIST - ELECTROMAGNETIC FOCUS

```

100 PRINT*, 'ANALYTICAL MODEL OF SEC VIDICON CAMERA
105 PRINT*, 'ELECTROMAGNETIC FOCUSING WITHOUT SUPPRES OR MESH'
110 DIMENSION SNRAIM(14), SNR(14), TM(14), TCAM(14)
115 DIMENSION ISYS(14), IIS(14), TELB(14), SPAT(14)
120 DIMENSION USCENE(14), UNOISE(14), SIGAVA(14)
125 DIMENSION SIGSYS(14), TMA(14), TII(14), TMES(14)
130 COMMON /CRD, FLIX, RESP, TAVA(14), TPAR(14)
135 REAL IFET
140 DATA IIS/.945,.985,.97,.95,.94,.91,.87,.82,.75,.675,8
145 .6, .525,.45,.37/
150 DATA TELB/.98,.965,.94,.905,.855,.78,.72,.66,.61,.56,%
155 .52,.46,.41,.36/
170 DATA TII/.87,.7,.55,.4,.29,.21,.16,.12,.08,.06,.05,.04,.03,.02/
175 DATA TMES/1.,1.,1.,1.,1.,1.,1.,1.,1.,1.,%
180 1.,1.,1.,1./
185 10 READ(5,*, PROMPT='EXPOSURE (SEC), SPIN RATE (RPM), %
190 BANDWIDTH :') EXPT, SPIN, BAND
195 20 READ(5,*, PROMPT='FOCAL LENGTH (M), F NUMBER, CONTRAST %
200 RATIO :') FOC, FNUM, CR
215 30 READ(5,*, PROMPT='PHASE ANGLE, INCIDENCE ANGLE, %
220 REFLECTION ANGLE (DEGREES) :') PAD, AID, RAD
225 40 READ(5,*, PROMPT='INTENSIFIER STAGE? YES=1., NO=0 :') STAGE
230 PA=PAD/57.2958
235 AI=AID/57.2958
240 RA=RAD/57.2958
245 Q=1.602E-19
250 GI=32.
255 GT=70.
260 RE=.8
265 D=20.F-6
270 AELEM=(3.1416/4.) *D**2
275 TEMP=301.

```

```

270      BK=1.38E-23
275      RL=2.E8
280      IFET=7.E-3
285      GMFET=13.4E-3
290      CS=35.E-12
295      T1=10.E-6
300      SNRL=10.
305      CALL IRNATM(PA, AI, RA, FNJM)
310      CALL MTFAVA(FNJM, SPIN, EXPT, FOC, CR)
315      CALL VTAR(T1)
320      DO 300 K=1,14
325      SPAT(K)=K*5.E3
330      BBP=BBP+TAR(K)**2*TELB(K)**2*TMES(K)**2
335      BB(K)=(BBP*50000.)/SPAT(K)

340      IF (STAGE)250,250,300
345      250 GI=1.
350      TII(K)=1.
355      320 CONTINUE
360      300 CONTINUE
365      SIGFLT=4.*BAND*GI*GT*AELEM*CURD*EXPT*RE
370      UREAD=SQRT(BAND*Q*SIGFLT)
375      ULOAD=SQRT((4.*BK*TEMP*BAND)/RL)
380      UAMPL=SQRT((8.*Q*[FET*BAND**3*CS**2]/GMFET**2)
385      DO 400 K=1,14
390      USCENE(K)=SQRT(BB(K)**2*(GT+1.)*BAND*Q*SIGFLT*RE*GI)
395      UNOISE(K)=SQRT(ULOAD**2+UAMPL**2+UREAD**2%
400      +USCENE(K)**2)
405      TCAM(K)=TAR(K)*TIS(K)*TELB(K)*TMES(K)*TII(K)
410      TSCENE=(CR-1.)/(CR+1.)
415      TSY(K)=TCAM(K)*TAVA(K)
420      SIGAVA(K)=SIGFLT*TCAM(K)
425      SIGSYS(K)=SIGFLT*TSY(K)
430      SNRAIM(K)=SIGAVA(K)/UNOISE(K)
435      SNR(K)=SIGSYS(K)/UNOISE(K)
440      TMA(K)=SNRL/SNRAIM(K)
445      TM(K)=SNRL/SNR(K)
450      400 CONTINUE
455      PRINT 620,(TIS(I),I=1,14)
460      PRINT 625,(TELB(I),I=1,14)
470      PRINT 635,(TMES(I),I=1,14)
475      PRINT 640,(TII(I),I=1,14)
480      PRINT 680,(TCAM(I),I=1,14)
485      PRINT 695,(TSYS(I),I=1,14)
490      PRINT 700,(BB(I),I=1,14)
495      PRINT 702,(TMA(I),I=1,14)
500      PRINT 705,(TM(I),I=1,14)
505      PRINT 715,(SNR(I),I=1,14)
510      PRINT 720,(SNRAIM(I),I=1,14)
515      PRINT 722,(SPAT(I)/1000.,I=1,10)
520      PRINT 725,(SIGSYS(I),I=1,10)
525      PRINT 730,(SIGAVA(I),I=1,10)

```

```

530 PRINT 735, (UNOISE(I), I=1, 10)
535 PRINT 740, (USCENE(I), I=1, 10)
540 PRINT*, ' '
545 PRINT 745, IREAD
550 PRINT 750, ILOAD
555 PRINT 755, IAMPL
560 620 FORMAT(' TIS ', 3X, 14F6.3)
565 625 FORMAT(' TELB ', 3X, 14F6.3)
575 635 FORMAT(' TMES ', 3X, 14F6.3)
580 640 FORMAT(' TIL ', 3X, 14F6.3)
585 680 FORMAT (' TCAM ', 3X, 14F6.3)
590 695 FORMAT (' TSYS ', 3X, 14F6.3)
595 700 FORMAT (' BB ', 3X, 14F6.3)
600 702 FORMAT(' TMA ', 3X, 14F6.3)
605 705 FORMAT (' TM ', 3X, 14F6.3)
610 715 FORMAT (' SNR ', 3X, 14F6.1)
615 720 FORMAT (' SNRAIM', 3X, 14F6.1)
620 722 FORMAT(' SPAT ', 1X, 10I9)
625 725 FORMAT (' SIGSYS', 3X, 10E9.3)
630 730 FORMAT (' SIGAVE', 3X, 10E9.3)
635 735 FORMAT (' UNOISE', 3X, 10E9.3)
640 740 FORMAT (' USCENE', 3X, 10E9.3)
645 745 FORMAT(' READ NOISE =', E10.2, ' AMPS')
650 750 FORMAT(' THERMAL NOISE =', E10.2, ' AMPS')
655 755 FORMAT(' FET SHOT NOISE =', E10.2, ' AMPS')
660 STOP
665 END

```

B.4.3

ESC PROGRAM LIST - ELECTROSTATIC FOCUS

```

100 PRINT*, 'ANALYTICAL MODEL OF THE ELECTROSTATIC STORAGE CAMERA'
105 DIMENSION SNRAIM(14), SNR(14), TM(14), TCAM(14)
110 DIMENSION TSYS(14), TIS(14), TELB(14), TFIB(14), SPAT(14)
115 DIMENSION BB(14), USCENE(14), UNOISE(14), SIGAVA(14)
120 DIMENSION SIGSYS(14), TMA(14)
125 COMMON CURD, FLUX, RESP, TAVA(14), TTAR(14)
130 REAL M, IFET
135 DATA TIS/.98,.9,.79,.65,.51,.36,.22,.08,.001,.001,%.
140 .001, .001, .001, .001/
145 DATA TFIB/.995,.98,.95,.9,.83,.75,.67,.62,.54,.5,.45,.4,.35,.3/
150 10 READ(5,*, PROMPT='EXPOSURE(SEC), SPIN RATE(RPM), %
155 BANDWIDTH :') EXPT, SPIN, BAND
160 20 READ(5,*, PROMPT='FOCAL LENGTH(M), F NUMBER, CONTRAST %
165 RATIO : ') FOC, FNUM, CR
170 30 READ(5,*, PROMPT='PHASE ANGLE, INCIDENCE ANGLE,%
175 REFLECTION ANGLE (DEGREES) :') PAD, AID, RAD

```

```

180 PA=PAD/57.2958
185 AI=AID/57.2958
190 RA=RAD/57.2958
195 A=.5
200 SET=1.1
210 SEM=2.2
215 H=SET+1.
220 BEAM=3.3E-10
225 M=.13
230 D=20.E-6
235 ABEAM=(3.1416/4.)*D**2
240 Q=1.602E-19
245 GT=100.
250 GM=1.E4
255 FT=1.
260 C=5.4E-9
265 AELEM=ABEAM
270 TEMP=300.
275 BK=1.38E-23
280 RL=2.E8
285 IFET=7.E-3
290 GMFET=13.4E-3
295 CS=20.E-12
300 SNRL=10.
305 CALL IRWATT(PA, AI, RA, FNJM)
310 CALL MTFAVA(FNJM, SPIN, EXPT, FOC, CR)
315 CALL SDTAR
317 DATA TELB/.98,.965,.94,.905,.855,.78,.72,.66,.61,.56,%
318 .52,.46,.41,.36/
320 DO 300 K=1,14
325 SPAT(K)=K*5.E3
335 BBP=BBP+TTAR(K)**2*TELB(K)**2
340 BH(K)=(BBP*5000.)/SPAT(K)
345 300 CONTINUE
350 UMULT=A*SET/(SEM-1.)
355 UREAD=A**2*SET**2
360 ULOAD=SQRT((4.*BK*TEMP*BAND)/RL)
365 UAMPL=SQRT((8.*Q*IFET*BAND**3*CS**2)/GMFET**2)
370 USEC=A**2*(H-SET)*SET
375 UEAP=A*(1.-A)*SET
380 UBEAM=SQRT(2.*GM**2*Q*BEAM*BAND*(UMULT+UREAD+USEC+UEAP))
385 UCHAR=(M*SET*BEAM/(C*10000.*ABEAM))**2
390 UANAL=Q*BEAM*(1.+(H-2.)*SET)/(2.*BAND)
395 UDIEL=SQRT(UCHAR*UANAL*GM**2)
400 UQUANT=(Q*AELEM*GT*CURD*EXPT)
410 DO 400 K=1,14
415 UJSCENE(K)=SQRT(GM**2*(BH(K)**2)*(GT+1.)*UQUANT*UCHAR)
420 SIGFLT=(GM*M*SET*2.*BEAM*GT*CURD*EXPT)/(C*10000.)
425 UNOISE(K)=SQRT(ULOAD**2+UAMPL**2+UJSCENE(K)**2+UDIEL**2+UBEAM**2)
430 TCAM(K)=TTAR(K)*UIS(K)*TFIB(K)*TELB(K)

```

```

435   TSCENE=(CR-1.)/(CR+1.)
440   TSYS(K)=TCAM(K)*TAVA(K)
445   SIGAVA(K)=SIGFLT*TCAM(K)
450   SIGSYS(K)=SIGFLT*TSYS(K)
455   SNRAIM(K)=SIGAVA(K)/UNOISE(K)
460   TMA(K)=SNRL/SNRAIM(K)
465   SNR(K)=SIGSYS(K)/UNOISE(K)
470   TM(K)=SNRL/SNR(K)
475   400 CONTINUE
480   PRINT 620,(TIS(I),I=1,14)
482   PRINT 625,(TELB(I),I=1,14)
485   PRINT 630,(TFIB(I),I=1,14)
490   PRINT 680,(TCAM(I),I=1,14)
495   PRINT 695,(TSYS(I),I=1,14)
500   PRINT 700,(BB(I),I=1,14)
505   PRINT 702,(TMA(I),I=1,14)
510   PRINT 705,(TM(I),I=1,14)
515   PRINT 715,(SNR(I),I=1,14)
520   PRINT 720,(SNRAIM(I),I=1,14)
525   PRINT*,' '
530   PRINT 722,(SPAT(I)/1000.,I=1,10)
535   PRINT 725,(SIGSYS(I),I=1,10)
540   PRINT 730,(SIGAVA(I),I=1,10)
545   PRINT 735,(UNOISE(I),I=1,10)
550   PRINT 740,(JSCENE(I),I=1,10)
555   PRINT*,' '
560   PRINT 745,UREAM
565   PRINT 746,UDIEL
570   PRINT 750,UILOAD
575   PRINT 755,UIAMPL
580   620 FORMAT(' TIS      ',3X,14F6.3)
585   625 FORMAT(' TELB     ',3X,14F6.3)
590   630 FORMAT(' TFIB     ',3X,14F6.3)
595   680 FORMAT(' TCAM     ',3X,14F6.3)
600   695 FORMAT(' TSYS     ',3X,14F6.3)
605   700 FORMAT(' BB       ',3X,14F6.3)
615   720 FORMAT(' SNRAIM',3X,14F6.1)
620   722 FORMAT(' SPAT    ',1X,10I9)
625   725 FORMAT(' SIGSYS',3X,10E9.3)
630   730 FORMAT(' SIGAVE',3X,10E9.3)
635   735 FORMAT(' UNOISE',3X,10E9.3)
640   740 FORMAT(' JSCENE',3X,10E9.3)
645   745 FORMAT(' READ NOISE =',E10.2,' AMPS')
650   750 FORMAT(' THERMAL NOISE =',E10.2,' AMPS')
655   755 FORMAT(' FET SHOT NOISE =',E10.2,' AMPS')
660   STOP
665   END

```

B.4.4

ESCMF PROGRAM LIST - ELECTROMAGNETIC FOCUS

```

100 PRINT*, 'ANALYTICAL MODEL OF THE ELECTROSTATIC STORAGE CAMERA'
102 PRINT*, 'ELECTROMAGNETIC FOCUSING AND 10 MICRON READ BEAM'
105 DIMENSION SNRAIM(14), SNR(14), FM(14), TCAM(14)
110 DIMENSION TSYS(14), TIS(14), TELB(14), SPAT(14)
115 DIMENSION BB(14), USCENE(14), UNOISE(14), SIGAVA(14)
120 DIMENSION SIGSYS(14), TMA(14)
125 COMMON CURD, FLUX, RESP, TAVA(14), TTAR(14)
130 REAL M, IFET
135 DATA TIS/.995,.985,.97,.95,.94,.91,.87,.82,.75,.675,%
140 .6,.525,.45,.37/
150 10 READ(5,*,PROMPT='EXPOSURE(SEC), SPIN RATE(RPM), %
155 BANDWIDTH :') EXPT,SPIN, BAND
160 20 READ(5,*,PROMPT='FOCAL LENGTH(M), F NUMBER, CONTRAST *
165 RATIO :') FOC, FNJM, CR
170 30 READ(5,*,PROMPT='PHASE ANGLE, INCIDENCE ANGLE,%
175 REFLECTION ANGLE (DEGREES) :') PAD, AID, RAD
180 PA=PAD/57.2958
185 AI=AID/57.2958
190 RA=RAD/57.2958
195 A=.5
200 SET=1.1
205 SEM=2.2
210 H=SET+1.
215 BEAM=.83E-10
220 M=.13
225 D=10.E-6
230 AREAM=(3.1416/4.)*D**2
235 Q=1.602E-19
240 GT=100.
245 GM=1.E4
250 FT=1.
255 C=5.4E-9
260 AELEM=AREAM
265 TEMP=300.
270 BK=1.38E-23
275 RL=2.E8
280 IFET=7.E-3
285 GMFET=13.4E-3
290 CS=20.E-12
295 SNRL=10.
300 CALL IRWATM(PA, AI, RA, FNJM)
305 CALL MTFAVA(FNJM, SPIN, EXPT, FOC, CR)
310 CALL SDTAR
315 DATA TELB/.997,.988,.973,.952,.926,.895,.86,.821,.779,.735,%
320 .689,.641,.594,.546/
325 DO 300 K=1,14
330 SPAT(K)=K*5.E3
335 BHP=BHP+TTAR(K)**2*TELB(K)**2
340 B3(K)=(BHP*5000.)/SPAT(K)
345 300 CONTINUE
350 UMULT=A*SET/(SEM-1.)

```

```

355 UREAD=A**2*SET**2
360 ULOAD=SQRT((4.*BK*TEMP*BAND)/RL)
365 UAMPL=SQRT((8.*Q*IFET*BAND**3*CS**2)/GMFET**2)
370 USEC=A**2*(H-SET)*SET
375 UEAP=A*(1.-A)*SET
380 UBEAM=SQRT(2.*GM**2*Q*BEAM*BAND*(UMULT+UREAD+USEC+UEAP))
385 UCHAR=(M*SET*BEAM/(C*10000.*ABEAM))**2
390 UANAL=Q*BEAM*(1.+(H-2.)*SET)/(2.*BAND)
395 UDIEL=SQRT(UCHAR*UANAL*GM**2)
400 UQUANT=(Q*AELEM*GT*CURD*EXPT)
405 DO 400 K=1,14
410 USCENE(K)=SQRT(GM**2*(BB(K)**2)*(GT+1.)*UQUANT*UCHAR)
415 SIGFLT=(GM*M*SET*2.*BEAM*GT*CURD*EXPT)/(C*10000.)
420 UNOISE(K)=SQRT(ULOAD**2+UAMPL**2+USCENE(K)**2+UDIEL**2+UBEAM**2)
425 TCAM(K)=TTAR(K)*TIS(K)*TELB(K)
430 TSCENE=(CR-1.)/(CR+1.)
435 TSYS(K)=TCAM(K)*TAVA(K)
440 SIGAVA(K)=SIGFLT*TCAM(K)
445 SIGSYS(K)=SIGFLT*TSYS(K)
450 SNRAIM(K)=SIGAVA(K)/UNOISE(K)
455 TMA(K)=SNRL/SNRAIM(K)
460 SNR(K)=SIGSYS(K)/UNOISE(K)
465 TM(K)=SNRL/SNR(K)
470 400 CONTINUE
475 PRINT 620,(TIS(I),I=1,14)
480 PRINT 625,(TELB(I),I=1,14)
490 PRINT 680,(TCAM(I),I=1,14)
495 PRINT 695,(TSYS(I),I=1,14)
500 PRINT 700,(BB(I),I=1,14)
505 PRINT 702,(TMA(I),I=1,14)
510 PRINT 705,(TM(I),I=1,14)
515 PRINT 715,(SNR(I),I=1,14)
520 PRINT 720,(SNRAIM(I),I=1,14)
525 PRINT*,' '
530 PRINT 722,(SPAT(I)/1000.,I=1,10)
535 PRINT 725,(SIGSYS(I),I=1,10)
540 PRINT 730,(SIGAVA(I),I=1,10)
545 PRINT 735,(UNOISE(I),I=1,10)
550 PRINT 740,(USCENE(I),I=1,10)
555 PRINT*,' '
560 PRINT 745,UBEAM
565 PRINT 746,UDIEL
570 PRINT 750,ULOAD
575 PRINT 755,UAMPL
580 620 FORMAT(' TIS      ',3X,14F6.3)
585 625 FORMAT(' TELB     ',3X,14F6.3)
595 680 FORMAT(' TCAM      ',3X,14F6.3)
600 695 FORMAT(' TSYS      ',3X,14F6.3)
605 700 FORMAT(' BB        ',3X,14F6.3)

```

```

610      702 FORMAT(' TMA      ',3X,14F6.3)
615      705 FORMAT(' TM       ',3X,14F6.3)
620      715 FORMAT(' SNR      ',3X,14F6.1)
625      720 FORMAT(' SNRAIM',3X,14F6.1)
630      722 FORMAT(' SPAT    ',1X,10I9)
635      725 FORMAT(' SIGSYS',3X,10E9.3)
640      730 FORMAT(' SIGAVE',3X,10E9.3)
645      735 FORMAT(' UNOISE',3X,10E9.3)
650      740 FORMAT(' JSCENE',3X,10E9.3)
655      745 FORMAT(' READ NOISE =',E10.2,' AMPS')
660      746 FORMAT(' DIELECTRIC NOISE =',E10.2,' AMPS')
665      750 FORMAT(' THERMAL NOISE =',E10.2,' AMPS')
670      751 FORMAT(' FET SHOT NOISE =',E10.2,' AMPS')
675      STOP
680      END

```

B.4.5 CCD PROGRAM LIST

```

100      PRINT*, 'ANALYTICAL MODEL OF CHARGE-COUPLED CAMERA'
105      DIMENSION SNRAIM(14), SNR(14), TM(14), TCAM(14)
110      DIMENSION TSYS(14), SPAT(14), SIGSYS(14), QEPC(14)
115      DIMENSION BJ(14), JSCENE(14), UNOISE(14), SIGAVA(14)
120      DIMENSION RSIR(14), AJUP(14), WAVE(14), TMA(14), TTR(14)
125      COMMON DJM(3), TAVA(14)
130      REAL IFET, IDARK, NTL, NTCL
135      10 READ(5,*, PROMPT='EXPOSURE(SEC), SPIN RATE(RPM), %
140      BANDWIDTH(TH:)' EXPT, SPIN, BAND
145      20 READ(5,*, PROMPT='FOCAL LENGTH(M), F NUMBER, CONTRAST %
150      RATIO : ' ) FOC, FNJM, CR
155      30 READ(5,*, PROMPT='PHASE ANGLE, INCIDENCE ANGLE, %
160      REFLECTION ANGLE (DEGREES):' ) PAD, AID, RAD
165      PA=PAD/57.2958
170      AT=AID/57.2958
175      RA=PAD/57.2958
180      TL=.6
185      Q=1.602E-19
190      C=2.948E-34
195      H=6.52E-34
200      AJUP=.21
205      AELEM=(20.E-6)*.2
210      IDARK=4.E-13*AELEM*1.F4
215      SNRL=3.
220      NI=1400.
225      TEM=233.
230      HK=1.38E-23
235      RT=1.E9
240      IFET=7.E-3
245      CJ=.2E-12
250      GMFET=13.4E-3

```

```

250 EC=1.E-5
255 NTL=2.E15
260 AL=40.
265 WIN=2.*3.1416/EXPT
270 TS=3.E-5
275 BC=BAND*2.
280 WC=2.*3.1416*BC
285 NTCL=2.E15
290 DATA RSIR/.256, .545, .712, 1., .968, .859, .831, .753, .682,%
295 .615, .552, .493, .443, .416/
300 DATA AJJP/ .25, .31, .36, .42, .5, .5, .49, .49, .47, .44,%
305 .39, .34, .33, .32/
310 DATA QEPC/.001,.5,.7,.8,.84,.82,.77,.7,.67,.6,.55,.4,.3,.2/
315 DATA TFAR/.96,.87,.74,.6,.464,.326,.224,.08,.05,.001,%
320 .001,.001,.001,.001/
325 DO 200 K=1,14
330 WAVE(K)=(250.+K*50.)
335 SUMF=SUMF+WAVE(K)*1.E-9*RSIR(K)*AJJP(K)
340 SUMI=SUMI+WAVE(K)*1.E-9*RSIR(K)*AJJP(K)*QEPC(K)
345 200 CONTINUE
350 CONS=(SIRP*TL*COS(AI)*COS(RA))/(4.*H*C*AIJ**2*FNJM**2)
355 FLUX=CONS*SUMF*500.
360 CURD=CONS*Q*SUMI*500.
365 QE=CURD/(FLUX*Q)
370 CALL MTFAVA(FNJM, SPIN, EXPT, FOC, CR)
375 DO 300 K=1,14
380 SPAT(K)=K*5.E3
385 BBP=BBP+TFAR(K)**2
390 BB(K)=(BBP*5000.)/SPAT(K)
395 300 CONTINUE
400 SIGFLT=(2.*AELEM*CURD*EXPT)*(1.-TN*EC)
405 ULOAD=SQRT(TEMP*BK/(R1*BAND))
410 UAMPL=SQRT((2./GMFET**2)*IFET*Q*BAND*CS**2)
415 UDARK=SQRT((2.*Q*IDARK*EXPT)+(2.*Q*TN*IDARK/BC))
420 XP=TEMP*(BK/Q)*AELEM
425 IF(WC.GE.1.0/TS) GO TO 500
430 Y=SQRT((NTCL*XP*TN/AL)*ALOG(1./(WC*TS)))+(4.*NTCL*XP*TN/AL)*Q
435 GO TO 501
440 500 Y=SQRT((NTCL*XP*TN*4.)/(WC*TS*AL))*Q
445 501 CONTINUE
450 X=SQRT((NTL*XP/AL)*ALOG(1./(WIN*TS)))+(4.*NTL*XP/AL)*Q
455 DO 400 K=1,14
460 USCENE(K)=SQRT((BB(K)**2*(QE+1.))*Q*AELEM*CURD*EXPT)
465 UNOISE(K)=SQRT(ULOAD**2+UAMPL**2+UDARK**2+USCENE(K)**2+x**2+y**2)
470 TCAM(K)=TFAR(K)
475 TSCENE=(CR-1.)/(CR+1.)
480 TSYS(K)=TCAM(K)*TAVA(K)
485 SIGAVA(K)=SIGFLT*TCAM(K)
490 SIGSYS(K)=SIGFLT*TSYS(K)
495 SNRAIM(K)=SIGAVA(K)/UNOISE(K)
500 SNR(K)=SIGSYS(K)/UNOISE(K)
505 TMA(K)=SNRL/SNRAIM(K)
510 TM(K)=SNRL/SNR(K)

```

```

515      400 CONTINUE
521      PRINT 680,(TCAM(I),I=1,14)
525      PRINT 695,(TSYS(I),I=1,14)
530      PRINT 700,(BB(I),I=1,14)
535      PRINT 702,(TMA(I),I=1,14)
540      PRINT 705,(TM(I),I=1,14)
545      PRINT 715,(SNR(I),I=1,14)
550      PRINT 720,(SNRAIM(I),I=1,14)
555      PRINT*,' '
560      PRINT 722,(SPAT(I)/1000.,I=1,10)
565      PRINT 725,(SIGSYS(I),I=1,10)
570      PRINT 730,(SIGAVA(I),I=1,10)
575      PRINT 735,(UNOISE(I),I=1,10)
580      PRINT 740,(USCENE(I),I=1,10)
585      PRINT*,' '
590      PRINT 635,(WAVE(I),I=1,14)
595      PRINT 640,(QEPC(I),I=1,14)
600      PRINT 645,(RSIR(I),I=1,14)
605      PRINT 650,(AJIP(I),I=1,14)
610      PRINT*,' '
615      PRINT 800,CURD
620      PRINT 805,FLUX
625      PRINT 810,QE
630      PRINT 750,ILOAD
635      PRINT 755,IAMPL
640      PRINT 760,JDARK
645      PRINT 765,X
650      PRINT 770,Y
655      680 FORMAT (' TCAM ',3X,14F6.3)
660      695 FORMAT (' TSYS ',3X,14F6.3)
665      700 FORMAT (' BB ',3X,14F6.3)
670      702 FORMAT (' TMA ',3X,14F6.3)
675      705 FORMAT (' TM ',3X,14F6.3)
680      715 FORMAT (' SNR ',3X,14F6.1)
685      720 FORMAT (' SNRAIM',3X,14F6.1)
690      722 FORMAT (' SPAT ',1X,10I9)
695      725 FORMAT (' SIGSYS',3X,10E9.3)
700      730 FORMAT (' SIGAVE',3X,10E9.3)
705      735 FORMAT (' UNOISE',3X,10E9.3)
710      740 FORMAT (' USCENE',3X,10E9.3)
715      750 FORMAT (' THERMAL NOISE =',E10.2,' COUL')
720      755 FORMAT (' FET SHOT NOISE =',E10.2,' COUL')
725      760 FORMAT (' DARK CURRENT =',E10.2,' COUL')
730      765 FORMAT (' NOISE "X" =',E10.2,' COUL')
735      770 FORMAT (' NOISE "Y" =',E10.2,' COUL')
740      635 FORMAT (' WAVE ',3X,14I6)
745      640 FORMAT (' QEPC ',3X,14F6.3)
750      645 FORMAT (' RSIR ',3X,14F6.3)
755      650 FORMAT (' AJIP ',3X,14F6.3)
760      800 FORMAT (' CURRENT DENSITY =',E10.2,' AMP/SQ.METER')
765      805 FORMAT (' FLUX =',E10.2,' PHOTONS/SQ.METER')
770      810 FORMAT (' INTEGRATED QE =',E10.2,' ELECTRONS/PHOTON')
775      STOP
780      END

```

B.4.6

ICDEF PROGRAM LIST - ELECTROSTATIC FOCUS

```

100 PRINT*, 'ANALYTICAL MODEL OF INTENSIFIED CHARGE-COUPLED CAMERA'
105 PRINT*, 'WITH ELECTROSTATIC IMAGE SECTION'
110 DIMENSION SNRAIM(14), SNR(14), FM(14), FCAM(14)
115 DIMENSION TSYS(14), SPAT(14), SIGSYS(14), TFS(14), RS20(14)
120 DIMENSION BK(14), USCENE(14), UNOISE(14), SIGAVA(14)
125 DIMENSION RSIR(14), AJUP(14), WAVE(14), TMA(14), TFA(14),
    TFIB(14), RFIB(14)
130 DIMENSION ALB(9), AUJ(9)
135 COMMON DUM(3), TAVA(14)
140 REAL IFET, IDARK, NTL, NTCL
145 10 READ(5,*, PROMPT='EXPOSURE(SEC), SPIN RATE(RPM), %
150 BANDWIDTH:') EXPT, SPIN, BAND
155 20 READ(5,*, PROMPT='FOCAL LENGTH(M), F NUMBER, CONTRAST %
160 RATIO : ') FOC, FNUM, CR
165 30 READ(5,*, PROMPT='PHASE ANGLE, INCIDENCE ANGLE, %
170 REFLECTION ANGLE (DEGREES): ') PAD, AID, RAD
175 40 READ(5,*, PROMPT='BODY NUMBER : ') I
180 DATA ALB/1., .92, .85, .49, .26, .61, .42, .42, .14/
185 DATA AUJ/5.2, 5.2, 5.2, 5.2, 5.2, 9.54, 19.18, 30.1, 39.4/
190 PA=PAD/57.2958
195 AI=AID/57.2958
200 RA=RAD/57.2958
205 TL=.6
210 Q=1.602E-19
215 S20P=.0626
220 SIRP=.2006
225 AELEM=(20.E-6)**2
230 GT=2000.
235 IDARK=4.E-13*AELEM*1.E4
240 SNRL=10.
245 TN=1400.
250 TEMP=233.
255 BK=1.38E-23
260 RI=1.E9
265 IFET=7.E-3
270 CS=.2E-12
275 GMFET=13.4E-3
280 EC=1.E-5
285 NTL=2.E15
290 AL=40.
295 WIN=2.*3.1416/EXPT
300 TS=3.E-5
305 BC=BAND*2.
310 NTCL=2.E15
315 WC=2.*3.1416*BC
320 DATA RS20/ .14, .68, .96, .952, .791, .645, .501, .356, .211, %
325 .085, .019, .001, .001, .001/
330 DATA RSIR/ .256, .545, .712, 1., .968, .859, .831, .753, .682, %
335 .615, .552, .493, .443, .416/
340 DATA RFIB/ .001, .38, .71, .8, .8, .8, .8, .8, .8, .8, .8, .8, .8/
345 DATA AJUP/ .25, .31, .36, .42, .5, .5, .49, .49, .47, .44, %

```

```

350 .39, .34, .33, .32/
355 DATA TIS/.98,.9,.79,.65,.51,.36,.22,.08,.001,.001,%
360 .001,.001,.001,.001/
365 DATA TAR/.96,.87,.74,.6,.464,.326,.224,.08,.05,.001,%
370 .01,.01,.001,.001/
375 DATA TFIH/.995,.98,.95,.9,.83,.75,.67,.62,.54,.5,.45,%
380 .4,.35,.3/
385 IF(T.E.1)GO TO 150
390 DO 10 K=1,14
395 AJUP(K)=1
400 CONTINUE
405 150 CONTINUE
410 DO 200 K=1,14
415 WAVE(K)=(250.+K*50.)
420 SUMFES=JMF+RSIR(K)*AJUP(K)*RFIB(K)*ALB(T)
425 SUMIES=IMI+RSIR(K)*AJUP(K)*RS20(K)*RFIB(K)*ALB(T)
430 200 CONTINUE
435 CONS=(SIRP*TL*COS(AT)*COS(RA))/(4.*AJU(T)**2*FNJM**2)
440 FLUX=CONS*SUMF*500.
445 CURD=CONS*SUMI*500.*S20P
450 RESP=CURD/FLUX
455 CALL MTFAVA(FNJM, SPIN, EXPT, FOC, CR)
460 DO 300 K=1,14
465 SPAT(K)=K*5.E3
470 BRP=BRP+TTAR(K)**2
475 BK(K)=(BRP*50J.)/SPAT(K)
480 300 CONTINUE
485 SIGFLT=(2.*AELEM*CURD*EXPT*GT)*(1.-TN*EC)
490 JLOAD=SQRT(TEMP*BK/(RT*BAND))
495 JAMPL=SQRT((2./GMFET**2)*IFET*Q*BAND)*CS**2)
500 JDARK=SQRT((2.*J)*IDARK*EXPT)+(2.*Q*TN*IDARK/BC)
505 XP=TEMP*(BK/Q)*AELEM
510 IF(WC.GE.1.0/TS) GO TO 500
515 Y=SQRT((NTCL*XP*TN/AL)*ALOG(1./(WC*TS)))+(4.*NTCL*XP*TN/AL)**2)
520 GO TO 501
525 500 Y=SQRT((NTCL*XP*TN*4.)/(WC*TS*AL))*Q
530 501 CONTINUE
535 X=SQRT((NTL*XP/AL)*ALOG(1./(WIN*TS)))+(4.*NTL*XP/AL)**2)*Q
540 DO 400 K=1,14
545 USCENE(K)=SQRT((BK(K)**2*(GT+1.))*Q*AELEM*CURD*EXPT*GI)
550 JNOISE(K)=SQRT(JLOAD**2+JAMPL**2+JDARK**2+USCENE(K)**2+X**2+Y**2)
555 TCAM(K)=TTAR(K)*TIS(K)*TFIB(K)
560 TSCENE=(CR-1.)/(CR+1.)
565 TSYS(K)=TCAM(K)*TAVA(K)
570 SIGAVA(K)=SIGFLT*TCAM(K)
575 SIGSYS(K)=SIGFLT*TSYS(K)
580 SNRAIM(K)=SIGAVA(K)/JNOISE(K)
585 SNR(K)=SIGSYS(K)/JNOISE(K)
590 TMA(K)=SNRL/SNRAIM(K)
595 TM(K)=SNRL/SNR(K)
600 CONTINUE

```

```

605 PRINT 680,(TCAM(I),I=1,14)
610 PRINT 695,(TSYS(I),I=1,14)
615 PRINT 700,(BB(I),I=1,14)
620 PRINT 702,(TMA(I),I=1,14)
625 PRINT 705,(TM(I),I=1,14)
630 PRINT 715,(SNR(I),I=1,14)
635 PRINT 720,(SNRAIM(I),I=1,14)
640 PRINT*, ' '
645 PRINT 722,(SPAT(I)/1000.,I=1,10)
650 PRINT 725,(SIGSYS(I),I=1,10)
655 PRINT 730,(SIGAVA(I),I=1,10)
660 PRINT 735,(JNOISE(I),I=1,10)
665 PRINT 740,(JSCENE(I),I=1,10)
670 PRINT*, ' '
675 PRINT 635,(WAVE(I),I=1,14)
680 PRINT 640,(RS20(I),I=1,14)
685 PRINT 645,(RSIR(I),I=1,14)
690 PRINT 650,(AJUP(I),I=1,14)
695 PRINT*, ' '
700 PRINT 800,CHRG
705 PRINT 805,FLUX
710 PRINT 810,RESP
715 PRINT 750,LOAD
720 PRINT 755,AMPL
725 PRINT 760,DARK
730 PRINT 765,X
735 PRINT 770,Y
740 680 FORMAT (' TCAM ',3X,14F6.3)
745 695 FORMAT (' TSYS ',3X,14F6.3)
750 700 FORMAT (' BB ',3X,14F6.3)
755 702 FORMAT (' TMA ',3X,14F6.3)
760 705 FORMAT (' TM ',3X,14F6.3)
765 715 FORMAT (' SNR ',3X,14F6.1)
770 720 FORMAT (' SNRAIM',3X,14F6.1)
775 722 FORMAT (' SPAT ',1X,10I9)
780 725 FORMAT (' SIGSYS',3X,10E9.3)
785 730 FORMAT (' SIGAVE',3X,10E9.3)
790 735 FORMAT (' JNOISE',3X,10E9.3)
795 740 FORMAT (' JSCENE',3X,10E9.3)
800 750 FORMAT (' THERMAL NOISE =',E10.2,' COUL')
805 755 FORMAT (' FET SHOT NOISE =',E10.2,' COUL')
810 760 FORMAT (' DARK CURRENT =',E10.2,' COUL')
815 765 FORMAT (' NOISE "X" =',E10.2,' COUL')
820 770 FORMAT (' NOISE "Y" =',E10.2,' COUL')
825 635 FORMAT (' WAVE ',3X,14I6)
830 640 FORMAT (' RS20 ',3X,14F6.3)
835 645 FORMAT (' RSIR ',3X,14F6.3)
840 650 FORMAT (' AJUP ',3X,14F6.3)
845 800 FORMAT (' CHARGE DENSITY =',E10.2,' AMPS/METER')
850 805 FORMAT (' FLUX =',E10.2,' WAT./METER')
855 810 FORMAT (' RESPONSIVITY =',E10.2,' AMPS/WATT')
860 STOP
865 END

```

ICCD PROGRAM LIST - ELECTROMAGNETIC FOCUS

```

100 PRINT*, 'ANALYTICAL MODEL OF INTENSIFIED CHARGE-COUPLED CAMERA'
105 PRINT*, 'WITH ELECTROMAGNETIC IMAGE SECTION'
110 DIMENSION SNRAIM(14), SNR(14), TM(14), TCAM(14)
115 DIMENSION TSYS(14), SPAT(14), SIGSYS(14), TIS(14), RS20(14)
120 DIMENSION BB(14), USCENE(14), UNOISE(14), SIGAVA(14)
125 DIMENSION RSIR(14), AJUP(14), WAVE(14), TMA(14), TFAR(14)
130 DIMENSION ALB(9), AUJ(9)
135 COMMON DIM(3), TAVA(14)
140 REAL IFET, IDARK, NTL, NTCL
145 10 READ(5,*, PROMPT='EXPOSURE(SEC), SPIN RATE(RPM), %
150 BANDWIDTH(:) EXPT, SPIN, BAND
155 20 READ(5,*, PROMPT='FOCAL LENGTH(M), F NUMBER, CONTRAST %
160 RATIO : ') FOC, FNUM, CR
165 30 READ(5,*, PROMPT='PHASE ANGLE, INCIDENCE ANGLE,*
170 REFLECTION ANGLE (DEGREES) : ') PA0, AID, RA0
175 40 READ(5,*, PROMPT='BODY NUMBER : ') I
180 DATA LBZ1, .92, .85, .49, .26, .61, .42, .42, .14/
185 DATA WJZ5, 2.5, 2.5, 2.5, 2.5, 2.5, 2.9, 5.4, 19.18, 30.1, 39.44/
190 PA=PA0/57.2958
195 AI=AID/57.2958
200 RA=RA0/57.2958
205 TL=.6
210 Q=1.602E-19
215 S20P=.0626
220 SIRP=.2036
225 AELEM=(20.E-6)**2
230 GT=2000.
235 IDARK=4.E-13*AELEM*1.E4
240 SNRL=10.
245 TN=1400.
250 TEMP=23.
255 BK=1.38E-23
260 RT=1.E9
265 IFET=7.E-3
270 CS=.2E-12
275 GMFET=13.4E-3
280 EC=1.E-5
285 NTL=2.E15
290 AL=40.
295 WIN=2.*3.1416/EXPT
300 TS=1.E-6
305 BC=BAND*2.
310 NTCL=2.E14
315 WC=2.*3.1416*BC
320 DATA RS20/ .14, .68, .96, .952, .791, .645, .501, .356, .211, .6
325 .085, .019, .011, .011, .011/
330 DATA RSIR/ .256, .545, .712, 1., .968, .859, .831, .753, .682, *
335 .615, .552, .493, .433, .416/
340 DATA AJUP/ .25, .31, .36, .42, .5, .5, .49, .49, .47, .44, *
345 .39, .34, .33, .32/
350 DATA TIS/ .995, .985, .97, .95, .94, .91, .87, .82, .75, .675, .6, .525, .45, .37/ -
355 DATA TFAR/ .96, .87, .74, .6, .464, .326, .274, .08, .05, .011, *

```

Reproduced from
best available copy.



```

360 .001,.001,.001,.001/
365 IF(T.EQ.1)GO TO 150
370 DO 100 K=1,14
375 AJUP(K)=1
380 100 CONTINUE
385 150 CONTINUE
390 DO 200 K=1,14
395 WAVE(K)=(250.+K*50.)
400 SUMF=SUMF+RS[R(K)*AJUP(K)*ALB(T)
405 SUMI=SUMI+RS[R(K)*AJUP(K)*RS20(K)*ALB(T)
410 200 CONTINUE
415 CONS=(SIRP*TL*COS(AI)*COS(RA))/(4.*AJJ(T)**2*FNJM**2)
420 FLUX=CONS*SUMF*500.
425 CURD=CONS*SUMI*500.*S20P
430 RESP=CURD/FLUX
435 CALL MTFAVA(FNJM, SPIN, EXPT, FOC, CR)
440 DO 300 K=1,14
445 SPAT(K)=K*5.E3
450 BBP=BBP+TTAR(K)**2
455 BB(K)=(BBP*5000.)/SPAT(K)
460 300 CONTINUE
465 SIGFLT=(2.*AELEM*CURD*EXPT*GT)*(1.-TN*EC)
470 ULOAD=SQRT(TEMP*BK/(RI*BAND))
475 JAMPL=SQRT((2./GMFET**2)*IFET*Q*BAND*CS**2)
480 JDARK=SQRT((2.*Q*IDARK*EXPT)+(2.*Q*TN*(DARK/BC))
485 XP=TEMP*(BK/Q)*AELEM
490 IF(WC.GE.1.0/TS) GO TO 500
495 Y=SQRT((NTCL*XP*TN/AL)*ALOG(1./(WC*TS))+(.4*NTCL*XP*TN/AL)**2)
500 GO TO 501
505 500 Y=SQRT((NTCL*XP*TN*4.)/(WC*TS*AL))*Q
510 501 CONTINUE
515 X=SQRT((NTL*XP/AL)*ALOG(1./(WIN*TS))+(4.*NTL*XP/AL)**2)
520 DO 400 K=1,14
525 USCENE(K)=SQRT((BB(K)**2*(GT+1.))*Q*AELEM*CURD*EXPT*GT)
530 UNOISE(K)=SQRT(ULOAD**2+JAMPL**2+JDARK**2+USCENE(K)**2+X**2+Y**2)
535 TCAM(K)=TTAR(K)*TIS(K)
540 TSCENE=(CR-1.)/(CR+1.)
545 TSYS(K)=TCAM(K)*JAVA(K)
550 SIGAVA(K)=SIGFLT*TCAM(K)
555 SIGSYS(K)=SIGFLT*TSYS(K)
560 SNRAIM(K)=SIGAVA(K)/UNOISE(K)
565 SNR(K)=SIGSYS(K)/UNOISE(K)
570 TMA(K)=SNRL/SNRAIM(K)
575 TM(K)=SNRL/SNR(K)
580 400 CONTINUE
585 PRINT 680,(TCAM(I), I=1,14)
590 PRINT 695,(TSYS(I), I=1,14)
595 PRINT 700,(BB(I), I=1,14)
600 PRINT 702,(TMA(I), I=1,14)

```

```

605 PRINT 705,(TM(I),I=1,14)
610 PRINT 715,(SNR(I),I=1,14)
615 PRINT 720,(SNRAIM(I),I=1,14)
620 PRINT*,' '
625 PRINT 722,(SPAT(I)/1000.,I=1,10)
630 PRINT 725,(SIGSYS(I),I=1,10)
635 PRINT 730,(SIGAVA(I),I=1,10)
640 PRINT 735,(JNOISE(I),I=1,10)
645 PRINT 740,(JSCENE(I),I=1,10)
650 PRINT*,' '
655 PRINT 635,(WAVE(I),I=1,14)
660 PRINT 640,(RS20(I),I=1,14)
665 PRINT 645,(RSIR(I),I=1,14)
670 PRINT 650,(AJJP(I),I=1,14)
675 PRINT*,' '
680 PRINT 800,CURD
685 PRINT 805,FLUX
690 PRINT 810,RESP
695 PRINT 750, JLOAD
700 PRINT 755, JAMPL
705 PRINT 760, JDARK
710 PRINT 765,x
715 PRINT 770,y
720 680 FORMAT (' TCAM ',3X,14F6.3)
725 695 FORMAT (' TSYS ',3X,14F6.3)
730 700 FORMAT (' BR ',3X,14F6.3)
735 702 FORMAT (' TMA ',3X,14F6.3)
740 705 FORMAT (' TM ',3X,14F6.3)
745 715 FORMAT (' SNR ',3X,14F6.1)
750 720 FORMAT (' SNRAIM',3X,14F6.1)
755 722 FORMAT (' SPAT ',1X,10I9)
760 725 FORMAT (' SIGSYS',3X,10E9.3)
765 730 FORMAT (' SIGAVE',3X,10E9.3)
770 735 FORMAT (' JNOISE',3X,10E9.3)
775 740 FORMAT (' JSCENE',3X,10E9.3)
780 750 FORMAT (' THERMAL NOISE =',E10.2,' COUL')
785 755 FORMAT (' FET SHOT NOISE =',E10.2,' COUL')
790 760 FORMAT (' DARK CURRENT =',E10.2,' COUL')
795 765 FORMAT (' NOISE "X" =',E10.2,' COUL')
800 770 FORMAT (' NOISE "Y" =',E10.2,' COUL')
805 635 FORMAT (' WAVE ',3X,14I6)
810 640 FORMAT (' RS20 ',3X,14F6.3)
815 645 FORMAT (' RSIR ',3X,14F6.3)
820 650 FORMAT (' AJJP ',3X,14F6.3)
825 800 FORMAT (' CHARGE DENSITY =',E10.2,' AMPS/SQ.METER')
830 805 FORMAT (' FLUX =',E10.2,' WATT/SQ.METER')
835 810 FORMAT (' RESPONSIVITY =',E10.2,' AMPS/WATT')
840 STOP
845 END

```

B.4.8

RBV PROGRAM LIST

```

L
1000 PRINT*, 'ANALYTICAL MODEL OF RETURN BEAM VIDICON'
1005 DIMENSION SNRAIM(14), SNR(14), TM(14), TCAM(14), TMES(14)
1010 DIMENSION TSYS(14), TELB(14), SPAT(14), SIGSYS(14), QEPC(14)
1015 DIMENSION BB(14), USCENE(14), UNOISE(14), SIGAVA(14)
1020 DIMENSION RSIR(14), AJJP(14), WAVE(14), TMA(14)
1025 COMMON DUM(3), TAVA(14), TTAR(14)
1030 REAL M, IFET
1035 10 READ(5,*, PROMPT='EXPOSURE(SEC), SPIN RATE(RPM), %
1040 BANDWIDTH :') EXPT, SPIN, BAND
1045 20 READ(5,*, PROMPT='FOCAL LENGTH(M), F NUMBER, CONTRAST %
1050 RATIO : ') FOC, FNUM, CR
1055 30 READ(5,*, PROMPT='PHASE ANGLE, INCIDENCE ANGLE, %
1060 REFLECTION ANGLE (DEGREES) :') PAD, AID, RAD
1065 PA=PAD/57.2958
1070 AI=AID/57.2958
1075 RA=RAD/57.2958
1080 TL=.6
1085 Q=1.602E-19
1090 C=2.998E8
1095 H=6.62E-34
1100 AUJ=5.2
1105 SIRP=.21
1110 D=20.E-6
1115 AELEM=(3.1416/4.)*D**2
1120 QEP=.47
1125 GM=1000.
1130 TEMP=233.
1135 BK=1.38E-23
1140 RL=2.E8
1145 IFET=7.E-3
1150 GMFET=13.4E-3
1155 CS=20.E-12
1160 TF=.55
1161 TL=.6
1165 T1=1.E-6
1170 RE=.3
1175 M=.3
1180 SEM=2.2
1185 SNRL=3.
1190 DATA QEPC/.001,.001,.001,.09,.275,.71,1.,.84,.38,.12,%
1195 .03,.001,.001,.001/
1200 DATA TELB/.98,.965,.94,.905,.855,.78,.72,.66,.61,.56,%
1205 .52,.46,.41,.36/
1210 DATA TMES/.99,.985,.98,.975,.97,.96,.95,.94,.92,.9,%
1215 .88,.86,.83,.8/
1220 DATA RSIR/.256,.545,.712,1.,.968,.859,.831,.753,.682,%
1225 .615,.552,.493,.443,.416/
1230 DATA AJJP/.25,.31,.36,.42,.5,.5,.49,.49,.47,.44,%
1235 .39,.34,.33,.32/
1240 DO 200 K=1,14
1245 WAVE(K)=(250.+K*50.)
1250 SUMF=SUMF+WAVE(K)*1.E-9*RSIR(K)*AJJP(K)

```

```

1255     SUMI=SUMI+WAVE(K)*1.E-9*RS[R(K)*AUJ[K]*QEPC(K)*QE]
1260     200 CONTINUE
1265     CONS=(SRP*TL*COS(AI)*COS(RA))/(4.*H*C*AUJ* 2*FNJM*2)
1270     FLUX=CONS*SUMF*500.
1275     CURD=CONS*Q*SUMI*500.
1280     RESP=CURD/FLUX
1285     QE=CURD/(FLUX*Q)
1290     CALL MFAVA(FNUM, SPIN, EXPT, FDC, CR)
1295     CALL VTAR(T1)
1300     PRINT*, ' '
1305     DO 300 K=1,14
1310     SPAT(K)=K*5.E3
1315     BBP=BBP+T1AR(K)**2*TELB(K)**2*TMES(K)**2
1320     BB(K)=(BBP*500.)/SPAT(K)
1325     300 CONTINUE
1330     SIGFLT=4.*BAND*AELEM*CURD*EXPT*GM*TF*RE
1335     UJ2=2.*GM**2*Q*BAND
1340     UJ1=SIGFLT/(2.*GM*TF*RE)
1345     UMILT=SQRT(UJ1*UJ2*TF*RE*(1.-M)/(M*(SEM-1.)))
1350     UREAD=SQRT(UJ1*UJ2*TF*RE/M)
1355     ULOAD=SQRT((4.*BK*TEMP*BAND)/RL)
1360     UAMPL=SQRT((8.*Q*(FET*BAND**3*CS**2)/GMFET**2)
1365     DO 400 K=1,14
1370     USCENE(K)=SQRT(BB(K)**2*TF**2*RE**2*(QE+1.)*UJ1*UJ2)
1375     UNOISE(K)=SQRT( ULOAD**2+UAMPL**2+UMILT**2*
1380     +UREAD**2+USCENE(K)**2)
1385     TCAM(K)=TFAR(K)*TELB(K)*TMES(K)
1390     TSCENE=(CR-1.)/(CR+1.)
1395     TSYS(K)=TCAM(K)*FAVA(K)
1400     SIGAVA(K)=SIGFLT*TCAM(K)
1405     SIGSYS(K)=SIGFLT*TSYS(K)
1410     SNRAIM(K)=SIGAVA(K)/UNOISE(K)
1415     SNR(K)=SIGSYS(K)/UNOISE(K)
1420     TMA(K)=SNRL/SNRAIM(K)
1425     TM(K)=SNRL/SNR(K)
1430     400 CONTINUE
1435     PRINT 625,(TELB(I), I=1,14)
1440     PRINT 626,(TMES(I), I=1,14)
1445     PRINT 680,(TCAM(I), I=1,14)
1450     PRINT 695,(TSYS(I), I=1,14)
1455     PRINT 700,(BB(I), I=1,14)
1460     PRINT 702,(TMA(I), I=1,14)
1465     PRINT 705,(TM(I), I=1,14)
1470     PRINT 715,(SNR(I), I=1,14)
1475     PRINT 720,(SNRAIM(I), I=1,14)
1480     PRINT*, ' '
1485     PRINT 722,(SPAT(I)/1000., I=1,10)
1490     PRINT 725,(SIGSYS(I), I=1,10)
1495     PRINT 730,(SIGAVA(I), I=1,10)
1500     PRINT 735,(UNOISE(I), I=1,10)
1505     PRINT 740,(USCENE(I), I=1,10)
1510     PRINT*, ' '

```

```

1515 PRINT 635,(WAVE(I),I=1,14)
1520 PRINT 640,(QEPC(I),I=1,14)
1525 PRINT 645,(RSIR(I),I=1,14)
1530 PRINT 650,(AJUP(I),I=1,14)
1535 PRINT*,' '
1540 PRINT 800,CURD
1545 PRINT 805, FLUX
1550 PRINT 810,QE
1555 PRINT 745, UREAD
1560 626 FORMAT(' TMESH ',3X,14F6.3)
1565 PRINT 750, ULOAD
1570 PRINT 755, UAMPL
1575 PRINT 760, UMILT
1580 625 FORMAT (' TELB ',3X,14F6.3)
1585 680 FORMAT (' TCAM ',3X,14F6.3)
1590 695 FORMAT (' TSYS ',3X,14F6.3)
1595 700 FORMAT (' BB ',3X,14F6.3)
1600 702 FORMAT(' TMA ',3X,14F6.3)
1605 705 FORMAT (' TM ',3X,14F6.3)
1610 715 FORMAT (' SNR ',3X,14F6.1)
1615 720 FORMAT (' SNRAIM',3X,14F6.1)
1620 722 FORMAT(' SPAT ',1X,10I9)
1625 725 FORMAT (' SIGSYS',3X,10E9.3)
1630 730 FORMAT (' SIGAVE',3X,10E9.3)
1635 735 FORMAT (' UNOISE',3X,10E9.3)
1640 740 FORMAT (' USCENE',3X,10E9.3)
1645 745 FORMAT(' READ NOISE =',E10.2,' AMPS')
1650 750 FORMAT(' THERMAL NOISE =',E10.2,' AMPS')
1655 755 FORMAT(' FET SHOT NOISE =',E10.2,' AMPS')
1660 760 FORMAT(' MULT NOISE =',E10.2,' AMPS')
1665 635 FORMAT(' WAVE ',3X,14I6)
1670 640 FORMAT(' QEPC ',3X,14F6.3)
1675 645 FORMAT(' RSIR ',3X,14F6.3)
1680 650 FORMAT(' AJUP ',3X,14F6.3)
1685 800 FORMAT(' CURRENT DENSITY= ',E10.2,' AMPS/SQ.METER')
1690 805 FORMAT(' FLUX= ',E10.2,' PHOTONS/SEC/SQ.METER')
1695 810 FORMAT(' INTEGRATED QE= ',E10.2,' ELECTRONS/PHOTON')
1700 STOP
1705 END

```

```

L
100 PRINT*, 'ANALYTICAL MODEL OF SILICON DIOXIDE VIDICON CAMERA'
105 DIMENSION SNRAIM(14), SNR(14), TM(14), TCAM(14)
110 DIMENSION TSYS(14), TIS(14), TELB(14), TFIB(14), SPAT(14)
115 DIMENSION BB(14), USCENE(14), UNOISE(14), SIGAVA(14)
120 DIMENSION SIGSYS(14), TMA(14)
125 COMMON CURD, FLUX, RESP, TAVA(14), TTAR(14)
130 REAL IFET
135 DATA TIS/.98,.9,.79,.65,.51,.36,.22,.08,.001,.001,%
140 .001,.001,.001,.001/
145 DATA TELB/.98,.965,.94,.905,.855,.78,.72,.66,.61,.56,%
150 .52,.46,.41,.36/
155 DATA TFIB/.995,.98,.95,.9,.83,.75,.67,.62,.54,.5,.45,%
160 .4,.35,.3/
165 10 READ(5,*,PROMPT='EXPOSURE(SEC), SPIN RATE(RPM), %
170 BANDWIDTH:') EXPT,SPIN,BAND
175 20 READ(5,*,PROMPT='FOCAL LENGTH(M), F NUMBER, CONTRAST %
180 RATIO : ') FOC, FNUM, CR
185 30 READ(5,*,PROMPT='PHASE ANGLE, INCIDENCE ANGLE,%
186 REFLECTION ANGLE (DEGREES) :') PAD,AID,RAD
190 PA=PAD/57.2958
191 AI=AID/57.2958
192 RA=RAD/57.2958
195 Q=1.602E-19
200 GT=100.
204 D=20.E-6
205 AELEM=(3.1416/4.)*D**2
206 TEMP=300.
207 BK=1.38E-23
208 RL=2.E8
209 IFET=7.E-3
210 GMFET=13.4E-3
211 CS=20.E-12
212 RE=.95
215 SNRL=3.
220 CALL IRWATT(PA,AI,RA,FNUM)
225 CALL MTFAVA(FNUM, SPIN, EXPT, FOC, CR)
230 CALL SDTAR
240 DO 300 K=1,14
245 SPAT(K)=K*5.E3
250 BBP=BBP+TTAR(K)**2*TELB(K)**2
255 BB(K)=(BBP*5000.)/SPAT(K)
260 300 CONTINUE
265 SIGFLT=4.*BAND*GT*AELEM*CURD*EXPT*RE
275 UREAD=SQRT(BAND*Q*SIGFLT)
276 ULOAD=SQRT((4.*BK*TEMP*BAND)/RL)
277 UAMPL=SQRT((8.*Q*IFET*BAND**3*CS**2)/GMFET**2)
280 DO 400 K=1,14
285 USCENE(K)=SQRT(BB(K)**2*(GT+1.)*BAND*Q*SIGFLT*RE)
290 UNOISE(K)=SQRT(ULOAD**2+UAMPL**2+UREAD**2)
295 +USCENE(K)**2)
300 TCAM(K)=TTAR(K)*TIS(K)*TFIB(K)*TELB(K)

```

```

305     TSCENE=(CR-1.)/(CR+1.)
310     TSYS(K)=TCAM(K)*TAVA(K)
315     SIGAVA(K)=SIGFLT*TCAM(K)
320     SIGSYS(K)=SIGFLT*TSYS(K)
325     SNRAIM(K)=SIGAVA(K)/UNOISE(K)
330     SNR(K)=SIGSYS(K)/UNOISE(K)
335     TMA(K)=SNRL/SNRAIM(K)
340     TM(K)=SNRL/SNR(K)
345     400 CONTINUE
350     PRINT 620,(TIS(I),I=1,14)
355     PRINT 625,(TELB(I),I=1,14)
360     PRINT 630,(TFIB(I),I=1,14)
365     PRINT 680,(TCAM(I),I=1,14)
370     PRINT 695,(TSYS(I),I=1,14)
375     PRINT 700,(BB(I),I=1,14)
380     PRINT 702,(TMA(I),I=1,14)
385     PRINT 705,(TM(I),I=1,14)
390     PRINT 715,(SNR(I),I=1,14)
395     PRINT 720,(SNRAIM(I),I=1,14)
400     PRINT*,' '
405     PRINT 722,(SPAT(I)/1000.,I=1,10)
410     PRINT 725,(SIGSYS(I),I=1,10)
415     PRINT 730,(SIGAVA(I),I=1,10)
420     PRINT 735,(UNOISE(I),I=1,10)
425     PRINT 740,(TSCENE(I),I=1,10)
430     PRINT*,' '
435     PRINT 745,UREAD
440     PRINT 750,ULOAD
445     PRINT 755,UAMPL
455     620 FORMAT(' TIS      ',3X,14F6.3)
460     625 FORMAT(' TELB     ',3X,14F6.3)
465     630 FORMAT(' TFIB     ',3X,14F6.3)
470     680 FORMAT(' TCAM     ',3X,14F6.3)
475     695 FORMAT(' TSYS     ',3X,14F6.3)
480     700 FORMAT(' BB       ',3X,14F6.3)
485     702 FORMAT(' TMA      ',3X,14F6.3)
490     705 FORMAT(' TM       ',3X,14F6.3)
495     715 FORMAT(' SNR      ',3X,14F6.1)
500     720 FORMAT(' SNRAIM  ',3X,14F6.1)
505     722 FORMAT(' SPAT    ',1X,10I9)
510     725 FORMAT(' SIGSYS   ',3X,10E9.3)
515     730 FORMAT(' SIGAVE   ',3X,10E9.3)
520     735 FORMAT(' UNOISE   ',3X,10E9.3)
525     740 FORMAT(' TSCENE   ',3X,10E9.3)
530     745 FORMAT(' READ NOISE =',E10.2,' AMPS')
535     750 FORMAT(' THERMAL NOISE =',E10.2,' AMPS')
540     755 FORMAT(' FET SHOT NOISE =',E10.2,' AMPS')
550     STOP
555     END

```

B.4.10 SILV PROGRAM LIST

```

100 PRINT*, 'ANALYTICAL MODEL OF SILICON VIDICON CAMERA'
105 DIMENSION SNRAIM(14), SNR(14), TM(14), TCAM(14)
110 DIMENSION TSYS(14), TELB(14), SPAT(14), SIGSYS(14), NEPC(14)
115 DIMENSION BB(14), USCENE(14), JNOISE(14), SIGAVA(14)
120 DIMENSION RSIR(14), AJJP(14), WAVE(14), TMA(14)
125 DIMENSION TII(14), TTAR(14), TLO(14), TDS(14), TFS(14)
130 COMMON DIM(3), TAVA(14)
135 REAL IDARK, IFET
140 10 READ(5,*, PROMPT='EXPOSURE (SEC), SPIN RATE (RPM), *
145 BANDWIDTH: ') EXPT, SPIN, BAND
150 20 READ(5,*, PROMPT='FOCAL LENGTH (M), F NUMBER, CONTRAST *
155 RATIO : ') FOC, FNJM, CR
160 30 READ(5,*, PROMPT='PHASE ANGLE, INCIDENCE ANGLE, *
165 REFLECTION ANGLE (DEGREES) : ') PAD, AID, RAD
170 40 READ(5,*, PROMPT='INTENSIFIER STAGE? YES=1., NO=0 : ') IASF
175 PA=PAD/57.2958
180 AI=AID/57.2958
185 RA=RAD/57.2958
190 RE=.8
195 TL=.6
200 Q=1.602E-19
205 C=2.948E8
210 H=6.62E-34
215 AIJ=5.2
220 SIRP=.2006
225 GI=22.
226 GC=.286E3
230 D=20.E-6
235 AELEM=(3.1416/4.)*D**2
240 IDARK=1.E-9
245 TEMP=233.
250 BK=1.38E-23
255 RL=2.E8
260 IFET=7.E-3
265 GMFET=13.4E-3
270 CS=20.E-12
275 SNRL=3.
280 DATA TELB/.98,.965,.94,.905,.85,.78,.72,.66,.61,.56,*
285 .52,.46,.41,.36/
290 DATA RSIR/.256,.545,.712,1.,.968,.859,.831,.753,.682,*
295 .615,.552,.493,.443,.416/
300 DATA AJJP/.25,.31,.36,.42,.5,.5,.49,.49,.47,.4,*
305 .39,.34,.33,.32/
310 DATA NEPC/.001,.5,.7,.8,.84,.82,.77,.7,.67,.6,*
315 .55,.4,.3,.2/
320 DATA TII/.87,.7,.55,.4,.29,.21,.16,.12,.08,.06,.05,.04,.03,.02/
325 DO 200 K=1,14
330 WAVE(K)=(250.+K*50.)
335 SUMF=SUMF+WAVE(K)*1.E-9*RSIR(K)*AJJP(K)
340 SUMI=SUMI+WAVE(K)*1.E-9*RSIR(K)*AJJP(K)*NEPC(K)
345 200 CONTINUE
350 CONS=(SIRP*TL*COS(AI)*COS(RA))/ (4.*H*C*AIJ**2*FNJM**2)
355 FLUX=CONS*SUMF*500.

```

```

360 CURD=CONS*Q*SUMI*500.
365 QE=CURD/(FLUX*Q)
370 CALL MFAVA(FNUM, SPIN, EXPT, FOC, CR)
375 DATA TLD/.967,.879,.765,.65,.52,.48,.41,.35,.19,.001,
.001,.001,.001,.001/
380 DATA TDS/.99,.958,.908,.84,.757,.662,.558,.45,.341,.234
,.133,.042,.001,.001/
385 DATA TFS/.911,.833,.764,.702,.648,.594,.55,.516,.481,.45.
.422,.396,.373,.352/
390 DO 290 K=1,14
395 T1AR(K)=TLD(K)*TDS(K)*TFS(K)
400 290 CONTINUE
405 PRINT 305,(TLD(I),I=1,14)
410 PRINT 310,(TDS(I),I=1,14)
415 PRINT 315,(TFS(I),I=1,14)
420 PRINT 320,(T1AR(I),I=1,14)
425 305 FORMAT(' TLD ',3X,14F6.3)
430 310 FORMAT(' TDS ',3X,14F6.3)
435 315 FORMAT(' TFS ',3X,14F6.3)
436 320 FORMAT(' T1AR ',3X,14F6.3)
440 PRINT*,' '
445 DO 300 K=1,14
450 SPAT(K)=K*.E3
455 BHP=BHP+T1AR(K)**2*TELB(K)**2
460 HB(K)=(BHP*5000.)/SPAT(K)
465 IF(STAGE)250,250,300
470 250 GI=1.
472 GC=1.
475 TII(K)=1.
485 300 CONTINUE
490 SIGFLT=4.*BAND*RE*GI*(AELEM*CURD*EXPT
495 UDARK=SQRT(2.*Q*(DARK*BAND)
500 UREAD=SQRT(BAND*Q*SIGFLT)
505 ULOAD=SQRT((4.*BK*TEMP*BAND)/RL)
510 UAMPL=SQRT((8.*Q*(FET*BAND)**3 CS* 2)/GMFET**2)
515 DO 400 K=1,10
520 USCENE(K)=SQRT((HB(K)**2*(QE+1.))*(BAND*RE*GC*Q*SIGFLT))
525 UNOISE(K)=SQRT(ULOAD**2+UAMPL**2+UDARK**2+UREAD**2*
530 +USCENE(K)**2)
535 TCAM(K)=T1AR(K)*TELB(K)*TII(K)
540 TSCENE=(CR-1.)/(CR+1.)
545 TSYS(K)=TCAM(K)*FAVA(K)
550 SIGAVA(K)=SIGFLT*TCAM(K)
555 SIGSYS(K)=SIGFLT*TSYS(K)
560 SNRAIM(K)=SIGAVA(K)/UNOISE(K)
565 SNR(K)=SIGSYS(K)/UNOISE(K)
570 TMA(K)=SNRL/SNRAIM(K)
575 TM(K)=SNRL/SNR(K)
580 400 CONTINUE
585 PRINT 625,(TELB(I),I=1,14)
590 PRINT 630,(TII(I),I=1,14)
595 PRINT 680,(TCAM(I),I=1,14)
600 PRINT 695,(TSYS(I),I=1,14)
605 PRINT 700,(HB(I),I=1,14)
610 PRINT 702,(TMA(I),I=1,14)

```

```

615 PRINT 705,(TM(I),I=1,14)
620 PRINT 715,(SNR(I),I=1,14)
625 PRINT 720,(SNRAIM(I),I=1,14)
630 PRINT*,*
635 PRINT 725,(SPAT(I)/10.0),I=1,14)
640 PRINT 725,(SIGSYS(I),I=1,10)
645 PRINT 730,(SIGAVE(I),I=1,10)
650 PRINT 735,(UNOISE(I),I=1,10)
655 PRINT 740,(USCENE(I),I=1,10)
660 PRINT*,*
665 PRINT 635,(WAVE(I),I=1,14)
670 PRINT 640,(QEPC(I),I=1,14)
675 PRINT 645,(RSIR(I),I=1,14)
680 PRINT 650,(AJUP(I),I=1,14)
685 PRINT*,*
690 PRINT 800,CURR)
695 PRINT 805,FLIX)
700 PRINT 810,QE)
705 PRINT 745,(READ)
710 PRINT 750,(LOAD)
715 PRINT 755,(JAMPL)
720 PRINT 760,(DARK)
725 625 FORMAT(' TELB ',3X,14F6.3)
730 630 FORMAT(' TI ',3X,14F6.3)
735 680 FORMAT(' TCAM ',3X,14F6.3)
740 695 FORMAT(' TSYN ',3X,14F6.3)
745 700 FORMAT(' BB ',3X,14F6.3)
750 702 FORMAT(' TMA ',3X,14F6.3)
755 705 FORMAT(' TM ',3X,14F6.3)
760 715 FORMAT(' SNR ',3X,14F6.1)
765 720 FORMAT(' SNRAIM',3X,14F6.1)
770 722 FORMAT(' SPAT ',1X,10I9)
775 725 FORMAT(' SIGSYS',3X,10E9.3)
780 730 FORMAT(' SIGAVE',3X,10E9.3)
785 735 FORMAT(' UNOISE',3X,10E9.3)
790 740 FORMAT(' USCENE',3X,10E9.3)
795 745 FORMAT(' READ NOISE =',E10.2,' AMPS')
800 750 FORMAT(' THERMAL NOISE =',E10.2,' AMPS')
805 755 FORMAT(' FET SHOT NOISE =',E10.2,' AMP')
810 760 FORMAT(' DARK CURRENT =',E10.2,' AMP')
815 635 FORMAT(' WAVE ',3X,14I6)
820 640 FORMAT(' QEPC ',3X,14F6.3)
825 645 FORMAT(' RSIR ',3X,14F6.3)
830 650 FORMAT(' AJUP ',3X,14F6.3)
835 800 FORMAT(' CURRENT DENSITY =',E10.2,' AMP/CM MEETOR')
840 805 FORMAT(' FLIX =',E10.2,' PHOTONS/SEC/CM MEETOR')
845 810 FORMAT(' INTEGRATED QE =',E10.2,' ELECTRONS/PHOTON')
850 STOP
855 END

```

B.4.11

SSV PROGRAM LIST - DOPED SELENIUM PHOTOCONDUCTOR

```

1010 PRINT*, 'ANALYTICAL MODEL OF SLOW SCAN VIDICON'
1015 PRINT*, 'DOPED SELENIUM PHOTOCONDUCTOR'
1020 DIMENSION SNRAIM(14), SNR(14), TM(14), TCAM(14)
1025 DIMENSION TSYS(14), TELB(14), SPAT(14), SIGSYS(14), QESR(14)
1030 DIMENSION BR(14), USCENE(14), UNOISE(14), SIGAVA(14)
1035 DIMENSION RSIR(14), AJJP(14), WAVE(14), TMA(14)
1040 DIMENSION TII(14)
1045 COMMON DIM(3), TAVA(14), TTAR(14)
1050 REAL IDARK, IFET
1055 QESP=.1
1060 10 READ(5,*, PROMPT='EXPOSURE(SEC), SPIN RATE(RPM), %
1065 BANDWIDTH: ') EXPT, SPIN, BAND
1070 20 READ(5,*, PROMPT='FOCAL LENGTH(M), F NUMBER, CONTRAST %
1075 RATIO : ') FOC, FNUM, CR
1080 30 READ(5,*, PROMPT='PHASE ANGLE, INCIDENCE ANGLE, %
1085 REFLECTION ANGLE (DEGREES): ') PAD, AID, RAD
1090 40 READ(5,*, PROMPT='INTENSIFIER STAGE? YES=1., NO=0 : ') STAGE
1095 PA=PAD/57.2958
1100 AI=AID/57.2958
1105 RA=RAD/57.2958
1110 RE=.5
1115 GI=36.
1120 GC=.171E3
1125 TL=.6
1130 T1=.5E-6
1135 Q=1.602E-19
1140 C=2.998E8
1145 H=6.62E-34
1150 AUJ=5.2
1155 SIRP=.2016
1160 AELEM=(20.E-6)**2
1165 IDARK=4.E-9
1170 TEMP=300.
1175 BK=1.38E-23
1180 RL=2.E8
1185 IFET=7.E-3
1190 GMFET=13.4E-3
1195 CS=20.E-12
1200 SNRL=3.
1205 DATA TII/.87,.7,.55,.4,.29,.21,.16,.12,.08,.06,.05,.04,.03,.02/
1210 QESP=.25
1215 DATA QESR/.85,.98,1.,.84,.6,.61,.3,.04,.001,.001,%
1220 .001,.001,.001,.001/
1225 DATA TELB/.98,.965,.94,.905,.855,.78,.72,.66,.61,.56,%
1230 .52,.46,.41,.36/
1235 DATA RSIR/.256,.545,.712,1.,.968,.859,.831,.753,.682,%
1240 .615,.552,.493,.443,.416/
1245 DATA AJJP/.25,.31,.36,.42,.5,.5,.49,.49,.47,.44,%
1250 .39,.34,.35,.32/
1255 DO 200 K=1,14
1260 WAVE(K)=250.+K*50.
1265 SUMF=SUMF+WAVE(K)*1.E-9*RSIR(K)*AJJP(K)

```

```

1255 SJMI=SIJMI+WAVE(K)*1.E-9*RI[CR(K)*AJIP(K)*QESP(K)
1260 20] CONTINUE
1265 CONS=(SIRP*TL*COS(RA)*COS(AD))/((4.*H*Q*AIJ* 2+FNIM* 2)
1270 FLUX=CONS*SIJMI*500.
1275 CURD=CONS*Q*SIJMI*500*QESP
1280 QE=CURD/(FLUX*Q)
1285 CALL MFAVA(FNUM, SPIN, EXPT, FOC, CR)
1290 CALL VFAR(TI)
1295 PRINT*,' '
1305 DO 300 K=1,14
1310 SPAT(K)=K*5.E3
1315 BHP=BHP+TFAR(K)* 2*TELB(K)*+2
1320 HB(K)=(BHP*5000.)/SPAT(K)
1325 IF(STAGE)250,250,300
1330 250 GI=1.
1335 300 GI=1.
1340 320 CONTINUE
1345 300 CONTINUE
1350 SIGFLT=4.*BAND*RE*GI*AELEM*CURD*EXPT
1355 ULOAD=SQRT((4.*BK*TEMP*BAND)/RL)
1360 JAMPL=SQRT((8.*Q*IFET*BAND)* 3*CS*+2)/GMFET* 2)
1365 UDARK=SQRT(2.*Q*(DARK*BAND))
1370 UREAD=SQRT(BAND*Q*SIGFLT)
1375 DO 400 K=1,14
1380 USCENE(K)=SQRT((HB(K)**2*((QE+1.))**2*(BAND*RE*GC*Q*SIGFLT))
1385 UNOISE(K)=SQRT(ULOAD**2+JAMPL**2+UDARK**2+UREAD**2*
1390 +USCENE(K)**2)
1395 TCAM(K)=TFAR(K)*TELB(K)*TII(K)
1400 TSCENE=(CR-1.)/(CR+1.)
1405 TSYS(K)=TCAM(K)*FAVA(K)
1410 SIGAVA(K)=SIGFLT*TCAM(K)
1415 SIGSYS(K)=SIGFLT*TSYS(K)
1420 SNRAIM(K)=SIGAVA(K)/UNOISE(K)
1425 SNR(K)=SIGSYS(K)/UNOISE(K)
1430 TMA(K)=SNRL/SNRAIM(K)
1435 TM(K)=SNRL/SNR(K)
1440 400 CONTINUE
1445 PRINT 625,(TELB(I), I=1,14)
1450 PRINT 630,(TII(I), I=1,14)
1455 PRINT 680,(TCAM(I), I=1,14)
1460 PRINT 695,(TSYS(I), I=1,14)
1465 PRINT 700,(HB(I), I=1,14)
1468 PRINT 702,(TMA(I), I=1,14)
1470 PRINT 705,(TM(I), I=1,14)
1475 PRINT 715,(SNR(I), I=1,14)
1480 PRINT 720,(SNRAIM(I), I=1,14)
1485 PRINT*,' '
1490 PRINT 722,(SPAT(I)/1000., I=1,10)
1495 PRINT 725,(SIGSYS(I), I=1,10)
1500 PRINT 730,(SIGAVA(I), I=1,10)
1505 PRINT 735,(UNOISE(I), I=1,10)
1510 PRINT 740,(USCENE(I), I=1,10)
1515 PRINT*,' '

```

```

1520 PRINT 635,(WAVE(I),I=1,14)
1525 PRINT 640,(QESR(I),I=1,14)
1530 PRINT 645,(RSIR(I),I=1,14)
1535 PRINT 650,(AJJP(I),I=1,14)
1540 PRINT*,' '
1545 PRINT 800,CURD
1550 PRINT 805, FLUX
1555 PRINT 810,QE
1560 PRINT 745, JREAD
1565 PRINT 750, JLOAD
1570 PRINT 755, JAMPL
1575 PRINT 760, JDARK
1580 625 FORMAT (' TELB ',3X,14F6.3)
1585 630 FORMAT (' TII ',3X,14F6.3)
1590 680 FORMAT (' TCAM ',3X,14F6.3)
1595 695 FORMAT (' TSYST ',3X,14F6.3)
1600 700 FORMAT (' BH ',3X,14F6.3)
1605 702 FORMAT (' TMA ',3X,14F6.3)
1610 705 FORMAT (' TM ',3X,14F6.3)
1615 715 FORMAT (' SNR ',3X,14F6.1)
1620 720 FORMAT (' SNRAIM',3X,14F6.1)
1625 722 FORMAT (' SPAT ',1X,10I9)
1630 725 FORMAT (' SIGSYS',3X,10E9.3)
1635 730 FORMAT (' SIGAVE',3X,10E9.3)
1640 735 FORMAT (' UNOISE',3X,10E9.3)
1645 740 FORMAT (' JSCENE',3X,10E9.3)
1650 745 FORMAT (' JREAD NOISE =',E10.2,' AMPS')
1655 750 FORMAT (' THERMAL NOISE =',E10.2,' AMPS')
1660 755 FORMAT (' FET SHOT NOISE =',E10.2,' AMPS')
1665 760 FORMAT (' DARK CURRENT =',E10.2,' AMPS')
1670 635 FORMAT (' WAVE ',3X,14I6)
1675 640 FORMAT (' QESR ',3X,14F6.3)
1680 645 FORMAT (' RSIR ',3X,14F6.3)
1685 650 FORMAT (' AJJP ',3X,14F6.3)
1690 800 FORMAT (' CURRENT DENSITY =',E10.2,' AMPS/SQ.METER')
1695 805 FORMAT (' FLUX =',E10.2,' PHOTONS/SEC/SQ.METER')
1700 810 FORMAT (' INTEGRATED QE =',E10.2,' ELECTRONS/PHOTOJ')
1705 STOP
1710 END

```

B.4.12 SSV PROGRAM LIST - ASOS

```

1000 PRINT*, 'ANALYTICAL MODEL OF SLOW SCAN VIDICON'
1005 PRINT*, 'ASOS PHOTOCONDUCTOR'
1010 DIMENSION SNRAIM(14), SNR(14), TM(14), TCAM(14)
1015 DIMENSION TSYS(14), TELB(14), SPAT(14), SIGSYS(14), QESR(14)
1020 DIMENSION BB(14), USCENE(14), UNOISE(14), SIGAVA(14)
1025 DIMENSION RSIR(14), AJUP(14), WAVE(14), TMA(14)
1030 DIMENSION TII(14)
1035 DIMENSION DIM(3), TAVA(14), TIAR(14)
1040 REAL IDARK, IFET
1045 WFSPE=.1
1050 DO READ(5,*, PROMPT='EXPOSURE(SEC), SPIN RATE(RPM), *
1055 BANDWIDTH(:) EXPT, SPIN, BAND
1060 DO READ(5,*, PROMPT='FOCAL LENGTH(M), F NUMBER, CONTRAST *
1065 RATIO : :) FOC, FNJM, CR
1070 DO READ(5,*, PROMPT='PHASE ANGLE, INCIDENCE ANGLE,*
1075 REFLECTION ANGLE (DEGREES): :) PAD, AID, RAD)
1080 DO READ(5,*, PROMPT='INTENSIFIER STAGE? YES=1., NO=0 : :) STAGE
1085 PA=PAD/57.2958
1090 AI=AID/57.2958
1095 RA=RAD/57.2958
1100 RE=.3
1105 GI=23.7
1106 GC=.14E3
1110 TL=.6
1112 T1=1.E-6
1120 DO READ(5,*, PROMPT='IDARK=4.E-9
1125 N=1.002E-19
1130 C=2.948E8
1135 H=6.2E-34
1140 AJU=.2
1145 SIRP=.206
1150 U=20.E-6
1151 AELFM=(3.1416/4.)*D**2
1155 IDARK=4.E-11
1160 TEMP=233.
1165 BK=1.38E-23
1170 RL=2.E8
1175 IFET=7.E-3
1180 GMFET=13.4E-3
1185 CS=20.E-12
1190 SNRL=3.
1195 DATA TII/.87,.7,.55,.4,.29,.21,.16,.12,.08,.06,.05,.04,.03,.02/
1200 QESP=.47
1205 DATA QESR/.001,.001,.001,.09,.275,.71,1.,.84,.38,.12,*
1210 .091,.01,.011,.001/
1215 DATA TELB/.98,.965,.94,.905,.85,.78,.72,.56,.51,.56,*
1220 .52,.46,.41,.36/
1225 DATA RSIR/.256,.545,.712,1.,.968,.859,.831,.753,.682,*
1230 .615,.542,.493,.443,.416/
1235 DATA AJUP/.25,.31,.36,.42,.5,.5,.49,.49,.47,.44,*
1240 .39,.34,.33,.32/
1245 DO 200 K=1,14

```



```

1250 WAVE(K)=250.+K*50.
1255 SUMF=SUMF+WAVE(K)*1.E-9*RSIR(K)*AJJP(K)
1260 SUMI=SUMI+WAVE(K)*1.E-9*RSIR(K)*AJJP(K)*QESR(K)
1265 200 CONTINUE
1270 CONS=(SIRP*TL*COS(RA)*COS(AI))/(4.*H*C*AUJ**2*FNJM**2)
1275 FLUX=CONS*SUMF*500.
1280 CURD=CONS*Q*SUMI*500*QESP
1285 QE=CURD/(FLUX*Q)
1290 CALL MTFAVA(FNJM, SPIN, EXPT, FOC, CR)
1295 CALL VTAR(T1)
1300 PRINT*, ' '
1305 DO 300 K=1,14
1310 SPAT(K)=K*5.E3
1315 BBP=BBP+TTAR(K)**2*TELB(K)**2
1320 BB(K)=(BBP*5000.)/SPAT(K)
1325 IF(STAGE)250,250,300
1330 250 GI=1.
1335 GC=1.
1340 TII(K)=1.
1345 320 CONTINUE
1350 300 CONTINUE
1355 SIGFLT=4.*BAND*RE*GI*AELEM*CURD*EXPT
1360 ULOAD=SQRT((4.*BK*TEMP*BAND)/RL)
1365 JAMPL=SQRT((8.*Q*IFET*BAND)**3*CS**2)/GMFET**2)
1370 UDARK=SQRT(2.*Q*IDARK*BAND)
1375 UREAD=SQRT(BAND*Q*SIGFLT)
1380 DO 400 K=1,14
1385 JSCENE(K)=SQRT((BB(K)**2*(QE+1.))*(BAND*RE*GC*Q*SIGFLT))
1390 JNOISE(K)=SQRT(ULOAD**2+JAMPL**2+UDARK**2+UREAD**2)
1395 JSCEN(K)**2)
1400 TCAM(K)=TTAR(K)*TELB(K)*TII(K)
1405 TSCENE=(CR-1.)/(CR+1.)
1410 TSYS(K)=TCAM(K)*TAVA(K)
1415 SIGAVA(K)=SIGFLT*TCAM(K)
1420 SIGSYS(K)=SIGFLT*TSYS(K)
1425 SNRAIM(K)=SIGAVA(K)/JNOISE(K)
1430 SNR(K)=SIGSYS(K)/JNOISE(K)
1435 TMA(K)=SNRL/SNRAIM(K)
1440 TM(K)=SNRL/SNR(K)
1445 400 CONTINUE
1450 PRINT 625,(TELB(I),I=1,14)
1455 PRINT 630,(TII(I),I=1,14)
1460 PRINT 680,(TCAM(I),I=1,14)
1465 PRINT 695,(TSYS(I),I=1,14)
1470 PRINT 700,(BB(I),I=1,14)
1475 PRINT 702,(TMA(I),I=1,14)
1480 PRINT 705,(TM(I),I=1,14)
1485 PRINT 715,(SNR(I),I=1,14)
1490 PRINT 720,(SNRAIM(I),I=1,14)
1495 PRINT*, ' '
1500 PRINT 720,(SPAT(I)/1000.,I=1,10)
1505 PRINT 725,(SIGSYS(I),I=1,10)
1510 PRINT 730,(SIGAVA(I),I=1,10)

```

```

1510 PRINT 735,(UNOISE(I),I=1,10)
1515 PRINT 740,(USCENE(I),I=1,10)
1520 PRINT*, ' '
1525 PRINT 635,(WAVE(I),I=1,14)
1530 PRINT 640,(QESR(I),I=1,14)
1535 PRINT 645,(RSIR(I),I=1,14)
1540 PRINT 650,(AJUP(I),I=1,14)
1545 PRINT*, ' '
1550 PRINT 800,CURD
1555 PRINT 805, FLUX
1560 PRINT 810,QE
1565 PRINT 745, UREAD
1570 PRINT 750, ILOAD
1575 PRINT 755, IAMPL
1580 PRINT 760, UDARK
1585 625 FORMAT (' TELB ',3X,14F6.3)
1590 630 FORMAT(' TIT ',3X,14F6.3)
1595 680 FORMAT (' TCAM ',3X,14F6.3)
1600 695 FORMAT (' TSYN ',3X,14F6.3)
1605 700 FORMAT (' BB ',3X,14F6.3)
1610 702 FORMAT(' TMA ',3X,14F6.3)
1615 705 FORMAT (' TM ',3X,14F6.3)
1620 715 FORMAT (' SNR ',3X,14F6.1)
1625 720 FORMAT (' SNRAIM',3X,14F6.1)
1630 722 FORMAT(' SPAT ',1X,10I9)
1635 725 FORMAT (' SIGSYS',3X,10E9.3)
1640 730 FORMAT (' SIGAVE',3X,10E9.3)
1645 735 FORMAT (' UNOISE',3X,10E9.3)
1650 740 FORMAT (' USCENE',3X,10E9.3)
1655 745 FORMAT(' READ NOISE =',E10.2,' AMPS')
1660 750 FORMAT(' THERMAL NOISE =',E10.2,' AMPS')
1665 755 FORMAT(' FET SHOT NOISE =',E10.2,' AMPS')
1670 760 FORMAT(' DARK CURRENT =',E10.2,' AMPS')
1675 635 FORMAT(' WAVE ',3X,14(b)
1680 640 FORMAT(' QESR ',3X,14F6.3)
1685 645 FORMAT(' RSIR ',3X,14F6.3)
1690 650 FORMAT(' AJUP ',3X,14F6.3)
1695 800 FORMAT(' CURRENT DENSITY= ',E10.2,' AMPS/SQ.METER')
1700 805 FORMAT(' FLUX= ',E10.2,' PHOTONS/SEC/SQ.METER')
1705 810 FORMAT(' INTEGRATED QE =',E10.2,'ELECTRONS/PHOTON')
1710 STOP
1715 END

```

B.4.13

SUBROUTINE IRWATM PROGRAM LIST

```

L
1000 SUBROUTINE IRWATM(PA, AI, RA, FNJM)
1005 DIMENSION RS20(14), RSIR(14), AJJP(14), WAVE(14)
1010 DIMENSION ALB(9), AUJ(9)
1015 COMMON CURD, FLUX, RESP
1020 TL=.6
1025 10 READ(5,*, PROMPT='BODY NUMBER :') T
1030 DATA ALB/1., .92, .85, .49, .26, .61, .42, .42, .14/
1035 DATA AUJ/5.2, 5.2, 5.2, 5.2, 5.2, 9.54, 19.18, 30.1, 39.44/
1040 S20P=.0626
1045 SIRP=.2006
1050 DATA RS20/ .14, .68, .96, .952, .791, .645, .501, .356, .211, *
1055 .085, .019, .001, .001, .001/
1060 DATA RSIR/.256, .545, .712, 1., .968, .859, .831, .753, .682, *
1065 .615, .52, .493, .443, .416/
1070 DATA AJJP/ .25, .31, .36, .42, .5, .5, .49, .49, .47, .44, *
1075 .39, .34, .33, .32/
1080 IF(T.EQ.1) GO TO 150
1085 DO 100 K=1,14
1090 AJJP(K)=1.
1105 100 CONTINUE
1110 150 CONTINUE
1115 DO 200 K=1,14
1120 WAVE(K)=250.+K*50.
1125 SUMI=SUMI+RSIR(K)*AJJP(K)*RS20(K)*ALB(T)
1130 SUMF=SUMF+RSIR(K)*AJJP(K)*ALB(T)
1135 200 CONTINUE
1140 CONS=(SIRP*TL*COS(AI)*COS(RA))/(4.*AUJ(T)**2*FNJM**2)
1145 CURD=S20P*CONS*SUMI*500.
1150 FLUX=CONS*SUMF*500.
1155 RESP=CURD/FLUX
1160 PRINT*, ' '
1165 PRINT*, ' '
1170 PRINT 635, (WAVE(I), I=1,14)
1175 PRINT 640, (RS20(I), I=1,14)
1180 PRINT 645, (RSIR(I), I=1,14)
1185 PRINT*, ' '
1190 PRINT 800, CURD
1195 PRINT 805, FLUX
1200 PRINT 810, RESP
1205 635 FORMAT(' WAVE ',3X,14I6)
1210 640 FORMAT(' RS20 ',3X,14F6.3)
1215 645 FORMAT(' RSIR ',3X,14F6.3)
1220 800 FORMAT(' CURRENT DENSITY= ',E10.2,' AMPS/SQ.METER')
1225 805 FORMAT(' FLUX= ',E10.2,' WATT/SQ.METER')
1230 810 FORMAT(' RESPONSIVITY= ',E10.2,' AMPS/WATT')
1235 RETURN
1240 END

```

B.4.14 SUBROUTINE SDTAR PROGRAM LIST

```
1000 SUBROUTINE SDTAR
1005 DIMENSION SPAT(14)
1010 COMMON DIM(17), T1AR(14)
1015 T1=.5E-6
1020 DK=3.9
1025 DO 200, K=1,14
1030 SPAT(K)=K*5.E3
1035 RPKT=(4.*3.1416*SPAT(K)*T1)
1040 T1AR(K)=((1.-EXP(-RPKT))/RPKT)*((2.*DK)/((DK+1.)+(DK-1.))*
1045 *EXP(-RPKT))
1050 IF (T1AR(K))185,185,186
1055 185 T1AR(K)=.001
1060 186 CONTINUE
1065 200 CONTINUE
1070 PRINT 320,(T1AR(I),I=1,14)
1075 320 FORMAT(' T1AR ',3X,14F6.3)
1080 RETURN
1085 END
```

B.4.15 SUBROUTINE VTAR PROGRAM LIST

```
1000 SUBROUTINE VTAR(T1)
1005 DIMENSION SPAT(14)
1010 COMMON DIM(17), T1AR(14)
1025 DO 200 K=1,14
1030 SPAT(K)=K*5.E3
1035 RPK=(4.*3.1416*SPAT(K))
1040 T1AR(K)=(1.-EXP(-RPK*T1))/(RPK*T1)
1045 IF(T1AR(K))185,185,186
1050 185 T1AR(K)=.001
1055 186 CONTINUE
1060 200 CONTINUE
1065 PRINT 320,(T1AR(I),I=1,14)
1070 320 FORMAT(' T1AR ',3X,14F6.3)
1075 RETURN
1080 END
```

REFERENCES

1. "Spaceborne Electronic Imaging Systems", NASA SP-8078, Space Vehicle Design Criteria, June, 1971.
2. "Study of Follow-on Pioneer Missions to Jupiter", Final Report, Vols. 1-3, TRW Systems, #20406-6004-RO-00, August 13, 1971.
3. "Grand Tour Outer Planet Missions Definition Phase", Report of the Imaging Science Team, February 1, 1972.
4. Kazan & Knoll, "Electronic Image Storage", Academic Press, 1968.
5. L. M. Biberman & S. Nudelman, "Photoelectronic Imaging Devices", Volume 2, Plenum Press, 1971.
6. L. Altman, "The New Concept for Memory and Imaging: Charge Coupling", Electronics, June 21, 1971.
7. W. S. Boyle & G. E. Smith, "Charge-coupled devices - A new approach to MIS device structures", IEEE Spectrum, July, 1971.
8. R. W. Engstrom & G. A. Robinson, "Choose the Tube for L³TV", Electro-Optical Systems Design, June, 1971.
9. Edward Eberhardt, "Source-Detector Spectral Matching Factors", Applied Optics, pp. 2037-47, October 1968.
10. Niels Jensen, "Optical and Photographic Reconnaissance Systems", John Wiley and Sons, pp. 73-76, 1967.
11. "The Practical Application of Modulation Transfer Functions", Symposium held at Perkin-Elmer, March 1963.
12. Irwin Krittman, "Resolution of Electrostatic Storage Targets", IEEE Transactions on Electron Devices, Vol. ED-10, No. 6, pp. 404-409, Nov. 1963.
13. M. H. Crowell and E. F. Labuda, "The Silicon-Diode-Array Camera Tube", Bell System Technical Journal, pp. 1481-1528, May-June 1969.
14. Frank Scott, "The Relationship Between Three-Bar Target Resolving Power and Modulation Transfer Function", presented at Perkin-Elmer, September 1965.

15. Otto H. Schade, "Resolving Power Functions and Integrals of High-Definition Television and Photographic Cameras - A New Concept of Image Evaluation", RCA Review, Vol. 32, December 1971.
16. Beck, A. J., ed., "Proceedings of the Jupiter Radiation Belt Workshop", JPL July 1971, NASA Tech. Memo #33-543.
17. Malanoski, R. J., Westinghouse Apollo Telescope Mount Camera Study.
18. Brucker, G. J., and Cope, A. D., "Radiation Sensitivity of Silicon Imaging Sensors on Missions to the Outer Planets", IEEE Trans. on Nuclear Science Vol. NS-19, No. 6, Dec. 1972.
19. Ando, K. J., "TOPS Silicon Vidicon Radiation Effects Study", JPL Interoffice Memo 3210-FY'71-212.
20. Barbe, D. F., "The Charge-Coupled Concept", Report on N.R.L. Progress, March 1972.
21. Wallmark, G., CBS Laboratories, Personal Communication.
22. Ando, K. J., "Electron Radiation Effects in the GEC Se-S Vidicon", JPL Interoffice Memo 8210-FY'72-023.
23. "Preliminary Mission Designs for Jupiter Orbiter Missions", NASA TM X-2565, May 1972.
24. "The Planet Jupiter, 1970", NASA SP-8069, December 1971.
25. "Orbital Imaging for Planetary Exploration-Imaging Sensor System Scaling Laws", Volume IV, IIT Research Institute, September 1970.
26. D. A. Kawachi, "Image Motion Due to Camera Rotation", Photogrammetric Engineering, Vol. 31, No. 5, pp. 861-867, September 1965.
27. D. A. Kawachi, "Image Motion and its Compensation for the Oblique Frame Camera", Photogrammetric Engineering, Volume 31, No. 1, pp. 154-165, January 1965.
28. "Remote Sensor Systems for Unmanned Planetary Missions", Contract No. NAS2-5647, North American Rockwell Space Division, September 1970.
29. Slater and Johnson, "A Study of Photographic and Spectrometric Subsystems for Voyager", Tech. Memo S-1, Astro Sciences Center, IIT Research Institute, Chicago, 1965.

30. A. M. Mohsen, "The Influence of Interface States on Incomplete Charge Transfer in Overlapping Gate Charge-Coupled Devices", IEEE Journal of Solid State Circuits, Vol. SC-8, No. 2, April 1973.
31. Swenson, B. L., et al, "Preliminary Mission Designs for Jupiter Orbiter Missions", NASA TM X-2565.
32. Bashe and Kennedy, "Martian Orbital Photographic Study", Technical Summary Report, NASA CR-61854, 1967.
33. Montgomery and Adams, "Optics and the Mariner Imaging Instrument", Applied Optics, Vol. 9, No. 2, Feb. 1970, p. 277.
34. Westinghouse booklet on image tubes.
35. Dr. Martin Green, Westinghouse, personal communication.
36. Miller, J. D., "Sensor Accessories", draft report of the Advanced Imagers and Scanners Group. Sect. 5, 27 November 1972. Sponsored by NASA Goddard.
37. Signetics Read-Write MOS Memory, similar to part No. 2682, but with 4096 bit storage. To be marketed starting December 1973.
38. "Electrostatic Camera Systems Functional Design Study", Final Report, NASA-CR-129093, Feb. 1972.
39. R. Johnson, S. Juchnowycz and R. Ruth, CBS Laboratories.
40. George Zivkovich et al, "Cost Prediction Model for Optical Experiments", No. X-262-66-502, NASA Goddard Space Flight Center, December 1966.
41. David Clemens, "A Cost Estimating Relationship for Radiometer Experiments and Sensors for Unmanned Satellites", No. X-264-71-510, NASA Goddard Space Flight Center, December 1971.
42. Boyd, A. J., "An Introduction to System Cost Modeling", Accession No. N72-30982, NTIS, May 1972.
43. Otto H. Schade, "An Evaluation of Photographic Image Quality and Resolving Power", Journal SMPTE, 73: 81-119, February 1964.
44. G. W. Timm and A. Van der Ziel, "Noise in Various Electron Multiplication Methods Used in Imaging Devices", IEEE Transactions on Electron Devices, Vol. ED-15, No. 5, pp. 314-320, May 1968.
45. Frederick A. Rosell, "Television Camera Tube Performance Data and Calculations", Photoelectronic Imaging Devices, Vol. 2, edited by Biberman and Nudelman, Plenum Press, pp. 527-577, 1971.

ABBREVIATIONS

AIM	aerial image modulation
ASOS	antimony trisulfide-oxisulfide
AU	astronomical unit
CCD	charge-coupled device
CER	cost estimating relationship
EBIC	electron-bombardment induced conductivity
ESC	electrostatic storage camera
FET	field effect transistor
V/H	velocity/height
ICCD	intensified charge-coupled device
II	image intensifier
IMC	image motion compensation
IO	image orthicon
IR	infrared
ISILV	intensified silicon vidicon
ISSV	intensified slow-scan vidicon
JPL	Jet Propulsion Laboratory
MIS	metal-insulator-semiconductor
MTBF	mean time between failures
MTF	modulation transfer function
NASA	National Aeronautics and Space Administration
RMS	root-mean-square
RTG	radioisotope thermoelectric generator

SDV	silicon dioxide vidicon
SEC	secondary electron conduction
SECV	secondary-electron-conduction vidicon
SiO ₂	silicon dioxide
SILV	silicon vidicon
SIT	silicon intensifier target
SITV	silicon intensifier target vidicon
SNR	signal-to-noise ratio
SSV	slow-scan vidicon